

**Integrated stratigraphy, astronomical dating and proxy records
of the Ain el Beida and Loulja sections (NW Morocco)**

Implications for regional climate change, glacial history and the Messinian Salinity Crisis

Erwin van der Laan

GEOLOGICA ULTRAIECTINA

Mededelingen van de
Faculteit Geowetenschappen
departement Aardwetenschappen
Universiteit Utrecht

No. 324

Members of the dissertation committee:

Dr. Elena Turco

Dipartimento di Scienze della Terra, Università degli Studi di Parma
Parma, Italy

Prof. dr. David Hodell

Department of Earth Sciences, University of Cambridge
Cambridge, United Kingdom

Prof. dr. Henk Brinkhuis

Department of Biology, Utrecht University
Utrecht, the Netherlands

Prof. dr. Gert J. de Lange

Department of Earth Sciences, Utrecht University
Utrecht, the Netherlands

This study was supported by the Netherlands Organisation for Scientific Research (NWO).

The research for this thesis was carried out at the Stratigraphy/Paleontology Group, Department of Earth Sciences, Utrecht University, Budapestlaan 4, 3584 CD, Utrecht, the Netherlands.

The author can be reached through e-mail; erremans@gmail.com

ISBN 978-90-5744-185-1

Graphic design: GeoMedia [7708], Faculty of Geosciences, Utrecht University

Integrated stratigraphy, astronomical dating and proxy records of the Ain el Beida and Loulja sections (NW Morocco)

Implications for regional climate change, glacial history and the Messinian Salinity Crisis

Geïntegreerde stratigrafie, astronomische datering en proxy data van de Ain el Beida en Loulja secties (NW Marokko)

Implicaties voor regionale klimaatverandering, glaciële geschiedenis en de 'saliniteitscrisis' van het Messiniën

(met een samenvatting in het Nederlands)

PROEFSCHRIFT

ter verkrijging van de graad van doctor aan de Universiteit Utrecht
op gezag van de rector magnificus, prof. dr. J.C. Stoof,
ingevolge het besluit van het college voor promoties
in het openbaar te verdedigen
donderdag 8 april 2010 des middags te 2.00 uur

door

Erwin van der Laan

geboren op 9 januari 1974
te Groningen

Promotor:
Prof. dr. G.J. van der Zwaan

Co-promotores
Dr. F.J. Hilgen
Dr. L.J. Lourens

Let the whirlwind blow
through the ice, the melting snows
Let the whirlwind blow
across the freezing skies
and the tiny lights below
Let the whirlwind blow

(from: Whirlwind, New Model Army)
Sullivan & Heaton, 1990

*“Doar broest de zee, doar hoelt de wind
Doar soest ’t aan diek en wad”*

(uit: Grönnens Laid, trad.)
Geert Teis Pzn., 1919

Voor Roelf, Jannie, Bootje, Willem, Sienie en Freerktje

Contents

Chapter 1	
Introduction and Summary	11
Chapter 2	
Revised astrochronology for the Ain el Beida section (Atlantic Morocco): No glacio-eustatic control for the onset of the Messinian Salinity Crisis	17
Chapter 3	
Regional climate and glacial control on high-resolution oxygen isotope records from Ain el Beida (latest Miocene, northwest Morocco): A cyclostratigraphic analysis in the depth and time domain	39
Chapter 4	
No major deglaciation across the Miocene-Pliocene boundary: Integrated stratigraphy and astronomical tuning of the Loulja sections (Bou Regreg area, NW Morocco)	67
Chapter 5	
Astronomical forcing of Northwest African climate and glacial history during the late Messinian (6.5-5.5 Ma)	103
Chapter 6	
Astronomical tuning as the basis for high resolution chronostratigraphy: The intricate history of the Messinian Salinity Crisis	145
Bibliography	155
Appendix 1	
Habitat characteristics of calcareous nannofossils	169
Appendix 2	
Habitat characteristics of planktonic foraminifera	177
Samenvatting in het Nederlands (Summary in Dutch)	179
Acknowledgements	183
Curriculum Vitae	185

Introduction and Summary

The open marine succession of late Miocene to early Pliocene age exposed in the Bou Regreg area in NW Morocco and located on the Atlantic side of the Mediterranean is studied with two main objectives:

- 1) to reconstruct the origin of the sedimentary colour cycles which are dominantly precession controlled and may be related to the well-known sapropels in the Mediterranean, and;
- 2) to provide a better understanding of the Messinian Salinity Crisis in the Mediterranean by investigating open marine parallel sections situated just outside one of the two marine gateways that connected the Mediterranean with the Atlantic prior, and possible also during, the crisis.

1.1 Sapropels

Sapropels are dark, organic-rich and often well-laminated layers that are frequently found in deep marine successions of the Mediterranean late Neogene and that have been intensively studied ever since they were first discovered. However, despite all these studies, the exact mechanism(s) behind sapropel formation is/are still not fully understood. This applies both to the underlying oscillatory climate system as well as to the classic controversy whether increased productivity or enhanced preservation is responsible for sapropel formation.

Sapropels were first studied by Bradley [1938] and Kullenberg [1952], who linked them to enhanced precipitation and run-off during glacial periods, causing basin-wide stagnation, following the idea that high-latitude glacials correspond to low-latitude pluvials [see Deuser et al., 1976]. They were related to enhanced melt-water outflow via the Black Sea during deglaciation when isotope studies revealed that Pleistocene sapropels correspond to interglacials rather than to glacials [e.g. Thunell et al., 1977].

However, the youngest, Holocene sapropel S1 proved to significantly post-date the major deglaciation, weakening the argument for a (de)glacial scenario of sapropel formation [Rossignol-Strick et al., 1982]. By contrast, this sapropel coincided in time with enhanced precipitation at equatorial latitudes, which led to the now widely held view that sapropels of late Pleistocene age are controlled by precession induced variations in African monsoonal intensity. More specifically, precession minima, when Earth resides in perihelion during boreal summer, resulted in Northern Hemisphere summer insolation maxima and, hence, monsoonal precipitation maxima. Through Nile river run-off, the heavy rains led to a low-salinity surface layer in the eastern Mediterranean, resulting in a reduction of the deepwater flux and, hence, in stagnant bottom waters and sapropel formation [Rossignol-Strick et al., 1982].

It further became evident that all sapropels and related carbonate cycles in the Mediterranean late Neogene essentially have the same origin, being related to the same dominantly precession controlled climate system. The system comprises an additional but weak(er) obliquity influence and results in “dry-wet” climate oscillations. As mentioned above, the climate system held most widely responsible for sapropel formation is the African monsoon [e.g., Rossignol-Strick et al., 1982; Ruddiman, 2007]. However, it has been argued that simultaneous increases in fluvial outflow from the northern borderlands of the Mediterranean may have played an additional role in lowering sea surface salinities [Rossignol-Strick, 1987; Rohling and Hilgen, 1991]. Such simultaneously enhanced northern contributions can not be directly linked to the African monsoon but has to be related to the Atlantic system. Indeed, studies from lacustrine successions of the Pleistocene of Italy, the Pliocene of Greece and the Miocene of Spain have produced compelling evidence for dominantly precession controlled variations in climate that regulated lake level [e.g., Van Vugt et al., 1998; Steenbrink et al., 1999; Abdul Aziz et al., 2003]. Moreover, the Miocene sections in Spain also revealed an additional influence of obliquity [Abdul Aziz et al., 2003].

Climate modeling of orbital extremes confirmed the orbital precession scenario for the African monsoon [Kutzbach, 1981; Tuenter et al., 2003]. In addition, the results of the modeling experiments hinted at a remote obliquity control on the African monsoon that largely results from the heating of the Eurasian landmass at higher latitudes, thus explaining the constant obliquity influence on sapropel formation. However, the results of the climate modeling also pointed at the potential influence of the Atlantic system through precession and obliquity induced changes in winter precipitation [SON, Tuenter, 2004]. Combining the outcome of the climate modeling with a Mediterranean circulation model suggests that sea surface salinities during February, thought to be critical for sapropel formation, were most affected by orbitally induced changes in net evaporation across the basin rather than by enhanced outflow of the Nile or the northern rivers [Meijer and Tuenter, 2007]; these changes are largely controlled by the Atlantic system.

A logical first place to investigate the direct influence of orbitally induced changes in the Atlantic system is the Atlantic side of the Mediterranean. These areas are located outside the Mediterranean and outside the – direct and indirect – influence of the African monsoon. Indications for an Atlantic influence came from a detailed study of Pliocene well logs [gamma-ray, sonic; Sierro et al., 2000] from the Gulf of Cadiz. The logs revealed patterns that are identical to the patterns observed in sapropels and associated carbonate cycles in the classical Rossello composite section, including intricate details related to precession-obliquity interference [Sierro et al., 2000]. Unfortunately no cores were available for high-resolution multi-proxy studies at these sites.

The open marine succession of late Miocene to early Pliocene age exposed in the Bou Regreg area on the Atlantic side of NW Morocco provides an excellent opportunity to carry out such a multi-proxy study of the potential influence of orbitally controlled changes in the Atlantic system. These successions have initially been studied to establish a calcareous plankton biostratigraphy with the aim to determine their age [e.g., Wernli, 1977]. However, the sections exposed along road-cuts and in open clay pits also revealed prominent and intriguing colour cycles. Cita and Ryan [1978] were the first to describe these cycles, which they interpreted as to have a climatic origin. The cycle pattern was studied in detail by Dick Benson and co-workers [1995] who established an astronomical tuning of the cycles in the Ain el Beida section using image analysis techniques in combination with signature template comparison.

All the above led us to decide to carry out 1) an integrated stratigraphic study to establish tuned age models for the Ain el Beida and Loulja sections located in the Bou Regreg area followed by 2) a multi-proxy study of the colour cycles with the aim to unravel their origin.

1.2 Messinian salinity crisis and glacial history

Apart from the colour cycles, the sediments in the Bou Regreg area are important because they cover the entire Messinian in an open marine succession at the time that the Mediterranean became progressively isolated from the Atlantic Ocean and huge amounts of evaporites were deposited during the so-called Messinian salinity crisis (MSC; in fact the base of the Messinian is formally defined through its GSSP in the Oued Akrech section in the Bou Regreg area [Hilgen et al., 2000]). As such it provides an invaluable open marine parallel section of the MSC located in a critical area just outside one of the two gateways connecting the Mediterranean with the Atlantic prior to and possibly also during – part of – the crisis.

The notion of the existence of a Messinian salinity crisis was initially based on the study of land-based evaporite occurrences in marginal basins [e.g., Ogniben, 1957; Ruggieri, 1967]. However, a major impetus came from the study of deep-sea cores that were recovered during DSDP legs 13 and 42, which revealed the presence of vast amounts of evaporites in the deep central basins of the Mediterranean [Hsü et al., 1973]. Over the next decades, the origin of the MSC and the supposedly associated sea-level lowering due to evaporitic drawdown, became subject of intense debate, with the shallow-marine versus deep-marine nature of the evaporitic sediments, and a tectonic versus glacio-eustatic climate control on the progressive deterioration of the Atlantic-Mediterranean connection as main controversies.

However, it also became clear that these controversies could only be solved by a much improved age model for Messinian successions both within the Mediterranean as well as outside the Mediterranean. With the advent of integrated high-resolution stratigraphy and astronomical tuning in the early nineteen-nineties, time was ripe for the next step in understanding the MSC. The Miocene-Pliocene boundary marking the abrupt reflooding of the Mediterranean following the end of the MSC was dated astronomically at 5.33 Ma [Lourens et al., 1996]. In addition a tuned age model was constructed for the pre-evaporitic Messinian, dating the basin-wide synchronous onset of the main evaporitic phase of the MSC at 5.96 Ma [Krijgsman et al., 1999a]. Despite its distinct cyclicity, tuning of the evaporite succession proved more problematical and was mainly based on correlating successive cycles starting from the onset of evaporite formation upwards and from the Miocene-Pliocene boundary downwards to precession and insolation, leaving a short but substantial gap of ~ 80,000 years between the Lower and Upper Evaporite unit [Krijgsman et al., 2001]. Recently, attempts have been made to improve this initial tuned age model for the Messinian evaporites [e.g., Manzi et al., 2009].

However, to correctly interpret the progress and evolution of the MSC, it is of crucial importance that the same time interval is also studied in unprecedented detail in a tuned open marine succession, using a multi-proxy approach to detect and separate tectonic control from regional and global climate change. For instance, stable oxygen isotopes in benthic foraminiferal carbonate can be used to reconstruct changes in ice volume which may have influenced sea-level in the

progressively shallowing corridor(s) and, thereby, Atlantic-Mediterranean water exchange. Such glaciations were already inferred for the late Miocene [e.g., Peck et al., 1979] and have been linked to 41-kyr minima in obliquity (minima in NH summer insolation at high latitudes) resulting in the construction of a stable oxygen isotope stratigraphic timeframe for this period in time [e.g., Shackleton and Hall, 1997; Hodell et al., 1994]. The reconstruction and timing of the Messinian glacial history and its potential causal connection with the MSC is one of the prime goals of this study. This history can then be compared in detail with the Pliocene-Pleistocene glacial history in terms of astronomical control and phase relations with the orbital parameters, also by varying the values for the tidal dissipation and dynamical ellipticity in the astronomical solution.

Preferably this succession should have been deposited close to one of the gateways at that time in order to trace potential changes in water exchange. So apart from the cyclic nature, we also studied the open marine succession in the Bou Regreg area and then especially the Ain el Beida and Loulja sections to better understand the forcing mechanisms behind the MSC.

1.3 Summary of the investigation

The main goal of this thesis is to provide a better understanding of the origin of the sedimentary colour cycles in the Bou Regreg area in Northwest Morocco. These cycles of Late Miocene to early Pliocene age were already thought to be precession controlled and may be equivalents of the well-known sapropels from the Mediterranean of Pliocene-Pleistocene age. In addition, by studying these late Miocene open marine parallel sections on the Atlantic side of the Mediterranean, a better understanding of the Messinian salinity crisis is anticipated. The focus hereby is to discriminate between tectonic influences and global and regional climate variations in initiating and ending the crisis, and on the phase relations between the individual astronomical forcing parameters and the resulting response in proxy climate indicators.

To start with, a high-resolution integrated stratigraphy and tuned age model was established for the Ain el Beida (AEB) section that is presented in **Chapter 2**. Initial age control using magnetostratigraphy and biostratigraphy already pointed to a precessional origin of the basic sedimentary colour cycles. Moreover, the 44 basic cycles reveal a 1:5:20 ratio that is commonly observed in sediment records that are influenced by precession and eccentricity. The cycles have been astronomically tuned to the 65°N insolation target curve of the La93_(1,1) solution [Laskar et al., 1993], which was the latest and most accurate astronomical solution available at that time. The tuning resulted in a late Messinian age for the AEB section, ranging from 6.47 to 5.52 Ma. The detailed stable isotopic and quantitative analyses on planktonic foraminifera revealed that the reddish layers are characterized by minima in $\delta^{18}\text{O}$ and maxima in *Globigerinoides*, suggesting that they are the equivalent of sapropels in the Mediterranean. Within the newly established astrochronology, new ages were obtained for all bioevents, magnetic reversals and also for the peak glacial stages TG22 (5.79 Ma), TG20 (5.75 Ma) and TG12 (5.55 Ma) in the stable oxygen isotope records that clearly revealed an obliquity controlled 41-kyr glacial cyclicity. Stages TG22 and TG20, previously linked to the onset of evaporite formation in the Mediterranean, clearly post-date this event by ~ 200 kyr. Moreover, there is no indication that the initiation of the MSC at 5.96 Ma is associated with a major eustatic sea-level drop, as there is no significant correlative peak in the benthic oxygen isotope record.

In **Chapter 3** we elaborate on the transformation of the $\delta^{18}\text{O}$ depth series of AEB into time series. It appeared that the ratio of spectral peaks in the depth and time domain were not constant and are caused by changes in sedimentation rate that are positively correlated with precession amplitude and by a long-term trend in the sedimentation rate. We constructed a simple model of nonlinear response of sedimentation rate to the eccentricity modulation of the precession amplitude to simulate the observed changes in spectral peak position. Cross-spectral analysis revealed that the $\delta^{18}\text{O}$ related precession signal varies in-phase with the ETP record, a combined record of Eccentricity, Tilt (Obliquity) and negative precession. This in-phase relationship is partly due to the tuning procedure adopted in Chapter 1. The $\delta^{18}\text{O}$ related obliquity signal revealed a small lag to obliquity of ~ 2 kyr which is slightly reduced at the time of the MSC. We attribute this lag to the obliquity-paced slow buildup of ice caps while the precession signal dominantly reflects regional climate changes in the same way as was previously shown for sapropels of Pliocene–Pleistocene age in the Mediterranean. The $\delta^{18}\text{O}$ records of AEB fit well in a newly established global oxygen isotope framework that reflects glacial history during the latest Miocene (late Messinian).

The studied part of the AEB section ends at 5.52 Ma, just after peak glacial stage TG12. Therefore the section does not cover the end of the Messinian salinity crisis and reflooding of the Mediterranean dated at 5.33 Ma [Lourens et al., 1996]. We thus had to extend the integrated (cyclo) stratigraphic framework in the Bou Regreg area upwards to include the Miocene–Pliocene (M–P) boundary interval. This was accomplished with the help of a new section, named Loulja, located close to Ain el Beida. This section is exposed in two quarries that were already assumed to be younger in age than AEB. The integrated stratigraphy of the Loulja–A and –B sections is presented in **Chapter 4**. The older Loulja–A section revealed a dominantly precession driven colour cyclicity similar to that at AEB, and the astronomical tuning to precession resulted in an age for the Loulja–A and –B sections between 5.59 and 5.12 Ma. At this stage, a new astronomical solution had become available, termed La04_(1,1) [Laskar et al., 2004], which showed only minor differences in the age (~ 1 kyr) of age control points as compared to the older solution La93_(1,1). The astronomical tuning of the Loulja–A section implied an overlap of about 80,000 years with the AEB section and that the M–P boundary was reached. As for AEB, the $\delta^{18}\text{O}$ signal of Loulja–A was found to be dominantly obliquity controlled. The M–P boundary, however, coincides with a minor, precession-related shift to lighter $\delta^{18}\text{O}$ values. This shift does not seem to coincide with the interglacial stage TG5 as previously assumed [e.g., Shackleton et al., 1995b] but with an extra, weak obliquity related cycle between interglacial stages TG7 and TG5. We therefore conclude that other factors than glacio-eustatic sea level rise, such as tectonics or headward fluvial erosion, played a critical role in the reflooding of the Mediterranean. The major deglaciation step between stages TG12 and TG11 at ~ 5.54 Ma, however, could well be linked to the onset of the deposition of the Upper Evaporite unit in the Mediterranean, suggesting that the associated sea level rise may at least be partly responsible for the onset of intermittently restricted conditions after the main desiccation phase.

To further examine the origin of the colour cycles and their content, a high-resolution multi-proxy study was carried out on the AEB section. The results are shown in **Chapter 5**. We couple the precession related variations in the colour cycles and in the chemical composition of the sediments to ‘dry-wet’ oscillations, whereby more humid conditions in Northwest Africa occurred during precession minima, while more arid conditions prevailed during precession maxima. This scenario is linked to the Atlantic climate system rather than to the African monsoon because of the location

of Ain el Beida that is probably out of reach of the influence of the monsoon. Furthermore, planktonic foraminifera and calcareous nannofossil assemblages showed an important precession component as well, indicating that sea surface temperatures (SST) increased during the humid phases while productivity increased during the more arid phases. Both short and long-term eccentricity cycles can also be clearly recognized in many of the studied proxies, which is explained by a non-linear climatic response to precession forcing. Overall more humid climate conditions existed during eccentricity maxima. Apart from the precession related variations, obliquity-controlled glacial-interglacial cycles dominate the planktonic and benthic $\delta^{18}\text{O}$ records of AEB, and to a lesser degree SST and humidity (i.e. Ti/Al) variations in Northwest Africa. We attribute the observed warmer and wetter climates during interglacial periods to more active Atlantic depressions, associated with a direct thermal response to the waning ice sheets. The obliquity-controlled stable carbon isotope records of AEB are inversely related to the oxygen isotope records, with more depleted values during glacial stages. This is also known from the Pliocene and Pleistocene, and the resemblance of the AEB $\delta^{13}\text{C}$ records and those from the open ocean may point to large-scale glacial-controlled variations in the deep-sea carbon reservoir. The planktonic $\delta^{13}\text{C}$ record showed in addition a marked $\sim 1.0\text{‰}$ negative excursion at 6.0 Ma, which is coupled to a final step in the closure of the Rifian Corridor, restricting the outflow of Mediterranean water enriched in $\delta^{13}\text{C}$.

Finally, **Chapter 6** gives an overview of the potential of astronomical tuning in establishing a high resolution chronostratigraphy, in this case applied to the MSC in the Mediterranean. It is stated that both tectonic gateway closure and climate evolution played a role in the evolution of the MSC. The climate factor can be subdivided in dominantly precession controlled regional climate change and dominant obliquity driven glacial cycles. The application of an integrated high-resolution stratigraphy in combination with an astronomical tuned age model resulted in a much better understanding of the various successive stages of the MSC and of the forcing factors that were responsible, or not, for its stepwise evolution.

Revised astrochronology for the Ain el Beida section (Atlantic Morocco): No glacio-eustatic control for the onset of the Messinian Salinity Crisis

with W. Krijgsman¹, S. Gaboardi², F.J. Hilgen³, S. Iaccarino² and E. de Kaenel⁴

¹*Paleomagnetic laboratory "Fort Hoofddijk", Budapestlaan 17, 3584 CD Utrecht, The Netherlands*

²*Dip. di Scienze della Terra, Università di Parma, Parco Area della Scienze 1571A, 43100 Parma, Italy*

³*IPPU, Utrecht University, Budapestlaan 4, 3584 CD Utrecht, The Netherlands*

⁴*DPR, Matile 51, CH-2000 Neuchâtel, Switzerland*

This chapter has been published in *Stratigraphy* as: Krijgsman, W., S. Gaboardi, F.J. Hilgen, S. Iaccarino, E. de Kaenel, and E. van der Laan, 2004. Revised astrochronology for the Ain el Beida section (Atlantic Morocco): No glacio-eustatic control for the onset of the Messinian Salinity Crisis, *Stratigraphy*, 1, 87-101.

Abstract

Glacio-eustatic sea level lowering has often been proposed as a key mechanism for explaining the onset of the Mediterranean evaporites during the Messinian Salinity Crisis (MSC). To examine the role of glacio-eustasy during the progressive isolation of the Mediterranean in more detail, we reinvestigated the Ain el Beida quarry section that is located at the Atlantic margin of Morocco and therefore free of destructive MSC-related complications. The section consists of deep marine, cyclically bedded (reddish/beige), silty marls of late Messinian age. The reddish layers reveal the same characteristic signals as found in the Mediterranean sapropels (*Globigerinoides* spp. maxima and $\delta^{18}\text{O}$ minima), suggesting that they correspond to precession minima and, hence, (boreal) summer insolation maxima. We have established an integrated stratigraphy (calcareous plankton biostratigraphy, magnetostratigraphy, stable isotope stratigraphy and cyclostratigraphy) and an astronomical tuning of the Ain el Beida section by using conventional techniques and calibration methods. The astronomical ages for the biostratigraphic events and paleomagnetic reversals are in good agreement with the Mediterranean chronology, and confirm our cyclostratigraphic correlations. Stable isotope analyses reveal that the peak glacial stages TG22 and TG20 clearly post-date the initiation of the Messinian evaporites in the Mediterranean and that there is no evidence for a glacio-eustatic control for the onset of the MSC. Only the TG12-11 transition seems to correspond to a major intra-MSC event, i.e. the beginning of the Upper Evaporites. The typical Lago Mare facies of the Upper Evaporites was thus deposited during warmer climate conditions and associated higher global sealevel stands.

2.1 Introduction

Ever since the discovery of thick Messinian evaporites all over the Mediterranean sea floor [Hsü et al. 1973; Ryan et al., 1973], scientific debate has been directed to the question if the so-called Messinian Salinity Crisis (MSC) had been initiated by regional tectonic activity in the Gibraltar area or by global glacio-eustatic sea level changes [Clauzon et al., 1996; Hodell et al., 1994, 2001; Kastens, 1992; Krijgsman et al., 1999a; Weijermars, 1988]. This controversy was impossible to solve by using MSC sequences because in the Mediterranean Basin it is extremely difficult to distinguish tectonic from climatic signals. The geological record from the open ocean provides continuous Messinian sequences that are relatively free of tectonic activity and less seriously affected by the MSC [Hodell et al., 2001; Shackleton et al., 1995a]. The sedimentary archives from the Atlantic Ocean should thus allow a successful study of the role of glacio-eustatic sea level on the major lithological changes of the MSC, provided that a high-resolution astronomical time frame for both the Mediterranean and the Atlantic Messinian is available.

Benson and coworkers inferred that the best place to study the sedimentary expression of the MSC in the ocean archives is on the Atlantic margin of Morocco, because the Rifian Corridor was thought to have been the final marine connection that exchanged waters between Mediterranean and Atlantic during the Miocene [Benson et al., 1991, 1995; Benson and Rakic-El Bied, 1996; Hodell et al., 1989, 1994]. Atlantic Morocco is one of the few areas in the world where a complete late Miocene marine succession can be studied on land. The sections and drill holes of the Bou Regreg valley, nearby Rabat, comprise a continuous stratigraphic sequence without the destructive effects of the MSC [Benson and Rakic-El Bied, 1996; Benson et al., 1991]. As a result, these marine deposits contain the complete history of climatic and paleoceanographic conditions during the Messinian and serve as important stratigraphic links between Mediterranean and deep sea sequences [Hodell et al., 1994]. In addition, Benson et al. [1995] established an astronomical tuning for the late Messinian sediments of the Ain el Beida section using image analysis techniques in combination with signature template comparison. At that time, however, detailed correlations to the MSC events were still hampered by the absence of a high-resolution astrochronology for the Mediterranean pre-evaporite deposits.

Recently, an astronomical polarity time scale (APTS) has been developed for the Mediterranean Messinian [Hilgen and Krijgsman, 1999; Krijgsman et al., 1999a, 2001] and astronomical ages were obtained for nine major Mediterranean planktonic foraminiferal events and all the Messinian paleomagnetic reversals [Hilgen et al., 1995; Krijgsman et al., 1999a; Sierro et al., 2001]. The astronomical ages for the magnetic reversals are in good agreement with ages derived from sea floor spreading rates [Krijgsman et al., 1999a] and with the astrochronology for the South Atlantic [Shackleton and Crowhurst, 1997]. However, significant discrepancies exist – also for biostratigraphic events – with the astrochronology of the Ain el Beida section [Benson et al., 1995]. These discrepancies might be related to the image analysis technique used by Benson et al. [1995] instead of the more conventional tuning methods, because the astrochronology of the nearby but older Oued Akrech section proved to be in excellent agreement with the Mediterranean record [Hilgen et al., 2000].

The discrepancies in the astronomical ages hamper a straightforward and detailed comparison between the Mediterranean and open ocean records. For this reason, we have decided to restudy the Ain el Beida quarry section using similar techniques as in the Mediterranean sections. In this paper, the astronomical ages for all sedimentary cycles, bioevents and paleomagnetic reversals of Ain el Beida are obtained by tuning the characteristic sedimentary cycle patterns to the 65° Nlat

summer insolation curve of the Laskar et al. [1993] and [2004] solutions, thus allowing us to evaluate the synchronous and diachronous nature of bioevents in the Atlantic and Mediterranean records. Furthermore, the benthic oxygen isotope record of Ain el Beida can be compared with the Mediterranean event stratigraphy to investigate the possible relation between glacio-eustatic sea level changes and the onset of the MSC. The astronomical tuning of the Ain el Beida section will in addition provide the high-resolution age model necessary for detailed paleoclimatic and paleoceanographic studies directed at the stability of phase relations.

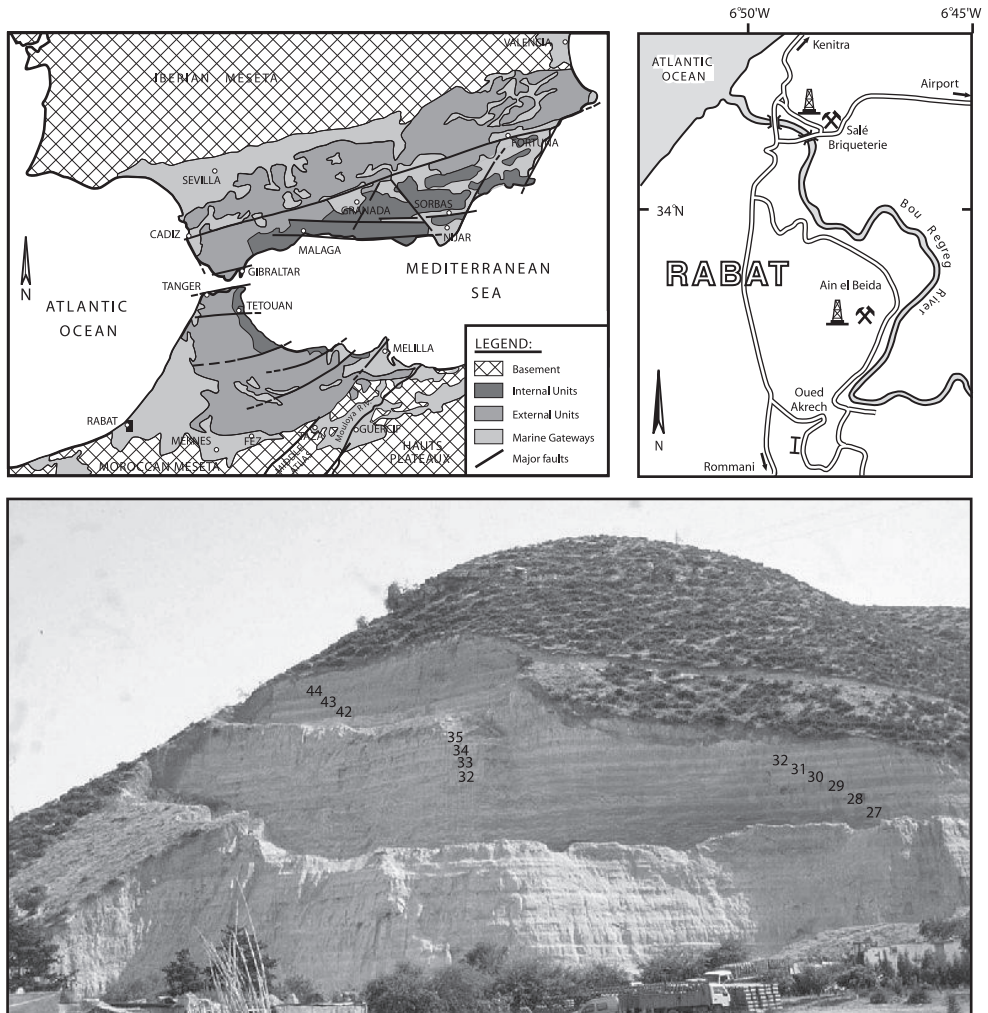


Figure 2.1 Simplified geological sketch map of the Gibraltar area (upper left), showing the Bou Regreg area near Rabat in the context of the marine Atlantic-Mediterranean gateways during the late Miocene. The detailed map of the Bou Regreg area (upper right, after Benson et al., 1991) showing the location of the Ain el Beida quarry section, the Tortonian/Messinian GSSP section of Oued Akrech, and the Salé quarry. The photograph of the Ain el Beida section (bottom) is taken several years after our sampling campaign in 1996. The quarry phase is constantly changing due to ongoing excavations. Numbers in the picture correspond to AEB cycles.

2.2 Background studies

The Ain el Beida section is located in a brick quarry along the Bou Regreg river, a few kilometres south of Rabat (Fig. 2.1). It consists of deep marine, cyclically bedded, silty marls of late Miocene age, which are locally referred to as the “Blue Marls” as they appear when freshly exposed. The first studies of Ain el Beida dealt with the planktonic foraminiferal biostratigraphy of the Moroccan Neogene [Feinberg and Lorenz, 1970; Wernli 1977]. Cita and Ryan [1978] were the first to investigate the section in search of the sedimentary expression of the MSC outside the Mediterranean. Moreover, they already noticed the correlation potential of the sedimentary cyclicity, which they interpreted to have a climatic origin.

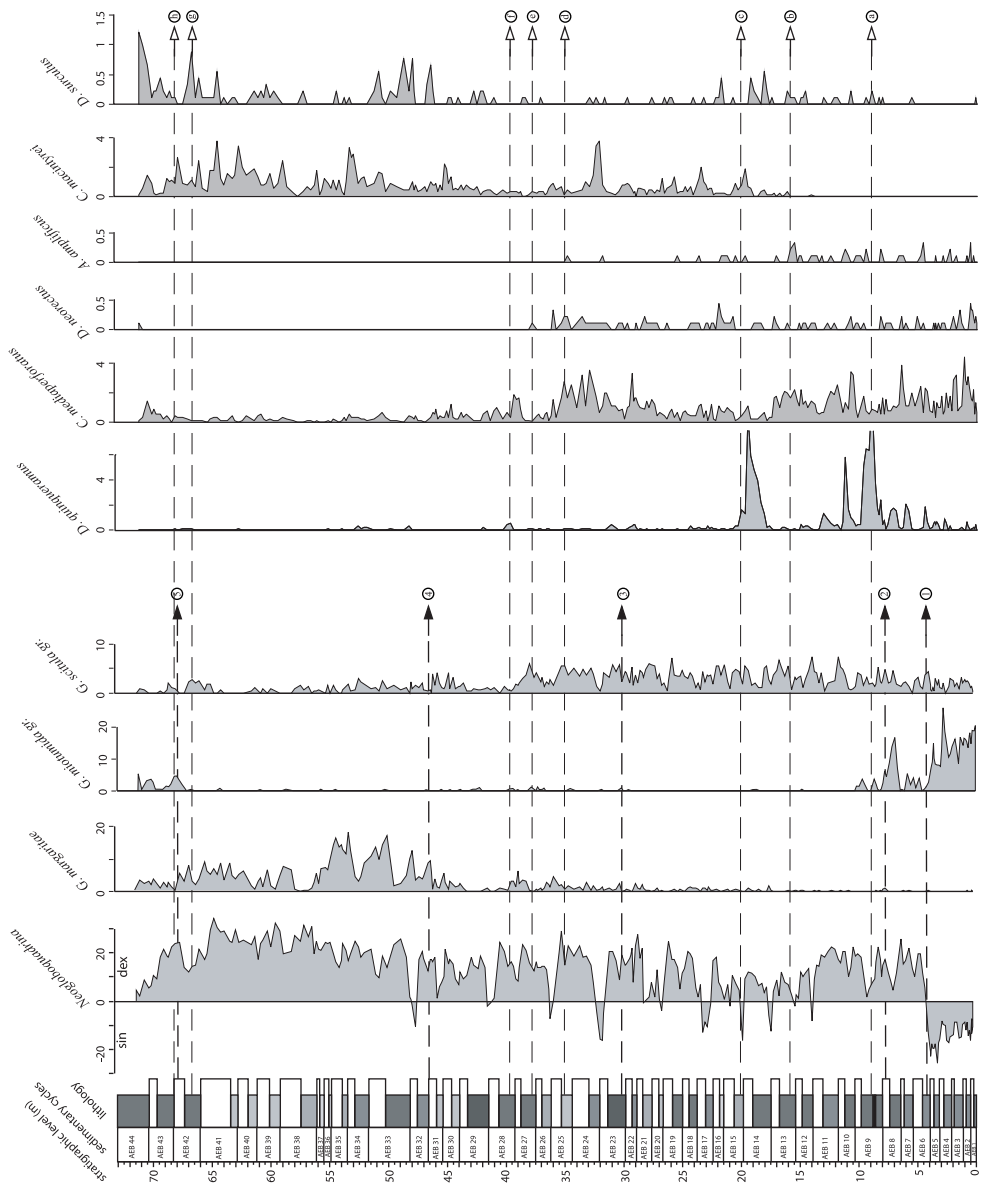
The stratigraphic importance of the Bou Regreg area significantly increased with the drilling of long cores at Ain el Beida and Salé, allowing a detailed study of the entire stratigraphic interval between 7.5 and 4.4 Ma [Benson et al., 1991; Hodell et al., 1994]. Planktonic and benthic foraminifera, calcareous nannofossil, and ostracod studies have resulted in a detailed biostratigraphic frame for the Messinian of Atlantic Morocco, although discrepancies exist in the location of several biostratigraphic events between Ain el Beida and Salé [Benson et al., 1991, 1995; Benson and Rakic-El Bied, 1996; Hodell et al., 1989, 1994]. The paleomagnetic signal is reported as very good in the fresh drill cores and sufficiently strong in the outcrops [Benson et al., 1995; Hodell et al., 1994]. Consequently, the magnetic polarity sequences of both Ain el Beida and Salé allow a straightforward correlation to the geomagnetic polarity time scale (GPTS). Oxygen isotope studies display regular variations with an estimated period of 40 kyr and are interpreted to reflect changes in global ice volume caused by obliquity-induced (41 kyr) changes in solar insolation at high latitudes [Hodell et al., 1994]. By contrast, the basal sedimentary cyclicity was inferred to reflect the climatic precession signal (19 and 23 kyr) and was used to establish an astronomical tuning for the Ain el Beida section [Benson et al., 1995]. Finally, Benson and Rakic-El Bied [1996] have proposed the Ain el Beida section as the Global Stratotype Section and Point (GSSP) of the Pliocene, but this was never accepted. The boundary has recently been formally defined at the base of the Trubi Formation in the Eraclea Minoa section of Sicily at 5.33 Ma [Van Couvering et al., 2000].

→ **Figure 2.2** Cyclostratigraphy and calcareous plankton biostratigraphy of the Ain el Beida section. In the lithological column a distinction was made in the colour intensity of the reddish layers on a scale from 1 to 10. Quantitative distribution patterns of planktonic foraminiferal and calcareous nannofossil (horizontal nannofossil scale is in specimens/mm²) marker species and the position of the main events: Planktonic foraminifera – 1) Main sinistral to dextral coiling change of *Neoglobobadrina acostaensis*; 2) *Globorotalia miotumida* last regular occurrence (LRO) and *Globorotalia margaritae* first occurrence (FO); 3) decrease of dextrally coiled *Globorotalia scitula*; 4) base of *G. margaritae* acme; and 5) top of *G. margaritae* acme. Calcareous nannofossils – a) top of *Discoaster quinqueramus* acme; b) *Amaurolithus amplifucus* last regular occurrence (LRO) and *Calcidiscus macintyreii* (>11 mm) first regular occurrence (FRO); c) *Discoaster quinqueramus* LCO; d) *Amaurolithus amplifucus* LO and *Cryptococcolithus mediaperforatus* LCO; e) *Discoaster neorectus* (>20 mm) LO; f) *Discoaster quinqueramus* (>20 mm) LO; g) *Discoaster surculus* FCO; and h) *Discoaster quinqueramus* LO. The stratigraphic position (and ages) of the events is summarized in Table 2.2.

2.3 Integrated stratigraphy of Ain el Beida

2.3.1 Cyclostratigraphy

Colour cycles in the Ain el Beida section consist of regular alternations of indurated light beige coloured marls and softer, more clayey and reddish coloured marls. Apart from measuring bedding thickness, a visual distinction was made, on a scale from 1 to 10, in the colour intensity of the reddish layers (Fig. 2.2). In addition to the field observations, the colour of the collected samples was measured with a Minolta CM-508I spectrophotometer. The resulting red-green component



(a-values) of the colour records, which were measured on both wet and dry samples, matches the cyclicity observed in the field (Fig. 2.3).

In total 44 cycles were recognized at Ain el Beida. The thickness of the cycles ranges from 60–350 cm with an average thickness of 165 cm. The interval between cycles AEB 34 and AEB 42 is the most difficult part of the section; lithological colour variations are less distinct, thus complicating the determination of the exact number of cycles. The reddish coloured marls, and to a lesser extent the beige marls, reveal marked changes in thickness alternations of thicker and thinner beds in successive cycles (AEB 15–23). Intervals in which the contrast between red and

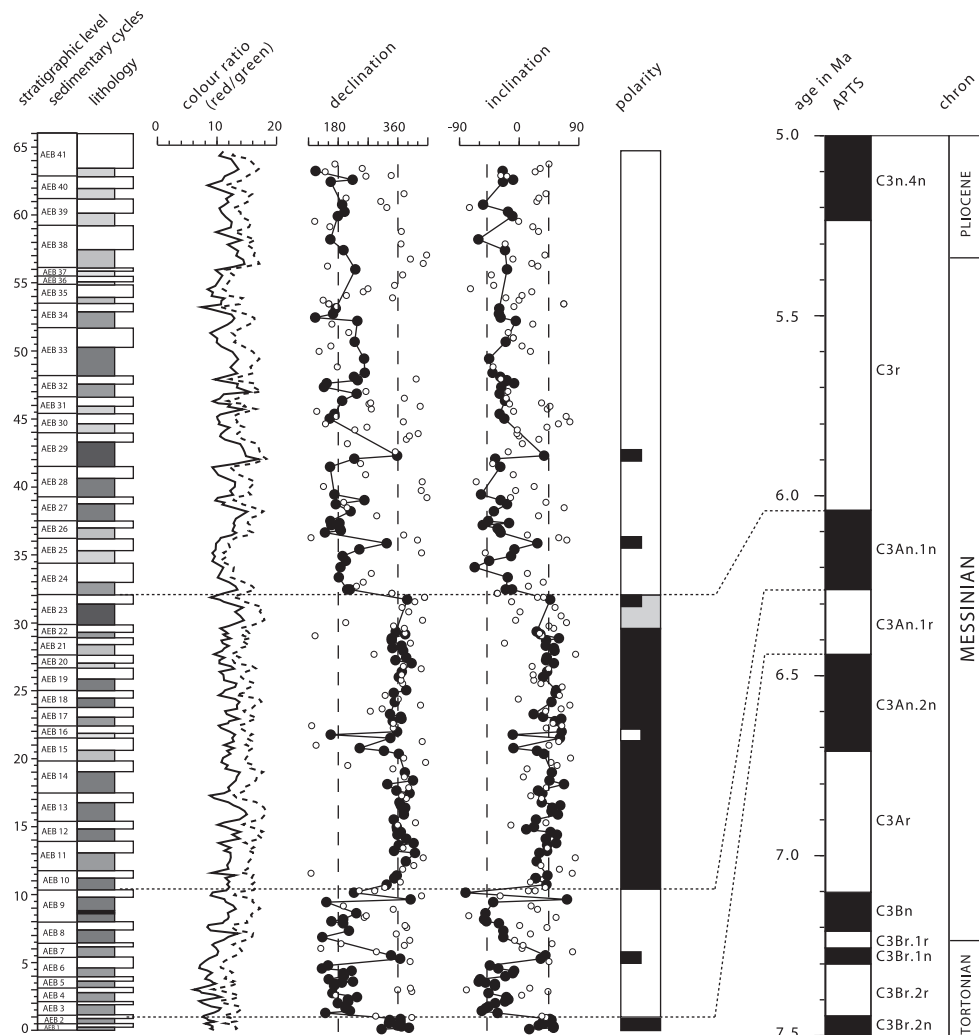


Figure 2.3 Paleomagnetic and colour ratio data from the Ain el Beida section and correlation to the APTS. Solid (open) circles in the declination and inclination curves denote reliable (unreliable) results (see text for explanation). In the polarity column black (white) denotes normal (reversed) polarity intervals. The colour reflectance records (a-values) are measured on dry (solid line) and wet (dashed line) samples.

beige marls is conspicuous, alternate with intervals of less distinct variations. Thick and prominent reddish layers usually reappear every five basic sedimentary cycles (AEB 9, AEB 13/14, AEB 19, AEB 23, AEB 28/29, AEB 33/34, AEB 38, AEB 42/43/44). Intervals marked by thicker and more prominent reddish layers can also be distinguished on a larger scale. These intervals (AEB 8-13, AEB 27-34 and AEB 42-44) contain 7 or 8 cycles but this number increases to slightly less than 20 when the less distinct cycles below or above are as well included in the count. This 1:5:20 ratio is commonly observed in sedimentary records where both precession and eccentricity play a role.

2.3.2 Biostratigraphy

2.3.2.1 Planktonic foraminifera

Micropaleontological analysis started with counting all planktonic foraminifera in the >125 mm fraction of 297 samples processed at the Department of Earth Sciences in Parma. Per sample, 250-300 specimens were counted in splits (using an Otto microsplitter) and identified at the species level. Preservation is generally good and on average better in the reddish than in the beige layers. The detrital component is generally poor. The low number of foraminiferal fragments (more common in the beige layers) excludes dissolution effects, while the number of undeterminable specimens is related to their small size, not to bad preservation. The planktonic foraminiferal biostratigraphy is based on the qualitative and quantitative records of several marker species, which allowed the recognition of the following events in stratigraphic order (Fig. 2.2):

- 1) the sinistral to dextral coiling change of *Neogloboquadrina acostaensis*
- 2) the *Globorotalia miotumida* last regular occurrence (LRO) and the *Globorotalia margaritae* first occurrence (FO)
- 3) the decrease of dextrally coiled *Globorotalia scitula*
- 4) the base of the acme of *G. margaritae*
- 5) the top of the acme of *G. margaritae*

The same events were recognised earlier by Sierro et al. [1993] and Benson et al. [1996] although a detailed comparison shows significant differences which need some discussion.

The shift of *Neogloboquadrina* coiling was recognised earlier in the study area [Benson and Rakic-El Bied 1996; Bossio et al., 1976; Cita and Ryan 1978; Hodell et al., 1989], while Sierro et al. [1993] recognised the same event (their PF-Event 4) in the NE Atlantic, the North Betic and South Rifian gateways, and the western Mediterranean. The sharp shift from sinistral to dextral coiling of *N. acostaensis* in cycle AEB 6 is followed, however, by 12 more or less pronounced sinistral influxes, most of them located in the interval between AEB 11 to AEB 32 (Fig. 2.2). Benson et al. [1995] only recognised 7 influxes, which is most likely related to a lower sample resolution. These influxes are commonly confined to the beige layers, apart from the influxes in AEB 20 and AEB 21, which include the red layer of cycle AEB 20.

Globorotalia margaritae is initially very rare and shows a regular increase in abundance to the upper part of the section where the *G. margaritae* acme is situated (Fig. 2.2). The base of the acme at 43 metres is coincident with a decrease in *Globorotalia juanai*. This event should be equated with PF-Event 6, although it occurs at a much higher level above PF-Event 5 than reported by Sierro et al. [1993]. Moreover, the top of the acme in the uppermost part of the section does not correspond to a real drop in abundance, as this taxon is still common in the Pliocene [Benson and Rakic-El Bied, 1996].

The *Globorotalia miotumida* group shows a distribution pattern characterised by a sharp decrease and last regular occurrence (LRO) in AEB 8, which coincides with the *G. margaritae* FO. This event directly postdates the sinistral to dextral coiling of *N. acostaensis* (Fig. 2.2) and closely corresponds to PF-Event 5 [Sierro et al., 1993]. Higher in the section, the *G. miotumida* group is very rare and randomly distributed up to AEB 42, where a second influx occurs.

Globorotalia scitula is dominantly dextral throughout the section, but from the middle part (39 metres) upward dextral forms decrease and sinistral specimens become more abundant. This decrease corresponds to PF-Event D that Sierro et al. [1993] consider useful for Atlantic-Mediterranean correlations.

Finally, *Globoquadrina altispira* is common in the lower part of the section, becomes rare upward, but is common again in the uppermost part. *Sphaeroidinellopsis* is regularly present throughout the section but is never common.

2.3.2.2 Calcareous nannofossils

The standard calcareous nannofossil biostratigraphy for the Messinian only comprises two bioevents, the *Amaurolithus primus* and/or *Amaurolithus delicatus* FO and the *Discoaster quinqueramus* LO [Martini, 1971; Okada and Bukry 1980]. In the present study, an attempt is made to determine additional biohorizons and bioevents to improve the biostratigraphic resolution of the late Messinian. A total of 297 samples were processed in the laboratory of DeKaenel Paleo Research (DPR) in Neuchâtel, Switzerland, using the settling methodology reported in De Kaenel and Villa [1996]. This settling technique uses a constant volume of sediment, and provides a uniform dispersion of calcareous nannofossils on each slide. Preservation is generally very good and abundance and diversity are very similar between the reddish and beige layers. The results reveal eight important events (Fig. 2.2):

- a) the top of an acme zone of *Discoaster quinqueramus*
- b) the *Amaurolithus amplificus* last regular occurrence (LRO) and the *Calcidiscus macintyreii* (>11 mm) first regular occurrence (FRO)
- c) the *Discoaster quinqueramus* LCO
- d) the *Amaurolithus amplificus* LO and the *Cryptococcolithus mediaperforatus* LCO
- e) the *Discoaster neorectus* (>20 mm) LO
- f) the *Discoaster quinqueramus* (>20 mm) LO
- g) the *Discoaster surculus* FCO
- h) the *Discoaster quinqueramus* LO

The top of an acme zone of *D. quinqueramus* (Fig. 2.2; only specimens with a prominent knob were included) is recorded in the reddish layer of AEB 9 and is marked by a drop in abundance from 11 specimens per mm² to 6 specimens per mm². This acme is not related to dissolution. The *D. quinqueramus* LCO is marked by the last important drop in abundance from 9 to 1.6 specimens per mm² and finally to 0.3 specimens per mm² and is recorded in the reddish layer of AEB 15 (Fig. 2.2). Rakic el Bied and Benson, [1996] recorded this event in Ain el Beida at an older level, directly following the sinistral to dextral coiling change of *Neogloboquadrina acostaensis*. The abundance of *D. quinqueramus* in the upper part of its range is very low, especially when compared to the records of the western Atlantic Ocean [Backman and Raffi 1997]. Nevertheless, even this weak distribution pattern provides some clear biostratigraphic signals. The *D. quinqueramus* (>20 mm) LO corresponds to the *D. quinqueramus* LRO and occurs in the reddish layer of AEB 28. The *D. quinqueramus* LO, which is used in most biostratigraphic zonal schemes, occurs at the boundary

between AEB 42 and AEB 43. Rakic el Bied and Benson [1996] recorded this event at a much older level (in C3An.1n). According to them, this event predates the *Globorotalia miotumida* LO and postdates the main sinistral to dextral coiling change of *Neogloquadrina acostaensis*.

Amaurolithus amplificus is rare but consistently recorded within the lower part of the section up to AEB 13. The *A. amplificus* LRO coincides with the *C. macintyreii* (>11 mm) FRO and occurs in the reddish layer of AEB 13 (Fig. 2.2). The *A. amplificus* LO is recorded in the reddish layer of AEB 25. The *A. amplificus* LO has been recognised in different oceans [e.g., Backman and Raffi 1997, Gartner 1992, Mazzei et al., 1979, Raffi and Flores 1995, Rio et al., 1990].

The *C. macintyreii* (>11 mm) FRO corresponds to the recurrence of morphotypes larger than 11 mm (morphotype A of Knappertsbusch [2000]). Very often, *C. macintyreii* (>11 mm) is not recorded in the lower part of the Messinian, but reoccurs in the upper part. A similar absence interval was observed for *Reticulofenestra pseudumbilica* (>7 mm) [Gartner 1992, Raffi and Flores 1995, Rio et al., 1990]. Young [1990] and Takayama [1993] described several late Miocene "small Reticulofenestra intervals" that can be correlated between the Atlantic, Indian and Pacific Oceans. The same sequential size variations are found in the genus *Calcidiscus* [Knappertsbusch 2000].

Cryptococcolithus mediaperforatus is continuously present throughout the section (its LO is a lower Pliocene event). The abundance pattern of *C. mediaperforatus* (Fig. 2.2) represents only forms larger than 5 mm. Smaller forms have been counted separately. The *C. mediaperforatus* LCO corresponds to a drop in abundance from 2.8 specimens per mm² to 0.3 specimens per mm² and is located in the reddish layer of AEB 25.

Discoaster neorectus (Fig. 2.2; only specimens larger than 20 mm are counted) is present in low but consistent abundances up to 37.82 m (0.1 mm⁻² corresponds to 1 specimen per two long traverses on a slide) where the *D. neorectus* LO occurs in the reddish layer of AEB 27. Smaller specimens (up to 17 mm) are present to the top of the section. Because *D. neorectus* is rare, its occurrence is often not reported in published nannofossil range charts. Nevertheless, the *D. neorectus* (>20 mm) LO is used as a secondary marker species to define the top of the *Discoaster neorectus* Subzone [Bukry 1973]. At Ain el Beida, *D. neorectus* occurs up to the *Amaurolithus primus* Subzone. This higher occurrence of *D. neorectus* has also been observed in the Atlantic Ocean where it was reported above the *A. delicatus* FO at the level of the *D. berggrenii* LO [Gartner 1992].

Discoaster surculus is rare and discontinuously present in the lower part of the section but becomes more common and continuously present in the upper part. The FCO of *D. surculus* occurs in the uppermost part of the section at cycle AEB 42 and is placed at an increase in abundance from 0.1 to 0.8 specimens per mm².

Furthermore, several additional bioevents have been recognised which include: 1) the *Discoaster calcaris* LO in the reddish layer of AEB 1, 2) the *Reticulofenestra rotaria* (>5 mm) LCO in the reddish layer of AEB 3 where its abundance drops from 4 specimens per mm² to 0.4 specimens per mm², 3) the top of an acme zone of *Discoaster brouweri* at the top of the beige layer of AEB 5, 4) the top of an acme zone of the *Scyphosphaera* group at the top of the reddish layer of AEB 10, 5) the *Discoaster berggrenii* LO between the reddish and beige layers of AEB 34, 6) the *Helicosphaera orientalis* LO between AEB 37 and AEB 38, 7) the *Helicosphaera stalis ovata* LO between AEB 38 and AEB 39, 8) the *Helicosphaera stalis stalis* last occurrence datum (LOD) between the reddish and whitish layers of AEB 42, 9) the *Triquetrorhabdulus rugosus* LOD between the reddish and the whitish layers of AEB 43, and 10) the *Reticulofenestra rotaria* (>5 mm) LO at the base of the reddish layer of AEB 44.

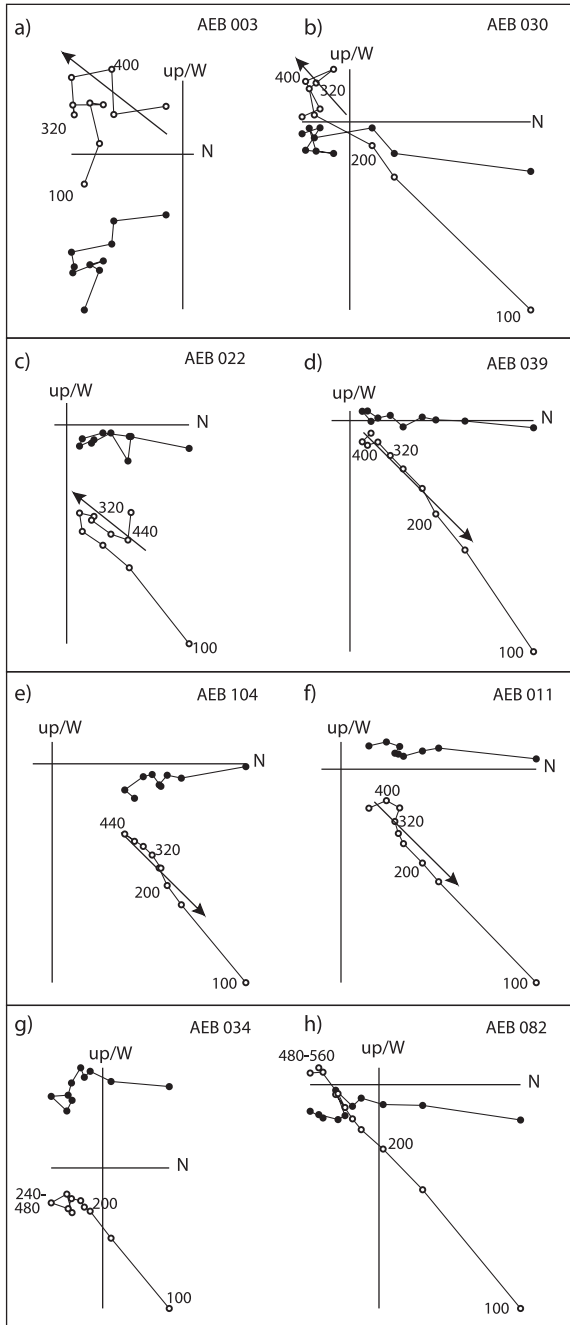


Figure 2.4 Representative examples of thermal demagnetization diagrams from selected samples of the Ain el Beida section. Closed (open) symbols represent the projection of vector-end-points on the horizontal (vertical) plane; values indicate temperatures in degrees Celcius (°C).

2.3.3 Magnetostratigraphy

The freshly excavated sediment in the basal part of the Ain el Beida quarry shows the characteristic blue colour, which rapidly changes (within days) to beige/reddish when exposed to air. This suggests that secondary haematite is formed within the sediment through weathering by chemical alteration (oxidation) of primary iron minerals like magnetite or iron sulfides. Hence, it may be expected that secondary overprints may significantly disturb the paleomagnetic signal. Therefore, thermal demagnetisation is applied with small temperature increments of 20-50°C up to a maximum temperature of 600°C to discriminate the primary component of the magnetisation. Paleomagnetic samples were taken from 247 levels with a water-cooled drill and oriented with a magnetic compass. The natural remanent magnetisation (NRM) was measured on a 2G Enterprises DC SQUID cryogenic magnetometer in the paleomagnetic laboratory Fort Hoofddijk of the Utrecht University. Principal component analysis was applied to determine the component directions of the NRM, chosen by inspection of vector end-point demagnetisation diagrams.

NRM intensities of the Ain el Beida section range between 0.5 and 2.5 mA/m and have an average value of approximately 1.0 mA/m. Thermal demagnetisation results revealed Zijderveld diagrams of mixed quality (Fig. 2.4). They generally show a randomly oriented viscous laboratory component, which is completely removed at temperatures of 100°C, and a low-temperature (LT) component of normal polarity that is demagnetised in the 100-240°C temperature range. This LT component is interpreted as a secondary present-day field component. Although the directions

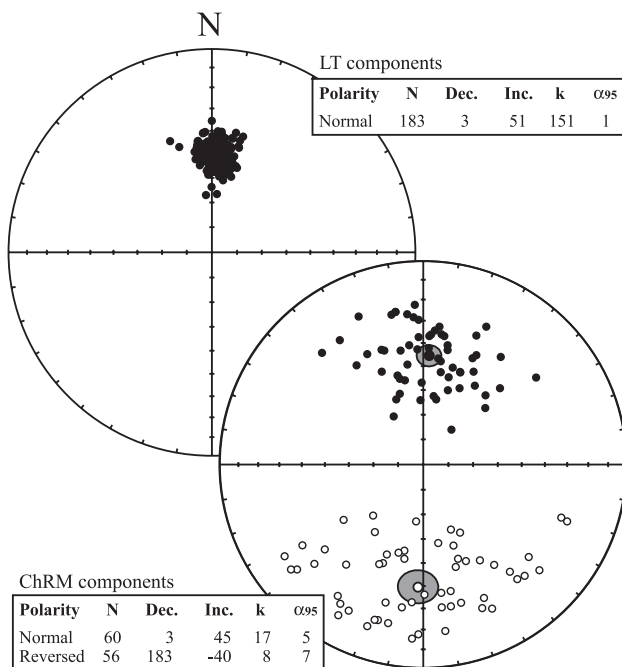


Figure 2.5 Equal area diagrams showing the paleomagnetic directions of the secondary (LT) and the ChRM components. The 95% confidence ellipse for the normal and reversed mean directions is indicated. Statistical information: N, number of samples; Dec., declination; Inc., inclination; k, Fisher's precision parameter, α_{95} , radius of the 95% confidence cone.

are slightly scattered, the average inclination of 51° for this present-day component closely coincides with the expected inclination of (53.5°) that corresponds to the latitude of Ain el Beida at 34°N (Fig. 2.5). Progressive demagnetisation in the $240\text{--}440^\circ\text{C}$ temperature range revealed additional normal or reversed components in approximately 50% of the Zijderveld diagrams. This $240\text{--}440^\circ\text{C}$ component is interpreted as the primary component or the characteristic remanent magnetisation (ChRM). One sample (AEB 082; 21.73m) showed atypical demagnetisation behaviour with a normal polarity component in the $240\text{--}400^\circ\text{C}$ range, but with a clear reversed polarity component at higher temperatures. This sample is interpreted as reversed and presented in the magnetostratigraphy column as a possibly reversed interval (Fig. 2.4h).

Reversed directions are interpreted as reliable when diagrams displayed a south/up component that showed a linear or scattered decay towards the origin (Fig. 2.4a,b) or when diagrams showed a clear linear decay of a reversed component without a trend towards the origin (Fig. 2.4c). In the latter case, it is assumed that another secondary component of normal polarity is present, but this component could not be properly demagnetised because heating towards temperatures higher than 440°C commonly resulted in the generation of a randomly oriented viscous component. Normal directions are only interpreted as reliable when diagrams displayed decay towards the origin in the $240\text{--}440^\circ\text{C}$ temperature range (Fig. 2.4d-f). Directions are qualified as unreliable when diagrams only show a cluster at temperatures higher than 240° (Fig. 2.4g) or when directions are so scattered that a reliable interpretation is impossible.

Declinations and inclinations were calculated for each characteristic component stable endpoint direction. The ChRM directions and polarity zones show that three polarity reversals are recorded (Fig. 2.3). Normal polarity intervals that only comprise one or two samples may correspond to short cryptochrons but more likely represent samples with a stronger secondary overprint. The normal and reversed directions are perfectly antipodal (Fig. 2.5) and pass the reversal test. The overall mean direction is: $\text{Dec}=3^\circ$, $\text{Inc}=43^\circ$ ($N=116$; $k=10$; $a_{95}=4$) which indicates that the area has not undergone any significant rotation. The clear E-W elongation in the distribution of directions (Fig. 2.5) suggests that the inclination of the primary component has probably been reduced by sediment inclination error [Tauxe and Kent 2004, Krijgsman and Tauxe 2004].

2.3.4 Stable Isotopes

Oxygen isotope analysis was performed on the calcitic tests of the benthic foraminiferal species *Planulina ariminensis* which were picked from the $>125\ \mu\text{m}$ fraction in 297 samples. All samples were processed in the laboratory of the Department of Earth Sciences in Utrecht and data are reported as per mil (‰) relative to the PeeDee belemnite (PDB) standard. For each sample, about twenty specimens of *P. ariminensis* were picked, yielding duplicate analyses for most samples. In order to remove any organic remains, each sample was roasted for 30 minutes at 470°C under vacuum. The samples were analyzed using an ISOCARB. This system is directly coupled to a mass spectrometer and has the capacity to measure 44 samples during a run, including 1 international (IAEA-CO-1), and 9 in-house (NAXOS) standards. Each sample reacted with 103% phosphoric acid (H_3PO_4) for 6 to 7 minutes at 90°C . The analytical precision and accuracy were determined by replicate analyses of samples and by comparison with the international standard. The relative standard deviations, analytical precision and accuracy were better than 0.1‰.

The benthic oxygen isotope record shows a close link to the lithology of Ain el Beida, with enrichments in $\delta^{18}\text{O}$ generally occurring in the beige layers and depletions in the reddish layers (Fig. 2.6). The amplitude of the $\delta^{18}\text{O}$ variations is $\sim 1.0\text{‰}$ with values ranging from about 0.4 to 1.3‰. The recurrence of thicker and more distinct reddish layers is marked by prominent

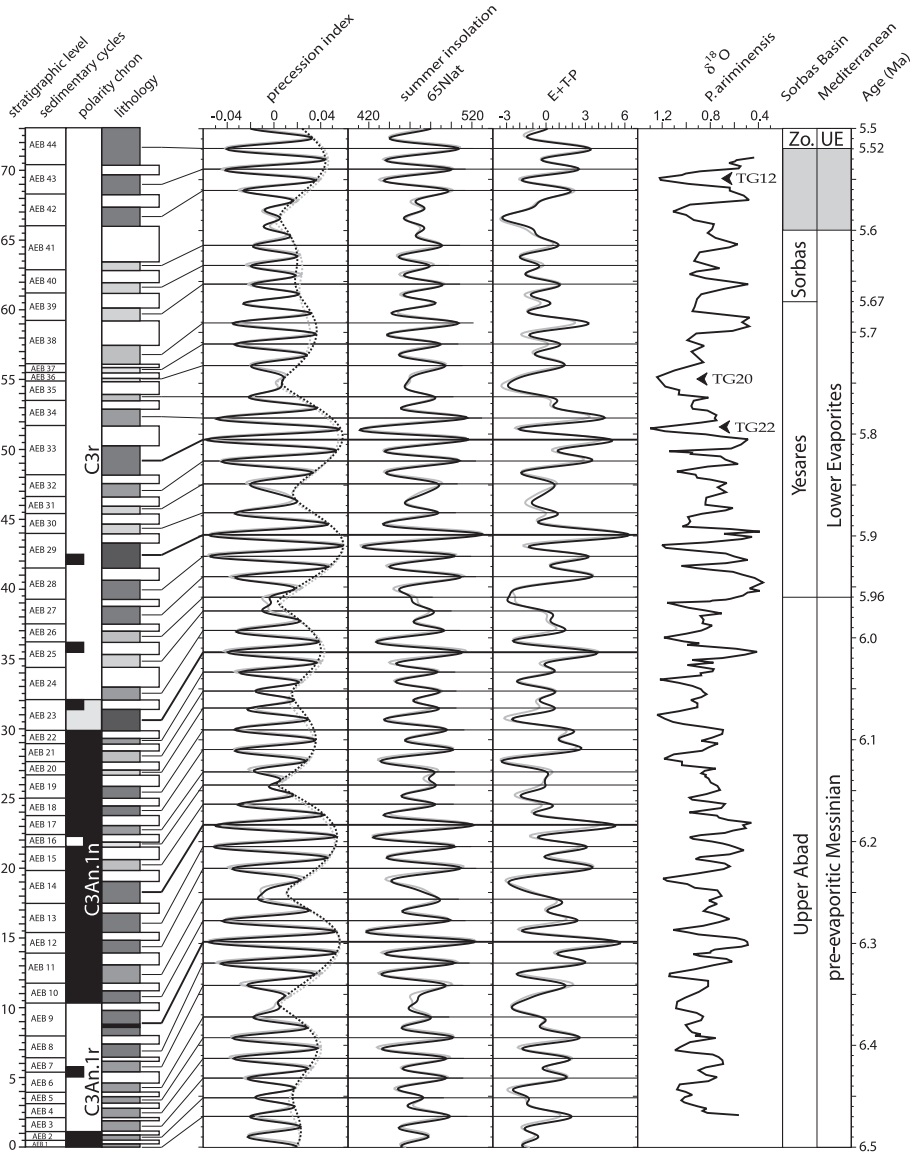


Figure 2.6 Tuning of the Ain el Beida colour cycles to the 65°Nlat summer insolation and precession curves of solution La93_(1,1). In addition, the combined ETP (Eccentricity, Tilt (obliquity), and negative Precession) curve is shown for comparison with the δ¹⁸O record from AEB [see Van der Laan et al., 2005 for all details]. Grey lines represent curves based on the new La2004_(1,1) solution [Laskar et al., 2004] and reveal minor differences with the curves of the La93_(1,1) solution (see also Tab. 1). Lithostratigraphic units of the Mediterranean Messinian and their ages are indicated in columns on the right side of the figure and are based on Krijgsman et al. [1999] and Krijgsman et al. [2001]. UE stands for Upper Evaporites and Zo. for Zorreras Member.

excursions to light $\delta^{18}\text{O}$ values, while most of the prominent excursions to heavy values occur in the beige layers within such “clusters” of distinct reddish layers. Apparently, variations in $\delta^{18}\text{O}$ are also present that are not related to lithology. These variations occur at intervals with a thickness of approximately two colour cycles. The heaviest $\delta^{18}\text{O}$ values are found in the beige layers of cycles AEB 33, AEB 35 and AEB 42 in the upper part of the section, although heavy values also occur in the beige layers of cycles AEB 19 and AEB 21 in the lower part of the section.

2.4 Astronomical dating of Ain el Beida

2.4.1 Astronomical origin of the sedimentary cycles

The standard procedure to establish an accurate and reliable astronomical tuning of any geological record involves a number of steps. First it has to be proven that the observed cyclicity is indeed astronomically controlled. This can be achieved by determining the periodicity of the cyclicity, which can be compared with the well-known periodicities of the astronomical cycles of precession (~20 kyr), obliquity (~40 kyr) and eccentricity (~100 kyr and ~400 kyr).

Biostratigraphic results from Ain el Beida confirm the late Messinian age of the section, as demonstrated by Benson et al. [1991, 1995], and indicate that the two complete magnetic intervals correspond to chrons C3An.1r and C3An.1n. These two intervals together comprise a total number of 20–21 sedimentary cycles, and correspond to 375 kyr according to the GPTS [Cande and Kent, 1995] and to 400 kyr according to the APTS [Krijgsman et al., 1999a]. The average periodicity of the basic sedimentary cyclicity in Ain el Beida thus arrives at 18–19 kyr (GPTS) or 19–20 kyr (APTS), which is in good agreement with a precessional control. The same conclusion was reached by Benson et al. [1995] who determined the number of cycles from an image-processed photograph in their study of the sedimentary cycles at Ain el Beida. Independent confirmation of an astronomical origin of the cyclicity in the Blue Marls comes from the nearby Oued Akrech section. The integrated stratigraphic results of Oued Akrech indicate that the basic cyclic alternation of indurated beige coloured marls and softer more clayey and reddish coloured marls is indeed dominantly precession-controlled [Hilgen et al., 2000].

2.4.2 Phase relation with the astronomical cycles

The next step is the determination of the phase relation of the observed cyclicities with the orbital parameters. This is well known for the marine sequences of the Mediterranean Neogene where marl-sapropel cycles are precession controlled, with the sapropels corresponding to precession minima and summer insolation maxima. Detailed quantitative planktonic foraminiferal analyses and stable isotope records reveal characteristic sapropel signals with maxima in *Globigerinoides* spp. and minima in $\delta^{18}\text{O}$ [Sprovieri et al., 1996]. On a larger scale, sapropel clusters correspond to eccentricity maxima – both for the 100 and 400 kyr cycle – and intervals without, or with poorly developed, sapropels to eccentricity minima [Hilgen, 1991a]. Maxima in eccentricity will enhance climate fluctuations on a precessional scale because eccentricity modulates the precession amplitude. Hence, it can be expected that eccentricity maxima will favour the formation of distinct cycles with strongly contrasting lithologies. By contrast, minima in eccentricity will result in intervals in which the cyclicity is poorly developed or absent. For different sedimentary environments, however, the astronomical origin of the cyclicity and the phase relation with the astronomical parameters needs to be determined before astronomical tuning can be established.

In the Ain el Beida section, the detailed quantitative planktonic foraminiferal analyses and stable isotope records reveal the same characteristic signal in the reddish layers as found in Mediterranean sapropels (*Globigerinoides* spp. maxima and $\delta^{18}\text{O}$ minima). This implies that the reddish intervals are equivalents of sapropels in the Mediterranean and thus correspond to precession minima and insolation maxima. Moreover, Ain el Beida reveals several intervals in which the lithological expression of the cyclicity is enhanced (AEB 9, AEB 13/14, AEB 19, AEB 23, AEB 28/29, AEB 33/34 and AEB 42/43/44) suggesting that these intervals correspond to eccentricity maxima. Consequently, intervals in which the cyclicity is less distinct should correspond to eccentricity minima. The link between the reddish layers and precession minima/insolation maxima has also been suggested for the Oued Akrech section. For this section, only one calibration was possible when its persuasive thick-thin alternations are interpreted to reflect precession-obliquity interference [Hilgen et al., 2000]. In contrast, the expression of the 100 kyr eccentricity cycle is almost completely lacking at Oued Akrech, which could be explained by the fact that the studied interval corresponds to a 2.35 Myr eccentricity minimum [Hilgen et al., 2000].

2.4.3 Astronomical tuning

To construct an independent astronomical tuning for the Ain el Beida section we refrain from using the Mediterranean-based astronomical ages for bioevents and paleomagnetic reversals. Nevertheless, all recent time scales indicate that the Ain el Beida section corresponds to the time interval between 6.5 and 5.5 Ma. The first order calibration involves the tuning to eccentricity. Intervals with distinct sedimentary cycles that contain prominent and thick reddish layers should correlate to eccentricity maxima while the interval of less distinct cycles should correspond to eccentricity minima. The most remarkable features in the eccentricity curve are the two suppressed 100-kyr eccentricity maxima at times of the 400 kyr eccentricity minimum around 5.6 Ma (Fig. 2.6). Consequently, the interval with less prominent sedimentary cycles (AEB 35-41) will correspond to the time interval between 5.8 and 5.6 Ma, when the maxima in 100-kyr eccentricity are reduced as a consequence of the 400 kyr minimum. Other possible correlations infer upward or downward shifts of 100 kyr. Evidently, these shifts make less sense because in those cases the well-developed cycles of AEB 33/34 or AEB 42/43/44 would then correlate with low amplitude eccentricity maxima where the lithological expression is expected to be less distinct.

The preferred first order correlation can furthermore be tested by the subsequent tuning of the basic sedimentary cycles to insolation. Between AEB 14 and 23 we observed nine more or less regularly developed cycles with cycles AEB 18 and 19 better developed and AEB 16 and 20 slightly less developed. This interval fits perfectly to the insolation curve interval between 6.0 and 6.2 Ma. Upward tuning is also in excellent agreement with the astronomical curve as the darker red layers of cycles AEB 23, 28/29, 33/34 and 38 nicely correspond to the highest amplitudes in insolation (Fig. 2.6). The tuning of the upper part of the section is less straightforward. We expect that the well-developed cycles AEB 42/43/44 will correlate to the increase in amplitude above 5.6 Ma. This implies that the number of observed cycles is too low and that several low amplitude precession/insolation cycles lack sedimentary expression.

We started the tuning from the La93_(1,1) solution [Laskar et al., 1993] with present-day values for dynamical ellipticity and tidal dissipation, hence (1,1), but repeated the whole tuning procedure for the new numerical solution La2004_(1,1) [Laskar et al., 2004]. This new solution has already been used to construct the new standard geological time scale for the Neogene [Lourens et al., 2004] and it is for this reason that we give the ages for the sedimentary cycles, calcareous plankton events

Table 2.1 Stratigraphic position and astronomical ages of mid-points of red and beige marl beds of each colour cycle in section Ain el Beida. The astronomical ages are based on the tuning shown in Figure 2.6 and refer to ages of the correlative insolation maximum and precession minimum. Ages in regular style are based on tuning the colour cycles to solution $L_a93_{(1,1)}$ and ages in italics are based on tuning the cycles to $L_a2004_{(1,1)}$.

Cycle	Lithol.	Insol.	Prec.	Insol.	Prec.	Cycle	Lithol.	Insol.	Prec.	Insol.	Prec.	Cycle	Lithol.	Insol.	Prec.	Insol.	Prec.
	beige	6,155	6,154	6,154	6,153		beige	5,867	5,866	5,866	5,864	AEB44	red	5,520	5,520	5,518	5,519
AEB15	red	6,164	6,164	6,163	6,163	AEB30	red	5,877	5,878	5,876	5,876		beige	5,531	5,530	5,530	5,529
	beige	6,174	6,174	6,173	6,173		beige	5,888	5,888	5,887	5,887	AEB43	red	5,540	5,541	5,539	5,540
AEB14	red	6,184	6,184	6,182	6,183	AEB29	red	5,898	5,899	5,897	5,898		beige	5,551	5,551	5,550	5,550
	beige	6,196	6,195	6,194	6,194		beige	5,911	5,910	5,909	5,908	AEB42	red	5,561	5,561	5,560	5,560
AEB13	red	6,205	6,205	6,204	6,204	AEB28	red	5,919	5,920	5,918	5,919		beige	*	*	*	*
	beige	6,216	6,216	6,215	6,215		beige	5,930	5,930	5,929	5,929	AEB41	red	5,615	5,615	5,613	5,614
AEB12	red	6,226	6,227	6,225	6,225	AEB27	red	5,940	5,941	5,939	5,940		beige	5,626	5,625	5,625	5,624
	beige	6,239	6,238	6,237	6,236		beige	5,953	5,951	5,952	5,951	AEB40	red	5,635	5,635	5,633	5,634
AEB11	red	6,257	6,256	6,256	6,248	AEB26	red	*	5,961	5,962	5,961		beige	5,644	5,644	5,643	5,643
	beige	6,268	6,267	6,267	6,266		beige	*	5,965	5,966	5,969	AEB39	red	5,653	5,653	5,652	5,653
AEB10	red	6,277	6,278	6,276	6,277	AEB25	red	5,975	5,973	5,974	5,971		beige	*	*	*	*
	beige	6,289	6,288	6,287	6,287		beige	5,984	5,983	5,983	5,982	AEB38	red	5,691	5,691	5,690	5,691
AEB9	red	6,298	6,299	6,297	6,297	AEB24	red	5,993	5,994	5,991	5,993		beige	5,703	5,702	5,702	5,701
	beige	6,310	6,309	6,309	6,308		beige	6,004	6,004	6,003	6,003	AEB37	red	5,712	5,712	5,711	5,711
AEB8	red	6,319	6,320	6,318	6,319	AEB23	red	6,014	6,014	6,013	6,013		beige	5,722	5,722	5,721	5,721
	beige	6,330	6,330	6,329	6,329		beige	6,025	6,024	6,024	6,023	AEB36	red	5,733	5,733	5,731	5,732
AEB7	red	6,341	6,341	6,340	6,340	AEB22	red	6,033	6,034	6,033	6,033		beige	5,753	5,745	*	*
	beige	*	*	*	*		beige	6,043	6,043	6,042	6,043	AEB35	red	5,764	5,764	5,764	5,763
AEB6	red	6,373	6,372	6,371	6,371	AEB21	red	6,053	6,052	6,052	6,052		beige	5,774	5,774	5,774	5,773
	beige	6,383	6,383	6,381	6,381		beige	6,061	6,061	6,061	6,061	AEB34	red	5,784	5,785	5,783	5,784
AEB5	red	6,392	6,393	6,391	6,391	AEB20	red	6,069	6,070	6,068	6,070		beige	5,796	5,795	5,795	5,794
	beige	6,404	6,403	6,402	6,402		beige	6,080	6,080	6,079	6,079	AEB33	red	5,805	5,805	5,804	5,804
AEB4	red	6,413	6,413	6,412	6,412	AEB19	red	6,090	6,090	6,089	6,089		beige	5,817	5,816	5,816	5,815
	beige	6,423	6,423	6,422	6,422		beige	6,101	6,100	6,099	6,099	AEB32	red	5,826	5,827	5,825	5,826
AEB3	red	6,432	6,433	6,431	6,432	AEB18	red	6,110	6,111	6,108	6,109		beige	5,838	5,838	5,837	5,837
	beige	6,443	6,442	6,443	6,442		beige	6,121	6,121	6,120	6,119	AEB31	red	5,850	5,849	5,848	5,848
AEB2	red	6,451	6,451	6,452	6,451	AEB17	red	6,132	6,130	6,130	6,129		beige	*	*	*	*
	beige	6,459	6,46	6,459	6,460		beige	6,138	6,139	6,138	6,138		beige	5,850	5,849	5,848	5,848
AEB1	red	*	*	*	*	AEB16	red	6,145	6,146	6,145	6,146		red	5,850	5,849	5,848	5,848

and magnetic reversal boundaries according to both solutions in Tables 2.1 and 2.2. As expected the application of the new solution does not change the tuning in a fundamental way and results in ages for the sedimentary cycles, calcareous plankton events and magnetic reversal boundaries that are only marginally different.

The tuning shows that the section comprises the time interval between 6.47 and 5.52 Ma and thus also the period during which the onset of evaporite deposition occurs in the Mediterranean: this onset is astronomically dated at 5.96 ± 0.02 Ma [Krijgsman et al., 1999a]. The astrochronology for the Ain el Beida section allows a detailed comparison of the AEB oxygen isotope record with the Mediterranean sequences, which can be used to investigate a possible glacio-eustatic control on the MSC events.

2.5 Discussion

2.5.1 Astrochronology of Ain el Beida compared to the Mediterranean APTS

The astronomical tuning of Ain el Beida implies that the section can be correlated cyclostratigraphically on a bed-to-bed scale to the Mediterranean sections (Fig. 2.7). The only two biostratigraphic events of Ain el Beida that are astronomically dated in the Mediterranean are the s/d coiling change in *N. acostaensis* and the *R. rotaria* LCO. The coiling change in *N. acostaensis* has frequently been recognised both in the Mediterranean and Atlantic and has an astronomical age of 6.361 Ma [e.g., Sierro et al., 2001 and references therein]. Although it is often used for biostratigraphic purposes, this change took place at a time when neogloboquadrinids were extremely rare in the Mediterranean. Therefore, the first abundant occurrence of dextral *N. acostaensis* is considered a more reliable and easily identifiable event. This event has been recognised in sections from Spain, Italy and Greece [Hilgen and Krijgsman 1999, Krijgsman et al., 1999a; Sierro et al., 2001] and is astronomically dated at 6.339 Ma. In Ain el Beida, the neogloboquadrinids are more common and the recognised event thus relates to the real change in coiling from dominantly sinistral to dextral forms. The astronomical age of 6.373 Ma for the coiling change of *N. acostaensis* is in good agreement with ages for the same event in the Mediterranean record and suggests that the tuning of Ain el Beida is basically correct. The s/d coiling change in Ain el Beida is followed by twelve influxes of sinistral *N. acostaensis* which all occur in the beige layers, apart from the prolonged influx that covers the red layer of AEB 20 as well (Fig. 2.2). In the Mediterranean, the coiling direction is dominantly dextral above the main s/d coiling change. This is not surprising because in the Mediterranean, neogloboquadrinids are absent in those parts of the sedimentary cycles that correspond to the beige marls of Ain el Beida (probably as a consequence of cyclically raised salinities in this pre-evaporitic part of the Mediterranean Messinian). The only exception is the single sinistral influx in the sapropel that corresponds to the red layer of AEB 20, again confirming the correctness of the tuning.

The *R. rotaria* LCO is recorded in the Metochia section on Gavdos (Greece) with an astronomical age of 6.940 Ma [Raffi et al., 2003], while our results reveal an age of 6.429 Ma (Tab. 1). An explanation for this discrepancy is that less favourable environmental conditions have decreased the abundance of *R. rotaria* in the Mediterranean Sea and/or that several acme intervals may occur in the distribution pattern of *R. rotaria*. Raffi et al. [2003] identified an acme zone of *R. rotaria* in Metochia at about 6.4 Ma that corresponds with the LCO level at the AEB section. Therefore the *R. rotaria* (>5 mm) LCO seems to be a reliable biostratigraphic event for correlations between the Mediterranean Sea and the Atlantic Ocean.

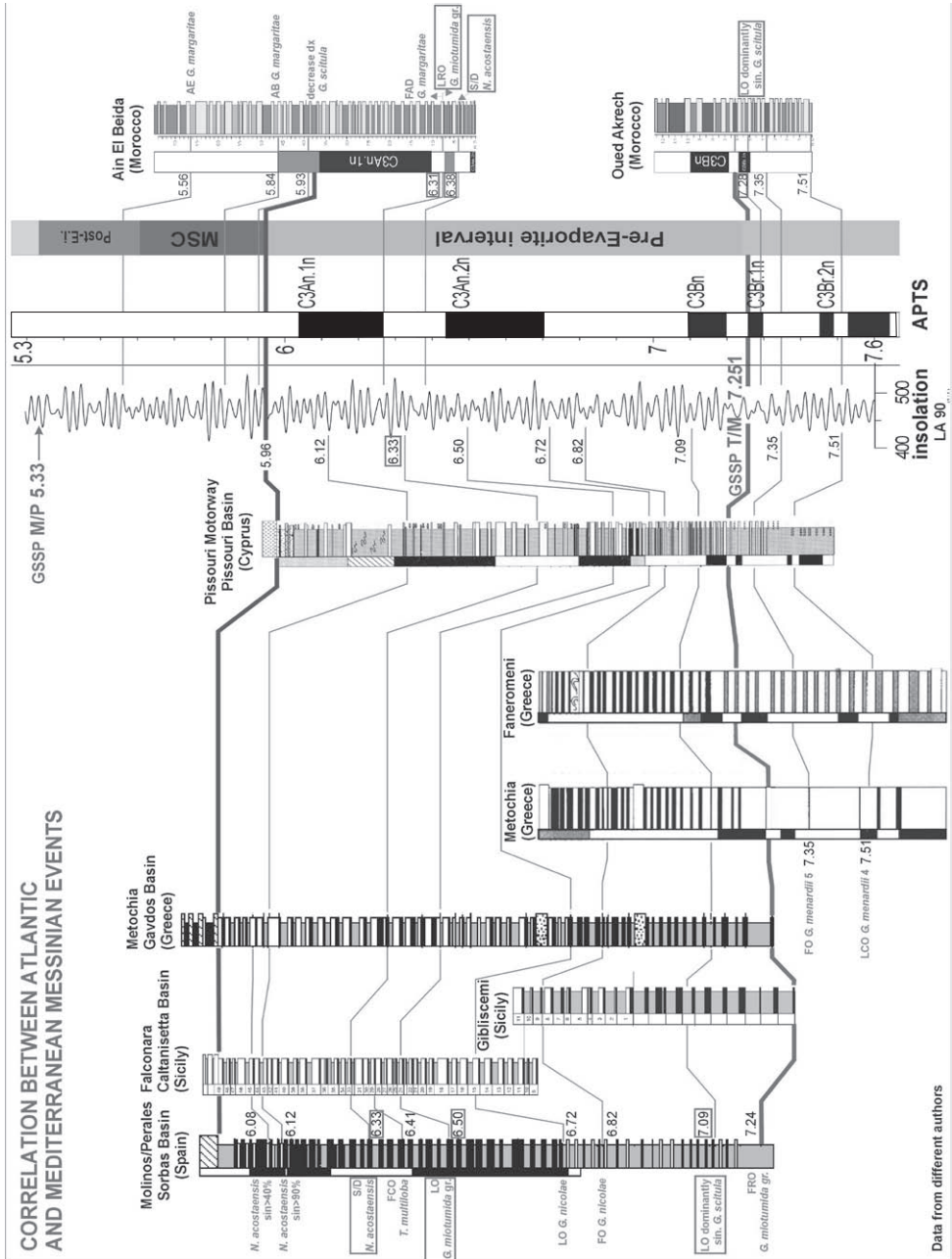


Figure 2.7 Correlation between the Atlantic events in sections Ain el Beida/Oued Akrech (Morocco) and the Mediterranean events in sections Molinos/Perales (Spain), Gibliscemi/Falconara (Sicily), Metochia/Faneromeni (Greece) and Pissouri (Cyprus). For detailed information about these sections the reader is referred to [Hilgen et al., 1995; Hilgen et al., 2000; Krijgsman et al., 1999a; Krijgsman et al., 2002]

Table 2.2 Stratigraphic position, cycle position and astronomical ages of calcareous plankton events and magnetic reversal boundaries in section Ain el Beida. Astronomical ages are presented both for the La93_(1,1) (regular style) and La2004_(1,1) (italics) solution.

Species/reversal	Event	Strat. range (m)	Age range (Ma)	Age range (Ma)
Planktonic foraminifera				
<i>G. margaritae</i>	top acme	66.80 - 67.15	5.561 - 5.558	<i>5.560 - 5.557</i>
<i>G. margaritae</i>	bottom acme	46.02 - 46.11	5.845 - 5.843	<i>5.843 - 5.841</i>
<i>G. scitula</i>	decrease dex	38.95 - 39.15	5.931 - 5.929	<i>5.930 - 5.928</i>
<i>G. miotumida</i>	LRO	7.73 - 7.87	6.311 - 6.309	<i>6.309 - 6.308</i>
<i>G. margaritae</i>	FO	7.32 - 7.57	6.315 - 6.312	<i>6.314 - 6.311</i>
<i>N. acostaensis</i>	sin/dex	3.99 - 4.21	6.380 - 6.375	<i>6.378 - 6.373</i>
Calcareous nannofossils				
<i>D. quinqueramus</i>	LO	68.20 - 68.50	5.548 - 5.545	<i>5.547 - 5.544</i>
<i>D. surculus</i>	FCO	66.47 - 66.80	5.566 - 5.561	<i>5.564 - 5.560</i>
<i>D. quinqueramus</i> (>20)	LO	39.66 - 39.96	5.923 - 5.920	<i>5.922 - 5.919</i>
<i>D. neorectus</i> (>20)	LO	37.82 - 38.13	5.945 - 5.941	<i>5.944 - 5.940</i>
<i>C. mediaperforatus</i>	LCO	35.34 - 35.79	5.972 - 5.968	<i>5.970 - 5.966</i>
<i>A. amplificus</i>	LO	34.83 - 35.10	5.976 - 5.973	<i>5.975 - 5.972</i>
<i>D. quinqueramus</i>	LCO	20.01 - 20.31	6.166 - 6.163	<i>6.166 - 6.163</i>
<i>A. amplificus</i>	LRO	15.85 - 16.12	6.208 - 6.205	<i>6.207 - 6.204</i>
<i>C. macintyreii</i> (>11)	FRO	15.85 - 16.12	6.208 - 6.205	<i>6.207 - 6.204</i>
<i>D. quinqueramus</i>	top acme	8.92 - 9.16	6.298 - 6.296	<i>6.297 - 6.295</i>
<i>R. rotaria</i>	LCO	1.43 - 1.62	6.435 - 6.431	<i>6.434 - 6.430</i>
Magnetic reversal				
C3An.1n (y)	N>R	28.81 - 32.11	6.041 - 5.999	<i>6.040 - 5.998</i>
C3An.1n (o)	R>N	10.51 - 10.71	6.282 - 6.279	<i>6.281 - 6.278</i>
C3An.2n (y)	N>R	1.05 - 1.28	6.443 - 6.438	<i>6.443 - 6.438</i>

Benson et al. [1995] do not provide astronomical ages of biostratigraphic events so that we can only discuss their position relative to the magnetostratigraphic data. Our position of the main coiling change of *N. acostaensis* in the middle of the reversed chron C3An.1r is in good agreement with the results from Salé, but is reported from a younger level (lower part C3An.1n) at Ain el Beida by Benson et al. [1995]. Also in the Mediterranean and North Atlantic records this event falls within chron C3An.1r [Hodell et al., 2001, Krijgsman et al., 1999a, Sierro et al., 2001]. The *G. margaritae* FO is reported by Benson et al. [1995] in both Ain el Beida and Salé at a much lower level (middle of C3An.2n) than in our record (upper part of C3An.1r). This can be explained by the limited downward extension of the Ain el Beida quarry section as compared with the Ain el Beida and Salé cores studied by Benson et al. [1991]. Our position of the acme of *G. margaritae* (lower part C3r) is in good agreement with both the Ain el Beida and Salé records of Benson et al. [1995].

The astronomical ages for the paleomagnetic reversals in Ain el Beida are in good agreement with the ages determined in the Mediterranean Sorbas basin [Krijgsman et al., 1999a, Sierro et al., 2001]. We have found the reversals at approximately the same stratigraphic level as Benson et al. [1995], as shown by the position of the bioevents and specific sedimentary cycles. However, the age for the reversals at Ain el Beida determined by the signature template technique [Benson et al., 1995] is clearly younger. The almost constant offset of ~100 kyr between the two dating techniques

suggests that the image analysed record of Benson et al. [1995] was tuned to one eccentricity cycle younger. The ATS of Benson and co-workers is hampered by the fact that the number of sedimentary cycles does not match the number of precession cycles in the correlative interval of the orbital time series. Extraordinarily thick sedimentary cycles may represent double cycles, and thus explain the discrepancy in cycle numbers, but this adjustment will at the same time disrupt the characteristic cycle thickness pattern on which the tuning is based.

2.5.2 Implications for the Messinian salinity crisis

Now that we have established a reliable and accurate time frame for the Ain el Beida section, we are able to compare the high-resolution $\delta^{18}\text{O}$ record of AEB to $\delta^{18}\text{O}$ records from both the Mediterranean Sea and the open ocean (Fig. 2.6). This is crucial for establishing the possible link between the obliquity (41 kyr) controlled glacial $\delta^{18}\text{O}$ cycles in the late Miocene [Hodell et al., 1994, 2001; Shackleton and Crowhurst, 1997; Shackleton et al., 1995a, 1995b; Vidal et al., 2002] and the initiation and ending of the Messinian Salinity Crisis in the Mediterranean in terms of glacio-eustatic sea level changes. The dominance of obliquity-scale variations in $\delta^{18}\text{O}$ in the area of Ain el Beida was already demonstrated by Hodell et al. [1994], and has recently been confirmed in detail by spectral analysis [Van der Laan et al., 2005]. By contrast, the cyclic variations in the Mediterranean marls and evaporites are dominated by precession [Hilgen et al., 1995; Krijgsman et al., 2001, Sierro et al., 1999].

The astronomical tuning of Ain el Beida immediately allows a detailed comparison of the benthic $\delta^{18}\text{O}$ record with the $\delta^{18}\text{O}$ records of Salé [Hodell et al., 1994], ODP Site 846 [Shackleton et al., 1995a, 1995b] from the eastern equatorial Pacific, ODP Site 926 [Shackleton and Crowhurst, 1997] at Ceara Rise in the equatorial Atlantic and ODP Site 982 [Hodell et al., 2001] in the North Atlantic [see Van der Laan et al., 2005, for a review]. The most pronounced glacial stages (with $\delta^{18}\text{O}$ values of 3.2 to 3.4‰) in these open ocean records are TG 22 and TG 20 as well as TG 12 [coding after Shackleton et al., 1995b], which can be relatively easily identified at AEB (Fig. 2.6). Various authors have linked the occurrence of peak glacials TG 22 and 20, which would imply sea level falls in the order of 50 m, to the onset of the Messinian evaporites in the Mediterranean [e.g., Clauzon et al., 1996, Kastens 1992, Shackleton et al., 1995b]. However, the astronomically derived ages of 5.79 and 5.75 Ma (La93_(1,1)) for the peak glacial stages TG 22 and TG 20 at AEB clearly postdate the onset of the MSC (Fig. 2.6), which is astronomically dated at 5.96 ± 0.02 Ma [Krijgsman et al., 1999a], by approximately 200 kyr. Hence, the sea level falls associated with these glacial stages cannot be the prime cause for the onset of the MSC. In addition, no comparable glacial event associated with a prominent $\delta^{18}\text{O}$ excursion around 5.96 Ma can be observed at Ain el Beida. This suggests a dominantly tectonic control on the isolation of the Mediterranean Sea from the open ocean resulting in the deposition of vast amounts of evaporites, probably with a superimposed effect of the ~400 kyr eccentricity cycle which reaches a minimum just before 5.96 Ma (Fig. 2.6 and 2.7). This conclusion was recently also reached by Hodell et al. [2001] who compared the ODP Site 982 $\delta^{18}\text{O}$ record with the Salé record and by Vidal et al. [2002] based on ODP Site 1085 in the SE Atlantic. These similar conclusions based on independent records provide important evidence that correlations between the onset of the MSC evaporites and glacio-eustatic peaks are definitely no longer acceptable. The ending of the MSC (at 5.33 Ma) can unfortunately not be documented in the stratigraphic record of the Ain el Beida section because the youngest exposed cycle has an age of 5.52 Ma (Fig. 2.6). Nevertheless, it has been shown earlier that there is no single “event” in the $\delta^{18}\text{O}$ record that corresponds to the end of the MSC and the reflooding of the Mediterranean [Hodell et al., 2001].

The only significant change in the $\delta^{18}\text{O}$ records that seems to correspond with a major MSC-event is the peak glacial stage TG12 at 5.55 Ma (Fig. 2.6). The transition from TG12 to TG11 that marks the end of the high-amplitude, glacial-interglacial cycles of the latest Miocene [Hodell et al., 2001] roughly correlates with the base of the Upper Evaporites in the Mediterranean dated approximately at 5.52 Ma [Krijgsman et al., 2001]. This implies that the Lago Mare facies of the Upper Evaporites, which was deposited when the Mediterranean was largely isolated from the Atlantic, corresponds to times of relatively high global sealevel stands and a warmer global climate than that of older parts of the Messinian.

2.6 Conclusions

We have established a high-resolution integrated stratigraphy for the Ain el Beida section of Atlantic Morocco by applying a multi-disciplinary approach that included cyclostratigraphy, biostratigraphy (planktonic foraminifera and calcareous nannofossils), magnetostratigraphy, and stable isotope ($\delta^{18}\text{O}$) stratigraphy. The 44 sedimentary cycles in Ain el Beida consist of alternating beige and reddish coloured marls and reveal marked changes in thickness on a one to five to twenty ratio, which is commonly observed in sedimentary records where both precession and eccentricity play a role. The planktonic foraminiferal analyses allowed the recognition of five events, the calcareous nannofossil results revealed eight important and ten additional bioevents. They all confirm the late Messinian age of the section. Thermal demagnetisation of the magnetic signal shows that three polarity reversals are recorded at Ain el Beida, corresponding to chron C3An. The benthic oxygen isotope record shows a close link to the lithology with enrichments in $\delta^{18}\text{O}$ generally occurring in the beige layers and depletions in the reddish intervals. The three heaviest peak values in $\delta^{18}\text{O}$ are observed in beige layers in the upper part of the section.

The average periodicity of the sedimentary cyclicity, using the paleomagnetic reversals as time constraints, is 18-19 kyr, which is in good agreement with a precessional control. Detailed quantitative planktonic foraminiferal analyses and stable isotope records reveal maxima in *Globigerinoides* spp. and minima in $\delta^{18}\text{O}$ in the reddish layers. This implies that the reddish intervals are equivalents of the sapropels in the Mediterranean and that they thus correspond to precession minima and insolation maxima. The astronomical calibration of the Ain el Beida section started with the tuning of clusters of sedimentary cycles to eccentricity, followed by the tuning of individual cycles to precession and insolation. Our calibration shows that the section comprises the time interval between 6.47 and 5.52 Ma and results in accurate astronomical ages for all sedimentary cycles, bioevents and magnetic reversals. Comparison with the Mediterranean APTS confirms that the revised astrochronology of Ain el Beida is basically correct. This allows a detailed comparison of the Ain el Beida $\delta^{18}\text{O}$ record with Mediterranean event stratigraphy. The pronounced glacial stages TG 22 and TG 20, which have earlier been linked to the onset of the Messinian evaporites in the Mediterranean, clearly postdate the first evaporite cycle by approximately 200 kyr. Moreover, there is no evidence at all for a glacio-eustatic control for the onset of the MSC. The only significant change in the $\delta^{18}\text{O}$ record that corresponds with a major MSC-event is the peak glacial stage TG12 at 5.55 Ma, which roughly correlates to the transition from marine evaporites to the brackish water deposits with typical Lago Mare facies in the Mediterranean.

Acknowledgements

We gratefully thank Dr. M. Dahmani of the 'Ministère de l'Énergie et des Mines' in Rabat for his very helpful collaboration and Dick Benson, Laura Bissoli, Kruna Rakic el Bied, and Giuliana Villa (sorry for that unexpected rain cloud) for their help in the field. We furthermore acknowledge the useful comments of the reviewers W.A. Berggren and D.V. Kent. Ragna Meijer did most of the paleomagnetic measurements. This study was partly supported by the Earth and Life Sciences Research Council (ALW) of the Netherlands Organisation for Scientific Research (NWO) and was carried out under the programs of the Vening Meinesz Research School of Geodynamics (VMGS) and the Netherlands Research School of Sedimentary Geology (NSG).

Regional climate and glacial control on high-resolution oxygen isotope records from Ain el Beida (latest Miocene, northwest Morocco): A cyclostratigraphic analysis in the depth and time domain

with F.J. Hilgen¹, L.J. Lourens¹ and S. Gaboardi²

¹*Dept. of Earth Sciences, Utrecht University, Budapestlaan 4, Utrecht, Netherlands*

²*Dept. of Earth Sciences, Univ. of Parma, Nuovo Campus Universitario, Parma, Italy*

This chapter has been published in *Paleoceanography* as: Van der Laan, E., S. Gaboardi, F. J. Hilgen, and L. J. Lourens, 2005. Regional climate and glacial control on high-resolution oxygen isotope records from Ain el Beida (latest Miocene, northwest Morocco): A cyclostratigraphic analysis in the depth and time domain, *Paleoceanography*, 20, PA1001, doi:10.1029/2003PA000995.

Abstract

High-resolution benthic and planktonic stable oxygen isotope records are presented for the upper Miocene Ain el Beida (AEB) section in northwestern Morocco and reveal the clear imprint of the (climatic) precession, obliquity and eccentricity cycles in the interval between 6.5 and 5.5 Ma. The $\delta^{18}\text{O}$ depth series were transformed into time series using astronomical tuning of the sedimentary colour cycles to the 65°N summer insolation curve of the La93 solution with present-day values for tidal dissipation and dynamical ellipticity. Spectral analysis and band-pass filtering show that the ratios of the astronomically related spectral peaks are not consistent in the depth and time domain. The inconsistencies are mainly due to variations in sedimentation rate that are positively correlated with precession amplitude (i.e. modulated by eccentricity). In addition they result from a long-term trend in sedimentation rate. A simple model of non-linear response of the sedimentation rate to the eccentricity modulation of precession was used to simulate the observed shifts in the relative position of the spectral peaks in the depth domain.

Cross-spectral analysis was carried out on the $\delta^{18}\text{O}$ time series and a combined eccentricity, tilt (obliquity) and precession (ETP) curve. The precession controlled $\delta^{18}\text{O}$ signal varies in-phase with ETP partly as a result of the tuning procedure, while the obliquity related signal reveals a small lag of 2-3 kyr relative to obliquity. This lag is slightly reduced at the time of the Messinian Salinity Crisis (MSC) and increases to 5-6 kyr if the tidal dissipation term in the astronomical solution is reduced to half its present-day value. The obliquity-related lag is most likely associated with the slow build-up of ice caps whereas the precession signal is interpreted as to dominantly reflect regional climate changes comparable to those associated with Mediterranean sapropels.

Finally, the benthic $\delta^{18}\text{O}$ record is compared with open ocean records and discussed in terms of an astronomically tuned oxygen isotope stratigraphic framework.

3.1 Introduction

The late Messinian (latest Miocene) represents an intriguing time interval marked by an obliquity (41 kyr) controlled glacial cyclicality [e.g., Hodell et al., 1994, 2001; Shackleton et al., 1995a] and the deposition of vast amounts of evaporites in the Mediterranean [Hsü et al., 1973; Ryan et al.,

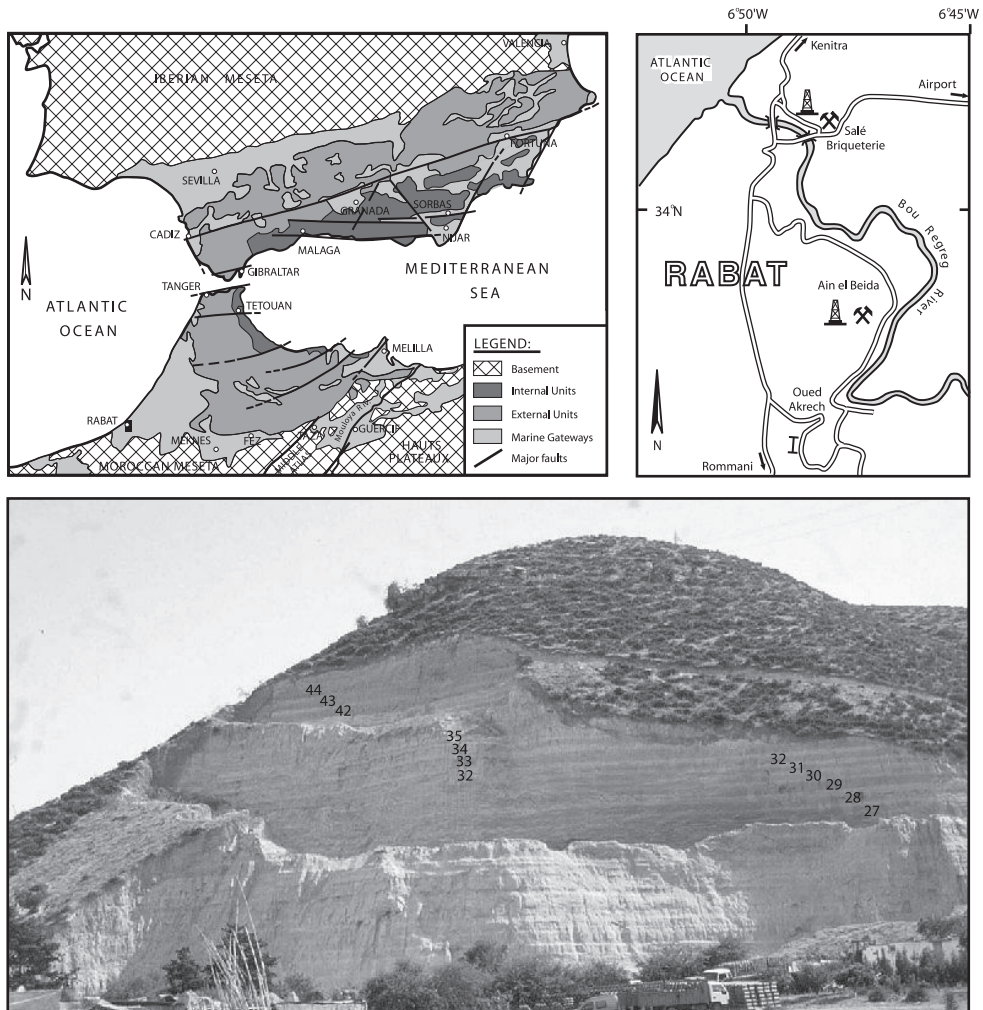


Figure 3.1 Simplified geological sketch map of the Gibraltar area during the late Miocene (upper left). Overview of the Bou Regreg area in northwestern Morocco and the location of Ain el Beida within the mouth of the former Rifian Corridor (upper right, after Benson et al., 1991). The Ain el Beida section with assigned lithological cycle numbers (bottom).

1973] during the so-called Messinian Salinity Crisis (MSC). Stable isotope records from the open ocean have resulted in a global oxygen isotope stratigraphy for the period immediately prior to and during the MSC [Hodell et al., 1994, 2001; Shackleton et al., 1995a, 1995b; Vidal et al., 2002]. Based on these records, a distinct series of obliquity controlled glacial cycles emerged with peak glacial stages TG22 and TG20 [Shackleton et al., 1995b] that should correspond to sea level lowerings of about 50 m [Kastens, 1992; Shackleton et al., 1995b]. The benthic $\delta^{18}\text{O}$ record of ODP Site 982 in the North Atlantic recorded the beginning of a series of glacial cycles, or at least the onset of intensification of glaciations at ~ 6.26 Ma [Hodell et al., 2001]. However, $\delta^{18}\text{O}$ records from the eastern equatorial Pacific indicate a more gradual beginning of this glacial episode [e.g., Shackleton et al., 1995a, 1995b]. The glacial series ends more or less abruptly at the termination of glacial stage TG12 dated astronomically at 5.54 Ma [Shackleton and Crowhurst, 1997].

The onset of major evaporite deposition in the Mediterranean during the MSC has been accurately dated at 5.96 ± 0.02 Ma [Krijgsman et al., 1999a]. It does not coincide with peak glacials TG22 and TG20 [Hodell et al., 2001; Krijgsman et al., 2004] nor with the inferred beginning or intensification of glaciations at ~ 6.26 Ma, but seems to be controlled mainly by the tectonic closure of the Rifian Corridor [Krijgsman et al., 1999b]. The beginning of the deposition of the Upper Evaporites roughly coincides with the termination of peak glacial stage TG12. The evaporite cycles in the Mediterranean are found to be dominantly precession-controlled, being related to regional low-latitude climate, rather than to obliquity-controlled glacial cyclicality and associated eustatic sea level change [Krijgsman et al., 2001].

One of the prime locations to study the interplay between the MSC, glacial cyclicality and regional climate change is the Ain el Beida (AEB) section. This section is ideally located at the Atlantic side of Morocco, within the mouth of the Rifian Corridor, the formerly existing connection between the Mediterranean Sea and the Atlantic Ocean. Previous studies of AEB yielded a biostratigraphic framework [e.g., Wernli, 1977] while Cita and Ryan [1978] were the first to describe the colour cycles and assign a paleoclimatic significance to them. Benson et al. [1991] related the sedimentary cyclicality to precessional forcing while a dominant obliquity influence was observed in benthic $\delta^{18}\text{O}$ records from AEB [Benson et al., 1995] and the nearby drilled Salé core [Hodell et al., 1994]. Here we present new high-resolution benthic and planktonic $\delta^{18}\text{O}$ records from AEB and determine their spectral characteristics in the depth and in the time domain, using a recently established astronomical age model [Krijgsman et al., 2004] to calculate the time series (see also **Chapter 2**). Subsequently, the phase relations relative to the orbital parameters and the correlation to the open ocean are discussed in terms of astronomical climate forcing and the MSC. In addition, we investigate the distorting influence of cycle-dependent changes in sedimentation rate on spectral peak positions.

3.2 Geological setting

The Ain el Beida section in northwestern Morocco is located on the Atlantic side of the Rifian Corridor which formed the final connection between the Mediterranean and the open ocean in the late Miocene before its tectonic closure around 6.0 Ma [Krijgsman et al., 1999a, 1999b]. The section contains near-horizontal strata that show a prominent cyclic alternation of softer reddish-coloured and more indurated beige marls (Fig. 3.1), both of which attain a grey-blue colour when freshly excavated. These marls were deposited in a normal open marine environment in contrast to the partly time equivalent evaporite deposits in the Mediterranean. In total, 45 colour cycles

with beds of varying thickness and colour intensity were identified (Fig. 3.2). The height of the section is approximately 75 m, resulting in an average thickness of the colour cycles of 1.65 m. The thickest cycles (i.e. 33, 38, 41 and 44) occur in the upper part of the section. The maximum cycle thickness (3.50 m) is reached in cycle 33. The reddish layers make up more than half of the cycle thickness in most of the cycles. Apart from measuring the cycle thickness, a visual distinction was made in the colour intensity of the reddish layers (prominent, distinct, less distinct, visible and vague). Linking bed thickness to colour intensity reveals that thick reddish layers are prominent or distinct, while thinner layers are less distinct to vague. The thickest reddish layer occurs in cycle 44, while the most prominent reddish layers are found in cycles 23 and 29. The more distinct and thicker reddish layers often occur in clusters of three while the thicker and more prominent cycles are concentrated in three intervals, namely between 6 and 19 m, between 37 and 53 m and between 66 m and the top of the section around 75 m (Fig. 3.2).

3.3 Age model

Three magnetic reversal boundaries (top C3An.2n at 1 m, bottom C3An.1n at 10.40 m and top C3An.1n at 32 m) and a single bioevent [PF-4 of Sierro et al., 1993] were used for first-order age calibration. The colour cycles were subsequently tuned to the 65°N summer insolation curve of solution La93, with present-day values for dynamical ellipticity and tidal dissipation. The values of these parameters are indicated in subscript as suffix to La93, i.e. La93_(1,1). Midpoints of the reddish layers were correlated to insolation maxima and midpoints of the beige layers to insolation minima [for details see Krijgsman et al., 2004]. The larger-scale cycles (clusters) provided a very useful constraint for the tuning of the individual colour cycles, with clusters of the thicker and more prominent reddish layers corresponding to eccentricity maxima.

The sedimentation rate curve that results from the tuning is shown in Figure 3.2. The average sedimentation rate is 7.7 cm/kyr, but the sedimentation rate is not constant and varies between 3 and 19 cm/kyr with a pronounced peak of 21 cm/kyr at 36.5 m (cycle 25-26 boundary). Intervals marked by the recurrence of thick and distinct reddish layers correspond to higher sedimentation rates at times of eccentricity maxima¹. The tuning procedure provided astronomical ages for each marl bed and proxy event and indicates that the (sampled part of the) Ain el Beida section ranges from 6.47 to 5.52 Ma (Fig. 3.2).

3.4 Methods

3.4.1 Oxygen isotope measurements

A number of 297 samples were taken with an average spacing of 24 cm resulting in an average sample resolution of ~3200 yr (3.2 kyr). Analyses were performed on the calcitic tests of the planktonic foraminiferal species *Globigerinoides obliquus* and the benthic foraminiferal species *Planulina ariminensis* and are reported as per mil (‰) relative to the PeeDee belemnite (PDB)

1 The tuning does not provide an explanation for the very high sedimentation rate of 21 cm/kyr at 36.5 m. We have therefore tested an alternative tuning of cycles AEB 25 to 35 by shifting them one precession cycle younger, but this resulted in an opposite (out-of-phase) relationship between obliquity and $\delta^{18}\text{O}$ in this interval and is therefore considered unlikely. Moreover, other proxy data suggest that the pronounced peak in sedimentation rate is not an artifact (lithogenic grainsize, unpublished data).

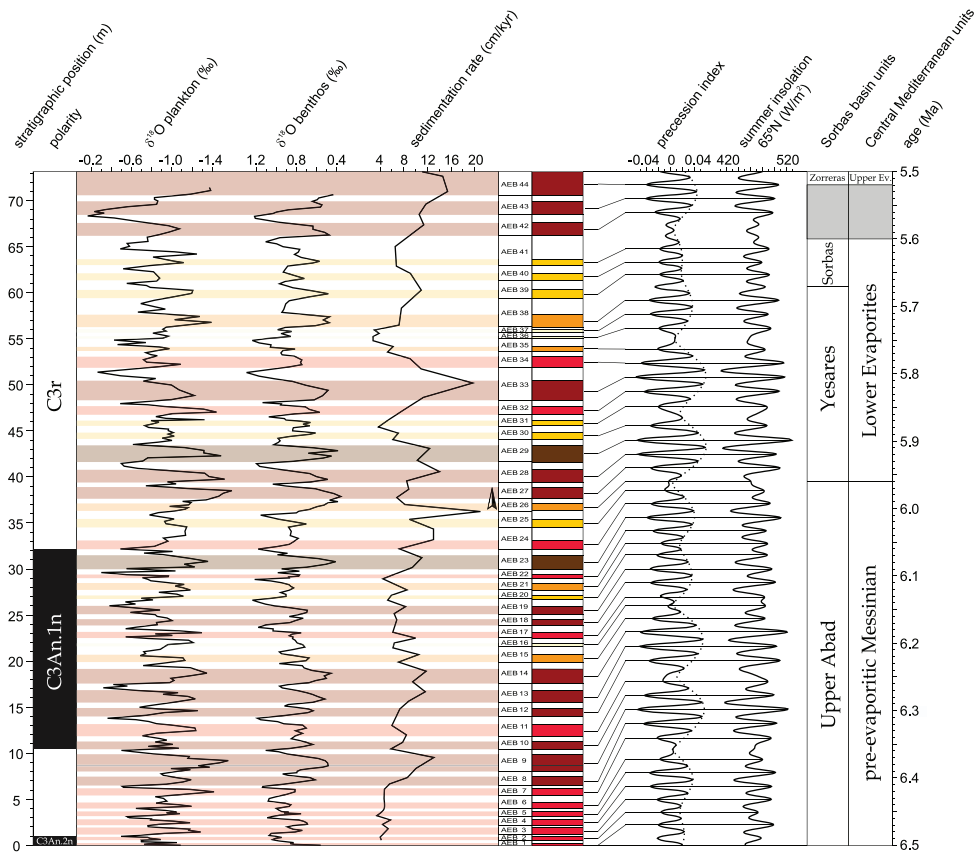


Figure 3.2 Cyclo- and magnetostratigraphy of Ain el Beida with planktonic and benthic $\delta^{18}\text{O}$ and sedimentation rate. Tuning of the sedimentary cyclicity to the 65°N summer insolation and precession curves of the $\text{La93}_{(1,1)}$ astronomical solution [Laskar et al., 1993]. Magnetostratigraphy is based on Krijgsman et al. [2004]. Time-equivalent lithologic units in the Mediterranean are shown at the right-hand side of the figure [after Krijgsman et al., 2001]. The initiation of the MSC at 5.96 Ma is indicated by an arrow.

standard. For each sample, about 10-15 specimens of *P. ariminensis* were picked as well as about 30-40 specimens of *G. obliquus*. In order to remove any organic remains, each sample was roasted for 30 minutes at 470°C under vacuum. The samples were analyzed using an ISOCARB, which is directly coupled to the mass spectrometer and has the capacity to measure 44 samples, of which 1 international (IAEA-CO-1) and 9 in-house (NAXOS) standards, during a run. Each sample reacted with 103% phosphoric acid (H_3PO_4) for 6 to 7 minutes at 90°C . The analytical precision and accuracy were determined by replicate analyses of samples and by the comparison with the IAEA-CO-1. The relative standard deviations, analytical precision and accuracy were better than 0.1‰.

3.4.2 Spectral analysis

Spectral analysis was carried out on the $\delta^{18}\text{O}$ records in the depth and time domain using the AnalySeries program version 1.0 of Paillard et al. [1996]. The $\delta^{18}\text{O}$ time series were generated

twice; first by tuning the colour cycles to insolation [Krijgsman et al., 2004] and secondly by tuning the colour cycles to precession. The latter option excludes the effect of obliquity on the precise age of the calibration points, thus avoiding the introduction of artificial obliquity frequencies in the time series.

Equally spaced $\delta^{18}\text{O}$ depth and time series were prepared by means of linear interpolation between calibration points; the series were detrended and normalized to unit variance with no pre-whitening. Subsequently, the Blackman-Tukey power spectral method was applied using a Bartlett window. All power spectra are reported as power density versus frequency. Band-pass filtering was performed to extract the most important frequency components from the depth and time series. Cross-spectral analysis was carried out to calculate coherency and phase between the same frequency components of the $\delta^{18}\text{O}$ and ETP (combined normalized eccentricity, tilt (obliquity) and precession (multiplied by -1) [Imbrie et al., 1984]) time series. ETP was preferred above insolation because the benthic and planktonic $\delta^{18}\text{O}$ spectra reveal distinct peaks in the eccentricity frequency band whereas eccentricity is present as an amplitude modulator in the insolation time series and, hence, does not show up in the spectrum. The cross-spectral procedure as described above was performed on both the insolation and precession tuned $\delta^{18}\text{O}$ time series.

3.5 Results

The benthic and planktonic $\delta^{18}\text{O}$ records show enrichments in the white layers and depletions in the reddish layers (Fig. 3.2). No obvious trend can be observed in either of the two records. Both records share the same features (correlation coefficient=0.57), but variations in planktonic $\delta^{18}\text{O}$ are stronger than those in benthic $\delta^{18}\text{O}$ ($\sim 1.3\text{‰}$ vs. $\sim 0.9\text{‰}$). Thick and distinct reddish layers are marked by prominent excursions to lighter $\delta^{18}\text{O}$ values. Clusters of reddish layers are characterized by prominent shifts to lighter values and high amplitude variability.

3.5.1 Power spectra

The power spectra of the $\delta^{18}\text{O}$ records and the sedimentation rate curve are shown in Figure 3.3 for both depth and time series. The $\delta^{18}\text{O}$ depth spectra reveal the strongest peak at ~ 3.4 m with additional strong peaks at ~ 2.4 and ~ 1.8 m. Less marked peaks occur at ~ 28 , ~ 10 , 1.57 and ~ 1.35 m in both spectra. The planktonic $\delta^{18}\text{O}$ spectrum shows an additional peak at ~ 4.9 m and the benthic $\delta^{18}\text{O}$ spectrum shows an extra peak at ~ 6.5 m and a “shoulder” at ~ 4.5 m. The spectrum of the sedimentation rate shows the strongest peak at ~ 9.5 m, a less marked peak at ~ 3.4 m and a minor peak at ~ 21 m. The power spectra of the $\delta^{18}\text{O}$ time series reveal the most prominent peak at the 41 kyr period of obliquity, followed by peaks at 23, 19 and ~ 300 kyr. Less marked peaks in both $\delta^{18}\text{O}$ spectra occur at ~ 125 , ~ 55 and ~ 30 kyr. An additional minor peak is observed at ~ 84 kyr in the benthic $\delta^{18}\text{O}$ spectrum. The spectra of the insolation and precession (dotted line in Fig. 3.3) tuned $\delta^{18}\text{O}$ time series are almost identical. Differences mainly concern a small decrease in power of the 41 kyr peak as well as small increases in the 23 and 19 kyr peaks when the precession tuned $\delta^{18}\text{O}$ time series is used. The spectrum of the sedimentation rate reaches highest power at ~ 135 kyr with a subsidiary peak at ~ 400 kyr. Marked peaks are furthermore observed at ~ 23.5 , ~ 55 and ~ 42 kyr.

The imprint of the main periods of eccentricity, obliquity and precession seems to be clearly represented in the $\delta^{18}\text{O}$ and sedimentation rate spectra. The spectral characteristics of the $\delta^{18}\text{O}$ depth and time series show strong similarities, but based on the assumption of a constant sedimentation rate of 7.7 cm/kyr (the average sedimentation rate), the dominant astronomical

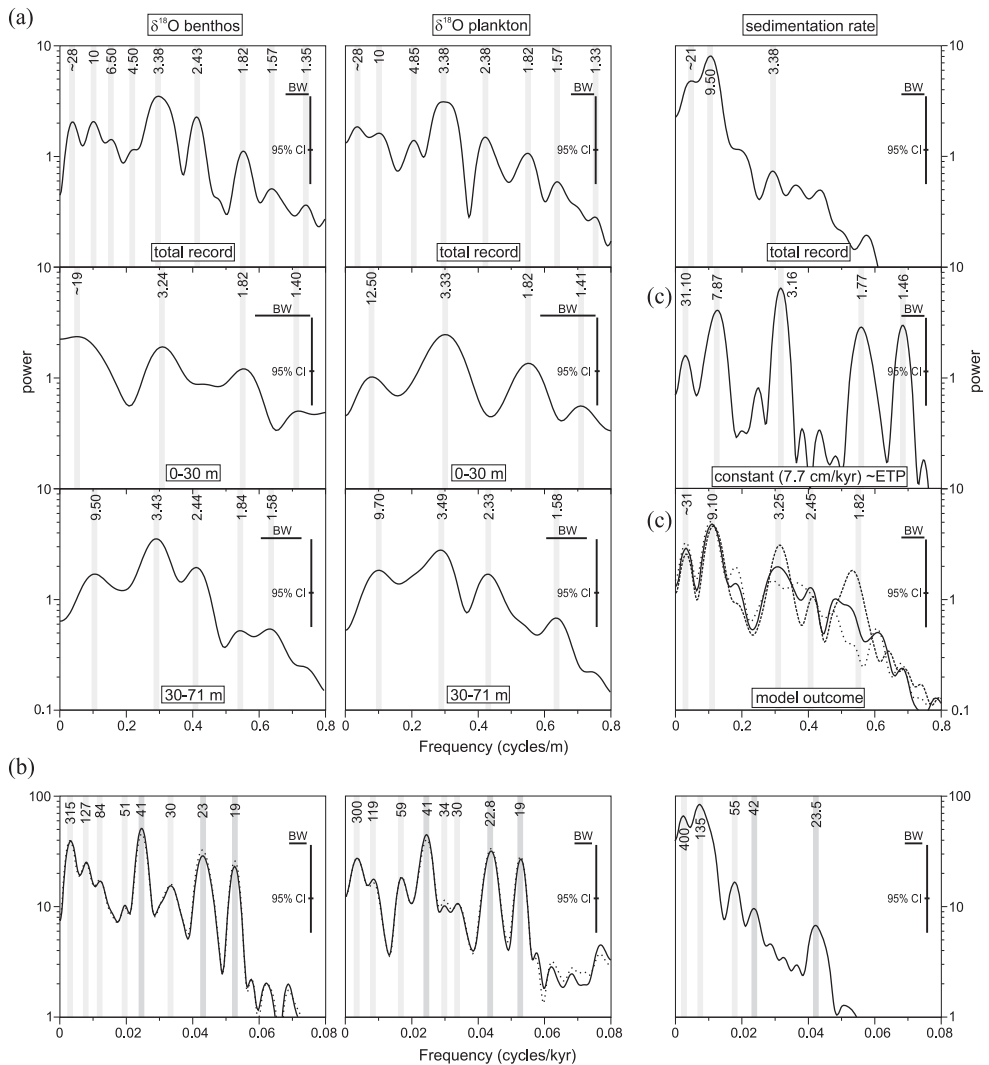


Figure 3.3 (a) Depth spectra of planktonic and benthic $\delta^{18}\text{O}$ and sedimentation rate with main periodicities (in meters) indicated. Planktonic and benthic $\delta^{18}\text{O}$ spectra are in addition shown for the interval 0-30 m and 30-71 m. Bandwidth (BW) is indicated by a horizontal bar, the 95% confidence interval (CI) by a vertical bar. BW=0.07 cycles/m for the total record, 0.17 cycles/m for the interval 0-30 m and 0.12 cycles/m for the interval 30-71 m. (b) Time spectra of planktonic and benthic $\delta^{18}\text{O}$ and sedimentation rate with main periodicities (in kyr) indicated. Solid spectral lines represent the insolation tuned $\delta^{18}\text{O}$ time series, dotted lines the precession tuned $\delta^{18}\text{O}$ series. Bandwidth (BW) is indicated by a horizontal bar, the 95% confidence interval (CI) by a vertical bar. BW=0.005 cycles/kyr. (c) Depth spectrum of transformed ETP (sum of normalized Eccentricity, Tilt and negative Precession) time series based on a constant sedimentation rate of 7.7 cm/kyr (upper panel) and of the same series with various sedimentation rates (Y=3, dotted line; Y=4, solid line; Y=5, dashed line) and accompanying multiplication factors. See text for detailed explanation.

Table 3.1 Observed average thicknesses of multiple-order sedimentary cycles in the AEB section as deduced from spectral analysis on $\delta^{18}\text{O}$ in the depth domain as compared to calculated thicknesses on the basis of the average duration of the main orbital periods when adopting the average value for sedimentation rate (7.7 cm/kyr) observed at AEB.

Astron. Period (kyr)	calculated thickness (cm)	observed thickness (cm)	offset (%)
404	3111	2800	90
127	978	1000	102
96	739	-	-
41	316	335	106
23	177	245	138
19	146	180	123

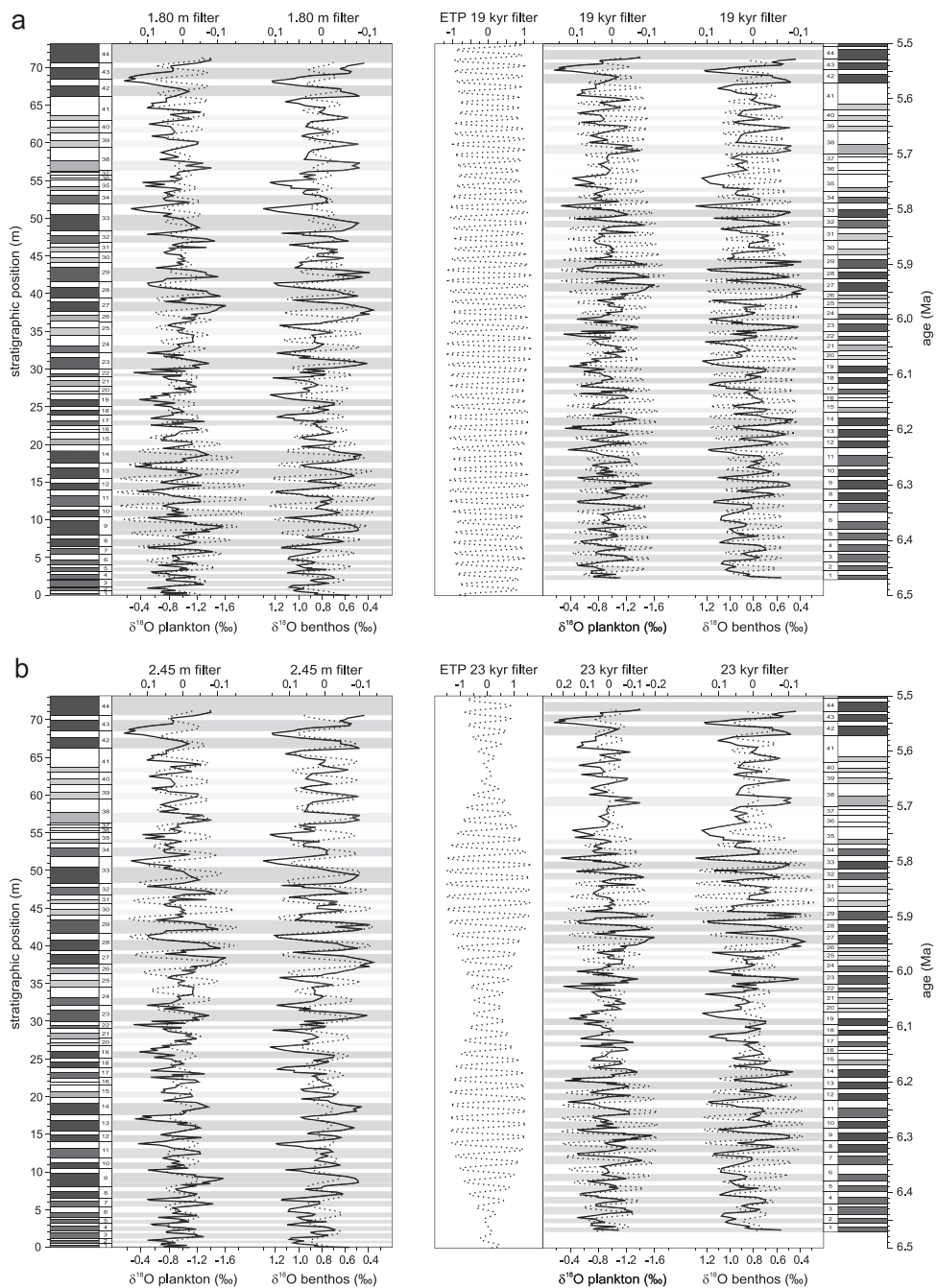
periods of 404, 127, (96), 41, 23 and 19 kyr would result in cycle thicknesses of 31.11, 9.78, (7.39), 3.16, 1.77 and 1.46 m, respectively (Tab. 1), whereas the dominant $\delta^{18}\text{O}$ periodicities are found at ~ 28 , ~ 10 , ~ 3.4 , ~ 2.4 and ~ 1.8 m.

To unravel the cause of these apparent offsets we used band-pass filters to extract and compare frequency components in $\delta^{18}\text{O}$ associated with the main spectral peaks in the depth and time domain. Following this approach, the dependence of peak positions in the depth spectra on changes in sedimentation rate can be evaluated. This is critical because the ~ 2.4 m and ~ 1.8 m cycles in $\delta^{18}\text{O}$ which correspond to periods of ~ 31 kyr and ~ 23 kyr based on the average sedimentation rate, could alternatively reflect the (secondary) 29 kyr component of obliquity and the 23 kyr component of precession, respectively.

3.5.2 Precession-related cyclicity

The filtered ~ 1.8 and ~ 2.4 m components of the $\delta^{18}\text{O}$ records in the depth domain are shown in Figure 3.4 and compared with the 19 and 23 kyr components in the time series and ETP. As expected, the number of ~ 1.8 and ~ 2.4 m cycles in the filtered records (respectively 39 and 30) is significantly less than the number of 19 and 23 kyr cycles of the tuned $\delta^{18}\text{O}$ time series and ETP (respectively 49 and 39). The filtered ~ 1.8 m cycle shows high amplitudes and an excellent fit with the colour cycles in the interval between 5 and 20 m and a similar good fit but with lower amplitudes between 30 and 42 m. The filtered ~ 2.4 m cycle reveals high amplitudes and a good fit with the colour cycles in the interval between 30 and 53 m apart from two misfits. These misfits are found at ~ 36 m and ~ 45 m where two colour cycles are represented by just a single ~ 2.4 m cycle in $\delta^{18}\text{O}$. A serious misfit for the ~ 2.4 m cycle is found in the lowermost 30 m of the section. Here only thirteen ~ 2.4 m cycles occur in the depth domain, whereas nineteen 23 kyr cycles are found

→ **Figure 3.4** (a) Comparison of 1.80 m and 19 kyr filtered components in planktonic and benthic $\delta^{18}\text{O}$ and the 19 kyr filtered ETP component (reflecting 19 kyr precession). The 1.80 m components were extracted using a Gaussian band-pass filter with a central frequency of 0.55 cycles/m and a bandwidth of 0.1 cycles/m. The 19 kyr components were extracted using a Gaussian band-pass filter with a central frequency of 0.0527 cycles/kyr and a bandwidth of 0.006 cycles/kyr. (b) Comparison of 2.45 m and 23 kyr filtered components in planktonic and benthic $\delta^{18}\text{O}$ and the 23 kyr filtered ETP component (reflecting 23 kyr precession). The 2.45 m components were extracted using a Gaussian band-pass filter with a central frequency of 0.41 cycles/m and a bandwidth of 0.08 cycles/m. The 23 kyr components were extracted using a Gaussian band-pass filter with a central frequency of 0.043 cycles/kyr and a bandwidth of 0.01 cycles/kyr. See text for further explanation.



in the corresponding time interval (Fig. 3.4b). Other misfits in the form of a reduced number of filtered $\delta^{18}\text{O}$ cycles in the depth domain as compared with the number of colour cycles (including “missing” cycles that lack sedimentary expression on the basis of our tuned age model) and of filtered 19 and 23 kyr components in $\delta^{18}\text{O}$ and ETP are found in all intervals marked by less distinct and/or “missing” cycles. These intervals are characterized by reduced sedimentation rates at times of minimum eccentricity (and thus reduced precession amplitudes).

To tackle the serious misfit between the number of ~ 2.4 m cycles in the depth domain and the number of 23 kyr cycles in the time domain, we carried out spectral analyses on the $\delta^{18}\text{O}$ records from 0 to 30 m and from 30 m to the top of the section (Fig. 3.3). These spectra clearly reveal that the ~ 1.8 m cycle is dominant in the lowermost 30 m, whereas the ~ 2.4 m cycle is prominent in the upper part. Apparently, the $\delta^{18}\text{O}$ spectra of the entire section combined the signals of both these intervals, thereby suggesting that they represent the 23 and 19 kyr components of precession. But the ~ 1.8 m cycle in the lower part appears to represent the 23 kyr precession component and matches perfectly with the 1.77 m cycle based on the assumption of a constant sedimentation rate of 7.7 cm/kyr (Tab. 3.1) and with the average colour cycle thickness of this interval. The absence of the ~ 2.4 m cycle in the lower 30 m explains the serious misfit between its number of cycles in the depth domain and the number of 23 kyr cycles in the time domain. On the contrary, the ~ 2.4 m cycle fits perfectly with the thicker colour cycles associated with eccentricity maxima in the upper

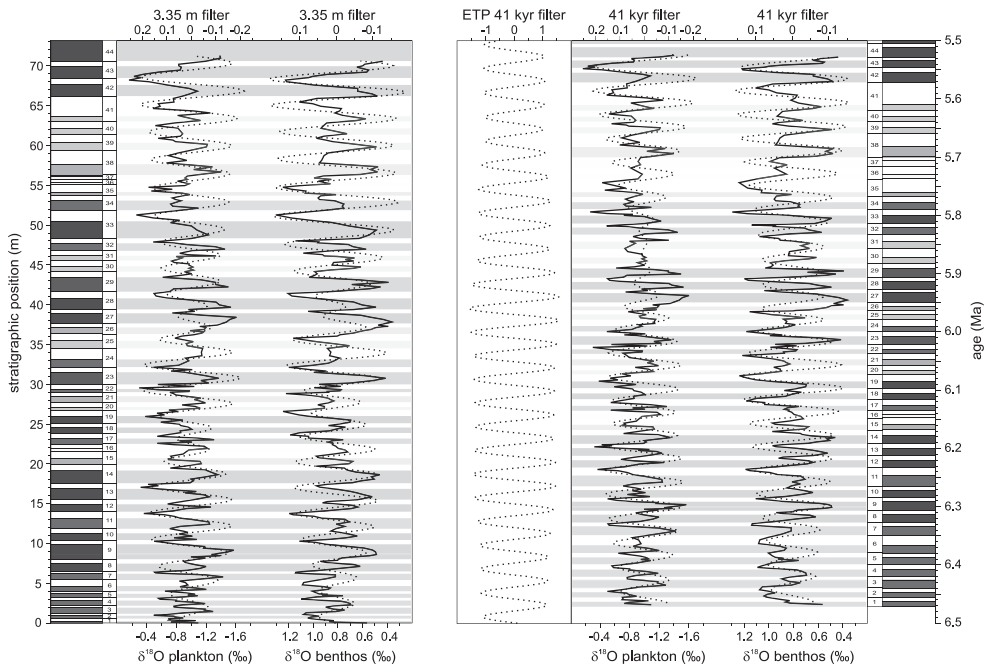


Figure 3.5 Comparison of 3.35 m and 41 kyr filtered components in planktonic and benthic $\delta^{18}\text{O}$ and the 41 kyr filtered ETP component (reflecting obliquity). The 3.35 m components were extracted using a Gaussian band-pass filter with a central frequency of 0.3 cycles/m and a bandwidth of 0.12 cycles/m. The 41 kyr components were extracted using a Gaussian band-pass filter with a central frequency of 0.0245 cycles/kyr and a bandwidth of 0.008 cycles/kyr. See text for further explanation.

part of the section. The two minor peaks at ~1.8 and ~1.6 m in the $\delta^{18}\text{O}$ spectra of this interval correspond to less thick colour cycles deposited during periods of low eccentricity values.

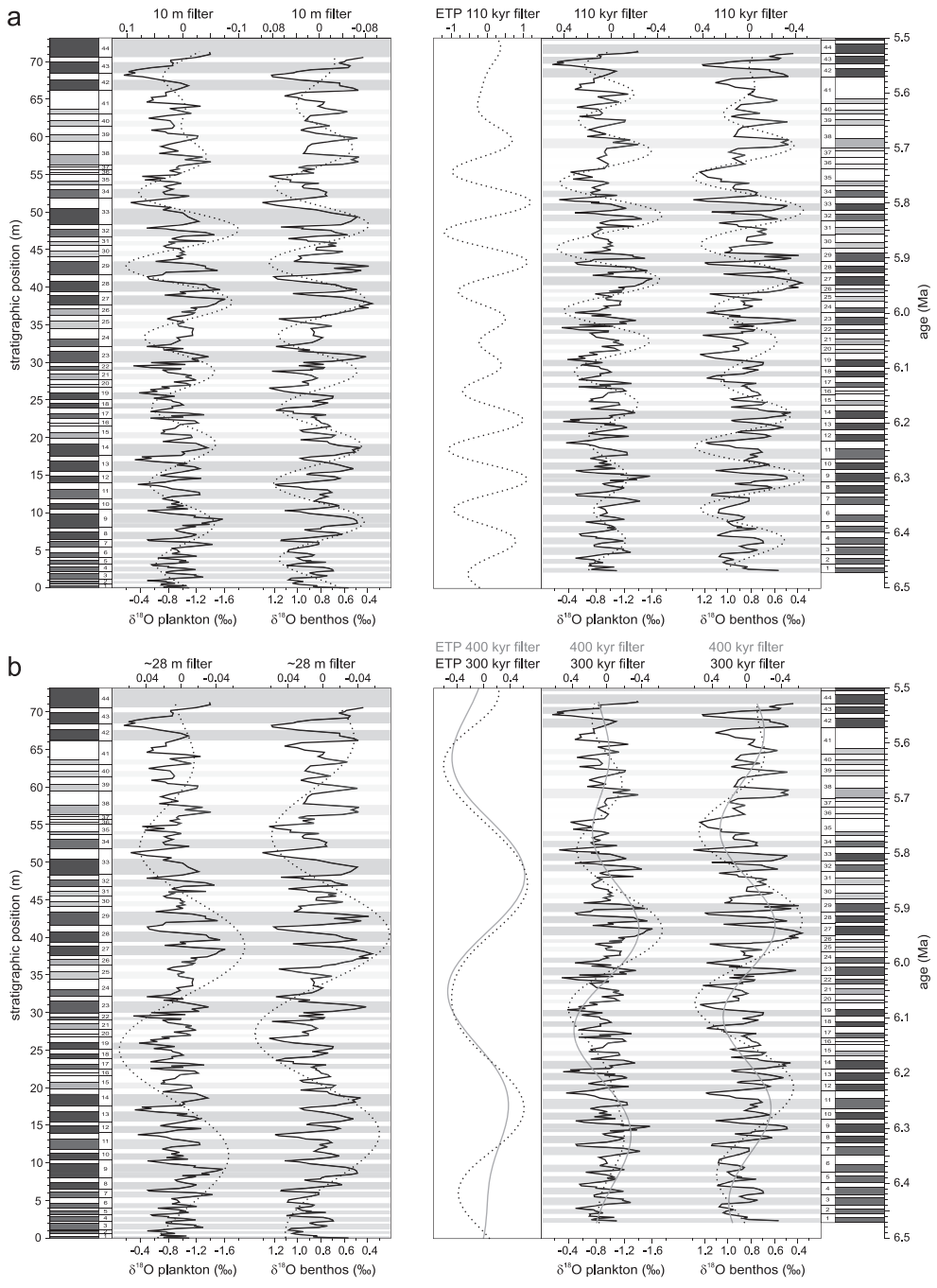
3.5.3 Obliquity-related cyclicity

A comparison between the filtered ~3.4 m cycle in $\delta^{18}\text{O}$ and the 41 kyr components in the $\delta^{18}\text{O}$ time series and ETP is shown in Figure 3.5. The number of twenty-two 3.38 m cycles in $\delta^{18}\text{O}$ is only one less than the number of 41 kyr cycles in the tuned $\delta^{18}\text{O}$ time series and ETP. This reduction is consistent with the 6% offset between the measured thickness of ~3.4 m and the expected thickness of 3.16 m calculated from the average sedimentation rate (Tab. 3.1). As a result, the filtered ~3.4 m cycle does not always follow the 41 kyr component in ETP and $\delta^{18}\text{O}$. Due to the very low sedimentation rates in the lowermost ~5 m of the section, the ~3.4 m filter reflects one cycle less, whereas one extra cycle is recorded in the interval between ~37 and ~43 m as a consequence of the very high sedimentation rates connected with the extreme precession minima around ~5.9 Ma. Finally, one obliquity-related cycle is not recognized at 55 m due to the extreme low sedimentation rate in this interval. Notwithstanding the changes in sedimentation rate, the position of the obliquity-related peak in the $\delta^{18}\text{O}$ depth spectra does not change between the lower and upper half of the section (Fig. 3.3).

3.5.4 Eccentricity-related cyclicity

The filtered ~10 m and ~28 m components of the $\delta^{18}\text{O}$ records are compared with their ~100 kyr and ~300 kyr components and the main eccentricity components in ETP in Figure 3.6. We have also extracted ~400 kyr filters from the $\delta^{18}\text{O}$ time series, which resemble almost perfectly the ~300 kyr filters due to the large overlap in the applied bandwidths. The filtered ~10 m cycle in $\delta^{18}\text{O}$ in the depth domain corresponds well with the ~100 kyr cycle in $\delta^{18}\text{O}$ in the time domain but reflects one cycle less due to the low sedimentation rate in the lowermost part of the section. The number of two-and-a-half ~28 m $\delta^{18}\text{O}$ cycles in the depth domain is similar to that of the filtered ~300/400 kyr cycles in $\delta^{18}\text{O}$ and ETP in the time domain (Fig. 3.6).

Thus, the position and hence the thickness of astronomical-related cycles in the AEB $\delta^{18}\text{O}$ depth records seems to be significantly affected by changes in sedimentation rate. Three intervals can be distinguished based on the spectral characteristics in the depth domain and the average thickness of the colour cycles. The first interval comprises the lowermost ~5 meters of the section. Colour cycles in this interval have an average thickness of less than 1 m, suggesting that sedimentation rates are very low. A corresponding peak does not show up however in the $\delta^{18}\text{O}$ depth spectra probably because of the limited thickness of this interval. As a consequence, the number of cycles will be underestimated when band-pass filters are applied to extract the dominant precession-related components of the $\delta^{18}\text{O}$ spectra calculated for the entire section. The second interval, between ~5 and ~30 m, results in $\delta^{18}\text{O}$ spectra and band-pass filters that are generally in good agreement with what could be expected from the average sedimentation rate of 7.7 cm/kyr. This interpretation is consistent with the derived sedimentation rate curve, which revealed only minor variations in this interval. The third and last interval comprises the top ~40 meters of the section. The thickness of the obliquity related cycle in $\delta^{18}\text{O}$ remains the same as in the lower part of the section, but the 23 kyr precession-related cycle thickness increases from ~1.8 to ~2.4 m. This change coincides with the shift to strong(er) eccentricity-related variations in sedimentation rate.



← **Figure 3.6** (a) Comparison of ~10 m and ~110 kyr filtered components in planktonic and benthic $\delta^{18}\text{O}$ and the ~110 kyr filtered ETP component (reflecting short-term eccentricity). The 10 m components were extracted using a Gaussian band-pass filter with a central frequency of 0.1 cycles/m and a bandwidth of 0.04 cycles/m. The 110 kyr components were extracted using a Gaussian band-pass filter with a central frequency of 0.009 cycles/kyr and a bandwidth of 0.004 cycles/kyr. (b) Comparison of ~28 m and ~300/400 kyr filtered components in planktonic and benthic $\delta^{18}\text{O}$ and the ~400 kyr filtered ETP component (reflecting long-term eccentricity). The 28 m components were extracted using a Gaussian band-pass filter with a central frequency of 0.0355 cycles/m and a bandwidth of 0.05 cycles/m. The 300 and 400 kyr components were extracted using Gaussian band-pass filters with central frequencies of 0.0033 and 0.0025 cycles/kyr, and bandwidths of 0.004 and 0.002 cycles/kyr, respectively. See text for further explanation.

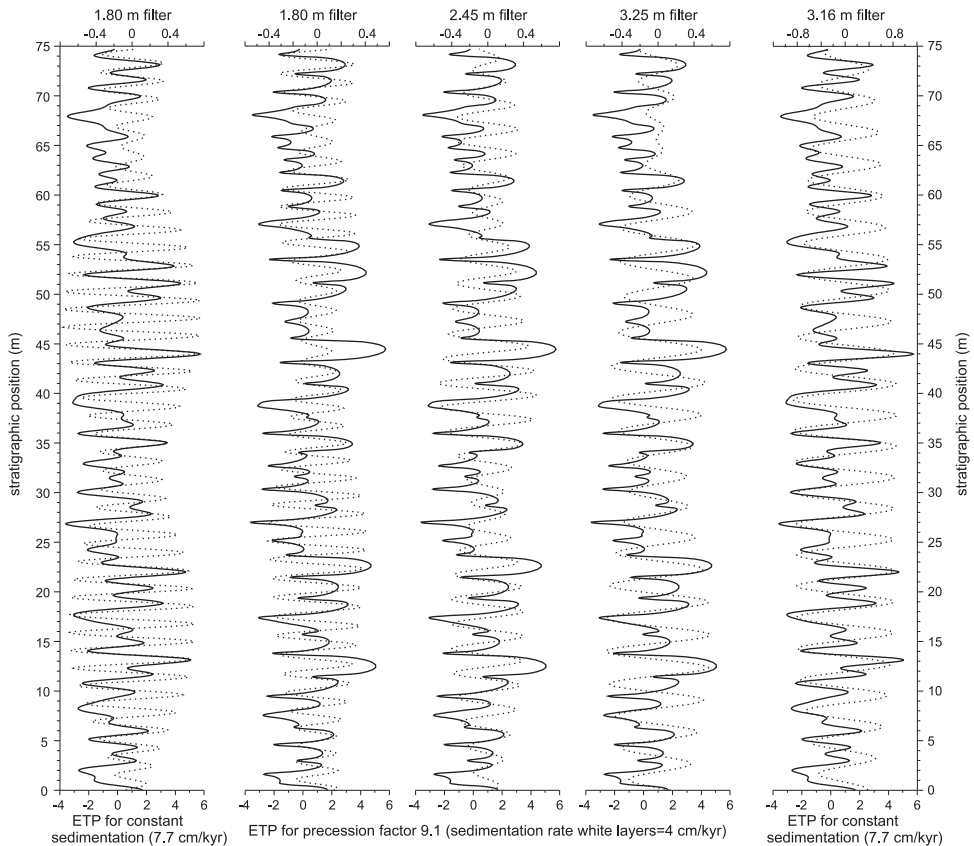


Figure 3.7 Depth-transformed ETP curve for a constant sedimentation rate of 7.7 cm/kyr and the same curve for a sedimentation rate (Y) of 4 cm/kyr and a linear multiplication factor (X) of 9.1. Dotted lines represent additional overlays of the ~1.8, ~2.4 and ~3.2 m filtered components of the same series. See also figure 3.3c. See text for further explanation.

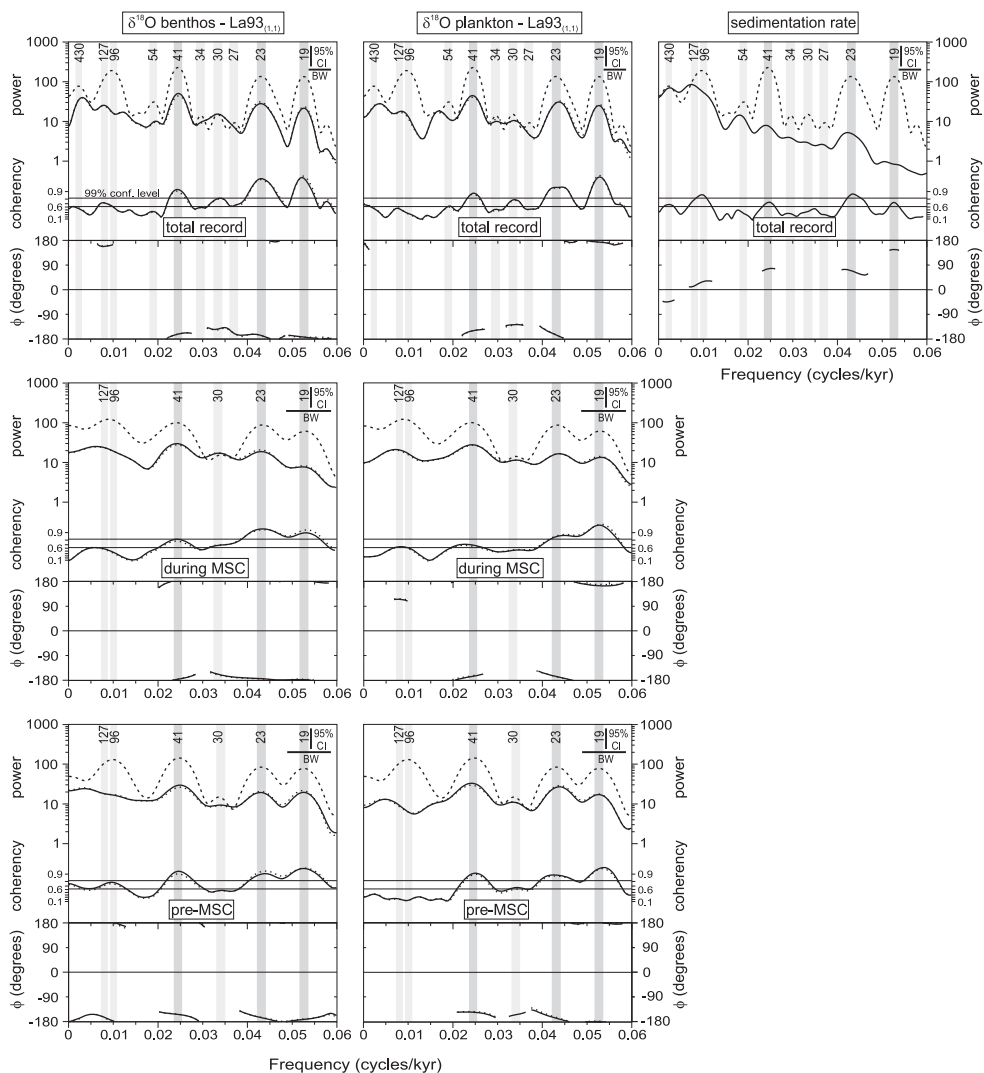


Figure 3.8 Cross-spectra of benthic $\delta^{18}\text{O}$, planktonic $\delta^{18}\text{O}$ and sedimentation rate against ETP based on solution La93_(1,1). Each panel shows the normalized variance density spectrum (upper part), coherency spectrum (middle part) and phase of the time series with respect to ETP (bottom part). Dashed line in upper part of each panel represents the ETP spectrum. Solid lines in each panel represent the insolation tuned $\delta^{18}\text{O}$ time series, dotted lines the precession tuned $\delta^{18}\text{O}$ series. Bandwidth (BW, horizontal bar) is 0.0053 for the total record and 0.0097 and 0.0105 for the pre-MSC and MSC parts of the record, respectively. The 95% confidence interval (CI) is marked by the vertical bar. The 95% and 99% confidence levels of non-zero coherency are marked by horizontal lines in the coherency spectrum. Phase is only shown for the $\geq 95\%$ significance level.

3.5.5 Non-linear precession-forced sedimentation rate changes

We have applied a simple sedimentation rate model to test the effect of eccentricity-related changes in sedimentation rate on the thicknesses of the $\delta^{18}\text{O}$ and colour cycles. For this purpose, the ETP record of the studied time interval of AEB (i.e. from ~6.47 to ~5.5 Ma) has been converted from the time to the depth domain using various scenarios for changes in the sedimentation rate. First we used the constant sedimentation rate of 7.7 cm/kyr (Fig. 3.7). Hence, the power spectrum of the ETP depth series reveals the expected peaks as summarized in Table 3.1 (Fig. 3.3c).

Secondly, the sedimentation rate was held constant at a fixed value Y at times that normalized precession values reached positive values, but was made to increase linearly with a fixed multiplication factor X when normalized precession values became negative. Both Y and X were chosen so that the average sedimentation rate arrived at 7.7 cm/kyr and hence the length of the simulated depth interval is identical to the studied interval at AEB. An example of the transformed ETP time series against depth for $Y=4$ and $X=9.1$ is shown in Figure 3.7. Evidently, the thickness of the intervals corresponding to precession minima and, hence, the reddish layers has been enhanced, whereas those corresponding to precession maxima and the beige layers are reduced. We selected different values for Y and X and carried out spectral analysis on the resulting ETP depth series (Fig. 3.3c). Our analyses reveal that a decrease in Y (i.e., a further reduction in sedimentation rate in the beige layers relative to the reddish layers) causes a reduction in power at ~1.8 m, but an increase at ~2.4 m (see Fig. 3.3). The peak position of the obliquity-related cycle remains more or less the same for Y values larger than 4. Band-pass filters show that the ~2.4 m cycle is dominant during eccentricity maxima and that this filter starts to pick up one precession-related cycle less at times of eccentricity minima. In these intervals, the ~1.8 m cycle results in a much better fit (Fig. 3.7). Hence, a non-linear response of the sedimentation rate to precessional forcing may largely explain the observed increase in the 23 kyr precession-related cycle thickness and the almost unchanged obliquity-related cyclicity within the upper interval of the AEB section. Evidently, a similar non-linear response to precessional forcing of lithology-bound proxies may explain the presence of spectral peaks in the eccentricity bands of the spectrum.

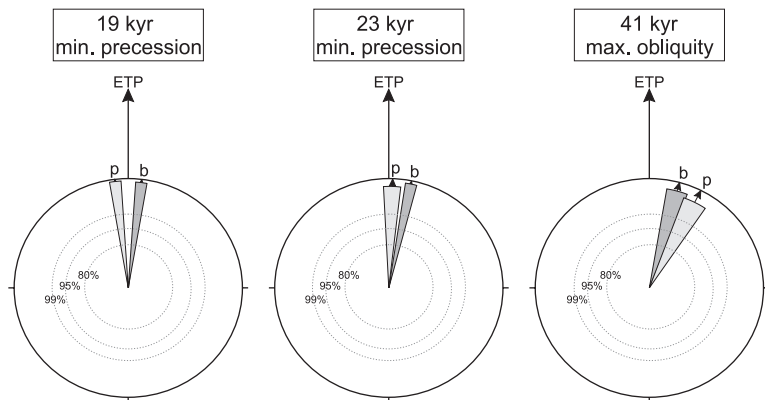
Distorted orbital signals in the depth-time domain due to variations in sedimentation rate have been modeled and described in detail by Herbert [Herbert, 1994]. In particular, his – modeled – example of a 100 kyr modulation of a 20 kyr cycle whereby the lower frequency cycle exerts an additional control on accumulation rate shows similarities with our modeled ETP record in terms of frequency and amplitude [see Figs. 6 and 7 in Herbert, 1994]. The main difference is that we assume an increase in sedimentation rate during minimum precession that is linked to amplitude (i.e. modulated by eccentricity) and keep the minimum sedimentation rate constant below a certain threshold value for precession (i.e. normalized precession ≥ 0). Herbert [1994] notices that the modulation by longer-term cycles (such as short- and long-term eccentricity) results in distortions in the higher-frequency end of the spectrum; the time-depth distortions act to produce artifacts at combination tones ($f_1 \pm nf_2$) where f_1 (frequency), f_2 is the shorter, modulated period, f_2 the modulating period and n an integer [Weedon, 1989]. Following this explication, the ~2.4, ~1.8, 1.57 and 1.35 m peaks in the $\delta^{18}\text{O}$ depth spectra would represent the primary 19 and 23 kyr precession cycles and the combination tones that result from the modulation by short-term eccentricity. In that case, combination tones will partly have the same frequencies as the primary components. At AEB, the situation is even more complicated because the ~2.4 m cycle starts to pick up the obliquity signal when the sedimentation rate is extremely low, while the obliquity related ~3.4 m cycle incorporates the 23 kyr signal when the sedimentation rate is extremely high.

Table 3.2 Coherency (k) and phase (ϕ) for planktonic and benthic $\delta^{18}\text{O}$ time series and ETP for solution La93_(1,1) in the main orbital frequency bands. Positive phases denote a lag and negative phases a lead for $-\delta^{18}\text{O}$ with respect to maximum ETP forcing. Periods and coherencies in bold are significant at the 95% confidence level ($k \geq 0.55$).

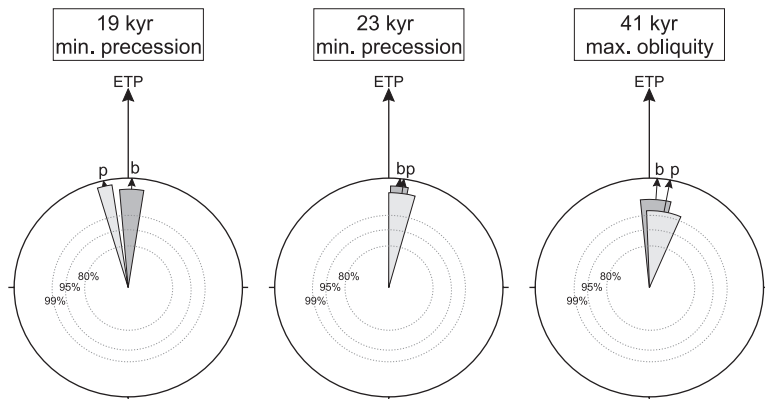
insolation tuned time series								
period (kyr)	proxy	k	ϕ (°)	low.	up.	limit \pm	ϕ (kyr)	limit \pm
Total record								
19,2	$\delta^{18}\text{O}$ benthos	0,97	7	-176	-170	3	0,4	0,2
18,9	$\delta^{18}\text{O}$ plankton	0,98	-7	170	176	3	-0,4	0,2
23,2	$\delta^{18}\text{O}$ benthos	0,97	12	-172	-165	3	0,7	0,2
22,4	$\delta^{18}\text{O}$ plankton	0,93	2	-183	-172	5	0,2	0,3
29,4	$\delta^{18}\text{O}$ benthos	0,81	38	-152	-133	10	3,1	0,8
29,7	$\delta^{18}\text{O}$ plankton	0,79	49	-142	-121	11	4,0	0,9
40,9	$\delta^{18}\text{O}$ benthos	0,92	16	-170	-158	6	1,8	0,7
40,5	$\delta^{18}\text{O}$ plankton	0,88	28	-159	-145	7	3,2	0,8
53,0	$\delta^{18}\text{O}$ benthos	0,45	4	-204	-149	28	0,5	4,0
51,6	$\delta^{18}\text{O}$ plankton	0,63	1	-196	-163	17	0,1	2,4
130	$\delta^{18}\text{O}$ benthos	0,72	-22	145	171	13	-7,8	4,7
135	$\delta^{18}\text{O}$ plankton	0,56	-48	112	152	20	-18,0	7,6
during MSC								
18,8	$\delta^{18}\text{O}$ benthos	0,90	2	-184	-171	7	0,1	0,3
19,0	$\delta^{18}\text{O}$ plankton	0,95	-13	162	171	4	-0,7	0,2
23,2	$\delta^{18}\text{O}$ benthos	0,93	6	-179	-168	5	0,4	0,3
22,4	$\delta^{18}\text{O}$ plankton	0,87	8	-180	-164	8	0,5	0,5
28,5	$\delta^{18}\text{O}$ benthos	0,70	16	-178	-150	14	1,3	1,1
28,8	$\delta^{18}\text{O}$ plankton	0,54	31	-170	-128	21	2,5	1,7
40,9	$\delta^{18}\text{O}$ benthos	0,81	4	-186	-166	10	0,5	1,1
44,2	$\delta^{18}\text{O}$ plankton	0,71	11	-183	-156	13	1,3	1,6
125	$\delta^{18}\text{O}$ benthos	0,58	-48	113	151	19	-16,7	6,7
119	$\delta^{18}\text{O}$ plankton	0,65	-65	99	131	16	-21,6	5,3
before MSC								
19,0	$\delta^{18}\text{O}$ benthos	0,94	10	-175	-165	5	0,5	0,3
18,6	$\delta^{18}\text{O}$ plankton	0,95	0	175	184	5	0,0	0,2
22,7	$\delta^{18}\text{O}$ benthos	0,90	12	-175	-162	7	0,7	0,4
23,5	$\delta^{18}\text{O}$ plankton	0,89	17	-170	-156	7	1,1	0,5
29,2	$\delta^{18}\text{O}$ benthos	0,56	29	-172	-131	20	2,3	1,6
29,2	$\delta^{18}\text{O}$ plankton	0,66	28	-167	-136	16	2,3	1,3
40,6	$\delta^{18}\text{O}$ benthos	0,92	26	-160	-148	6	2,9	0,6
39,8	$\delta^{18}\text{O}$ plankton	0,91	34	-153	-140	6	3,7	0,7
103	$\delta^{18}\text{O}$ benthos	0,78	5	-186	-164	11	1,4	3,2
129	$\delta^{18}\text{O}$ plankton	0,22	66	-177	-52	62	23,6	22,5

precession tuned time series								
period (kyr)	proxy	k	Ø (°)	low.	up.	limit ±	Ø (kyr)	limit ±
Total record								
19,0	δ ¹⁸ O benthos	0,98	7	-175	-170	3	0,4	0,2
19,0	δ ¹⁸ O plankton	0,98	-5	172	178	3	-0,3	0,1
23,3	δ ¹⁸ O benthos	0,97	14	-169	-162	3	0,9	0,2
22,3	δ ¹⁸ O plankton	0,93	-1	174	184	5	-0,1	0,3
23,4	δ ¹⁸ O plankton	0,93	19	-166	-155	6	1,2	0,4
29,5	δ ¹⁸ O benthos	0,80	36	-155	-134	10	2,9	0,8
29,6	δ ¹⁸ O plankton	0,77	51	-140	-118	11	4,2	0,9
41,4	δ ¹⁸ O benthos	0,91	16	-170	-157	6	1,9	0,7
40,8	δ ¹⁸ O plankton	0,87	30	-158	-142	8	3,4	0,9
53,1	δ ¹⁸ O benthos	0,41	6	-204	-144	30	0,9	4,5
51,9	δ ¹⁸ O plankton	0,60	3	-195	-159	18	0,4	2,6
130	δ ¹⁸ O benthos	0,72	-21	146	172	13	-7,5	4,7
135	δ ¹⁸ O plankton	0,58	-48	113	151	19	-18,0	7,3
during MSC								
18,7	δ ¹⁸ O benthos	0,92	4	-182	-170	6	0,2	0,3
18,8	δ ¹⁸ O plankton	0,96	-11	165	174	4	-0,6	0,2
22,8	δ ¹⁸ O benthos	0,92	6	-179	-168	6	0,4	0,4
22,1	δ ¹⁸ O plankton	0,88	5	-183	-168	7	0,3	0,4
28,6	δ ¹⁸ O benthos	0,70	16	-178	-150	14	1,3	1,1
28,8	δ ¹⁸ O plankton	0,56	31	-169	-129	20	2,5	1,6
41,1	δ ¹⁸ O benthos	0,78	5	-186	-164	11	0,6	1,3
44,2	δ ¹⁸ O plankton	0,69	14	-180	-151	14	1,7	1,8
126	δ ¹⁸ O benthos	0,56	-47	113	153	20	-16,5	7,0
119	δ ¹⁸ O plankton	0,63	-64	100	133	17	-21,0	5,5
before MSC								
18,9	δ ¹⁸ O benthos	0,94	11	-174	-164	5	0,6	0,3
18,7	δ ¹⁸ O plankton	0,94	1	-183	-174	5	0,1	0,3
22,6	δ ¹⁸ O benthos	0,92	13	-173	-161	6	0,8	0,4
23,4	δ ¹⁸ O plankton	0,88	17	-171	-156	7	1,1	0,5
29,3	δ ¹⁸ O benthos	0,56	31	-169	-129	20	2,6	1,6
29,3	δ ¹⁸ O plankton	0,61	33	-164	-129	18	2,7	1,4
40,8	δ ¹⁸ O benthos	0,90	27	-160	-147	7	3,0	0,7
40,0	δ ¹⁸ O plankton	0,90	35	-152	-139	7	3,9	0,7
104	δ ¹⁸ O benthos	0,75	2	-189	-166	12	0,7	3,4
139	δ ¹⁸ O plankton	0,21	60	-187	-54	66	23,0	25,5

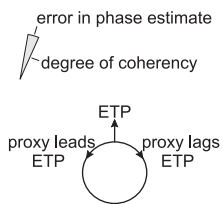
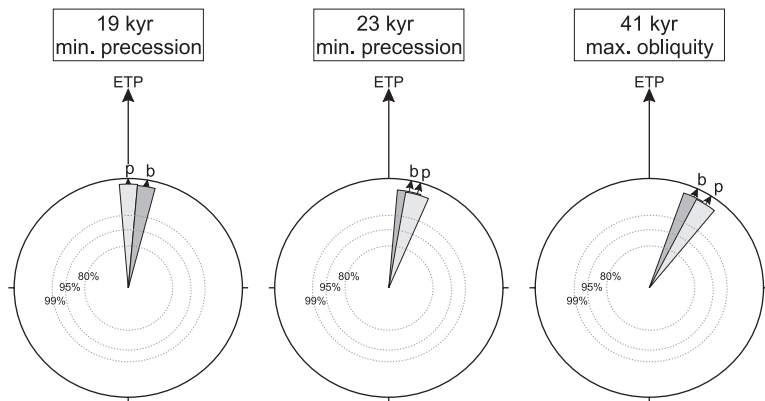
Total record



during MSC



before MSC



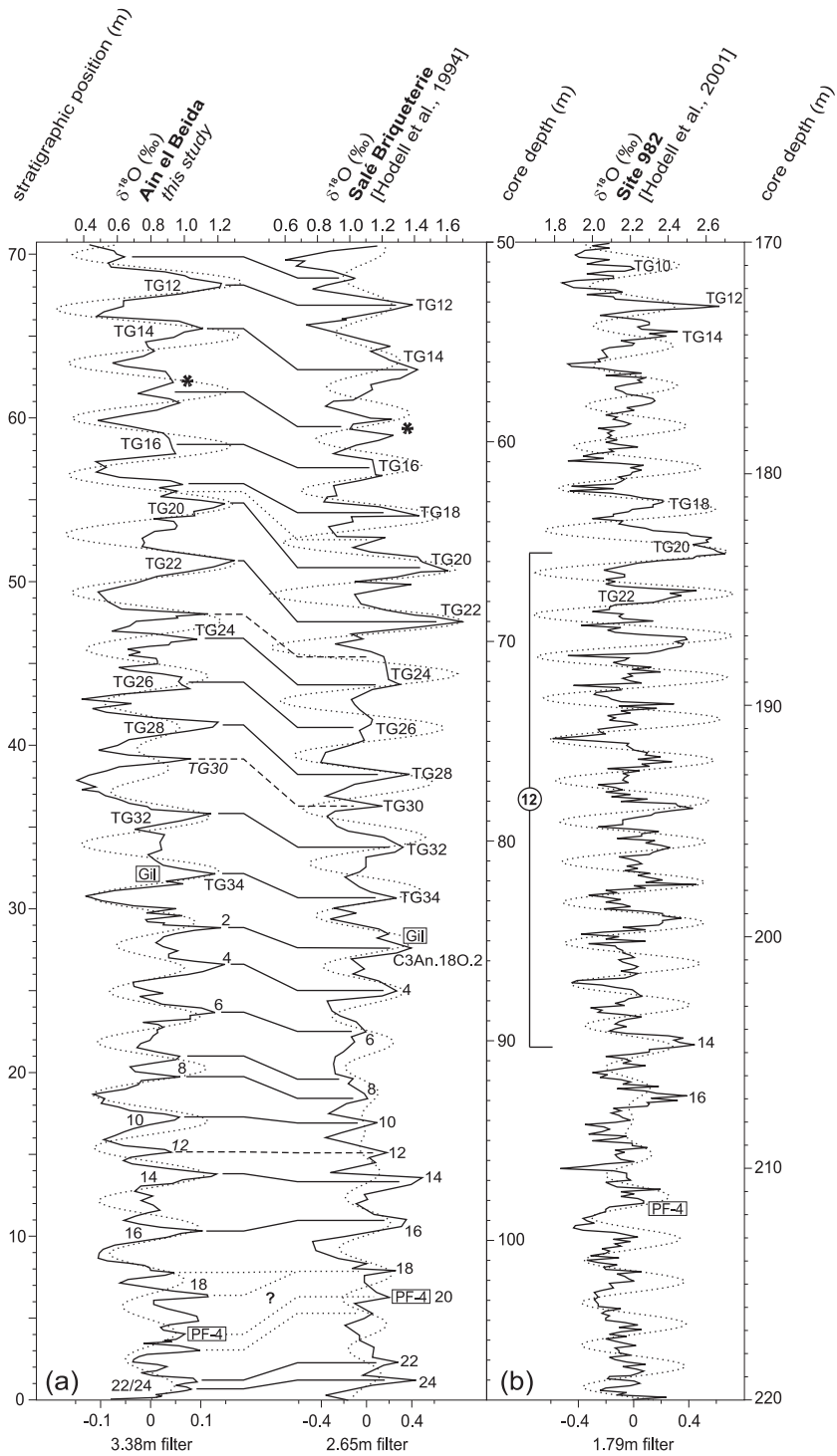
← **Figure 3.9** Phase wheels for planktonic and benthic $\delta^{18}\text{O}$ with respect to maximum ETP (i.e. maximum eccentricity (not shown), maximum obliquity and minimum precession) for solution La93_(1,1). For the phase of planktonic (p) and benthic (b) $\delta^{18}\text{O}$, 180° was added to change $\delta^{18}\text{O}$ in $-\delta^{18}\text{O}$ consistent with the phase relation for $\delta^{18}\text{O}$ with maximum ETP forcing. Phases plotted clockwise with respect to maximum ETP forcing denote a lag while counterclockwise they denote a lead to maximum ETP. Radius of sectors displays coherency with ETP; dotted circles indicate the 80% (inner circle), 95% and 99% (outer circle) coherency levels. Width of sectors indicates upper and lower phase limits. All coherency and phase values are presented in Table 3.2.

3.5.6 Cross-spectral analysis

We applied cross-spectral analysis to further unravel the phase relations between the filtered precession, obliquity and eccentricity components in the benthic and planktonic $\delta^{18}\text{O}$ time series and ETP (Fig. 3.8). Coherency and phase of the main astronomical cycles are presented for the entire AEB record as well as for the pre-MSC (~6.5 to 6.0 Ma) and MSC (6.0 to ~5.5 Ma) intervals separately (Tab. 3.2; Fig. 3.9). The cross-spectral analysis was carried out on both the insolation and precession tuned $\delta^{18}\text{O}$ time series but this resulted in negligible differences in coherency and phase.

The coherency between $\delta^{18}\text{O}$ and ETP is very high in the 19 and 23 kyr frequency bands and their phases (time lags) approximate zero as could be expected from the tuning procedure and the good correlation between $\delta^{18}\text{O}$ and lithology. During MSC times (upper interval), there seems to be a small reduction (~0.5 kyr) in the precession related lag with respect to the preceding interval. The $\delta^{18}\text{O}$ time series and ETP reveal high to very high coherencies in the main obliquity frequency band. $\delta^{18}\text{O}$ and ETP are not exactly in phase, but maxima (minima) in the 41 kyr component of $\delta^{18}\text{O}$ are lagging the minima (maxima) in obliquity by a few kyrs (Tab. 3.2; Fig. 3.9). The lag (but also the coherency) is slightly reduced in the MSC part relative to the pre-MSC part of the $\delta^{18}\text{O}$ time series. The coherency spectra further revealed highly significant coherencies for the 29 kyr and to a lesser degree for the 54 kyr component in $\delta^{18}\text{O}$ relative to ETP. Although these components are reflected by only minor peaks in the $\delta^{18}\text{O}$ power spectra, they probably represent secondary obliquity components, a combination tone of precession frequencies and/or the first-order harmonic of eccentricity [e.g., Herbert, 1994; Von Dobeneck and Schmieder, 1999].

The coherency between the ~100 and ~300/400 kyr components in $\delta^{18}\text{O}$ and ETP is relatively low and accompanied by considerable uncertainties in phase, which is not surprising for the ~300/400 kyr cycle, in view of the limited number (± 2.5) of cycles present. These uncertainties already became apparent from the comparison of the ~100 kyr and ~300/400 kyr cycles in $\delta^{18}\text{O}$ and ETP (Fig. 3.6). In the first place, only a single ~100 kyr cycle is found in the $\delta^{18}\text{O}$ time series between 6.15 and 5.95 Ma, whereas two eccentricity cycles should be present. This may at least be partly due to the shorter than average period of these eccentricity cycles and their small amplitudes, associated with the ~400 kyr eccentricity minimum around 6.05 Ma. Secondly, the filtered $\delta^{18}\text{O}$ signal tends to lead eccentricity and runs out-of-phase with the small-scale clusters of reddish layers, in particular for the interval younger than 6.0 Ma. These observations are confirmed by the results of the cross-spectral analyses, which revealed a lead of ~20 kyr between the $\delta^{18}\text{O}$ time series and ETP in the MSC interval (Tab. 2). Apparently, two saw tooth-like patterns in the $\delta^{18}\text{O}$ records are responsible for this out-of-phase relationship. They start with strongly depleted $\delta^{18}\text{O}$ values at the base of the two prominent reddish-layer clusters at ~5.92 and ~5.8 Ma and end with extremely heavy values in the overlying homogeneous intervals. Such patterns may point to an additional non-linearity in the system during the younger part of AEB, similar to the ~100 kyr



← **Figure 3.10** Comparison in the depth domain between the benthic $\delta^{18}\text{O}$ records of Ain el Beida and Salé [after Hodell et al., 1994] (a) and ODP Site 982 [after Hodell et al., 2001] (b). The main spectral peak – related to obliquity – of each depth record was filtered (dotted lines) using Gaussian band-pass filters with central frequencies of 0.295 (AEB), 0.38 (Salé) and 0.56 (Site 982) cycles/m and bandwidths of 0.12 (AEB), 0.08 (Salé) and 0.10 cycles/m (Site 982). Stage numbers of cold isotopic stages are indicated [after Shackleton et al., 1995b]; asterisks indicate unnamed stage (i.e. TG15.2). Stages in italics are related to precession and correlated by dashed lines; uncertain correlations are indicated by dotted lines. Positions of PF-4 bioevent (PF-4) and base of the Gilbert (Gil) Chron are indicated.

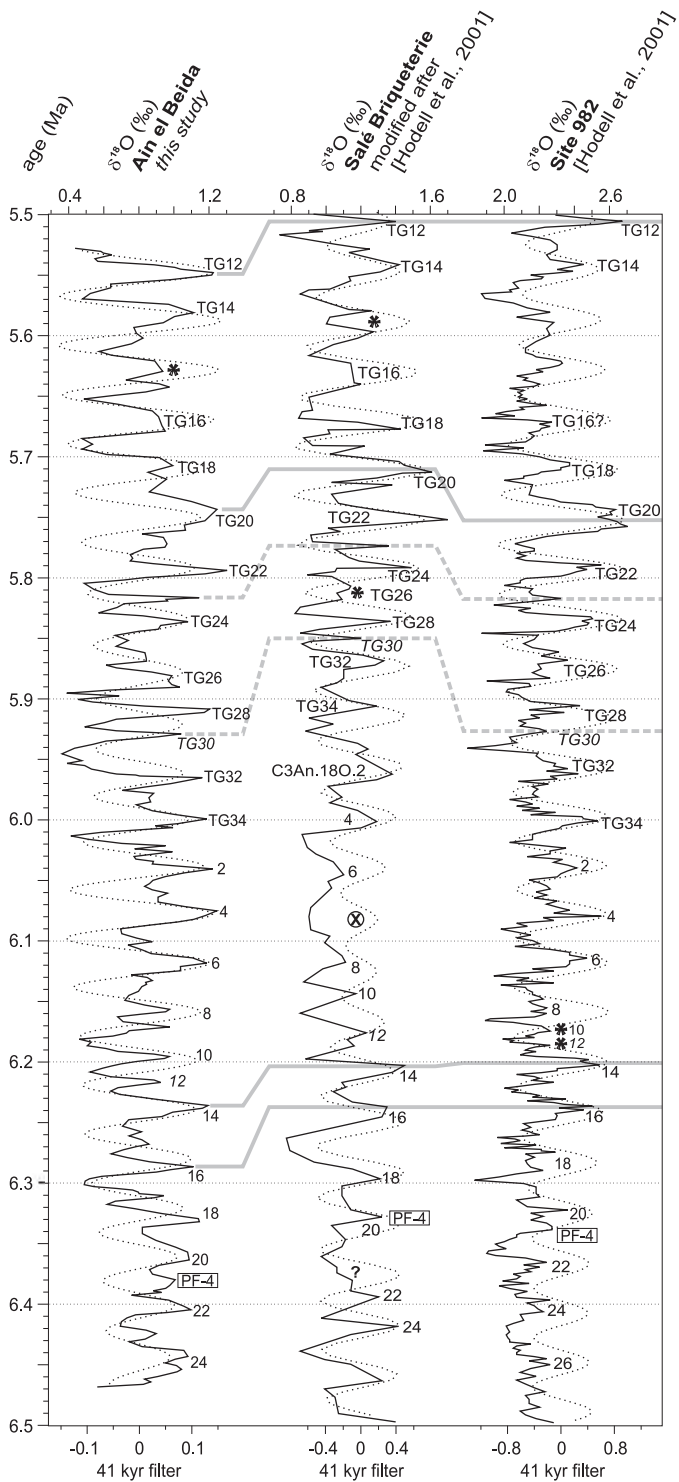
glacial cycles of the late Pleistocene. But it is clear that also the strength of the 41 kyr cycle in $\delta^{18}\text{O}$ may play a critical role in controlling this out-of-phase relationship in the 100 kyr frequency band.

Finally, there is a significant offset between the filtered ~300/400 kyr cycles in $\delta^{18}\text{O}$ and ETP (Fig. 3.6), but these offsets are not precisely the same for the benthic and planktonic $\delta^{18}\text{O}$ records for in particular the lower part of the AEB section. The apparent reason for these offsets are the strong depletions in $\delta^{18}\text{O}$ in the reddish layers of cycles 27–29 in combination with the strong enrichments in $\delta^{18}\text{O}$ in the beige layers of cycles 33 and 35.

3.6 Discussion

Hodell et al. [1994] convincingly showed that the benthic $\delta^{18}\text{O}$ record from the drill hole at Salé Briqueterie located 5 km north of AEB dominantly reflects obliquity-induced changes for the time interval under consideration. However, they could not demonstrate the presence of a precession signal in their $\delta^{18}\text{O}$ records due to a too low sample resolution. Moreover, their time control was poor in the upper part of the core because of a less clear magnetic signal and the lack of biostratigraphic events. Despite this lack of time control, the authors were able to identify the most important isotope stages TG12, TG14, TG20 and TG22 of Shackleton et al. [1995b]. Ages were assigned to the upper part of the core on the basis of an extrapolation of the sedimentation rate determined by the reliable magnetostratigraphic calibration of the lower part of the core to CK92 [Cande and Kent, 1992]. But the age estimate of Hodell et al. [1994] for isotope stage TG22 (5.63 Ma) was ~130 kyr younger than that of Shackleton et al. [1995b]; the latter estimate was based on the astronomical tuning of GRAPE density measurements of ODP Site 846 to the orbital insolation record of Berger and Loutre [1991].

Hodell et al. [2001] studied the latest Miocene to early Pliocene succession of ODP Site 982 from the Rockall Plateau in the North Atlantic to obtain an open ocean record that could be linked to events associated with the MSC in the Mediterranean. These sediments were astronomically tuned by correlating the record of gamma ray attenuation (GRA) bulk density to the 65°N summer insolation curve of La90_(1,1) and the benthic $\delta^{18}\text{O}$ record to obliquity [Hodell et al., 2001]. As starting point, Hodell et al. [2001] applied the ages of TG20 and TG12 derived from ODP Site 926 [Shackleton and Crowhurst, 1997] and those of several younger (Pliocene) stages from ODP Site 846 [Shackleton et al., 1995b], but re-tuned the latter stages one obliquity cycle older. In addition, they used the PF-4 bioevent of Sierro et al. [1993] dated astronomically at 6.36 Ma in the Mediterranean [Sierro et al., 2001]. The tuned benthic $\delta^{18}\text{O}$ record of ODP Site 982 was subsequently used to recalibrate the oxygen isotope chronology of Salé Briqueterie [Hodell et al., 2001], which resulted for instance in a significantly older estimate for TG22 (5.74 Ma) than previously determined by Hodell et al. [1994].



← **Figure 3.11** Correlation between the benthic $\delta^{18}\text{O}$ time series of Ain el Beida, Salé [Hodell et al., 1994; 2001] and ODP Site 982 [Hodell et al., 2001]. The 41 kyr component of each record was filtered using Gaussian band-pass filters with a central frequency of 0.0245 cycles/m and bandwidths of 0.006 (AEB), 0.005 (Salé) and 0.004 cycles/m (Site 982). Stage numbers of cold isotopic stages are indicated [after Shackleton et al., 1995b] as well as the PF-4 bio-event. Asterisks indicate unnamed stage and stages not picked up by the band-pass filters; encircled cross represents extra cycle picked up by the band-pass filter.

3.6.1 Comparison between AEB, Salé Briqueterie and ODP Sites 846, 926 and 982

To independently determine the validity of the age model of Hodell et al. [2001], we compared the benthic $\delta^{18}\text{O}$ records of AEB and Salé in the depth domain (Fig. 3.10a). In addition, filtered components of the dominant obliquity-related peak (centered at 3.34 and 2.65 m, respectively) are shown as an overlay on the $\delta^{18}\text{O}$ depth series. Both isotope records, which are based on *Planulina ariminensis*, can easily be correlated starting from the ‘paired’ glacial peak stages TG12/14, TG20/22 and C3An. $\delta^{18}\text{O}$.14/16. The identification of these stages is confirmed by the position of the PF-4 bioevent. At AEB, the filter picks up one cycle (TG18) less between TG20 and TG14 due to the extreme low sedimentation rate at that time (see Fig. 3.2). On the other hand the filter picks up one extra cycle (TG30) between TG22 and C3An. $\delta^{18}\text{O}$.14. This cycle corresponds to the extraordinary thick reddish layer of cycle 28 and marks the very high sedimentation rate associated with this precession related signal. But the number of cycles is consistent between both records if we take these “imperfections” in the record of AEB into account. The correlation is confirmed by details in the $\delta^{18}\text{O}$ pattern such as the precession-related signals and the poorly developed interglacial stages TG33, and C3An. $\delta^{18}\text{O}$.3 and 15.

The $\delta^{18}\text{O}$ depth series of ODP Site 982 is plotted in Figure 3.10b with the extracted component of the obliquity related spectral peak at 1.79 m as an overlay. Again the paired isotope stages TG12/14, TG20/22 and C3An. $\delta^{18}\text{O}$.14/16 are readily identified. The filtered record shows the same number of cycles between TG22 and C3An. $\delta^{18}\text{O}$.14 as in Salé and AEB, following the exposure of TG30 as a precession- rather than an obliquity- related signal. The filtered record reveals, however, one extra cycle between TG12 and TG22 at Site 982. This extra cycle is difficult to account for, but might be related to an uncertainty in the splice of Site 982.

Figure 3.11 shows all three $\delta^{18}\text{O}$ records in the time domain with the filtered 41 kyr obliquity as an overlay. The time series for both Salé and ODP Site 982 are based on the age model of Hodell et al. [2001]. Despite the rather consistent outcome of the comparison in the depth domain, the (filtered) $\delta^{18}\text{O}$ time series reveal discrepancies both in terms of the tuning of individual stages as well as the number of stages between characteristic tie points provided by the three pairs of distinct glacial stages TG12/14, TG20/22 and C3An. $\delta^{18}\text{O}$.14/16. Hodell et al. [2001] were probably misled by the extra cycle between TG12 and TG20 at ODP Site 982 when they equated TG20 at Salé [Hodell et al., 1994] with TG22. The tuning of stages TG22 and younger is consistent between the three localities if we eliminate the extra cycle between TG12 and 20 at Site 982 and tune stages TG12 to TG22 at Salé one obliquity cycle older. But these modifications do not eliminate all the discrepancies in the tuning of stages older than TG24 even though C3An. $\delta^{18}\text{O}$.14/16 at Salé now line up with the same stages at AEB following the revised tuning of Salé one obliquity cycle older. This consistency is somewhat misleading because the depth to time conversion at Salé resulted in the elimination of TG26 which is compensated by the introduction of an extra cycle between C3An. $\delta^{18}\text{O}$.6 and 8 as a consequence of the tuning. The inconsistency that remains in the tuning of the older stages at Site 982 disappears if an extra cycle is added between C3An. $\delta^{18}\text{O}$.8 and 14 as indicated by the results of the band-pass filtering in the depth

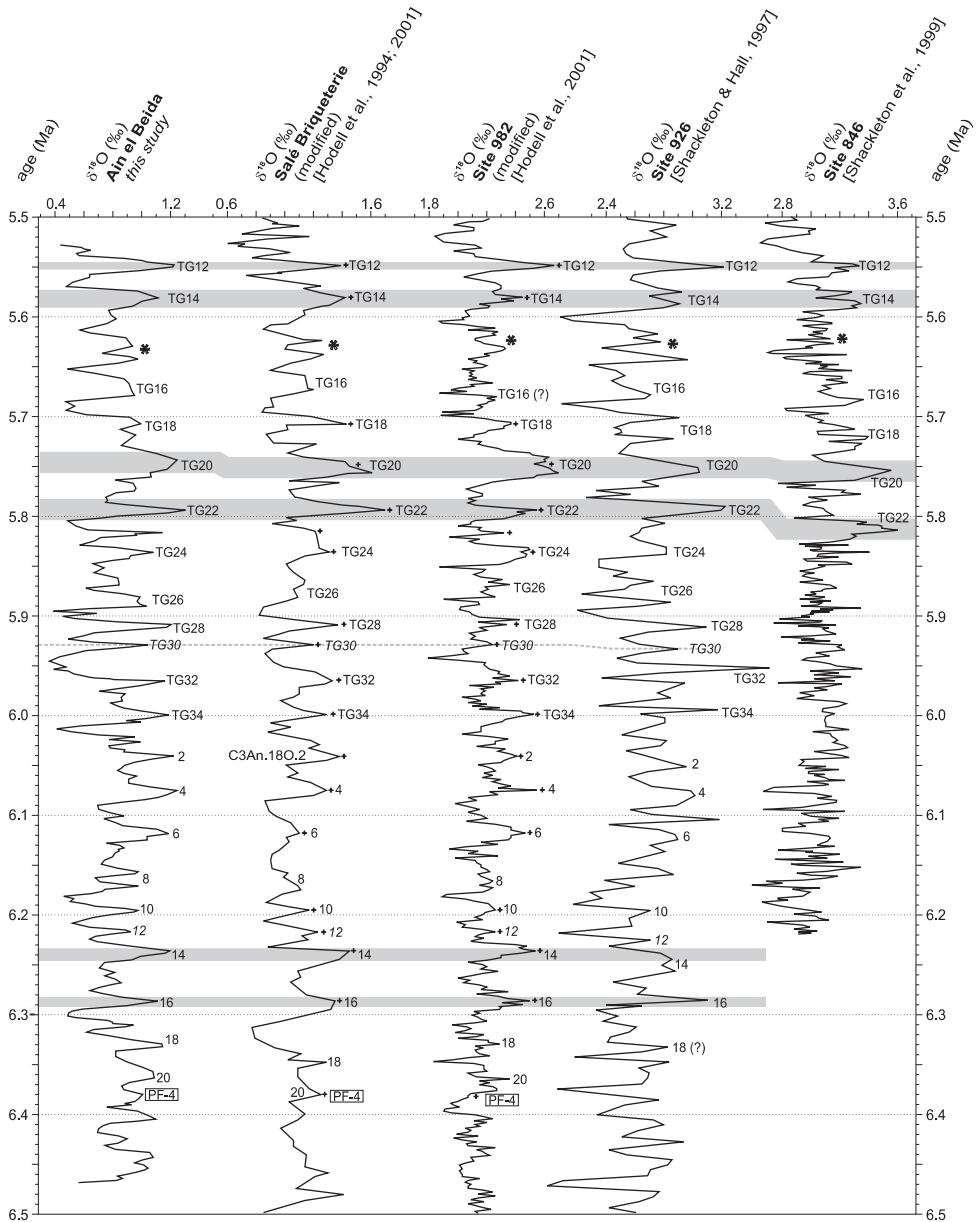


Figure 3.12 Correlation between the benthic $\delta^{18}\text{O}$ time series of Ain el Beida, the re-tuned Salé [Hodell et al., 1994; 2001] and ODP Site 982 [after Hodell et al., 2001] records and ODP Site 846 [Shackleton et al., 1995a, 1995b] and 926 [Shackleton and Hall, 1997]. Asterisks indicate unnamed stage (i.e. TG15.2). Plus-signs indicate cold isotopic stages of which the ages have been adopted from this study. See text for discussion.

domain. In that case the number of obliquity-controlled cycles is identical and the stages are tuned in the same way resulting in virtually identical ages for the main neogloboquadrinid-coiling shift (PF-4) at all three localities.

We revised the isotope chronologies of Salé and Site 982 according to the age model of AEB and compared them with the re-tuned [H. Pälike, pers. comm.] isotope chronology of ODP Site 846 [Shackleton et al., 1995a, 1995b] and the isotope chronology of ODP Site 926 [Shackleton and Crowhurst, 1997; Shackleton and Hall, 1997] in Figure 3.12. Again the paired glacial stages can easily be identified and they have been tuned in the same way thus providing independent confirmation for the correctness of our tuning. Shackleton et al. [1995b] interpreted the relatively long time interval between TG16 and TG14 at ODP Site 846 as one interglacial stage, TG15. In AEB, it appears that this interglacial stage comprises a clear obliquity controlled glacial stage, now called TG15.2. The $\delta^{18}\text{O}$ record of ODP Site 926 shows identical peaks as the other open ocean records, but the $\delta^{18}\text{O}$ maximum of TG34 is very prominent and even exceeds the $\delta^{18}\text{O}$ values of the peak glacial TG22 and TG20 at this site. Below stage C3An. $\delta^{18}\text{O}$.16, correlation and numbering of stages remain problematic.

3.6.2 Paleoclimatic interpretation

The outcome of the spectral analysis and comparison with open ocean records indicate that the cyclic variability in the $\delta^{18}\text{O}$ records is primarily controlled by obliquity and to a lesser degree by precession. Many authors have linked the dominant 41 kyr signal in late Messinian oxygen isotope records from the open ocean to obliquity controlled glacial cyclicity [e.g., Hodell et al., 1994, 2001; Shackleton et al., 1995b; Vidal et al., 2002]. Distinct benthic $\delta^{18}\text{O}$ excursions to positive values of tenths per mil above average are interpreted as glacial periods, which are linked to recurrent minima in the tilt of the Earth's axis. It is generally considered that maximum glacial buildup was reached during isotope stages TG22 and TG20 [Shackleton et al., 1995b], although the onset of distinct obliquity-controlled glacial cycles has started much earlier, i.e. at 6.30 Ma on the basis of our new age model.

A remarkable feature of the oxygen isotope records of AEB is the high covariance between planktonic and benthic $\delta^{18}\text{O}$ in both the obliquity and precession frequency bands. High covariance between benthic and planktonic isotope records can be interpreted as being indicative of seawater composition change caused by ice volume variations, simultaneous cooling of surface and deeper waters or bathing by the same water masses [e.g., Hodell and Kennett, 1986; Keigwin, 1987]. The good correlation between the benthic $\delta^{18}\text{O}$ records of AEB and the open ocean suggests that the precession component in the AEB $\delta^{18}\text{O}$ records is influenced by glacial variability as well. But the precession-related shifts in $\delta^{18}\text{O}$ are also tightly linked to the colour cycles, pointing to a low-latitude climatic signal comparable to that associated with sapropel cycles in the Mediterranean. The same climatic link between reddish layers and sapropels is indicated by maximum abundances of the oligotrophic warm-water planktonic foraminiferal Globigerinoides group [e.g., Lourens et al., 1992]. In fact these similarities were used in **Chapter 2** to tune the reddish layers at AEB to precession minima and/or Northern Hemisphere summer insolation maxima [Krijgsman et al., 2004]. Warmer surface waters at times of deposition of the reddish layers are most likely related to the enhanced summer insolation at times of precession minima and may explain the amplified precession-related planktonic $\delta^{18}\text{O}$ signal at AEB.

The shift in planktonic $\delta^{18}\text{O}$ to light values in Mediterranean sapropels is usually attributed to enhanced continental runoff (mainly via the river Nile [e.g., Rossignol-Strick, 1985]) that result in reduced surface water salinities as a consequence of dominantly precession-induced variations

in the intensity of the African monsoon. Similarly the shifts to lighter $\delta^{18}\text{O}$ values in the reddish layers of AEB may also be due to reduced sea surface salinities as a consequence of enhanced continental runoff, possibly in combination with simultaneous warming of the surface waters. But an increase in precipitation related to the African monsoon in northwest Africa at times of precession minima seems unlikely [e.g., COHMAP, 1988; Tuenter et al., 2003]. Alternatively, the inferred changes in precipitation can be related to the Atlantic system, which brings winter rain to the region today [e.g., Griffiths, 1972; Knippertz et al., 2002]. A similar interpretation was proposed by Sierro et al. [1999] to explain Pliocene carbonate dilution cycles in the Gulf of Cadiz. It is further in agreement with the work of Petit-Maire and Guo [1997], who linked high lake levels in northwest Africa during the early Holocene wet phase to the Atlantic system while lake levels further south were attributed to the monsoon.

Similar to the precession signal in $\delta^{18}\text{O}$, the obliquity-related signal is likely composed of two components; one component that is linked to the (obliquity-driven) glacial cyclicality and a second that is associated with (obliquity-driven) regional climate changes operating independently from the glacial signal. The latter obliquity component forms an intrinsic part of Mediterranean sapropel patterns [e.g., Lourens et al., 1996] and is thought to be responsible for the precession-obliquity interference patterns observed in the colour cycles of the nearby and slightly older Oued Akrech section [Hilgen et al., 2000].

3.6.3 Obliquity related time lags between astronomical forcing and climate response

Due to the slow buildup of ice caps, the $\delta^{18}\text{O}$ signal will exhibit a delayed response with respect to the orbital forcing which is proportional to the astronomical cycle in question. For the late Pleistocene glaciations, time lags of 5 and 8 kyr were adopted for the precession and obliquity components, respectively [Imbrie et al., 1984], while smaller ice caps will lead to a reduction in these time lags [Chen et al., 1995]. Consequently, we anticipated an increase in the obliquity-related time lag during the MSC interval with respect to the pre-MSI interval since peak glacial conditions became more intense during MSI times. The results of our cross-spectral comparison indicate however that the obliquity-related lag was slightly reduced at MSI times to a value almost identical to the precession-related lag. Possible explanations of a reduced glacial effect or a relative increase in the contribution of regional climate change to the obliquity signal in $\delta^{18}\text{O}$ during MSI times are less likely in view of the open ocean records and the insolation pattern, respectively.

The value of the obliquity-related lag also depends on the accuracy of the astronomical solution and the adopted values for dynamical ellipticity and tidal dissipation [Lourens et al., 1996, 2001]. Recently, a new full numerical solution, La2004 [Laskar et al., 2004], became available which is considered more accurate than the semi-analytical solution La93 although differences are very small for the time interval under consideration. In addition, we used present-day values for dynamical ellipticity and tidal dissipation in the La93 solution because this particular solution provided an excellent fit with intricate sedimentary cycle patterns in the Mediterranean Pliocene [Lourens et al., 1996]. Recently, however, Lourens et al. [2001] found an optimal fit between a Ti/Al time series (reflecting African aridity) and ETP in the interval between 2.9 and 2.4 Ma for La93 with tidal dissipation reduced to half its present-day value (i.e., La93_(1,0.5)). To investigate the effect of the new solution and modified tidal dissipation on our obliquity-related time lag, we repeated the whole cross-spectral procedure for La93_(1,0.5), La2004_(1,1) and La2004_(1,0.5) (Tab. 3.3, see electronic supplement).

Using La93_(1,0.5), ages for the sedimentary cycles become on average 3 kyr older as a consequence of the reduced tidal dissipation. A similar difference is found between La2004_(1,1) and La2004_(1,0.5) while the application of the new solution itself results in ages that are on average 1 kyr younger than for the old solution. More importantly, reducing the tidal dissipation to half its present-day value results in an increase of the obliquity lag by 3 kyr (i.e. from 1-3 to 4-6 kyr) for both solutions, which would better fit with the expected ice-sheet related effect. But the above analyses also show that the observed decrease in the obliquity lag from the pre-MSW to the MSW interval is similar for all solutions and is accompanied by a reduction in coherency with ETP, especially for planktonic $\delta^{18}\text{O}$ (Fig. 3.13; see electronic supplement).

At the moment, it is not possible to discriminate which astronomical solution and thus which value for the obliquity-related time lag in $\delta^{18}\text{O}$ is the more accurate. This uncertainty is not only related to the applied astronomical solution and the values for dynamical ellipticity and tidal dissipation, but also depends on the uncertainty in the precession-related time lag. We found a near-zero time lag for the precession component in $\delta^{18}\text{O}$ due to the direct link between $\delta^{18}\text{O}$ and lithology and the fact that we did not introduce a time lag between lithology and insolation when we constructed our age model. However, the good correlation between the benthic and planktonic $\delta^{18}\text{O}$ records of AEB and benthic $\delta^{18}\text{O}$ records from the open ocean suggests that the precession component in the $\delta^{18}\text{O}$ records of AEB is influenced by glacial variability as well and may thus show a time lag in the order of a few kyrs. Incorporation of such a precession-related time lag in our age model will automatically lead to an increase in the obliquity-related lag. Consequently, an increase in the precession-related time lag during the MSW interval with respect to the pre-MSW interval can be expected; this would result in an increase of the obliquity-related time lag during the MSW interval. Confirmation that this scenario is valid may come from a thorough cross-spectral comparison of proxy records from AEB that reveal distinct precession-obliquity interference patterns, which are not influenced by glacial variability.

Acknowledgements

Geert Ittmann and Gerrit van 't Veld are thanked for washing the samples. Arnold van Dijk performed the isotope analyses. Laurence Vidal and Heiko Pälike are thanked for critical comments which greatly improved the manuscript. This research was financially supported by the Netherlands Organization for Scientific Research NWO (PIONEER grant to F.J. Hilgen and E. van der Laan).

No major deglaciation across the Miocene-Pliocene boundary: Integrated stratigraphy and astronomical tuning of the Loulja sections (Bou Regreg area, NW Morocco)

with E. Snel¹, F.J. Hilgen¹, E. de Kaenel², and W. Krijgsman³

¹ IPPU, Utrecht University, Budapestlaan 4, 3584 CD Utrecht, The Netherlands

² DPR, Matile 51, CH-2000 Neuchâtel, Switzerland

³ Paleomagnetic Laboratory “Fort Hoofdijk”, Budapestlaan 17, 3584 CD Utrecht, The Netherlands

This chapter has been published in *Paleoceanography* as: Van der Laan E., E. Snel, E. de Kaenel, F.J. Hilgen, and W. Krijgsman, 2006. No major deglaciation across the Miocene-Pliocene boundary: Integrated stratigraphy and astronomical tuning of the Loulja sections (Bou Regreg area, NW Morocco, *Paleoceanography*, 21, PA3011, doi:10.1029/2005PA001193.

Abstract

An integrated high-resolution stratigraphy and orbital tuning is presented for the Loulja sections located in the Bou Regreg area on the Atlantic side of Morocco. The sections constitute the upward continuation of the upper Messinian Ain el Beida section and contain a well-exposed, continuous record of the interval straddling the Miocene-Pliocene (M-P) boundary. The older Loulja-A section, which covers the interval from ~5.59 to 5.12 Ma, reveals a dominantly precession-controlled colour cyclicity that allows for a straightforward orbital tuning of the boundary interval and for detailed cyclostratigraphic correlations to the Mediterranean; the high-resolution and high-quality benthic isotope record allows us to trace the dominantly obliquity-controlled glacial history. Our results reveal that the M-P boundary coincides with a minor, partly precession-related shift to lighter “interglacial” values in $\delta^{18}\text{O}$. This shift and hence the M-P boundary may not correlate with isotope stage TG5, as previously thought, but with an extra (weak) obliquity-controlled cycle between TG7 and TG5. Consequently, the M-P boundary and basal Pliocene flooding of the Mediterranean following the Messinian salinity crisis are not associated with a major deglaciation and glacio-eustatic sea level rise, indicating that other factors, such as tectonics, must have played a fundamental role. On the other hand, the onset of the Upper Evaporites in the Mediterranean marked by hyposaline conditions coincides with the major deglaciation step between marine isotope stage TG12 and TG11, suggesting that the associated sea level rise is at least partly responsible for the apparent onset of intermittently restricted marine conditions following the main desiccation phase. Finally, the Loulja-A section would represent an excellent auxiliary boundary stratotype for the M-P boundary as formally defined at the base of the Trubi marls in the Eraclea Minoa section on Sicily.

4.1 Introduction

The Miocene-Pliocene boundary formally defined at the base of the deep marine Trubi marls on Sicily [Van Couvering et al., 2000] marks the basal Pliocene flooding of the Mediterranean and the end of the Messinian salinity crisis (MSC). Although there are increasing indications that (restricted) marine conditions may have occurred already intermittently during deposition of the Upper Evaporites [e.g., Müller, 1990; Castradori, 1998; Spezzaferri et al., 1998; Iaccarino et al., 1999; Rouchy et al., 2001; Aguirre and Sánchez-Almazo, 2004], the base of the Trubi marls and time-equivalent sediments elsewhere in the Mediterranean represent the sedimentary expression of the re-establishment of full open marine conditions in the Mediterranean [Hsü et al., 1973; Cita, 1975; Hilgen and Langereis, 1993; Iaccarino et al., 1999]. To unravel the exact cause of the flooding event, the time-correlative level of the M-P boundary should be precisely pinpointed in a continuous orbitally tuned open marine succession outside the Mediterranean. In addition, an excellent benthic oxygen isotope record should be available to detect any significant reduction in ice volume associated with the flooding event.

Attempts have recently been made to pinpoint the position of the M-P boundary in marine cores from the open ocean. Shackleton et al. [1995a, 1995b], Clauzon et al. [1996], and McKenzie et al. [1999] all link the boundary to the prominent interglacial oxygen isotope stage TG5 defined by Shackleton et al. [1995b] in ODP Site 846, suggesting that the associated glacio-eustatic sea level rise played a primary role in controlling the Pliocene flooding of the Mediterranean. For this purpose, most of these studies compared the tuned age of 5.33 Ma for the base of the Trubi [Lourens et al., 1996] with the age of TG5 according to the initial tuned age model developed for Site 846 [Shackleton et al., 1995a]. However, the latter age model has subsequently been revised leaving a younger age of 5.31 Ma for TG5 [Shackleton et al., 1999].

In our opinion, the Bou Regreg area located on the Atlantic side of Morocco remains the location most critical to solve the problem of the exact timing and origin of the Pliocene flooding of the Mediterranean. The open marine succession in the area shows a distinct dominantly precession-controlled colour banding that is related to the sedimentary cyclicity in the Mediterranean, and the Trubi marls in particular. The colour cycles allow the sections to be astronomically tuned and to be correlated cyclostratigraphically to Mediterranean sections [Hilgen et al., 2000]. Secondly, high-quality benthic isotope records can be generated due to the good to excellent preservation of the foraminifera shells while the relatively high average sedimentation rate (of 7-8 cm/kyr) guarantees an optimal temporal resolution [Van der Laan et al., 2005].

In fact, Benson and Rakic-El Bied [1996] proposed to define the M-P boundary in a continuous open marine section, Ain el Beida, located outside the Mediterranean because they considered the Messinian to be a regional stage representing the sedimentary expression of the MSC only. For this purpose, they selected a much older level that corresponds with the younger end of Chron C3An. On the other hand, Suc et al. [1997], while recognizing the problem of the possible unconformable nature of the base of the Trubi, preferred to maintain the Mediterranean option. They proposed to define the M-P boundary near Salé, some 5 km northwest of Ain el Beida, at the stratigraphic level that corresponds with the base of oxygen isotope stage TG5. This isotope shift was supposed to reflect the marked deglaciation held responsible for the Pliocene flooding of the Mediterranean. The proposal was considered less favourable because the level was only indicated in the Salé drill core but not in any existing outcrop.

Nevertheless, the M-P boundary level might be present in one of the quarries located in between Ain el Beida, where this level is not reached, and Salé with its exposures of Early Pliocene

marine sediments. Because of the clearly visible colour banding we selected the Loulja section with the aim (1) to extend the tuned open marine succession exposed at Ain el Beida across the M-P boundary into the Pliocene and (2) to pinpoint as accurately as possible the position of the M-P boundary in a well-tuned, open marine section with an excellent oxygen isotope stratigraphic record in the Bou Regreg area. The outcome of this study may provide the final answer to the question whether glacio-eustatic sea level rise was involved in triggering the Pliocene flooding of the Mediterranean.

In addition, special attention will be given to identify the major isotope shift to lighter values between isotope stages TG12 and TG9. According to the tuned age model for Ain el Beida, only the beginning of this shift was reached in the topmost part of the section [Van der Laan et al., 2005]. This shift, which marks a more dramatic deglaciation than TG5 as noticed by Shackleton et al. [1995b], Hodell et al. [2001], and Vidal et al. [2002], is particularly interesting because it may be coincident with and thus responsible for the beginning of the Upper Evaporites in the Mediterranean [Shackleton et al., 1995b].

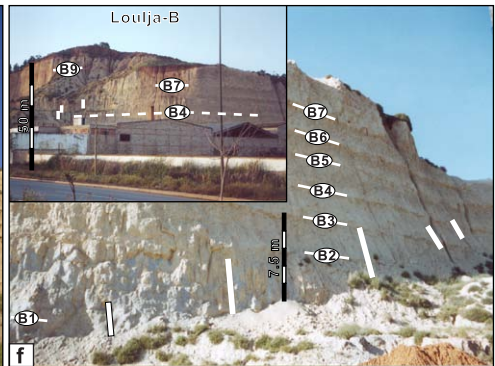
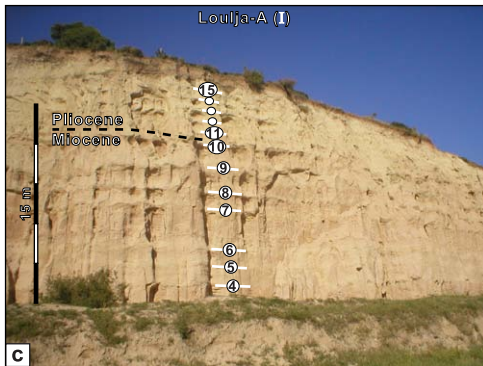
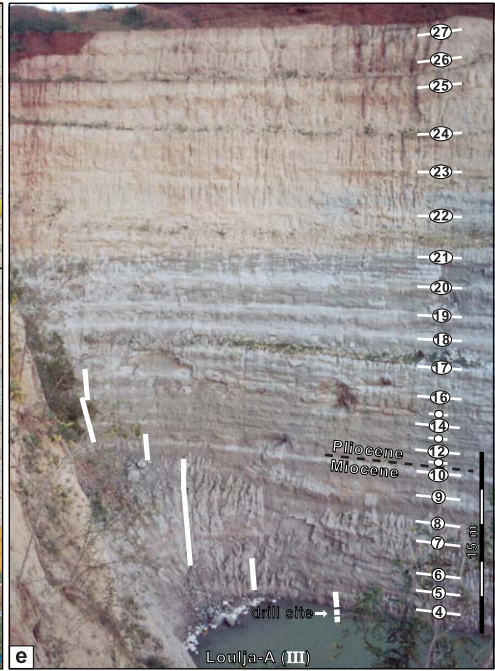
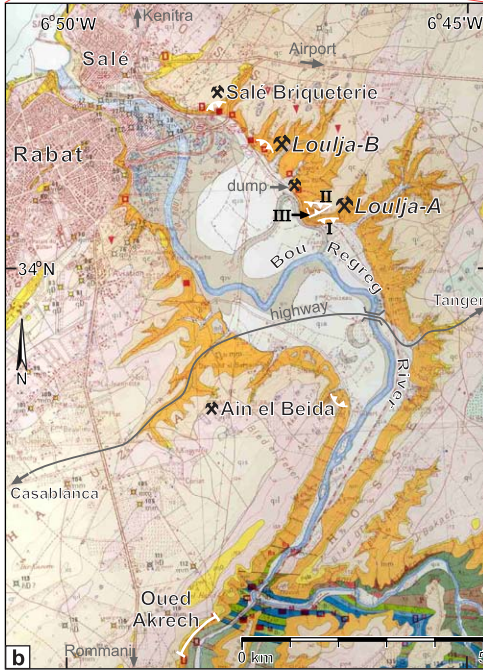
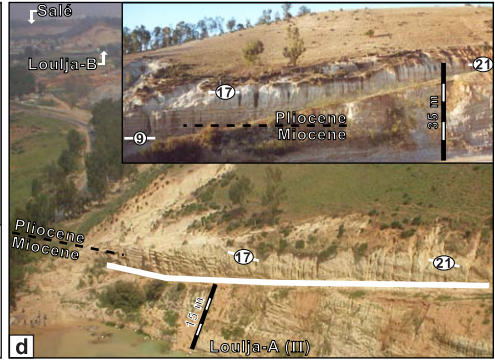
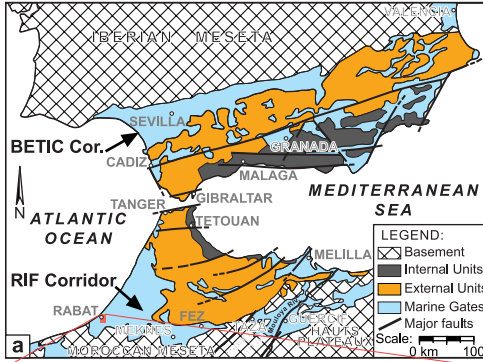
4.2 Setting and sections

4.2.1 Bou Regreg valley

The classic Blue Marl of Atlantic Morocco has been subject of numerous studies, reflecting the progress made in Neogene stratigraphy. It is best known from the Bou Regreg river valley where it constitutes a continuous open marine record from the late Tortonian into the Pliocene that overlies Devonian limestones with an angular unconformity [Benson and Rakic-El Bied, 1996]. The Blue Marl was deposited in the Gharb basin, which formed the westward extension of the Rifian Corridor (Fig. 4.1a). This corridor acted as an extensional foredeep and formed one of the two Atlantic-Mediterranean connections during the Late Miocene before its tectonic closure in the course of the Messinian [Benson et al., 1991; Krijgsman et al., 1999a]. Deposition of the Blue Marl in the Gharb Basin continued well into the Pliocene and its stratigraphic succession is exposed in a number of quarries and outcrops albeit in an incomplete way. The Oued Akrech section contains the basal part of the Blue Marl, straddling the Tortonian-Messinian boundary and covering the interval from 7.6 to 7.1 Ma [Hilgen et al., 2000]. The middle part of the Blue Marl is exposed in the Ain el Beida quarry and covers the interval from 6.5 to 5.5 Ma [Krijgsman et al., 2004], while lower Pliocene marine sediments are exposed at Salé [see Hodell et al., 1994; Benson and Rakic-El Bied, 1996]. The succession has been completed by drilling at Ain el Beida and Salé [Hodell et al., 1989; Benson et al., 1991; Hodell et al., 1994; Benson et al., 1995], but up to now, the interval straddling the Miocene-Pliocene boundary has not been documented in detail from any outcrop.

4.2.2 The Loulja-A section

The Loulja-A section is located in a brick quarry at the northern side of the Bou Regreg valley along the road to Salé (Figs. 4.1a and 4.1b). Colour banding is clearly visible in the steep south face of an old quarry next to the road, which shows a regular alternation of slightly protruding, light beige coloured silty marls and softer, darker (reddish) coloured, clayey marls (partial section I; Fig. 4.1c). A much larger quarry is located on the opposite northern side of the hill. The weathered south face (partial section II; Fig. 4.1d) of this quarry shows the same colour banding and pattern as observed along the road. The entire sequence is also exposed in the relatively fresh, north



← **Figure 4.1** a) Simplified geological map of the Gibraltar area with the location of the late Miocene Betic and Rifian Corridors [modified after Krijgsman et al., 2004]. b) Map of the lower Bou Regreg valley showing locations of the quarries of Loulja-A and Loulja-B, Ain el Beida, and Salé Briqueterie, and the road section of Oued Akrech [modified after Millies-Lacroix, 1974]. c) Old quarry of Loulja-A (partial section I) along the road to Salé. d) View in NW direction, towards the Loulja-B and Salé quarries showing the weathered side (section II) of the main Loulja-A quarry. White horizontal bar in inset shows detail of sample trajectory. e) Fresh north-facing side (section III) of the main Loulja-A quarry. White bars indicate sample trajectories. f) Detail of right, southeast-facing wall of the Loulja-B quarry (inset shows the entire quarry). Note the variable meter scales in c-f. Cycle numbers refer to the stratigraphy in Figure 4.2.

face (partial section III; Fig. 4.1e) of the quarry, which is approximately 60 m high. Younger stratigraphic levels showing relatively thick colour cycles are reached in the upper half of this quarry face. The colour cycles are less distinct in such fresh exposures and consist of alternating lighter and darker coloured bluish-gray marls.

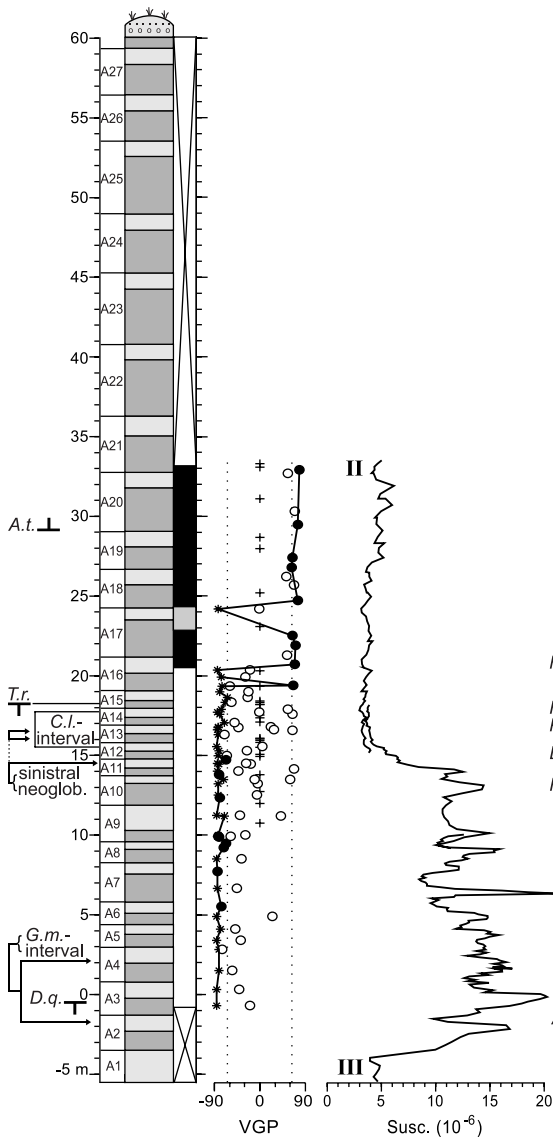
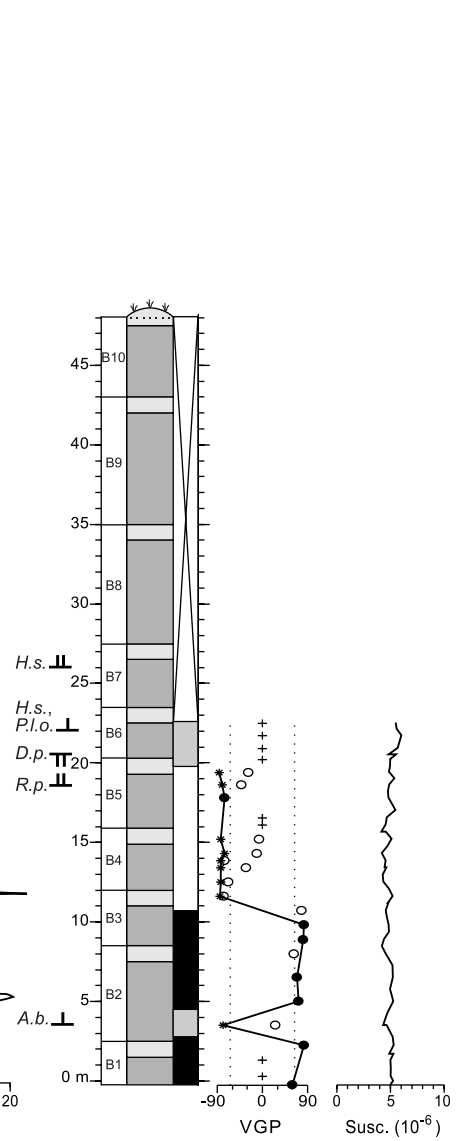
Sampling started at the base of the accessible eastern side of section Loulja-A III (lower 20 m.) and was continued along the path that crosses section II (from 9 to 33.5 m.). An additional 5.5 m was drilled below the reference level of the quarry floor with a hand drill at section III (Fig. 4.1e) to ensure a stratigraphic overlap with the top part of the (supposedly older) Ain el Beida section. Usually 8 to 10 samples were taken per cycle, which corresponds to a temporal resolution of 2-3 kyr in case the colour cycles are precession-related. In the drill hole, one sample was taken every 10 cm. Finally, additional samples with a resolution of two samples per cycle were taken from the lower part of section I and from the lower part of section II for a check on the cycle patterns and the correlations between partial sections. Sampling was not extended to include all the thick cycles observed in the top part of Loulja-A due to the intense weathering of section II and the steepness of the upper part of section III.

4.2.3 The Loulja-B section

The Loulja-A section can be extended upward in another brick quarry along the road to Salé (Figs. 4.1b and 4.1f), located about 1.5 km northwest of Loulja-A. This section, named Loulja-B, displays similar thick and well developed colour cycles as the upper half of the Loulja-A section. Inaccessibility of the vertical southwest face of this quarry limited the detailed sampling to the lower half of the exposed section. Nevertheless, seven additional samples were collected from the upper four cycles for biostratigraphic analysis.

4.3 Cyclostratigraphy

In total 27 cycles were recognized at Loulja-A, labelled LA-1 to LA-27 in stratigraphic order (Fig. 4.2a). In weathered outcrop, the cycles consist of an alternation of more indurated, light-beige coloured silty marls and softer, reddish coloured clayey marls. Rather arbitrarily, reddish marl layers are taken as to define the base of a cycle and labelled LA-X_R where X is the number of the cycle in the section and _R denotes the colour of the marl (red); the overlying beige marl is denoted LA-X_B. The lowermost 3 cycles are found only in the drill hole and are distinguished based on the geochemical data (see paragraph 4.6). Cycles LA-4 to base LA-21 were logged and sampled in detail in partial sections II and III whereas only the (approximate) thickness of cycles LA-21 to LA-27 was measured with a tape from the top of section III downward.

(a) Loulja-A**(b)** Loulja-B

The cycles reveal a very characteristic pattern (Fig. 4.2a). LA-1 to LA-10 reach an average thickness of 2 m with very thick reddish layers in LA-7 and LA-10 and relatively thin reddish layers in LA-5 and LA-6. The thickest whitish layers are found in LA-1 and LA-9. The lower part of the section is followed by a very characteristic interval that consists of six successive thin colour cycles (LA-10_B-15_B), which are very regular and have an approximate thickness of 1 m. This interval can be recognized both in partial section I as well as in sections II and III, and was used to correlate the different partial sections in detail. Cycle LA-16 has an intermediate thickness and marks the transition to thicker cycles LA-17 to LA-21 (and up to LA-27). The thickness of these cycles ranges from 2.5 to 4 m.

← **Figure 4.2** Litho-, bio-, and magnetostratigraphy of the (a) Loulja-A and (b) Loulja-B sections. Sedimentary cycle numbers are based on the colour cycles and, for the lowermost part of Loulja-A, also on the PC-1 data shown in Figure 4.4. Light shading marks the light coloured, relatively carbonate-rich marls, and darker shading marks the relatively clayey, often reddish coloured marls. Last and first (regular) occurrences of nannofossil species are indicated on the left side of the lithological columns: *D.g.*, *Discoaster quinqueramus*; *C.l.*, *Ceratolithus larrymayeri*; *T.r.*, *Triquetrorhabdulus rugosus*; *A.t.*, *Amaurolithus tricorniculatus*; *A.b.*, *Amaurolithus bizzarus*; *R.p.*, *Reticulofenestra pseudumbilicus* (>8 µm); *D.p.*, *Dictyococcites perplexus*; *P.l.o.*, *Pseudoemiliana lacunosa ovata*; *H.s.*, *Helicosphaera sellii*. Furthermore, *G.m.*-interval stands for the interval with common *Globorotalia menardii*. In the VGP curves, (open) solid circles denote (less) reliable ChRM directions; asterisks indicate great circle solutions; pluses are used for inconclusive results. In the polarity columns, black (white) denotes normal (reversed) polarity, gray indicates undetermined polarity, and crossed intervals are used for those parts of the sections where no paleomagnetic samples were taken. Magnetic susceptibility of untreated sediment is shown to the right of the VGP-curves; II and III refer to partial sections of Loulja-A (see Fig. 4.1). Stratigraphic scales are in meters.

The Loulja-B section contains 10 thick colour cycles labelled LB-1 to LB-10 (Fig. 4.2b). The lowermost 7 cycles have an average thickness of ~4 m with a very thick reddish layer of 5 m in LB-2. Cycles LB-8 and LB-9 are extremely thick and reach a thickness of 7.5-8 m, i.e. almost twice as thick as LB-1 to LB-7.

4.4 Magnetostratigraphy

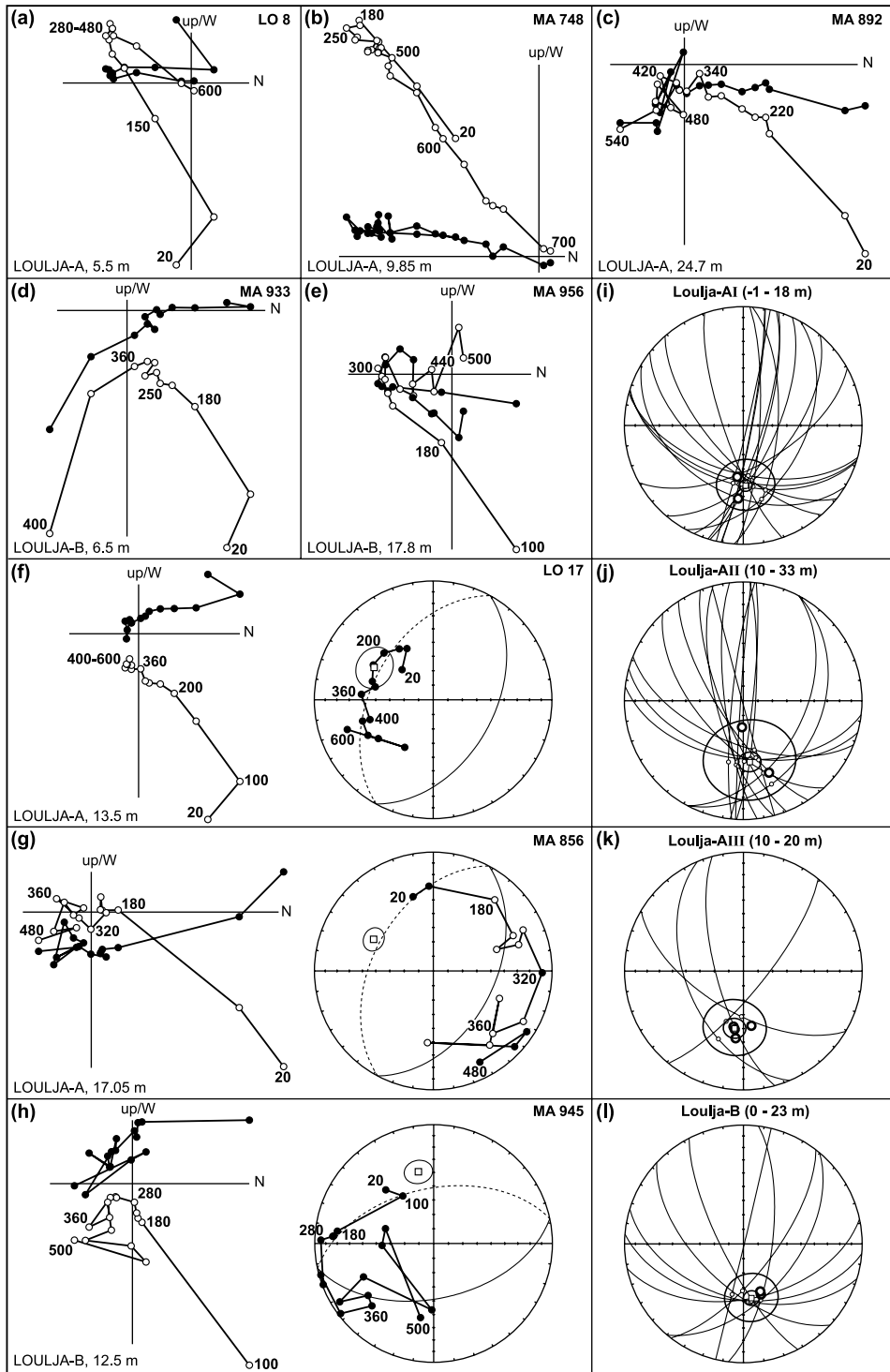
4.4.1 Sampling

Standard oriented paleomagnetic cores were drilled with the help of a water-cooled, generator-powered electric drill at two to twelve levels per sedimentary cycle (four on average). Samples were taken in partial sections I and II (between -1 and 33 m; Figs. 4.1c, 4.1d, and 4.2a). Care was taken to remove the weathered surface before drilling. In addition to the regular sampling, oriented hand-samples were collected from the middle part (10-20 m) of section III with a resolution of one sample per cycle. Standard cores were drilled from these samples with compressed air at the paleomagnetic laboratory Fort Hoofddijk.

4.4.2 Demagnetization

One specimen per sampling level was thermally demagnetized with temperature increments of 15-80°C up to a maximum temperature of 700°C in a magnetically shielded, laboratory-built furnace. The natural remanent magnetization (NRM) of the specimens was measured on a 2G Enterprises horizontal DC SQUID cryogenic magnetometer.

Demagnetization diagrams [Zijderveld, 1967] are of mixed quality (Fig. 4.3). A normal polarity component is generally removed at temperatures between 100 and 250°C (e.g., Fig. 4.3b). This relatively low-temperature component typically has a present-day field direction and is interpreted as a secondary, recent overprint, likely caused by weathering. Therefore, low intensity samples showing clustering from 250°C onward are ignored. A relatively high temperature component is gradually removed between temperatures of 280 and 360°C (as in Fig. 4.3d), after which spurious magnetizations prevail, probably due to the formation of pyrite or magnetite. In the last group of samples the high temperature component is removed between 280 and 600°C, up to 700°C (e.g., Fig. 4.3b), indicating magnetite or haematite as the principal carriers of the magnetization. The high-temperature component is taken as the characteristic remanent magnetization



← **Figure 4.3** Examples of stepwise thermal demagnetization of selected samples. Diagrams denote orthogonal projections of NRM vector end-points, where open (solid) symbols are used for the vertical (horizontal) plane. Values represent temperatures in °C; stratigraphic level is indicated in the lower left corner. Reliable samples show both (a, b, e) reversed and (c, d) normal polarity. f-h) For samples where the ChRM is less well resolved, great circles are used to approximate the (reversed) directions, with squares indicating the normals to the great circle planes and ellipses representing the maximum angular deviations. i-l) Best-fitting directions from the great circles are shown per analyzed interval in the Loulja-A and Loulja-B sections (small circles). Thick circles indicate the used setpoints; small and large ellipses denote the α_{95} and τ_{95} confidence limits [McFadden and McElhinny, 1988].

(ChRM) direction. In approximately 50% of the samples, the demagnetization diagrams allow straightforward interpretation of reversed (Figs. 4.3a, 4.3b, and 4.3e) or normal (Figs. 4.3c and 4.3d) polarity. In other samples, (linear) decay towards the origin is not shown but, apparently, decay to the reversed side of the diagram occurs (Figs. 4.3f-4.3h). In these cases, great circles are used to approximate the reversed ChRM directions. Best-fitting directions from the great circles (indicated by small circles in Figs. 4.3i-4.3l) are determined by using the reliable directions as setpoints (thick circles) according to the method of McFadden and McElhinny [1988].

The ChRM directions, represented as virtual geomagnetic polar (VGP) latitudes, reveal two intervals of normal polarity: from 20.53 ± 0.18 m upwards in the Loulja-A section (LA-16_B to LA-21_R; Fig. 4.2a), and below 10.70 ± 0.90 m in cycle LB-3 in the Loulja-B section (Fig. 4.2b).

4.4.3 Magnetic susceptibility

The initial bulk magnetic susceptibility (χ_{in}) was measured at room temperature on a KLY-2 Kappabridge [Hrouda, 1994]. Magnetic susceptibility (MS) is a measure of the magnetic response of a sample to a small, applied magnetic field and proportional to the concentration and grain size of ferro- and paramagnetic minerals in the sample. It can therefore be used to detect variations in lithology.

Magnetic susceptibility reaches relatively high values of $10\text{-}20 \cdot 10^{-6}$ SI units in samples from Loulja-A III, and from the hand-drilled samples below (-2 to 14 m), defining a marked peak interval (Fig. 4.2a). The record shows a distinct rhythmic pattern, which can easily be correlated with the sedimentary cycles in the more weathered outcrops (sections I and II). In this interval, peak values clearly correspond to the reddish layers. A very pronounced peak in MS is found between 6 and 7 m, followed by much lower values that are not consistent with the lithological expression of the corresponding colour cycle (LA-7).

By contrast, MS values are much lower in the younger cycles (LA-12 to LA-15, up to 18.15 m in section III) while changes are less pronounced. In addition, the records obtained from the basal part of section III (-5.5 to -2 m), from section II (14 to 33.5 m), and from Loulja-B ($0\text{-}23$ m) show low values of MS not exceeding $3\text{-}6 \cdot 10^{-6}$ SI units (Figs. 4.2a and 4.2b).

4.5 Biostratigraphy

4.5.1 Planktonic foraminifera

A semi-quantitative analysis of potential marker species was carried out on the >125 μm fraction of the washed residue of at least every other sample. In addition, the coiling direction of the neogloboquadrinids was determined. *Sphaeroidinellops* spp. and *Globorotalia margaritae* are present

throughout the section and do not reveal changes in abundance that allow recognition of the *Sphaeroidinellopis* acme and the *Globorotalia margaritae* FCO known from the Mediterranean. Next to *G. margaritae*, another species of left coiling keeled globorotalids, *G. menardii*, is commonly but discontinuously found over a short interval in the lower part of the section (from -1.75 ± 0.20 m up to 2.15 ± 0.05 m; Fig. 4.2a). Its distribution corresponds to the reappearance of common *G. miotumida* group in the top part of the underlying Ain el Beida section [Krijgsman et al., 2004].

The determination of the neogloboquadrinid coiling direction is complicated by the presence of two different types, *Neogloboquadrina acostaensis* and *N. humerosa*. The coiling direction of the small- to medium-sized *N. acostaensis* type is dominantly dextral. Approximately equal numbers of sinistral and dextral specimens are found at the 14.65 m level (LA-11_B), and a short but prominent incursion of left-coiling specimens occurs between 16.15 and 16.75 m (cycle LA-13; see also Fig. 4.2a). Specimens of the *N. humerosa* type, which are often large-sized, are frequently

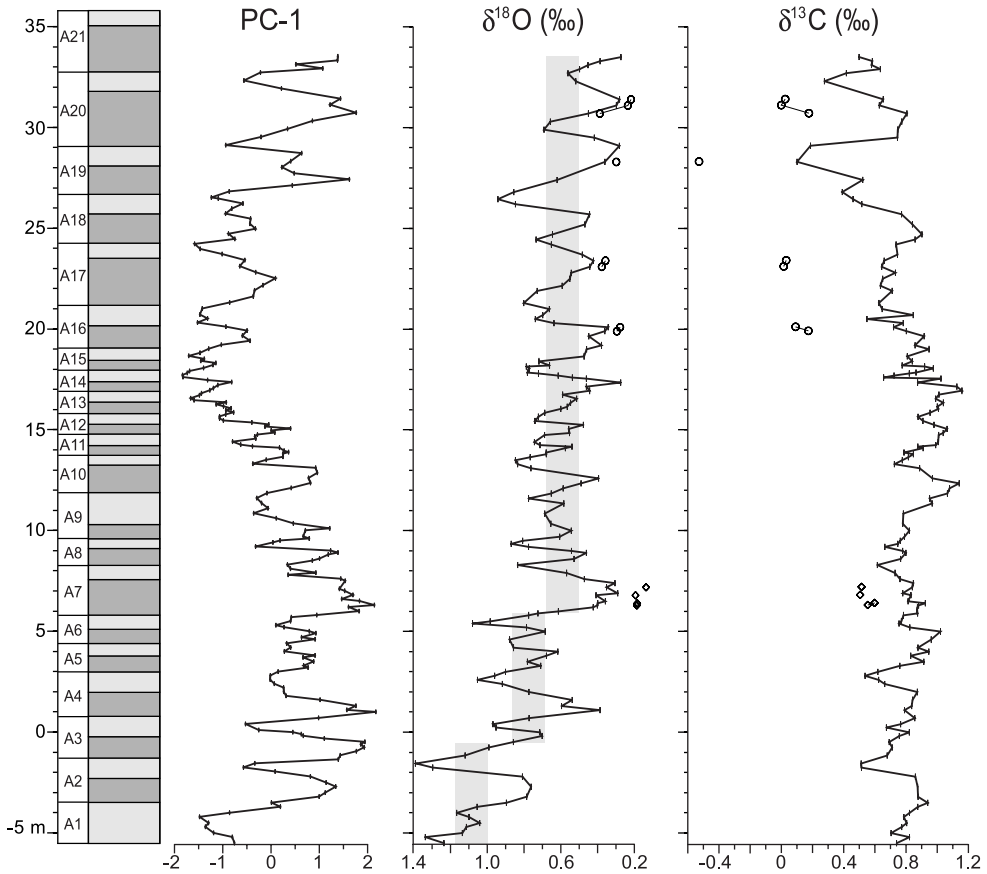


Figure 4.4 Geochemical records (PC-1, benthic $\delta^{18}\text{O}$, and benthic $\delta^{13}\text{C}$) of the Loulja-A section. For key, see caption to Figure 4.2. Open squares in the isotope records represent data obtained from *Cibicides dutemplei*; open circles denote the *C. pachyderma* values. Correction of the *Cibicides* values was done using a value equal to the average offset from the *Planulina* values; these values are 0.214 ($\delta^{18}\text{O}$) and 0.324 ($\delta^{13}\text{C}$) for *C. dutemplei* and 0.065 ($\delta^{18}\text{O}$) and 0.627 ($\delta^{13}\text{C}$) for *C. pachyderma*.

encountered in the lower part of the section although they are always less abundant than *N. acostaensis*. Their coiling direction is dominantly sinistral. Dominantly dextral *N. acostaensis* is the only neogloboquadrinid species present from the top of the marked (second) sinistral influx upwards.

An estimate of the paleobathymetry of the Loulja sections using the ratio of planktonic and benthic foraminifera [Van Hinsbergen et al., 2005] yielded values between 300 and 500 m. A check on this ratio for the Ain el Beida section revealed paleobathymetric values between about 600 and 1000 m, which are in good agreement with previous estimates [Benson and Rakic-El Bied, 1996].

4.5.2 Calcareous nannofossils

The samples selected for analysis of the calcareous nannofossil content were prepared according to standard preparation techniques [Bramlette and Sullivan, 1961]. Two samples per sedimentary cycle were qualitatively examined from both Loulja-A and Loulja-B. Samples from Loulja-A III (-5.5-21 m) provided the best-preserved nannofossil assemblages; all other samples yielded moderately to well-preserved nannofossils.

The Loulja-A section comprises several important nannofossil bioevents (Fig. 4.2). Only a single specimen of *Discoaster quinquerramus* was observed at -0.7 m in cycle LA-3, pinpointing the LO of the species between -0.7 m and -0.18 m (Fig. 4.2a). Rare specimens of *Ceratolithus larrymayeri* were found between 15.5 m and 17.9 m (cycles LA-12 to LA-14), defining the FO and LO of this species. The *Triquetrorhabdulus rugosus* LO was reached between 18.2 and 18.3 m (LA-15), while *Amaurolithus tricorniculatus* was first observed at 30.3 m (LA-20; *A. tricorniculatus* FO between 28.0 and 30.3 m).

In Loulja-B, *Amaurolithus bizzarus* was found at the 5 m level (LB-2; *A. bizzarus* FO between 2.25 and 5.0 m in Fig. 4.2b). The subbottom of *Reticulofenestra pseudoumbilicus* (>8 µm) is recorded between 17.8 m and 19.4 m, in cycle LB-5, while the *Dictyococcites perplexus* subtop is placed between 19.4 m and 21.7 m (LB-5_B and LB-6_R) and the *Pseudoemiliania lacunosa ovata* FO (forms with less than 12 rim slits) between 21.7 m and 22.5 m, in cycle LB-6. Finally, *Helicosphaera sellii* first appeared between 21.7 and 22.5 m (LB-6; *H. sellii* FO), and is more frequently present from between 25 and 27 m upwards (LB-7; *H. sellii* FRO).

4.6 Chemostratigraphy

4.6.1 Geochemistry

Samples were dried, crushed, powdered, and homogenized in an agate mortar prior to further treatment. Approximately 125 mg of each sample was then dissolved in 2.5 ml HF (40%) and 2.5 ml of mixed HNO₃ (16.25%) and HClO₄ (45.5%) and heated at 90°C in closed "Teflon" tubes (bombs) for a minimum of 8 hours. The solutions were subsequently evaporated (in open bombs) at a temperature of 160°C, after which approximately 25 ml HNO₃ (4.5%) was added to each residue. The resulting solutions were analyzed using a Perkin Elmer Optima 3000 ICP-OES apparatus for the elements Al, Ba, Ce, Ca, Co, Cr, Cu, Fe, K, Li, Mg, Mn, Na, Ni, P, S, Sc, Sr, Ti, V, Y, and Zn. The relative errors in duplicate measurements of international standards was lower than 3% for all elements, except for Ce, Co, P, S, Sr, and Y (>5%).

A standardized Principal Component Analysis (PCA) (SPSS software) was applied to extract the primary components responsible for the main variance in the data set. The first (PC-1) and

second principal component together describe already 73% of the total variance in the data, of which PC-1 explains about 59% and is statistically significant. The interpretation of the first principal component is based on the loadings of individual elements on this component (Tab. 4.1). PC-1 reveals very high positive loadings for K, Al, V, Fe, Ti, and Li whereas Ca displays the strongest negative loading. The elements that show high positive loadings are main constituents in clay minerals and often represented in the fine-grained (clayey) terrigenous sediment fraction. On the contrary, Ca is primarily associated with the marine (biological) fraction of the sediment. The PC-1 record shows obvious cyclic variations and follows the sedimentary colour cycles observed in the field, where PC-1 minima and Ca maxima correspond to the more indurated, beige coloured marls. The record comprises 21 cycles, which vary in thickness between about 1 and 4 m with thicker cycles generally showing higher-amplitude changes (Fig. 4.4). Thicker geochemical cycles are found between - 4.5 and +2.5 m (which correspond to colour cycles LA-2 to LA-4) and between 5.5 and 8 m (LA-7) in the lower part of the section and between ~21 m and 33.5 m (cycles 17-21) in the upper part. The middle part reveals a series of six thin geochemical cycles with low amplitude changes (Fig. 4.4). This part, which is marked by a decrease in PC-1 values, corresponds to the characteristic interval with thin colour cycles observed in the field (cycles LA-10_B-15_B; Figs. 4.1c and 4.2a).

4.6.2 Stable isotopes

For isotope analyses, between 15 and 40 specimens (size-dependent) of the benthic foraminifer *Planulina ariminensis* were picked from in total 145 samples. Preservation is generally good to excellent without any indication for recrystallization or pyritization. Where *P. ariminensis* was not abundant enough (<500 µg per sample), the *Cibicides* species *C. dutemplei* and *C. pachyderma* were picked in addition. In order to remove any organic remains, each sample was roasted for 30 minutes at 470°C under vacuum. The samples were analyzed using an ISOCARB, which is directly coupled to the mass spectrometer and has the capacity to measure 44 samples, including 1 international (IAEA-CO-1) and 9 in-house (NAXOS) standards, during a run. Each sample reacted with 103% phosphoric acid (H₃PO₄) for 6 to 7 minutes at 90°C. All isotope data are reported as per mil (‰) relative to the PeeDee belemnite (PDB) standard. After correction of the *Cibicides* values by adopting a value equal to the average offset from the *Planulina* values, twelve data points were incorporated in the δ¹⁸O series. The analytical precision and accuracy were determined by replicate analyses of samples and by comparison with the IAEA-CO-1 standard. The relative standard deviations, analytical precision, and accuracy were better than 0.1‰ both for δ¹⁸O as well as for δ¹³C.

4.6.2.1 The δ¹⁸O record

The δ¹⁸O record shows a stepwise shift in mean δ¹⁸O to lighter values from - 5.5 to +8 m. The average δ¹⁸O value is 1.05‰ for the interval between - 5.5 and - 0.5 m, 0.9‰ between - 0.5 and 6.25 m, and 0.6‰ between 6.25 and 30 m (Fig. 4.4). These intervals ("plateaus") are separated by two main shifts, which occur between - 1.5 and 1 m (from 1.4 to 0.4‰) and between 5.5 and 7 m (from 1.1 to 0.2‰). Less pronounced shifts to lighter values occur between - 5 and - 3 m and between 26.5 and 29 m. The most prominent shifts (of ~0.6‰) to heavier values are found between - 3 and - 1.5 m, 1 and 1.7 m, and 7 and 8.2 m (Fig. 4.4).

High-frequency variations in δ¹⁸O show a distinct relation with lithology with lighter values in the reddish layers (amplitude changes of ~0.5‰; Fig. 4.4). Close inspection of the δ¹⁸O record reveals additional high-frequency variability with a spacing of about twice that of the lithology-

bound changes. Most of the prominent shifts described above are part of this high-frequency variability.

4.6.2.2 The $\delta^{13}\text{C}$ record

The $\delta^{13}\text{C}$ record does not reveal a clear trend but significantly lighter values are reached in the top part of the record (Fig. 4.4). Higher-frequency variations are less prominent than in the $\delta^{18}\text{O}$ record. Nevertheless, lithology-bound changes are present with lighter values recorded in the beige layers. The expression of a cycle with approximately twice the thickness of a colour cycle is more evident. The signal follows the same frequency changes as in $\delta^{18}\text{O}$, with shifts to lighter $\delta^{13}\text{C}$ values coinciding with shifts to heavier $\delta^{18}\text{O}$ values (Fig. 4.4). This relation does not hold, however, in the uppermost part of the section, i.e., from ~27 m upwards.

4.7 Age model

4.7.1 Loulja-A

The Loulja-A section must be slightly younger than the Ain el Beida section of late Messinian age in view of the overall orientation of the bedding plane and its location approximately halfway between Ain el Beida and Salé (lower Pliocene). Moreover, the characteristic interval with six successive thin cycles (LA-10_B-15_B) is unknown from Ain el Beida. Paleobathymetric estimates of 300-500 m follow logically from the deeper estimates for the latter section. An age of around the M-P boundary is also suggested by the calcareous nannofossil biostratigraphy. The *Discoaster quinqueramus* LO, *Ceratolithus larrymayeri* FO and LO, and *Triquetrorhabdulus rugosus* FO are recorded in the same order across the boundary at ODP Site 926 in the equatorial Atlantic [Backman and Raffi, 1997]. The younger events are found in sediments of Early Pliocene age at DSDP Site 502 in the North Atlantic and in southern Italy, albeit not always in the same order [Driever, 1988; Lourens et al., 1996; Raffi et al., 1998; E. de Kaenel, unpublished data, 2001]. The nannofossil events exclude any other correlation than with the Miocene-Pliocene boundary interval.

The initial astronomical tuning of Loulja-A is based on the colour cycles. Because of the close proximity of the sections in the Bou Regreg area and the identical expression of the cycles, it is assumed that the phase relations between the colour cycles and the orbital parameters are the same as for Ain el Beida. Phase relations for the colour cycles in the latter section were based on similarities in proxy signals with sapropels in the Mediterranean for which the phase relations are known [Lourens et al., 1996; Krijgsman et al., 2004]. This implies that midpoints of individual, Ca-poor (paragraph 4.6.1), reddish layers correspond to precession minima and summer insolation maxima and that thicker and more prominent reddish layers correspond to high-amplitude precession minima and insolation maxima and, hence, to eccentricity maxima [Krijgsman et al., 2004].

We start the tuning from the characteristic interval of six thin cycles (LA-10_B up to LA-15_B). According to the phase relations and initial age constraints, these cycles correspond to the 400-kyr eccentricity minimum around 5.25 Ma (Fig. 4.5). Tuning the individual sedimentary cycles to the precession and/or insolation target curve usually follows such a first-order tuning. Instead, we preferred at this stage to introduce the PC-1 record as an additional tool in the tuning exercise because of its distinct cyclic character. A detailed study of the Ain el Beida section revealed a very good fit between a component with similar element loadings [E. van der Laan, unpublished data,

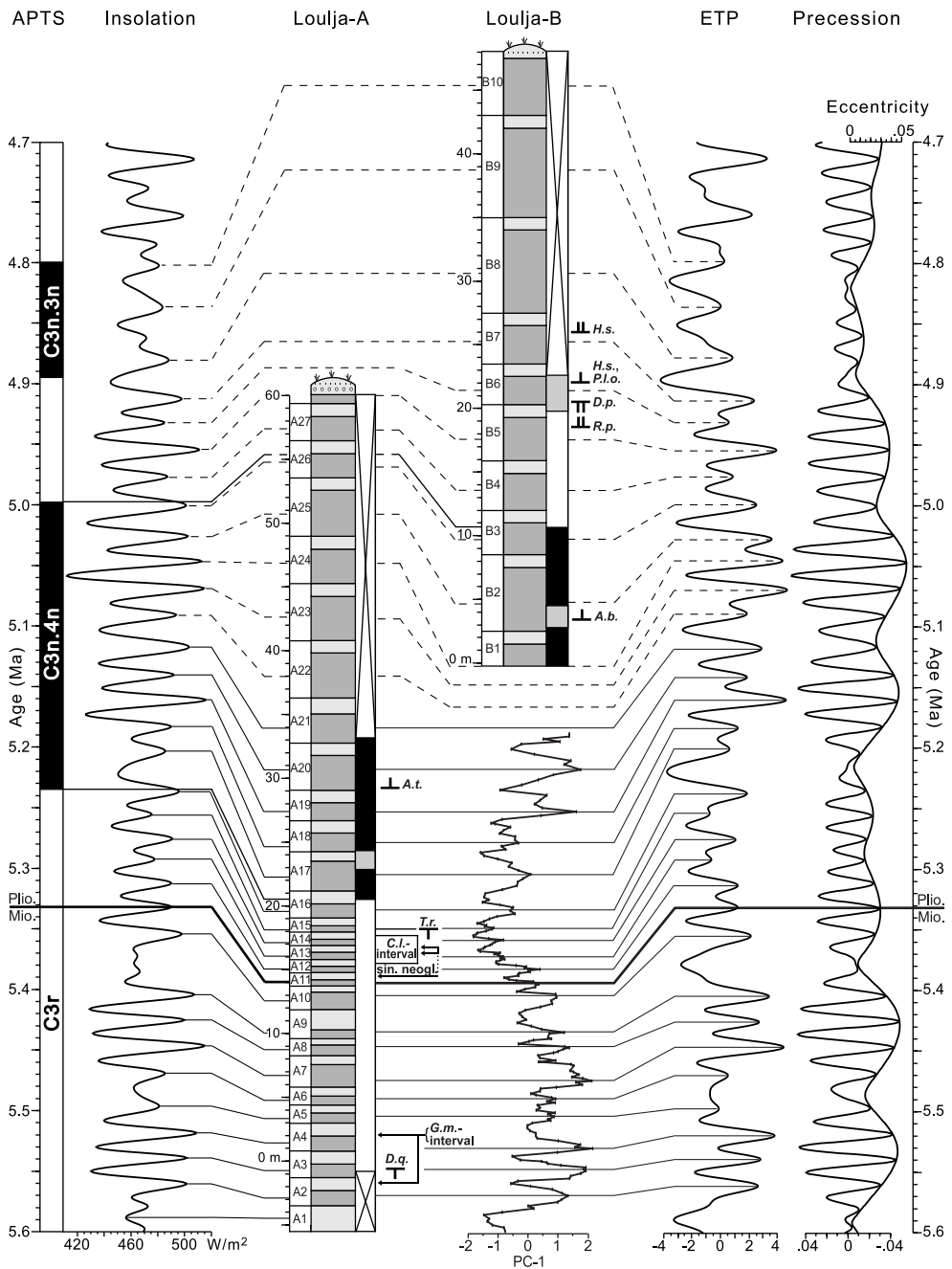


Figure 4.5 Calibration of the magnetostratigraphy of the Loulja-A and Loulja-B sections (for key, see caption to Fig. 4.2) to the astronomical polarity timescale [ATNTS2004 of Lourens et al., 2004] and tuning of colour cycles and PC-1 to the 65°N summer insolation and ETP (normalized eccentricity, tilt, and precession) time series of the La2004 solution [Laskar et al., 2004] with present-day values for dynamical ellipticity and tidal dissipation. Also shown are the precession and eccentricity curves of the same solution.

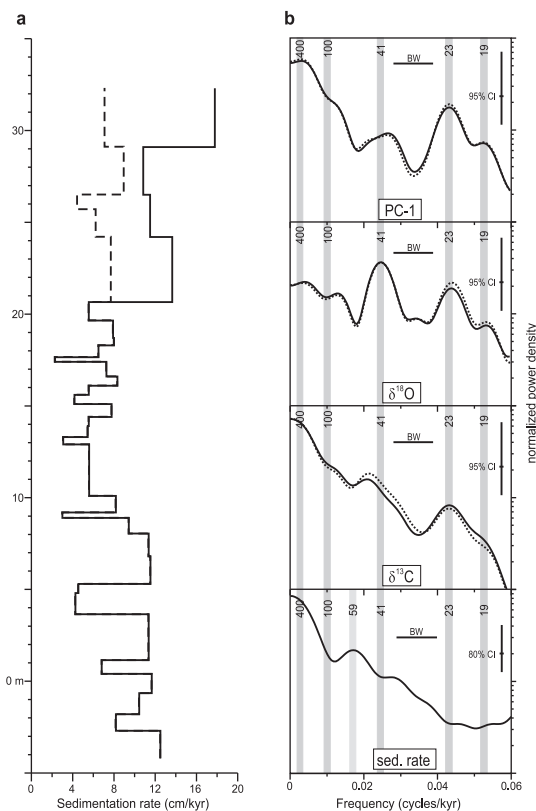


Figure 4.6 a) Sedimentation rate curve versus lithology of Loulja-A according to our preferred age model. Dashed line shows sedimentation rate if cycles LA-17-20 represent double cycles. b) Power spectra of PC-1, benthic $\delta^{18}\text{O}$, benthic $\delta^{13}\text{C}$, and sedimentation rate, using the preferred age model to generate time series. Solid and dotted lines in each spectral panel represent spectral power after tuning to ETP and insolation, respectively. Horizontal bar denotes the band width (BW) that is 0.011 for PC-1, $\delta^{18}\text{O}$, and $\delta^{13}\text{C}$ and 0.012 for sedimentation rate. Vertical bar denotes the 95% confidence interval (CI); for the sedimentation rate the 80% confidence interval is indicated.

2002] and the astronomical target curve. However, this component could better be compared with ETP (a combined record of normalized Eccentricity, Tilt (obliquity), and (negative) Precession [Imbrie et al., 1984]) than with insolation because of an apparent non-linear response to the insolation forcing. According to our phase relations, maxima in PC-1 correspond to maxima in ETP (maxima in obliquity and eccentricity/minima in precession).

The PC-1 record of Loulja-A is in almost excellent agreement with ETP, allowing for a straightforward tuning of the section up to at least cycle LA-16 (Fig. 4.5). The two groups of three distinct maxima in PC-1 in the lower part of Loulja-A (LA-2-4; LA-7-9) correlate with two similar clusters of maxima in ETP between 5.58 and 5.38 Ma, which reflect two successive prominent 100-kyr eccentricity maxima. The two weaker maxima of cycles LA-5 and LA-6 correlate with the two low-amplitude maxima in ETP that correspond to the intervening 100-kyr eccentricity minimum around 5.48 Ma. The amplitude pattern in PC-1 generally mimics that of ETP. The thick reddish layer LA-10_r is partly explained by the composite character of this cycle in

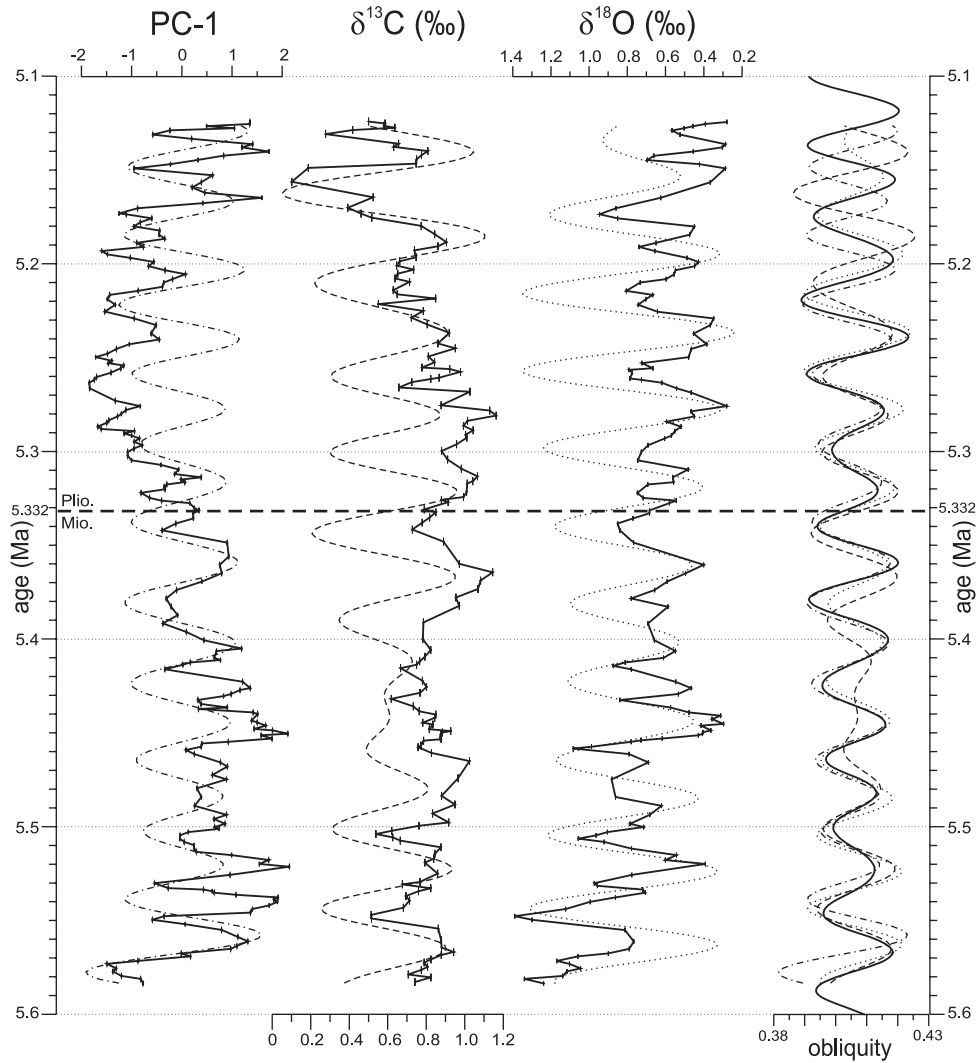


Figure 4.7 PC-1, benthic $\delta^{13}\text{C}$, and benthic $\delta^{18}\text{O}$ time series (solid lines) with 41-kyr filtered components (dotted and dashed lines) and comparison with obliquity. The proxy time series were filtered using Gaussian band-pass filters with central frequencies of 0.0255 (PC-1), 0.023 ($\delta^{13}\text{C}$), and 0.0245 ($\delta^{18}\text{O}$) and a band width of 0.012 cycles/kyr.

ETP. The correlative ETP maximum shows a “shoulder” at its base corresponding to an additional low-amplitude precession cycle. Similar shoulders (but in opposite direction) may explain the thickness of LA-1_B and LA-9_B. Following the tuning of cycles LA-1 to LA-10, the characteristic interval of thin colour cycles (LA-10_B to LA-15_B) can be correlated straightforwardly to the interval with reduced amplitude variations in ETP and insolation that corresponds to the 400-kyr eccentricity minimum around 5.25 Ma.

The tuning of cycles LA-17 to LA-21 proved more difficult. The preferred option is presented in Figure 4.5 and implies that all the colour cycles correspond to single precession cycles, even though this does not explain the extra peaks in PC-1 observed in some of the cycles. Following this option, LA-20_R correlates with the precession minimum/insolation maximum at 5.14/5.15 Ma. The relatively thick reddish layer of cycle LA-17 does not reflect a high-amplitude precession minimum/insolation maximum as expected, but is related to the longer than average duration of the correlative precession-insolation cycle. Sedimentation rates, which are 5 cm/kyr on average in the interval with the six thin cycles LA-10_B-15_B, increase to ~13 cm/kyr in cycle LA-17 and to ~16 cm/kyr in cycle LA-20 (Fig. 4.6). Other options imply that the reddish layers of one or all of cycles LA-18 to LA-21 contain an extra cycle that lacks sedimentary expression. Although double cycles are known from Ain el Beida, extra cycles are not developed in reddish layers in that section [Krijgsman et al., 2004].

We favour the first option for several reasons. Firstly, the increase in sedimentation rate resulting from this option is expected because sedimentation rate is positively correlated with eccentricity and hence with precession amplitude both in Ain el Beida [Van der Laan et al., 2005] as well as in the lower half of Loulja-A (see Fig. 4.4). Nevertheless, the increased sedimentation rate starts somewhat earlier than expected based on the amplitude changes in ETP and insolation. However, the increase markedly coincides with the top of the 400-kyr carbonate maximum in the deep marine Trubi marls in southern Italy; this maximum corresponds to the 400-kyr eccentricity minimum around 5.25 Ma and consists of the first six precession-related cycles of the Trubi [Hilgen, 1991b; Hilgen and Langereis, 1993]. Overall, the higher sedimentation rates are in good agreement with sedimentation rates calculated for the lower part of Loulja-A and Loulja-B (see paragraph 7.3) where cycles reach similar thicknesses at times of maximum eccentricity. The double cycle option does not result in higher sedimentation rates in the top part of Loulja-A, which is difficult to explain. Moreover, out-of-phase relationships between the 41-kyr component in $\delta^{18}\text{O}$ and obliquity start to develop if this option is used for tuning (not shown). Finally, the remaining cycles LA-22-27 should also represent double cycles since they reach similar thicknesses as cycles LA-18-21. However, as we demonstrate in paragraph 7.3, it is clear from the tuning of Loulja-B that the extremely thick cycles LB-8-9 (which do represent double cycles) should then be reached in the top part of Loulja-A, which is clearly not the case. We therefore prefer the tuning option in which all colour cycles are regarded as single precession cycles. The sampled time interval covered by the Loulja-A section thus ranges from ~5.59 to 5.12 Ma.

4.7.2 Spectral analysis

To test the correctness of our preferred age model further, we applied (cross-) spectral analysis and band-pass filtering using the Analyseries software of Paillard et al. [1996] to determine the main periodicities in our proxy records and the phase relationships relative to the astronomical forcing. The PC-1 spectrum reveals peaks at the main precession frequencies, which is not surprising because of the strong link with the colour cycles and the tuning to a precession-dominated target curve (Fig. 4.6). Additional variance near the main obliquity frequency is also apparent although a separate peak is lacking. In addition, power is concentrated around ~400 kyr, which is probably related to the long-term eccentricity cycle. The $\delta^{18}\text{O}$ spectrum reveals a strong peak at the main obliquity frequency and an additional peak at the 23-kyr precession period. Subsidiary peaks occur at the low-frequency end of the spectrum, at ~260 kyr and ~80 kyr. The $\delta^{13}\text{C}$ spectrum reveals a concentration of power at the low-frequency end of the spectrum, while a 'shoulder' is recorded at ~90 kyr, presumably related to short-term eccentricity. Additional peaks at the main

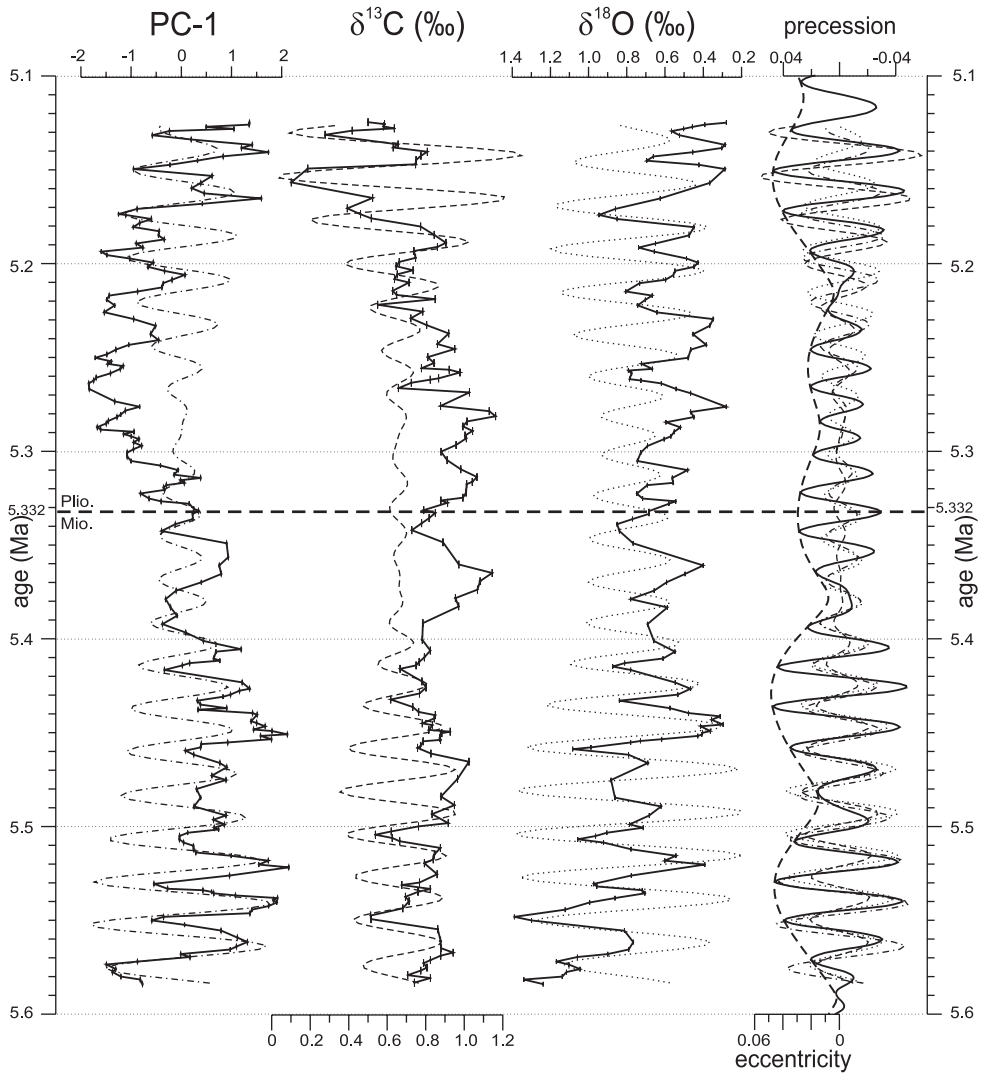


Figure 4.8 PC-1, benthic $\delta^{13}\text{C}$, and benthic $\delta^{18}\text{O}$ time series (solid lines) with 23-kyr filtered components (interrupted lines) and comparison with precession. Thick dashed line shows the eccentricity envelope of the precession curve. The proxy time series were filtered using Gaussian band-pass filters with central frequencies of 0.043 (PC-1), 0.042 ($\delta^{13}\text{C}$), and 0.0435 ($\delta^{18}\text{O}$) and band widths of 0.014 (PC-1), 0.015 ($\delta^{13}\text{C}$), and 0.011 ($\delta^{18}\text{O}$) cycles/kyr.

Element	Value
K	0.973
Al	0.962
V	0.939
Fe	0.938
Ti	0.913
Li	0.901
Ba	0.867
Mn	0.779
Cr	0.774
Ni	0.743
Zn	0.608
Na	0.248
Mg	0.046
Sr	-0.138
Ca	-0.764

Table 4.1 Loadings of individual elements on the first principal component (PC-1).

obliquity and precession frequencies are present although their power is relatively low. Because the $\delta^{18}\text{O}$ and $\delta^{13}\text{C}$ time series were constructed by means of tuning PC-1 to ETP, we carried out an independent check on the correctness of our age model by filtering the 41-kyr components in $\delta^{18}\text{O}$, $\delta^{13}\text{C}$, and PC-1 and comparing them with obliquity. The 41-kyr components generally show an in-phase relationship with obliquity and similar amplitude variations (Fig. 4.7), although the 41-kyr components in PC-1 and $\delta^{13}\text{C}$ start to run out of phase with obliquity in the younger part of the record (from 5.22 Ma onwards). For $\delta^{13}\text{C}$, the out-of-phase relationship stems from the fact that it does not co-vary inversely with $\delta^{18}\text{O}$ in this part of the record, as mentioned before (see paragraph 6.2.2). In addition, a clear obliquity-related signal is lacking in the interval between 5.48 and 5.36 Ma, where amplitude variations are low and the ~100-kyr signal is well developed (Fig. 4.7). For PC-1, the (near) out-of-phase relationship with obliquity in the younger (and oldest) part of the record stems from the high-amplitude precession-related variations in PC-1 associated with the eccentricity maxima at ~5.15 and 5.55 Ma; these strong variations prevent the filter from picking up the obliquity-related signal.

Results of cross-spectral analysis reveal that the precession components in PC-1, $\delta^{13}\text{C}$, and $\delta^{18}\text{O}$ vary in phase with ETP (Fig. 4.8). Again this is not surprising in view of the strong link of these components with lithology and the tuning (of PC-1) to a precession-dominated target curve. The results also confirm the in-phase relation for the 41-kyr component in $\delta^{18}\text{O}$ with respect to obliquity as inferred from the band-pass filtering. Note, however, that the latter in-phase relation changes to a lag of several kyr if the tidal dissipation in the La2004_(1,1,0) solution is reduced to half its present-day value (not shown). This outcome is comparable with the results from the slightly older Ain el Beida section [Van der Laan et al., 2005] and provides additional supportive evidence for our tuned age model of the Loulja-A section. Our age model provides astronomical ages, not only for the sedimentary cycles and for bioevents, but also for the dominantly obliquity-controlled $\delta^{18}\text{O}$ stages (Tabs. 4.2 and 4.3).

4.7.3 Loulja-B

The calcareous plankton biostratigraphic data from Loulja-B indicate that this section is slightly younger than Loulja-A (thereby confirming the information from the field) and that the N-R polarity reversal must represent the Upper Thvera. Using the position of the Upper Thvera, dated astronomically at 4.997 Ma [Lourens et al., 2004], as starting point the tuning of Loulja-B is rather straightforward (Fig. 4.5). The two very thick cycles LB-8 and 9 are interpreted as double

Cycle	Stratigraphic position (m)	Age (Ma)	
		ETP	Summer insolation
LA-2R	-2.70	5.561	5.560
LA-2B	-1.80	5.550	5.550
LA-3R	-0.65	5.539	5.539
LA-3B	0.40	5.530	5.530
LA-4R	1.15	5.519	5.518
LA-5R	3.65	5.497	5.496
LA-6R	4.80	5.470	5.469
LA-6B	5.30	5.459	5.459
LA-7R	6.80	5.446	5.446
LA-7B	8.05	5.435	5.436
LA-8R	8.90	5.426	5.425
LA-8B	9.20	5.416	5.416
LA-9R	10.10	5.405	5.404
LA-10R	12.90	5.355	5.354
LA-10B	13.30	5.342	5.343
LA-11R	13.90	5.331	5.332
LA-11B	14.40	5.322	5.322
LA-12R	15.10	5.313	5.312
LA-12B	15.60	5.301	5.302
LA-13R	16.10	5.292	5.292
LA-13B	16.60	5.286	5.285
LA-14R	17.40	5.275	5.275
LA-14B	17.65	5.264	5.265
LA-15R	18.30	5.254	5.255
LA-15B	18.70	5.249	5.248
LA-16R	19.65	5.237	5.236
LA-16B	20.65	5.219	5.222
LA-17B	24.20	5.193	5.193
LA-18B	26.50	5.173	5.173
LA-19B	29.10	5.149	5.151
LA-20B	32.30	5.131	5.130

Table 4.2 Stratigraphic position of midpoints of reddish and beige layers of lithologic cycles in the Loulja-A section and their astronomical ages after tuning to the ETP and summer insolation curves of the La2004_(1,1) solution [Laskar et al., 2004].

cycles in which one cycle lacks sedimentary expression and correspond to the 400-kyr eccentricity minimum around 4.85 Ma; this minimum is characterized by strongly reduced amplitudes in precession and hence insolation. In this case, the very weak summer insolation minima (precession maxima) at 4.87 and 4.83 Ma are not expressed in the sedimentary record as additional thin beige marls. This pattern strongly resembles that observed in the Trubi marl formation where cycles 21 and 22 represent double cycles as well [Hilgen, 1991b; Lourens et al., 1996]. The very thick reddish layer of cycle LB-2 is the only uncertainty that remains in the tuning of Loulja-B. Similarly, this cycle may represent a double cycle.

4.7.4 Calcareous plankton events and magnetic reversals

With the tuning of the Loulja sections, astronomical ages are obtained not only for the sedimentary and geochemical cycles but also for the calcareous plankton events and magnetic polarity reversals (Tab. 4.3). The *Discoaster quinqueramus* LO at 5.537 Ma and the *Triquetrorhabdulus rugosus* LO at 5.255 Ma are near synchronous with the low-latitude Atlantic (5.54 and 5.24 Ma, respectively; Backman and Raffi, 1997; Raffi et al., 1998). The *Ceratolithus larrymayeri* acme corresponds with the younger part of the short total range of this species at Ceara Rise [Raffi et al., 1998]. Consequently, also the *C. larrymayeri* LO is synchronous between Loulja and the low-latitude Atlantic. The *Amaurolithus tricorniculatus* FO, which is not considered a useful event in view of the rare and discontinuous presence of the species [Raffi et al., 1998], clearly postdates the same event in the equatorial Atlantic (5.15 versus 5.31 Ma; see also Tab. 4.3).

The three cosmopolitan nannofossil events recorded in the lower part of the Loulja-B section, namely the subbottom of *Reticulofenestra pseudoumbilicus* (>8 µm), the *Dictyococcites perplexus* subtop, and the *Pseudoemiliania lacunosa ovata* FO, were also recorded by Driever [1988] in the

	This study			Other Age (Ma)
	Cycle	Position (m)	Age (Ma)	
Magnetostratigraphy				
Reversal				
C3n.4n (odd)	LA-16B	20,35 - 20,70	5,222 ± 0,003	5,235 (1)
C3n.4n (young)	LB-3	9,8 - 11,6	4,994 ± 0,007	4,997 (1)
Biostratigraphy				
Bioevent				
interval with common <i>Globorotalia menardii</i>	LA-2B	-1,95 to -1,55	5,550 ± 0,002	5,556 ± 0,002 (2)
	LA-4B	2,10 - 2,20	5,511 ± 0,001	5,523 (2)
influx sinistral neogloboquadrinids	LA-11B	14,55 - 14,75	5,319 ± 0,001	5,325 ± 0,005 (3)
	LA-13A	16,15 - 16,25	5,291 ± 0,001	
influx sinistral neogloboquadrinids	LA-13B	16,65 - 16,75	5,285 ± 0,001	5,305 ± 0,005 (3)
L.O. <i>Discoaster quinqueramus</i>	LA-3R	-0,7 to -0,18	5,537 ± 0,002	5,58 / 5,59 (1); 5,537 (4)
F.O.D. <i>Ceratolithus larmyayeri</i>	LA-12B	15,50 - 15,55	5,303 ± 0,001	5,338 (4)
L.O.D. <i>Ceratolithus larmyayeri</i>	LA-14B	17,7 - 17,9	5,262 ± 0,002	5,264 (4)
L.O. <i>Trifarctohabidulus rugosus</i>	LA-15R	18,2 - 18,3	5,255 ± 0,001	5,231 (4)
F.O. <i>Amaurolithus iricomaculatus</i>	LA-20R	28,0 - 30,3	5,151 ± 0,008	5,31 (5)
F.O. <i>Amaurolithus bizzanus</i>	LB-2R	2,25 - 5,0	5,033 ± 0,004	5,24 (5)
subbottom <i>Reticulofenestra pseudoumbilicus</i> (>8 µm)	LB-5B	17,8 - 19,4	4,950 ± 0,005	4,91 (3)
subtop <i>Diclyococites perplexus</i>	LB-6B	19,4 - 21,7	4,938 ± 0,007	4,91 (3, 6)
F.O. <i>Pseudemiliania lacunosa ovata</i>	LB-6B	21,7 - 22,5	4,929 ± 0,003	4,91 (3, 6)
F.O. <i>Helicosphaera sellii</i>	LB-6B	21,7 - 22,5	4,929 ± 0,003	-4,55 (7)
F.R.O. <i>Helicosphaera sellii</i>	LB-7B	25,0 - 27,0	4,906 ± 0,008	-
Isotope stratigraphy				
Marine isotope stages				
TG14		-5,20	5,582	
TG13		-2,70	5,560	
TG12		-1,55	5,548	
TG11		1,10	5,519	
TG10.2		2,60	5,505	
TG10.0		5,40	5,458	
TG9		6,80	5,445	
TG8.2		8,30-9,35	5,433-5,414	
TG8.0		11,60	5,377	
TG7		12,60	5,359	
TG6.2		13,50	5,339	
[x]		14,10-15,25	5,327-5,309	
TG6.0		15,65	5,301	
TG5		17,35	5,276	
TG4.2		18,05	5,259	
TG4.1		18,65-20,10	5,248-5,230	
TG4.0		21,30	5,217	
TG3		23,10-25,70	5,202-5,180	
TG2		26,45	5,173	
TG1		28,30-31,40	5,151-5,136	

Table 4.3 Tuned ages of magnetic reversals, calcareous plankton events, and marine isotope stages in the Loulja sections and comparison with ages from other studies. Numbers in parentheses refer to (1) Lourens et al. [2004]; (2) Krijgsman et al. [2004]; (3) Lourens et al. [1996]; (4) Backman and Raffi [1997]; (5) Raffi et al. [1998]; (6) Driever [1988]; (7) Rio et al. [1997]. Marine isotope stages follow Shackleton et al. [1995b]; (sub) stages in italics and stage [x] are introduced by us and indicated in Figures 4.10 and 4.11.

Mediterranean Singa and Rossello composite sections dated astronomically by Lourens et al. [1996]. Our astronomical ages for these events are in good agreement with Driever [1988] and Lourens et al. [1996]. The difference of one cycle for the *D. perplexus* subtop is due to a difference in defining the n1-event of Driever [1988], which marks the transition from predominantly *D. perplexus* to predominantly *R. pseudoumbilicus* (>8 µm), rather than a problem of the astronomical tuning. The very rare occurrence of *P. lacunosa ovata* at the beginning of its range explains the slightly different age obtained for this event in the present study.

The planktonic foraminifera do not show clear-cut primary events, but the neogloboquadrinid coiling direction reveals two sinistral influxes of very short duration. Two similar influxes of sinistral neogloboquadrinids have also been found in the Mediterranean where they occur in the homogeneous marl of basic cycles 1 and 2 in the Trubi Formation [Di Stefano et al., 1996; Lourens et al., 1996]. The independent tuning of the Loulja colour cycles indicates that the first influx corresponds exactly in time with the first influx in the Mediterranean but that the second influx occurs one precession-related cycle later at Loulja.

The astronomical calibration implies that Loulja-A cycles 1-21 cover the time interval from 5.59 to 5.12 Ma. Therefore, the base of the normal polarity chronozone recorded between 20.35 and 20.7 m in cycle LA-16 should correspond to the base of the Thvera subchron (C3n.4n (o)); the astronomical age of 5.222 ± 0.005 Ma for the reversal at Loulja is very close to the astrochronologic age of 5.235 Ma [Lourens et al., 1996, 2004]. In addition, the reversal is neatly located five

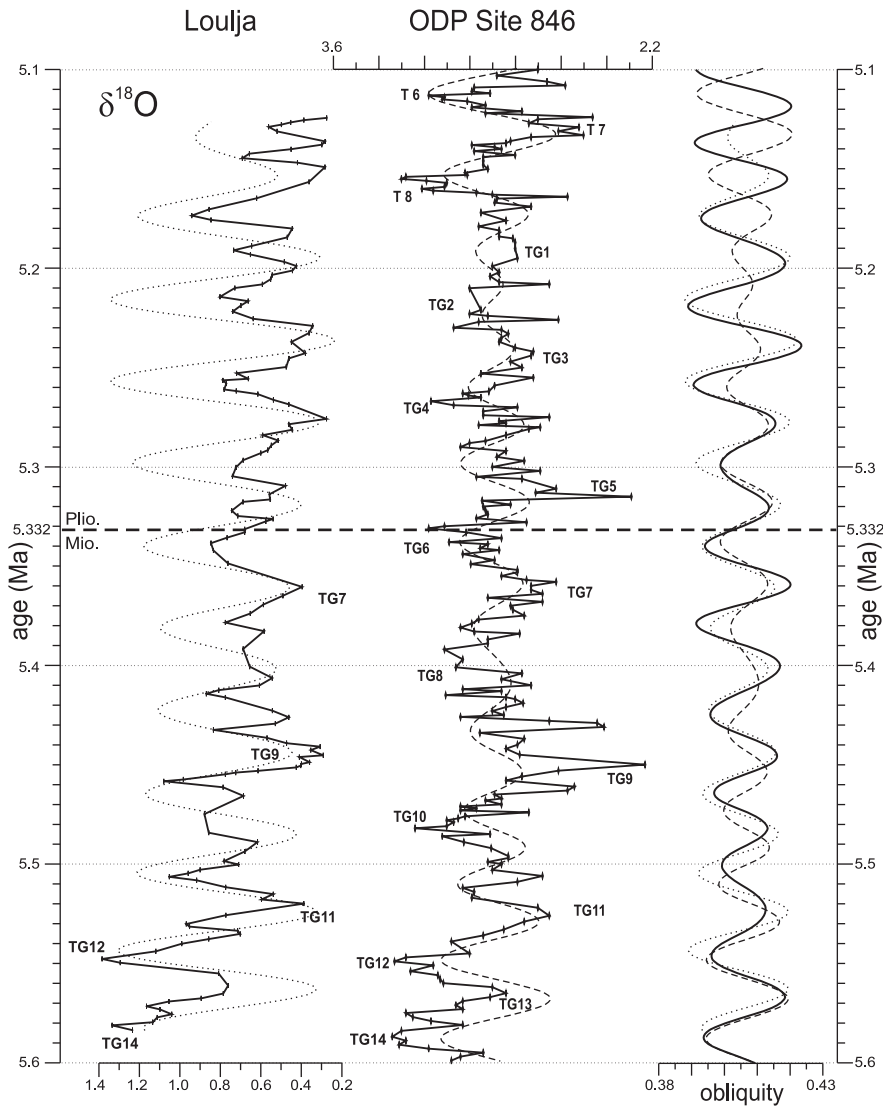


Figure 4.9 Comparison between the Loulja-A and ODP Site 846 $\delta^{18}\text{O}$ records in the time domain. For Site 846 the manually revised age model of Shackleton et al. [1999] was used to construct the proxy time series. The 41-kyr components are shown as overlays and were extracted using Gaussian band-pass filters with central frequencies of 0.0245 and a band width of 0.012 cycles/kyr. Indicated TG-stages for Site 846 are from Shackleton et al. [1995b].

precession cycles (~100 kyr) above the Miocene-Pliocene boundary, dated astronomically at 5.332 Ma [Lourens et al., 1996; Van Couvering et al., 2000], and pinpointed at 13.90 m in the middle of LA-11_R. The N>R transition below the 11 m level in LB-3_R corresponds to the Upper Thvera, as previously assumed. Its position is consistent with the Mediterranean, indicating that the very thick cycles LB-8 and 9 are indeed the equivalent of the double cycles 21 and 22 in the Trubi Formation. Note however that the position of this reversal was used during the tuning procedure.

4.8 Discussion

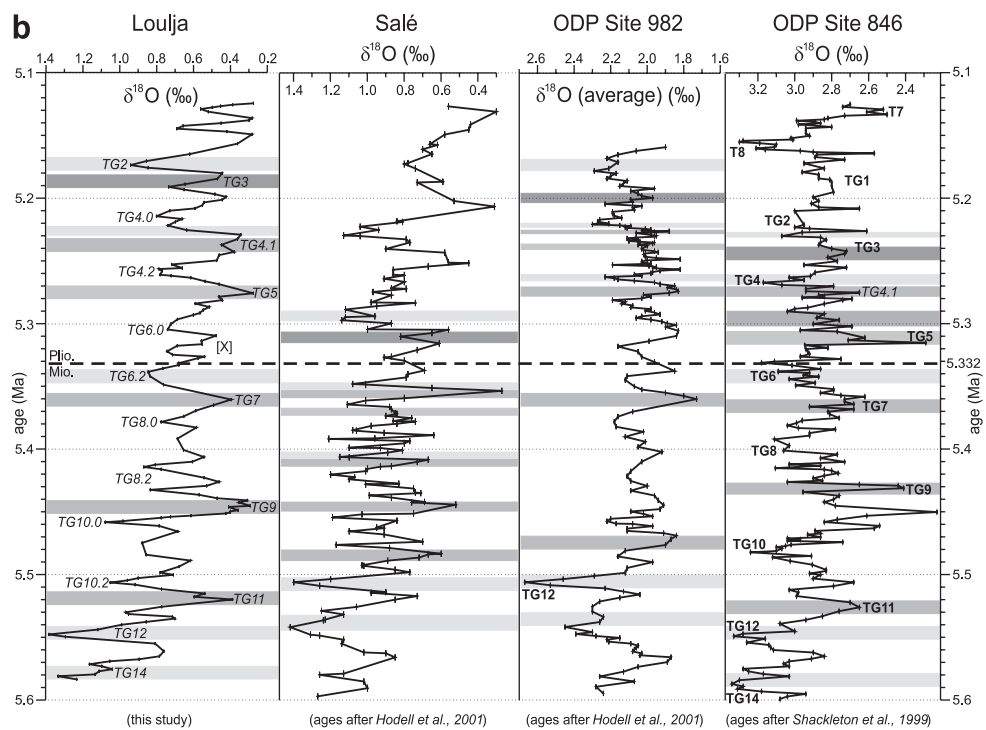
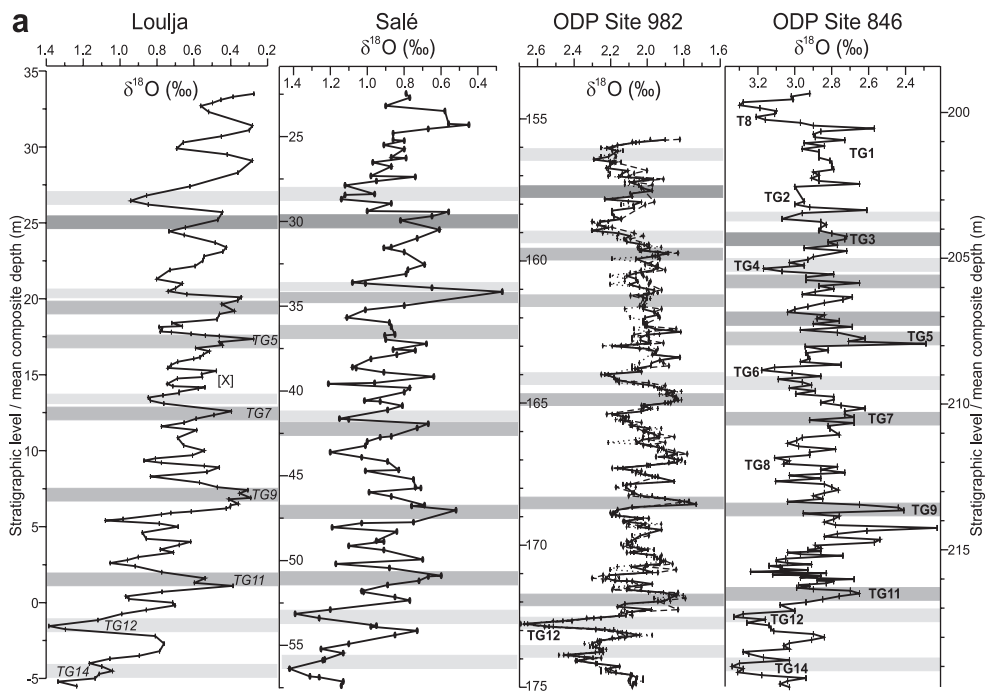
4.8.1 Isotope stratigraphy and chronology

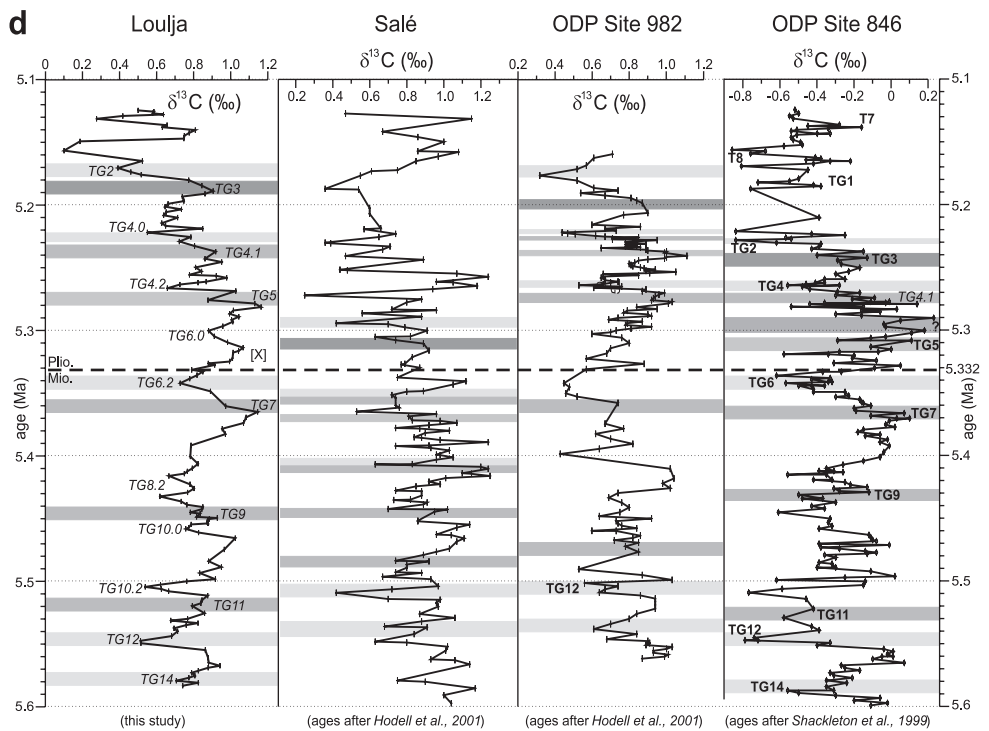
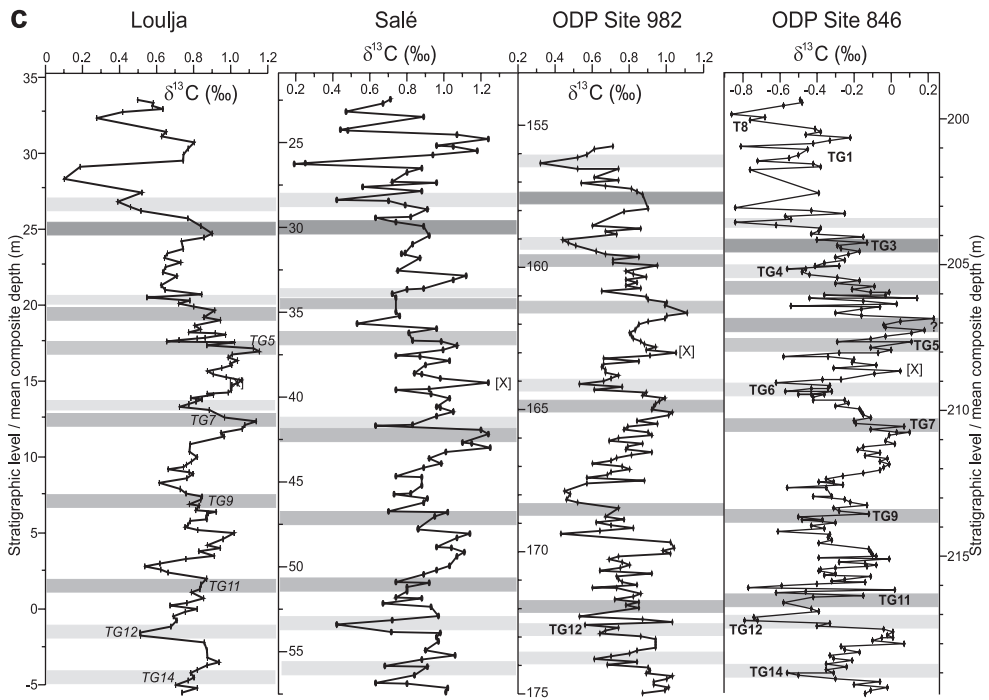
With the tuned age model for Loulja at hand it becomes timely to discuss the isotope stratigraphy and chronology for the latest Miocene and earliest Pliocene by comparing the Loulja isotope records with previously published records from the Bou Regreg area and with records from the open ocean [e.g., Hodell et al., 1994; Shackleton et al., 1995b, 1999; Hodell et al., 2001; Van der Laan et al., 2005]. Note that we will adopt our age model as basis for discussing the isotope stratigraphy and chronology. We will not attempt to match the Loulja isotope record to the isotope records from the open ocean and thus adopt alternative age models based on tuning of dominantly obliquity controlled isotope records. The reason for this is that we consider our age model an improvement because it is based on the tuning of precession dominated colour cycles, which reveal a much more distinctive pattern.

The Loulja-A $\delta^{18}\text{O}$ record reveals a much stronger obliquity-related signal than PC-1, which mainly tracks the colour cycles observed in the field. Because of the additional influence of precession, it is not always easy to recognize the obliquity-related signal in $\delta^{18}\text{O}$. The latter signal was illustrated by extracting the 41-kyr component in $\delta^{18}\text{O}$ and showing it as an overlay on the $\delta^{18}\text{O}$ time series; comparison with obliquity reveals an almost perfect in-phase relationship (Fig. 4.7).

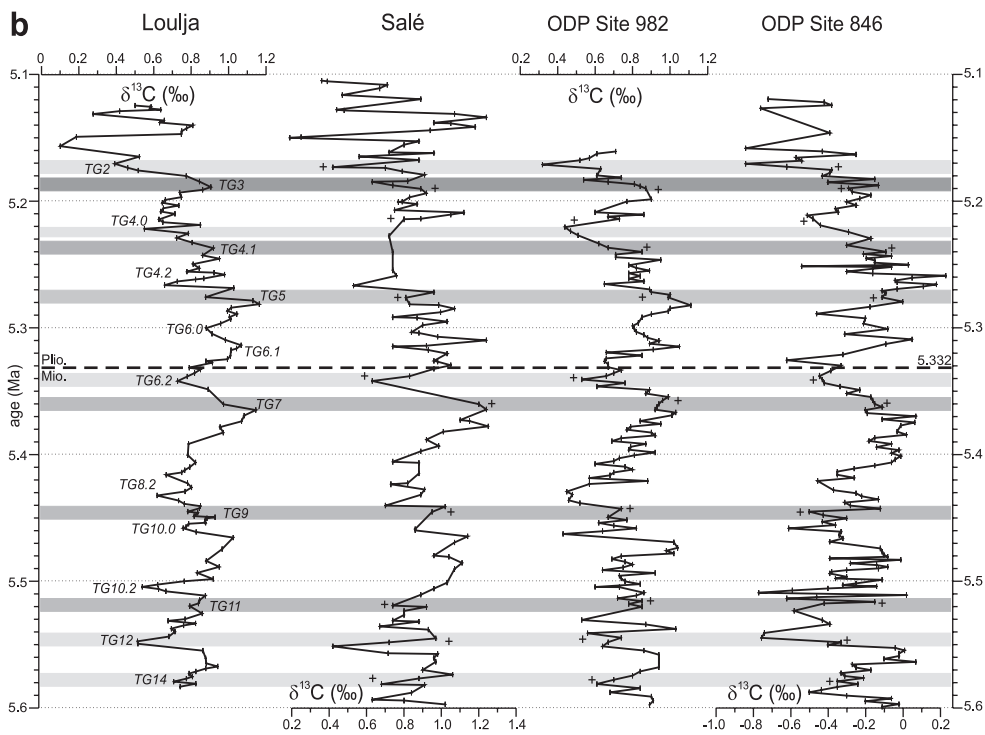
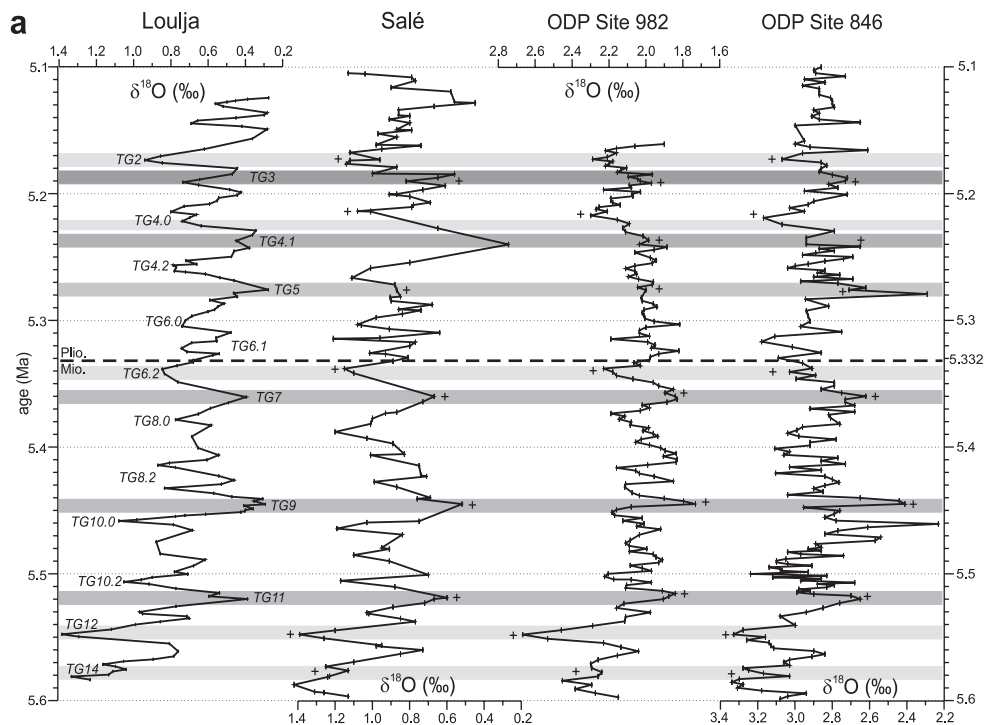
Like at Ain el Beida, the strong 41-kyr $\delta^{18}\text{O}$ cycle at Loulja-A is interpreted as to reflect a dominant obliquity-controlled glacial cyclicality, which has been recognized in open ocean benthic isotope records of latest Miocene to early Pleistocene age [e.g., Ruddiman et al., 1986; Raymo et al., 1989; Tiedemann et al., 1994; Shackleton et al., 1995b]. This glacial record reveals a characteristic pattern of distinct and less distinct glacial cycles. The more prominent peaks in $\delta^{18}\text{O}$ have been labelled to facilitate communication and global correlation of the oxygen isotope stages [Tiedemann et al., 1994; Shackleton et al., 1995b]. For the latest Miocene to Early Pliocene,

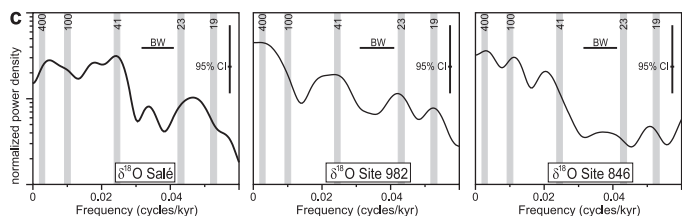
→ **Figure 4.10** Comparison in the depth domain and time domain between the (a-b) $\delta^{18}\text{O}$ and (c-d) $\delta^{13}\text{C}$ records of Loulja-A, Salé, and ODP Sites 846 and 982. Gray bands mark correlations based on glacial stages; green bands indicate correlations based on interglacial stages. Correlations are based on characteristic patterns in either $\delta^{18}\text{O}$ or $\delta^{13}\text{C}$ in the depth domain. The original stages defined by Shackleton et al. [1995b] are denoted in boldface next to the Site 846 record. Stages in boldface next to the record of Site 982 denote stage designations of Hodell et al. [2001], while stages in italics denote stage designations that result from our correlations. Question mark in the green band in the Site 846 $\delta^{13}\text{C}$ record indicates alternative option for TG5 based on the correlation with maximum $\delta^{13}\text{C}$ values from other records. The Salé record of Hodell et al. [1994] was redated by Hodell et al. [2001] using the same tuned age model as developed for ODP Site 982, which is based on the La90_(1,1) solution. The original age model for ODP Site 846 [Shackleton et al., 1995b] is based on the Be91 solution and was revised by Shackleton et al. [1999] using the La93_(1,1) solution.





No major deglaciation across the Miocene-Pliocene boundary





← **Figure 4.11** Comparison between the (a) $\delta^{18}\text{O}$ and (b) $\delta^{13}\text{C}$ time series of Loulja-A, Salé, and ODP Sites 846 and 982 after adopting revised age models based on control points (indicated by crosses) from Loulja-A. c) Resulting power spectra for $\delta^{18}\text{O}$; note the relatively strong power in the (23–19 kyr) precession band. In each spectral panel the horizontal bar denotes the band width (BW) that is 0.0093 for Salé, 0.0101 for Site 982, and 0.0097 for Site 846. Vertical bar denotes the 95% confidence interval (CI).

i.e. the time span covered by the Loulja-A section, the codification scheme of Shackleton et al. [1995b] based on ODP Site 846 in the eastern equatorial Pacific is used. This scheme links isotope stages to magnetochrons whereby, similar to other schemes, even numbers indicate cold stages. Shackleton et al. [1999] revised the initial tuned age model for the isotope record of Site 846 [Shackleton et al., 1995a] later on.

At Loulja-A, the correct identification of isotope stages is crucial if one aims to determine whether the basal Pliocene flooding of the Mediterranean is related to the (peak) deglaciation and associated sea level rise leading to TG5. The straightforward and unambiguous tuning of (the lower part of) Loulja-A reveals a stratigraphic overlap with Ain el Beida, indicating that the two prominent and characteristic maxima in $\delta^{18}\text{O}$ at -5 and -1.5 m correspond to TG14 and TG12 (Fig. 4.9). The identification of the younger stages depends on the detailed correlation to the $\delta^{18}\text{O}$ record of Site 846 in which they were originally defined [Shackleton et al., 1995b]. The stepwise shift to lighter isotope values between 5.55 Ma (TG12) and 5.45 Ma at Loulja is easily recognized at Site 846, indicating that the prominent $\delta^{18}\text{O}$ minimum at 5.45 Ma represents peak interglacial TG9. The $\delta^{18}\text{O}$ pattern in this interval is remarkably similar between both records showing additional precession-related variations that would allow a (further) subdivision of several of the stages (e.g., TG10). The Loulja-A record further confirms the presence of an extra obliquity-related cycle between TG11 and TG9.

The isotope stage identification is difficult from TG9 onward due to the relative low amplitude and therefore less characteristic pattern in $\delta^{18}\text{O}$ between 5.4 and ~ 5.2 Ma at ODP Site 846 [Shackleton et al., 1995b, 1999]. Comparison of the Loulja-A and ODP Site 846 $\delta^{18}\text{O}$ time series, using the revised tuning of Shackleton et al. [1999], shows that TG9 to TG3 occur in both records at the same time and are in phase with obliquity, but that the filtered 41-kyr component starts to run out of phase with obliquity between TG3 and T7 at Site 846 (Fig. 4.9). This would imply that the $\delta^{18}\text{O}$ minimum in the Loulja-A record at 5.315 Ma indeed corresponds to TG5 at Site 846.

However, this identification becomes less certain if one compares the carbon and oxygen isotope records of Site 846 in the depth and time domain. In addition, the isotope records from ODP Site 982 in the North Atlantic [Hodell et al., 2001] and from Salé Briqueterie [Hodell et al., 1994] located near Loulja were included in the comparison because ages for $\delta^{18}\text{O}$ stages at Site 982 and for those in the redated Salé record [Hodell et al., 2001] deviate significantly from our tuned ages. The comparison for $\delta^{18}\text{O}$ and $\delta^{13}\text{C}$ in the depth and time domain is shown in Figure 4.10 ($\delta^{18}\text{O}$: Figs. 4.10a and 4.10b; $\delta^{13}\text{C}$: Figs. 4.10c and 4.10d). For Site 846, the depth–time conversion results in an increase in sedimentation rate between TG7 and TG5 if the (manual) revision of the

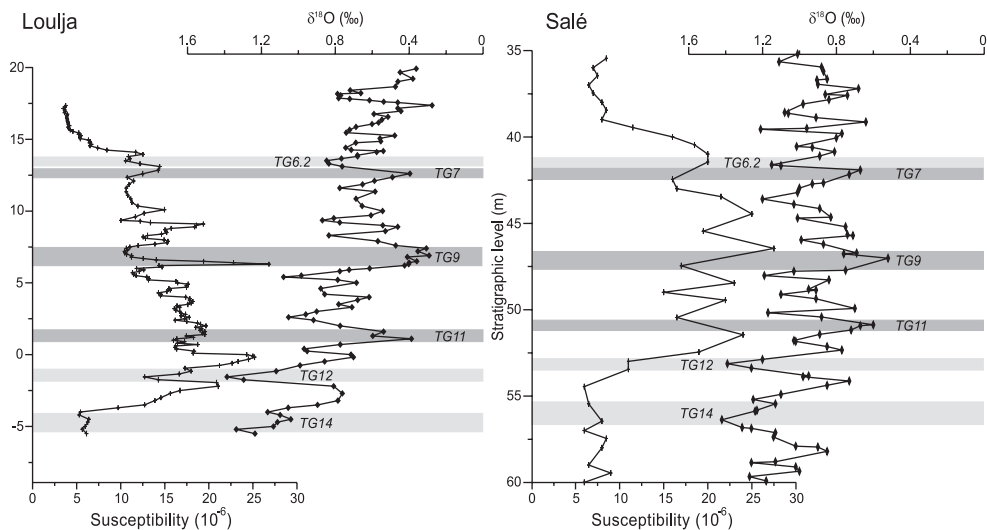


Figure 4.12 Comparison between the magnetic susceptibility of dehydrated samples (note difference from Fig. 4.2) and benthic $\delta^{18}\text{O}$ records from Loulja-A (partial section III) and from Salé [data from Hodell et al., 1994].

initial tuned age model by Shackleton et al. [1999] is adopted (Fig. 4.9). The TG7-5 interval is significantly thicker as that observed between regular obliquity-controlled cycles while these stages have been tuned to successive obliquity maxima. In fact, the Site 846 $\delta^{13}\text{C}$ record suggests that an additional obliquity-controlled cycle (labelled [x] in Fig. 4.10c) is present between TG7 and TG5. This characteristic interval reveals the highest $\delta^{13}\text{C}$ values throughout the critical interval across the M-P boundary and is preceded by a long-term increase leading to TG7. It can relatively easily be recognized in the other $\delta^{13}\text{C}$ records, showing a very similar character at Loulja and ODP Site 982 with three distinct $\delta^{13}\text{C}$ maxima. The first and last of these maxima correspond to stages TG7 and TG5 if we follow the $\delta^{18}\text{O}$ stage numbering of Shackleton et al. [1995b] and the expression of these stages in the Site 846 $\delta^{13}\text{C}$ record. Consequently, the extra (obliquity-controlled) stage is also recognized in the Site 982 and Loulja $\delta^{13}\text{C}$ depth records. The extra cycle would have the immediate consequence that the M-P boundary does not coincide with TG5 but with the unnamed extra cycle between TG5 and TG7, if we assume that the identification and tuning of TG7 is correct.

Using characteristic patterns in especially $\delta^{13}\text{C}$, the correlation between Loulja-A, Salé, and ODP Sites 846 and 982 can be extended up to TG2 (Figs. 4.10 and 4.11; Tab. 4.3). These patterns include the marked shift to lighter values between TG3 and TG2 and the “glacial” $\delta^{13}\text{C}$ signature of TG4 and TG6. Ideally, one would prefer to check the implications of the revised tuning up to the prominent glacial stages Si4 and Si6. However, this exercise is less straightforward and falls outside the scope of the present study, which aimed to unravel the influence of glacio-eustatic sea level change on the Pliocene flooding of the Mediterranean and the beginning of the Upper Evaporites.

Finally, the correlations between Loulja-A and Salé based on the stable isotope patterns are in agreement with the occurrence of a peak interval in magnetic susceptibility observed at both localities (Fig. 4.12). However, the relatively low sample resolution at Salé hampers a more detailed correlation of both susceptibility records.

4.8.2 Absolute isotope values

Although the isotope records discussed above correlate in considerable detail, they differ in absolute values. The absolute values of the oxygen isotopes are very similar for the Loulja and Salé sections, but are different for Sites 982 and 846. A shallower depth and higher bottom water temperatures at the Moroccan sites can explain this. Nevertheless, the overprint of the dominantly obliquity-controlled global ice volume signal is clearly reflected in all records and was used to correlate them in detail. The precession-related variations at Loulja most likely reflect a combination of a local temperature and/or salinity signal associated with the sedimentary colour cycles and a global ice volume signal. Indications for the presence of a precession-related component in global ice volume change during the latest Miocene previously came from comparing the slightly older record from Ain el Beida with records from the open ocean [Van der Laan et al., 2005].

The absolute carbon isotope values are very similar for Loulja, Salé, and ODP Site 982 but the values at Site 846 are considerably lower. This difference can best be explained by $\delta^{13}\text{C}$ aging of Pacific deep water [see, e.g., Ruddiman, 2001]. However, the overall pattern of all records is quite similar suggesting that whole-ocean processes (e.g., terrestrial-marine carbon transfer) control it.

4.8.3 Miocene-Pliocene boundary

Irrespective whether the low-amplitude $\delta^{18}\text{O}$ minimum at 5.315 Ma in the Loulja-A record corresponds to TG5, it is clear that the M-P boundary coincides with the very beginning of a minor shift to lighter values that, as far as the obliquity component is concerned, leads to the low-amplitude $\delta^{18}\text{O}$ minimum at 5.315 Ma. This transition (“deglaciation”) is interrupted by a precession-controlled shift to heavier values in $\delta^{18}\text{O}$ but it is unclear whether this precession component is also present in the $\delta^{18}\text{O}$ records from the open ocean. Such a presence may suggest a precession component in the glacial cyclicity, i.e. similar to the precession signal between TG14 and TG9 and for instance between TG32 and TG28 (i.e., TG30) and between C3An.18O.14 [codification of Hodell et al., 1994] and C3An.18O.10 (i.e., 12) at Ain el Beida [Van der Laan et al., 2005]. On the other hand, at Loulja-A, it can also easily be related to the dominantly precession-controlled regional climate oscillations that underlie the colour and PC-1 cyclicity.

Close inspection of the isotope record of Site 846 in fact indicates that the M-P boundary coincides with an extra obliquity-controlled and very weak interglacial between TG7 and TG5 and that TG5 represents an interglacial stage some 50 kyr younger than the M-P boundary (see paragraph 4.8.1; Figs. 4.10 and 4.11; Tab. 4.3). Comparison with our record further suggests that the actual Site 846 peak $\delta^{18}\text{O}$ values reached in TG5 may represent outliers because such exceptionally light values are found neither in our record nor in other records spanning the boundary [Hodell et al., 1994, 2001].

All this indicates that glacio-eustatic sea level rise (deglaciation) played only a minor role, if at all, in the basal Pliocene flooding of the Mediterranean. Probably, factors that are more important were extensional tectonics and/or ongoing headward erosion of an initially restricted connection between the Atlantic and Mediterranean. The latter situation may already have played a role during deposition of the Upper Evaporites in the Mediterranean with Atlantic waters intermittently entering the Mediterranean, thereby increasing seawater salinities.

The M-P boundary is formally defined at the base of the deep marine Trubi marls overlying the Upper Evaporites and Arenazzolo Formation of the Messinian at Eraclea Minoa [Van Couvering et al., 2000]. This level marks the onset of open marine conditions in the Mediterranean following the Messinian salinity crisis [Hsü et al., 1973; Cita, 1975; Hilgen and Langereis, 1993; Iaccarino et al., 1999]. This level was selected mainly for historical reasons but the possibly unconformable

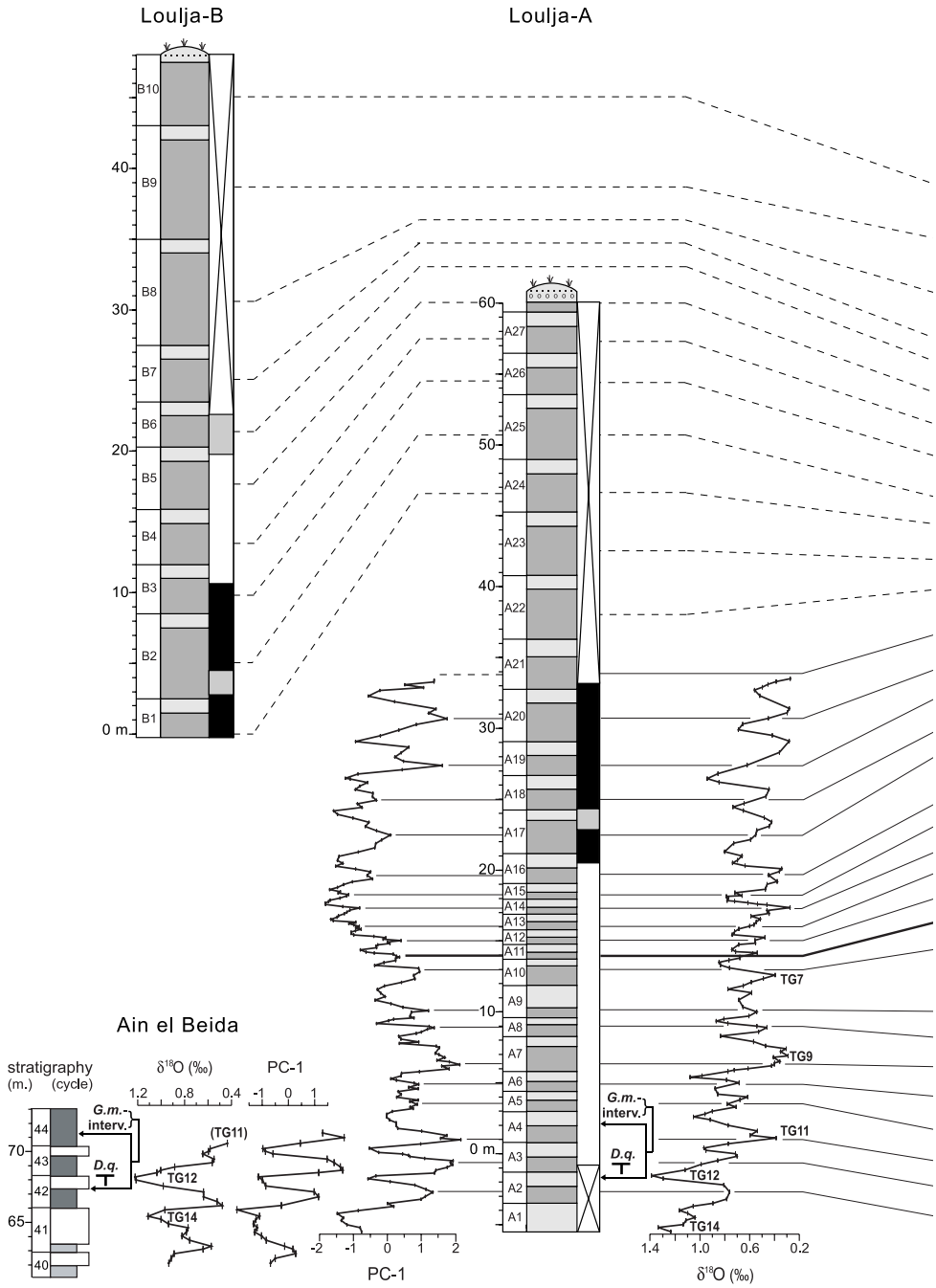
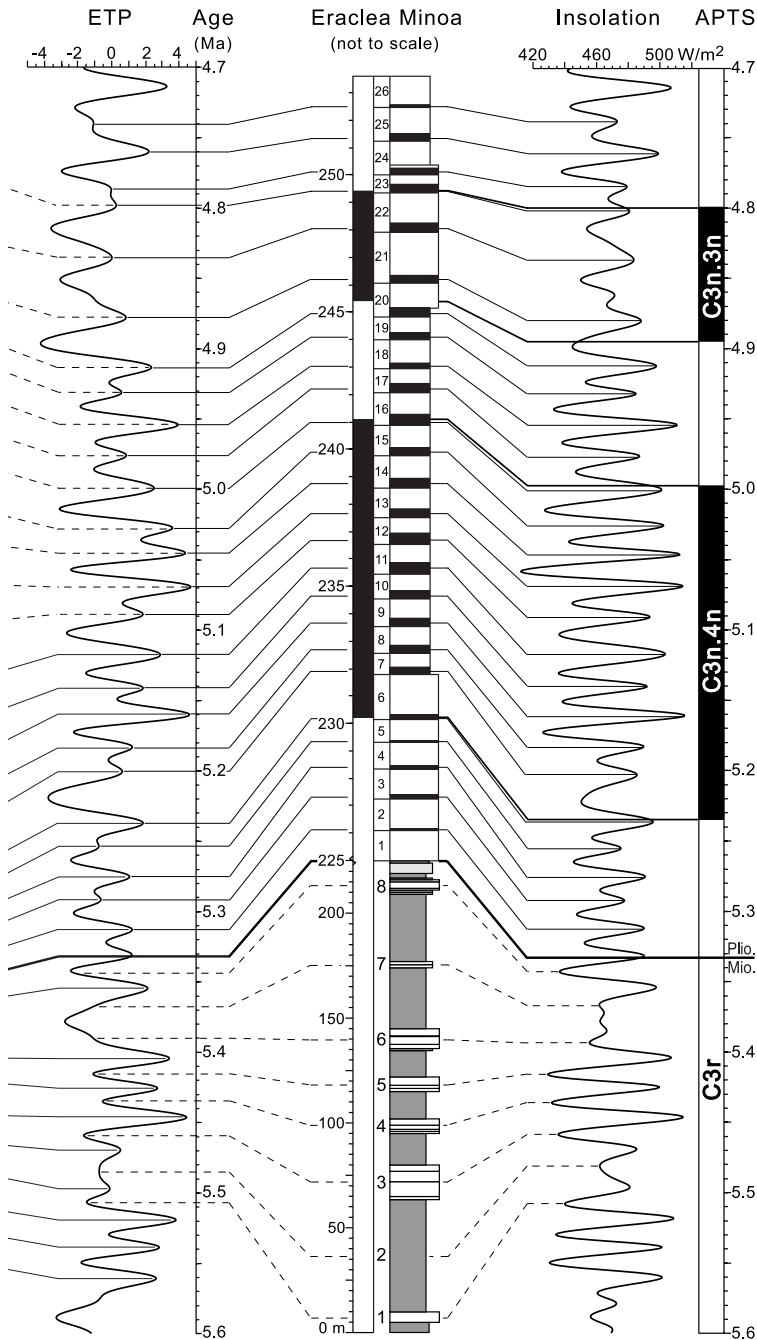


Figure 4.13 Cyclostratigraphic correlations of the Loulja-A and Loulja-B sections (for key, see caption to Fig. 4.2) to the Upper Evaporites and Trubi marls in the Eraclea Minoa section on Sicily, Italy (note scale change at the Miocene-Pliocene boundary). Eraclea Minoa tuning is partly based on the work of Lourens et al. [1996]. Correlations of the PC-1 and $\delta^{18}\text{O}$ records between the basal part of Loulja-A and the uppermost part of Ain el



Beida [Krijgsman et al., 2004; Van der Laan et al., 2005; E. van der Laan, unpublished data, 2003] are also shown. Isotope stages are numbered following the codification scheme of Shackleton et al. [1995b]; see caption to Figure 4.9 for further explanation.

No major deglaciation across the Miocene-Pliocene boundary

nature of the formation boundary in combination with the abrupt transition from nonmarine to fully marine conditions makes it in principle less suitable. Suc et al. [1997], recognizing the problem of the possible unconformable character of the contact, proposed to define the M-P boundary near Salé, some 5 km northwest of Ain el Beida, at the stratigraphic level that corresponds with the base of oxygen isotope stage TG5. The isotope shift was supposed to correspond with the base of the Trubi reflecting the marked deglaciation held responsible for the Pliocene flooding of the Mediterranean at that time. The proposal was considered less favourable because the level was only indicated in the Salé drill core but not in any existing outcrop.

Our results show that the M-P boundary is positioned at 13.90 m in the middle of LA_R-11 in section Loulja-A in an open marine succession located just outside the Mediterranean. Hence it might be preferable to designate Loulja-A as an auxiliary stratotype section for the M-P boundary. Our results also indicate however that the boundary does not coincide with TG5.

4.8.4 Upper Evaporites

The stepwise shift to lighter values between TG12 and TG9 marks a more dramatic deglaciation than TG5 [e.g., Shackleton et al., 1995b]. An important implication of the revised age model of Shackleton et al. [1999] is that the onset of the Upper Evaporites (UE) following the main desiccation phase of the Mediterranean is linked to the glacio-eustatic sea level rise associated with the deglaciation manifested in particular by the TG12 to TG11 transition. The number of 7/8 sedimentary cycles observed in the UE and correlative units throughout the Mediterranean [Vai, 1997; Krijgsman et al., 2001; Fortuin and Krijgsman, 2003] is consistent with such a scenario in case these cycles are precession-controlled (Fig. 4.13). Alternative options start from an obliquity control for the UE cyclicity [Vai, 1997]; this interpretation is inconsistent with linking the beginning of the UE to the TG12 to TG9 deglaciation. It further is not in agreement with a precession control for the evaporite cycles of the Lower Evaporites (LE) although the distinction between a precession or obliquity control on the UE cyclicity becomes problematical in view of the hiatus of ~100 kyr inferred between the LE and UE according to the precession scenario [Krijgsman et al., 1999a, 2001].

There are indications in the literature that the Mediterranean was not fully isolated from the world ocean during deposition of the UE but that marine incursions may have occurred. The gypsum cycles of the UE in the Eraclea Minoa section (Caltanissetta Basin, Sicily) display a facies evolution from fine-grained laminar gypsum at the base of each cycle to selenites at the top, accompanied by increasing strontium values indicating increasing salinity conditions [Rosell et al., 1998]. Partly backed-up by these data, Schreiber [1997] claimed a distinctly marine origin of the gypsum in this section alternating with non-marine beds and concludes that a connection with the open ocean existed throughout the MSC. In addition, Londeix [2004] interpreted the intercalated clays of Eraclea Minoa with dinocyst assemblages to be indicative of a shallow marine environment with occasionally hypersaline conditions and river influxes. However, according to Taberner et al. [2004] previous interpretations of the geochemical and biological markers from the Eraclea Minoa UE, supposedly indicative of a marine contribution, need reconsideration. Recycling of older Messinian evaporites may offer an alternative explanation for the observed isotopic composition of the sulphates. Nevertheless, Flecker et al. [2002] argued that neither the observed Sr isotopic offsets from ocean values nor the high salinities during evaporite precipitation require total isolation of the Mediterranean from the world ocean.

Also Clauzon et al. [1996] considered marginal basins (including Eraclea Minoa) in the Mediterranean to have received Atlantic waters during deposition of the LE and UE, although

their age model differs from the age model we prefer. From the uppermost Messinian of the Nijar Basin in SE Spain, Fortuin and Krijgsman [2003] reported marine microfaunas and suggested that short-lived connections with the Atlantic Ocean could have existed during periods of high sea level although reworking could not be excluded. Aguirre and Sánchez-Almazo [2004] are much more explicit by stating that the planktonic foraminiferal faunas from the Messinian post-evaporitic beds in the Nijar Basin are not reworked but represent *in situ* faunas. The latter would imply that open marine conditions already existed in the western Mediterranean area during the latest Messinian. Nevertheless, the arguments put forward by Aguirre and Sánchez-Almazo [2004] concerning the sometimes excellent preservation and the absence of reworked older faunas do by no means exclude reworking. Even on Cyprus, Rouchy et al. [2001] claim to have found authentic marine faunas in the local equivalent of the UE/Lago Mare, indicative of the persistence of marine influences. Müller [1990] mentioned that assemblages of low diversity and smaller sized calcareous nannofossils and planktonic foraminifera are found in the uppermost Messinian of the Tyrrhenian Sea, while Castradori [1998] observed anomalous nannofossil assemblages in the same interval in the Alboran, Balearic, and Levantine basins. From the latter basin and from the Mediterranean Ridge south of Crete, Spezzaferri et al. [1998] ascribed the presence of beds with planktonic foraminifera to an Atlantic origin, a conclusion that was shared, although with more caution, by Iaccarino and Bossio [1999] for sediments of the uppermost Messinian in the Balearic Basin. Iaccarino et al. [1999] stated that periodic spill-overs into the (western) Mediterranean occurred at the end of the Messinian, related to eustatic sea level changes.

The latter would favour an obliquity control because of the dominant obliquity forcing of glacial cyclicity and hence glacio-eustatic sea level change during the latest Miocene and Pliocene. Nevertheless, it is evident that the benthic isotope records reveal a well-defined precession signal in addition to obliquity in this interval, suggesting that precession exerted an additional control on glacial cyclicity and sea level in the interval between TG12 and TG5, i.e., the time that the UE were formed according to our preferred precession scenario. However, the precession control may also stem from precession-induced changes in regional climate. Such changes are also held responsible for the formation of gypsum cycles in the LE, i.e., between 5.96 and 5.59 Ma when obliquity-induced glacial cycles and associated sea level changes were operative as well [Krijgsman et al., 1999a].

Finally, it is remarkable that the Upper Evaporites according to the preferred precession scenario correspond exactly with the interval marked by peak magnetic susceptibility values in the Loulja-A section and the Salé drill core (Fig. 4.12). In addition, this peak interval corresponds to the 400-kyr eccentricity maximum around 5.45 Ma. The latter might explain our peak interval because magnetic susceptibility maxima are reached in reddish layers (Fig. 4.2) and the most prominent reddish layers are associated with enhanced precession amplitudes related to maximum eccentricity. Such an explanation does hold for the elemental data of PC-1, which clearly mimic the eccentricity modulation of the precession amplitude (see paragraph 4.7.1 and Fig. 4.5). However, in contrast to PC-1, magnetic susceptibility values remain low in sections Loulja-A and Loulja-B, i.e., during the next 400-kyr eccentricity maximum. Furthermore it does not explain why the marked decrease in magnetic susceptibility (Fig. 4.2) does not follow the precession/eccentricity pattern but coincides with the Miocene-Pliocene boundary and thus with the top of the Upper Evaporites and the Pliocene flooding of the Mediterranean. At present, a sound explanation for this apparent linkage between the magnetic susceptibility peak interval and the Upper Evaporites is lacking.

4.8.5 Deglaciation interval

Also the biostratigraphic record of *Globorotalia miotumida*/*Globorotalia menardii* has some bearing on (the termination of) the late Messinian interval marked by the occurrence of distinct glacials. The warm-water species *G. menardii* and *Neogloboquadrina humerosa* represent subtropical faunal elements, which occur together with species typical of the eastern boundary current fauna association. Remarkably enough, the short interval with *G. menardii* corresponds exactly with the major shift in $\delta^{18}\text{O}$ to lighter values between oxygen isotope stages TG12 and TG11 that marks the end of the characteristic interval with prominent obliquity-controlled glacial cycles of the late Messinian. The short distribution range of this warm water species is consistent with the deglaciation step inferred from the isotope data. This deglaciation step coincides with the increase in eccentricity following the distinct eccentricity minimum around 5.6 Ma. Stage TG10 corresponds with the next (100 kyr) eccentricity minimum around 5.48 Ma and the (second) deglaciation step from TG10 to TG9 with the subsequent increase in eccentricity just prior to 5.45 Ma. This coincidence suggests that eccentricity may have played a role in terminating the series of prominent glacial cycles in the late Messinian.

4.8.6 Glacial cycles and regional climate oscillations

At Loulja-A the PC-1 and sedimentary cycle records show a dominant precession-related signal, which suggests a regional low-latitude climate origin for these variations [Van der Laan et al., 2005]. The 23-kyr component in $\delta^{13}\text{C}$ is rather weak and is only present in intervals when enhanced precession amplitudes are reached at times of eccentricity maxima. This 23-kyr signal is essentially in phase with precession, with minima in $\delta^{13}\text{C}$ corresponding to maxima in precession (see also Fig. 4.8). The 23-kyr signal in $\delta^{13}\text{C}$ may be explained by enhanced surface water productivity, but a planktonic isotope record is needed to support this interpretation. The enhanced productivity might be a consequence of better vertical mixing of the water column due to colder and hence denser surface waters during summer at times of precession maxima. In addition, precession-induced changes in wind-stress and hence upwelling may have played a role. Alternatively, it may signal variations in the storage of carbon between the terrestrial and marine domain on precession time scales, although obliquity- and eccentricity-related variations in $\delta^{13}\text{C}$ seem to be more important here.

Cross-spectral analysis in addition revealed a weak 41-kyr component in PC-1 that is significantly coherent and essentially in phase with obliquity. This obliquity signal, which was also observed in the older Oued Akrech section [F.J. Hilgen, unpublished data, 2000], most likely reflects a direct response of regional climate to obliquity as suggested by Mediterranean sapropel patterns [Hilgen et al., 2000]. Contrary to expectation, no significant lag is observed between the obliquity component in $\delta^{18}\text{O}$ and PC-1, despite the fact that the 41-kyr component in $\delta^{18}\text{O}$ is much stronger than in PC-1 and supposedly reflects glacial cyclicity in addition to regional climate change. Consequently, no distinction can be made between an early response group and a (glacial controlled) late response group reflecting ice volume and related ice sheet response [compare Imbrie et al., 1992]. Similarly, the identical and in-phase relation between the 23-kyr components in PC-1, $\delta^{18}\text{O}$, and precession does not rule out a precession-induced ice volume signal in $\delta^{18}\text{O}$. The latter is actually suggested by the precession signal found in benthic $\delta^{18}\text{O}$ records from the open ocean (Fig. 4.11c).

Although a separate 41-kyr peak is lacking in the $\delta^{13}\text{C}$ spectrum, an inverse covariance with $\delta^{18}\text{O}$ is clearly recognized in the interval older than ~5.3 Ma. This inverse correlation is confirmed by the in-phase relationship between the 41-kyr $\delta^{13}\text{C}$ filter and obliquity up to at least 5.22 Ma

(see Fig. 4.7). It is furthermore interpreted as to mainly reflect glacial-interglacial cycles: during glacials (enriched $\delta^{18}\text{O}$ values), overall lighter $\delta^{13}\text{C}$ values are recorded in the marine realm due to increased storage of ^{13}C -depleted terrestrial-derived carbon in oceanic reservoirs [Shackleton, 1977; Ruddiman, 2001]. Alternatively, enhanced productivity linked to a strengthening in wind regimes inferred for glacial periods, causing better vertical mixing through the water column, could have caused the lighter $\delta^{13}\text{C}$ values. However, after TG9 (~5.45 Ma), obliquity-induced changes in $\delta^{13}\text{C}$ become less distinct and longer-term variations with a period of ~100 kyr start to dominate. The ~100-kyr band-pass filter reveals an in-phase relationship with short-term eccentricity whereby $\delta^{13}\text{C}$ minima coincide with eccentricity maxima (see Fig. 4.8). Only the interval of relatively depleted $\delta^{13}\text{C}$ values between 5.23 and 5.18 Ma causes the ~100-kyr $\delta^{13}\text{C}$ filter to slightly run out of phase with eccentricity.

4.9 Conclusions

The Loulja-A section contains a well-tuned, continuous open marine succession straddling the M-P boundary in the Bou Regreg area that can be correlated cyclostratigraphically in detail to the Mediterranean. In addition, the section provides a detailed history of glacial cyclicity through its high-resolution and high-quality benthic oxygen isotope record.

The M-P boundary does not coincide with a major deglaciation as previously assumed but with the beginning of a relatively minor shift to lighter values in $\delta^{18}\text{O}$. This shift does not coincide with marine isotope stage TG5 but actually corresponds to an extra (weak) obliquity-controlled cycle in between TG7 and TG5. On the other hand, the onset of the Upper Evaporites in the Mediterranean marked by hyposaline conditions coincides with the major deglaciation step between TG12 and TG11, suggesting that the associated sea level rise might at least be partly responsible for the onset of possibly (marginally) marine conditions following the main desiccation phase.

The section is perfectly suitable to act as auxiliary-boundary stratotype for the M-P boundary as formally defined at the base of the deep marine Trubi marls in the Eraclea Minoa section on Sicily, i.e., at the level that marks the definitive opening of the Atlantic-Mediterranean connection and the basal Pliocene flooding of the Mediterranean following the Messinian salinity crisis.

Acknowledgements

Nadia Barhoun from Université Hassan II Mohammedia, Casablanca, and Helmut Willems and Katarzyna Bison from Bremen University are kindly thanked for discussions and their invaluable assistance in the field. Mohamed Dahmani and Mohamed Haddane of the Geology Division of the Ministry of Energy and Mines at Rabat are kindly acknowledged for their cooperation and permission to carry out the fieldwork in Morocco. The manuscript benefited from Cor Langereis' critical review of the paleomagnetic part. We are grateful to David Hodell and an anonymous reviewer for their valuable comments and suggestions, which greatly improved an earlier version of the manuscript. Geert Ittmann and Gerrit van 't Veld are thanked for washing the samples, Arnold van Dijk for the isotope analyses, and Helen de Waard for the ICP-OES measurements. Douwe van Hinsbergen generously provided the paleobathymetric data.

This work was conducted under the programme of the Netherlands Research School of Sedimentary Geology (NSG) and the Vening Meinesz Research School of Geodynamics

(VMSG). The Netherlands Research Centre for Integrated Solid Earth Science (ISES) provided funds for sampling campaigns.

Astronomical forcing of Northwest African climate and glacial history during the late Messinian (6.5-5.5 Ma)

with F.J. Hilgen¹, L.J. Lourens¹, E. de Kaenel², S. Gaboardi³ and S. Iaccarino³

¹*Dept. of Earth Sciences, Utrecht University, Budapestlaan 4, Utrecht, The Netherlands*

²*DPR, Matile 51, CH-2000 Neuchâtel, Switzerland*

³*Dept. of Earth Sciences, Univ. of Parma, Nuovo Campus Universitario, Parma, Italy*

This chapter has been submitted to *Palaeogeography, Palaeoclimatology, Palaeoecology* as: Van der Laan, E., F.J. Hilgen, L.J. Lourens, E. de Kaenel, S. Gaboardi and S. Iaccarino. Astronomical forcing of Northwest African climate and glacial history during the late Messinian (6.5-5.5 Ma).

Abstract

High-resolution physical, chemical and biological-based climate proxies from the Ain el Beida (AEB) section in Atlantic Morocco reveal the imprint of the three main orbital parameters precession (19-23 kyr), obliquity (41 kyr) and eccentricity (95-125 and 400 kyr) between 6.5 to 5.5 million years before present (Ma). The precession-related variations are most prominently reflected in the colour reflectance and chemical composition of the sediment, showing that precession minimum configurations lead to more humid climate conditions in Northwest Africa probably related to the Atlantic system, while more arid climate conditions prevailed during precession maxima. In addition, precession-bound changes in planktonic foraminifera and calcareous nannofossils assemblages indicate that sea surface temperature (SST) increased during the humid phases, while productivity conditions increased during the dry periods. The clear imprint of the short and long-term eccentricity cycles is explained by a non-linear climatic response to the precession forcing with overall more humid climate conditions during eccentricity maxima. The obliquity-controlled variations in SST and aridity conditions concur with glacial-interglacial variability that is conspicuously recorded in both planktonic and benthic $\delta^{18}\text{O}$ records of AEB. The observed warm and wet climates during interglacial periods most likely reflect the direct ice driven thermal response to the reduced ice sheets and more active Atlantic depressions. Similar as during the Pliocene and Pleistocene, obliquity-controlled variations in the planktonic and benthic carbon isotope ($\delta^{13}\text{C}$) records of AEB are inversely related to the oxygen isotope records with more depleted values during glacial stages, although with a small lag. The close correspondence between the $\delta^{13}\text{C}$ records of AEB and other open ocean sites (i.e., Site 982 and 926) may therefore point to large-scale glacial-controlled variations in the deep-sea carbon reservoir. Superimposed on the orbital variations, the imprint of the – onset of the – Messinian Salinity Crisis can be traced by a marked $\sim 1.0\text{‰}$ negative excursion in planktonic $\delta^{13}\text{C}$ at 6.0 Ma, followed by a prominent peak in Ti/Al at ~ 5.97 Ma.

5.1 Introduction

The region of Northwest Africa, including the Sahelian, Saharan and Mediterranean belts, is characterized by a strong interplay between low-latitude and high-latitude climate oscillations. Today, the region is mainly influenced by the monsoon system in the south and the Atlantic system in the north. From the late Pliocene to the recent, dust flux records indicate that the precipitation regime in Northwest Africa was strongly influenced by dominantly obliquity-controlled glacial cycles as well as a strong 100-kyr cycle during the last 800 ka [Bloemendal and deMenocal, 1989; Tiedemann et al., 1994; Ruddiman et al., 1989; deMenocal, 1995], which occurred superimposed

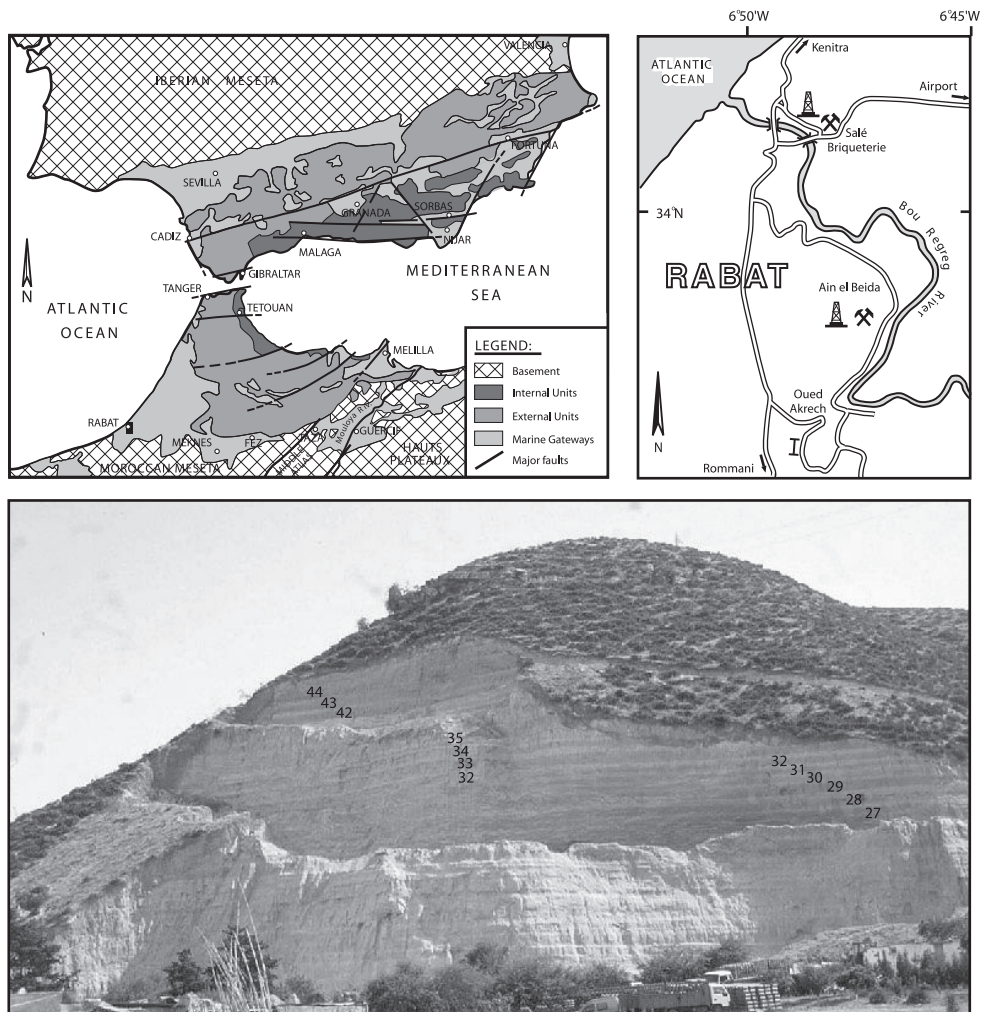


Figure 5.1 Geographical configuration of northern Morocco and southern Spain during the Miocene (upper left). Overview of the Bou Regreg area in northwestern Morocco and the location of Ain el Beida within the mouth of the former Rifian Corridor (upper right, after Benson et al., 1991). The Ain el Beida section with assigned lithological cycle numbers (bottom).

on precession induced regional changes in climate. Although less significant, this imprint of precession has also been found in the terrestrial element composition of deep-sea (piston) cores off Northwest Africa (30°N) for the last 250 ka [Moreno et al., 2001]. Evidently, maximum values in the precession-related components of the dust indicators Al and Fe/Al occur during precession minimum configurations, and lead thereby ice volume changes by ~3 kyr.

Prior to the onset of major Northern Hemisphere glaciations around 2.8 Ma, long paleoclimatic records off West Africa at ~20°N express a distinct precession signature with a relatively minor contribution of obliquity [Ruddiman et al., 1989; Tiedemann et al., 1994]. This cyclicity has been attributed to a direct response of the African monsoon to low-latitude insolation forcing. In contrast to the late Pleistocene, the off-shore West African sediments reveal an increased dust flux (i.e., carbonate depletions) during precession maxima (and obliquity minima). It has been argued that the increased dust flux during these periods is caused by more arid climate conditions at times that the monsoon circulation was reduced, whereas periods of enhanced (monsoon) rainfall during precession minima (and obliquity maxima) lead to an increased vegetation cover and a reduced dust flux (i.e., carbonate enriched sediments).

Sonic and gamma-ray cycles reflected in boreholes from the Gulf of Cadiz [Sierro et al., 2000] and sedimentary (e.g., sapropels) successions in the Mediterranean [Hilgen, 1991b] showed that, during the early Pliocene warm period, the precession cycle also dominated the regions immediately north of Northwest Africa. Similar to the West African region, it has been inferred that periods of maximum rainfall and runoff in southern Spain and the Mediterranean occur at times of precession minima [Sierro et al., 2000; Van Os et al., 1994; Foucault and Mélières, 2000; Schenau et al., 1999]. It was argued, however, that the sedimentary cycles in the Gulf of Cadiz are related to variations in annual precipitation coupled to the Atlantic system, and not to the monsoon. Enhanced winter precipitation in the northern borderlands of the eastern Mediterranean may also have set the stage for sapropel formation [Rohling and Hilgen, 1991], but still the most widely accepted theory is that increased African monsoon intensities reduced the Mediterranean anti-estuarine circulation and caused sapropel formation due to an increased Nile outflow [Rossignol-Strick, 1987].

At present, not much is known about the climate response to orbital forcing of Northwest Africa during the latest Miocene time period (i.e., Messinian) when vast amounts of evaporites were deposited in the Mediterranean during the so-called Messinian salinity crisis (MSC) [Hsü et al., 1973; Ryan et al., 1973]. At that time, the connection between the Mediterranean and the Atlantic Ocean was restricted and probably even interrupted at times, resulting in a significant lowering of sea level in the Mediterranean due to evaporitic drawdown. It can thus be questioned whether the early Pliocene orbital phase relations remained stable or underwent significant changes as a consequence of the changing boundary conditions [see Clemens et al., 1996]. In addition, this time period is marked by punctuated obliquity-controlled glacial cycles [Hodell et al., 1994, 2001; Shackleton et al., 1995b; Vidal et al., 2002, among others], which are clearly reflected in the oxygen isotope records of the marine successions at Ain el Beida and Loulja located in the Bou Regreg area on the Atlantic side of Morocco [Van der Laan et al., 2005, 2006]. By contrast, the sedimentary colour alternations of these successions are dominated by the precession cycle; most likely indicating aridity variations. Here, we will elaborate on the astronomical phase behavior of Northwest African climates during the latest Miocene by applying a multi-proxy approach, including physical, chemical and biological parameters of the Ain el Beida section. The main goal of this study is to discriminate between the role of regional climate changes versus glacial variability and the impact of the MSC. For this purpose we will apply cross-spectral analysis to determine phase relations with the orbital parameters.

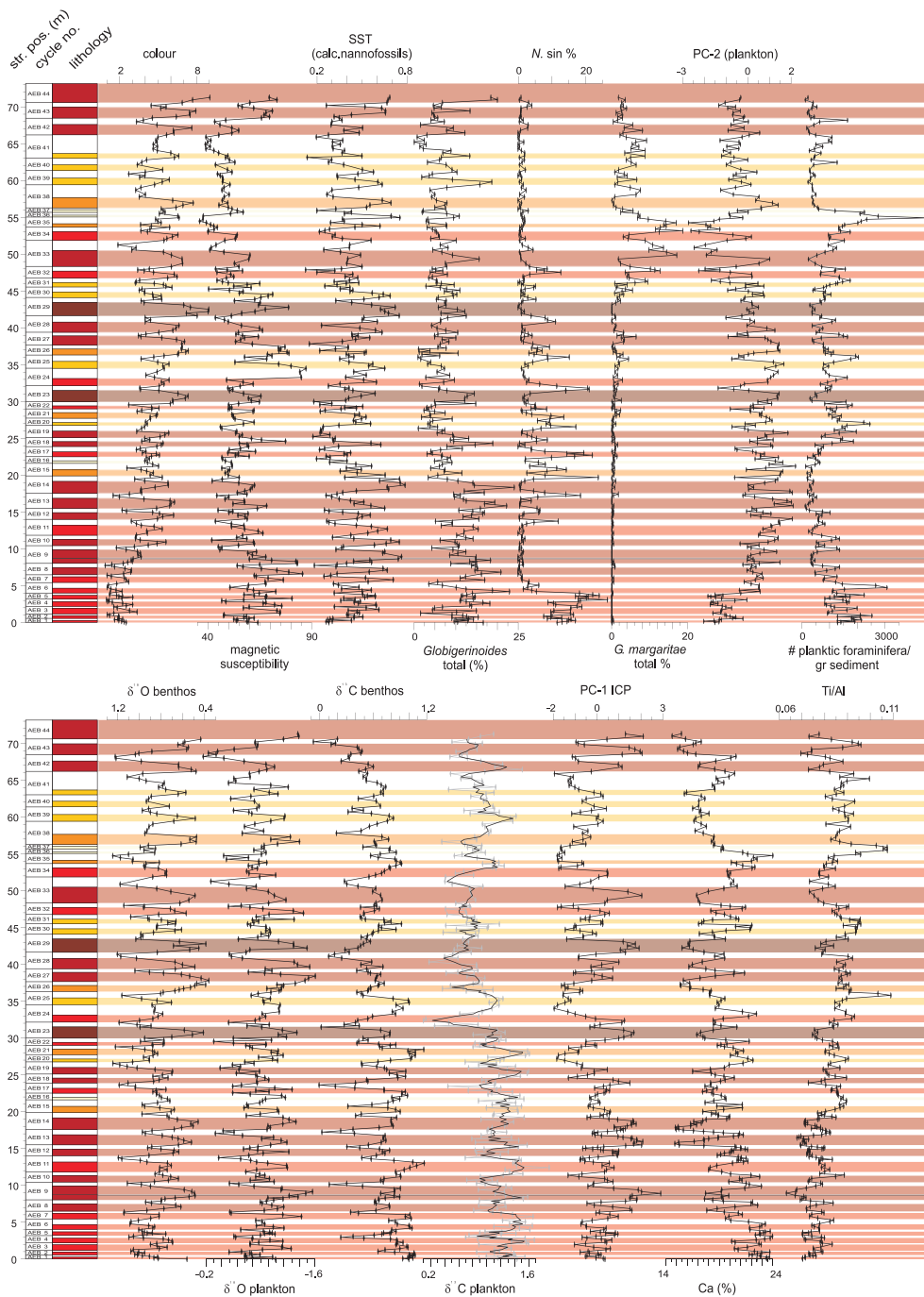


Figure 5.2 Overview of studied proxy records in the AEB section versus depth. Stratigraphic position, cycle number and lithology type are indicated on left-hand side.

5.2 Section and setting

The Ain el Beida (AEB) section is located in the Bou Regreg area in Northwest Morocco, in a brick-quarry a few km southeast of Rabat-Salé (Fig. 5.1). The section contains relatively deep marine sediments that belong to the Blue Marl formation. These homogeneous marly sediments have a grey-blue colour when freshly excavated, which gives the formation its informal name. Deposition of the Blue Marl in the Bou Regreg area started in the late Tortonian. The marls were deposited in the Gharb basin, representing the westward extension – and opening to the Atlantic – of the Rifian Corridor. This corridor acted as an extensional foredeep during the late Miocene to early Pliocene, separating the active Rif Orogen and nappe complex in the north from the Central Moroccan Meseta to the south [Benson and Rakic-El Bied, 1996]; it formed one of the two Atlantic-Mediterranean connections during the late Miocene. While the marine gateway was closed in the course of the Messinian, deposition of the Blue Marl in the Gharb Basin continued well into the Pliocene [e.g., Benson and Rakic-El Bied, 1996].

The Blue Marl exposed at AEB belongs to the middle part of the formation. The weathered outcrops are characterized by a regular alternation of yellow-beige and reddish layers (colour cycles). The AEB section contains in total 45 of these dominantly precession controlled colour cycles with varying thickness and distinctness, the reddish layers being softer and the beige layers more indurated (Fig. 5.2). The stratigraphic height of the section is about 75 m.

5.3 Material and methods

5.3.1 Sampling

A total of 297 samples were collected from 44 colour cycles. After removing the weathered surface, 6 to 8 samples were taken from each colour cycle using a water-cooled hand-drill. Unfortunately it was not possible to sample the uppermost steep part of the section. All samples were processed and subjected to physical, chemical and biological analyses to generate various proxy records for paleoclimatic reconstruction.

5.3.2 Physical parameters

Initially a visual distinction in the intensity of the colour of the reddish layers was made in the field. Quantitative colour measurements were subsequently performed on dry samples in the laboratory, using a Minolta CM-508I spectrophotometer. Measurements are automatically converted into reflectance (%) values for 10 nm intervals between 400 and 700 nm. The resultant red-green component (a^* values) is used in the present study because it best reflects the cyclicity as observed in the field.

Magnetic susceptibility is a measure of the strength of the magnetic signal in a sample after it has been subjected to a (weak) magnetic field. It was measured in the laboratory at room temperature on a KLY-2 Kappabridge [Hroudá, 1994].

5.3.3 Biological parameters

For calcareous nannofossil counts, all samples were processed using the settling method reported in De Kaenel and Villa [1996]. This technique provides a uniform dispersion of calcareous nannofossils on each slide that is necessary for quantitative counting. On average, nannofossils were counted on 3 long traverses on a slide and at 630x magnification (612 fields of view). This was

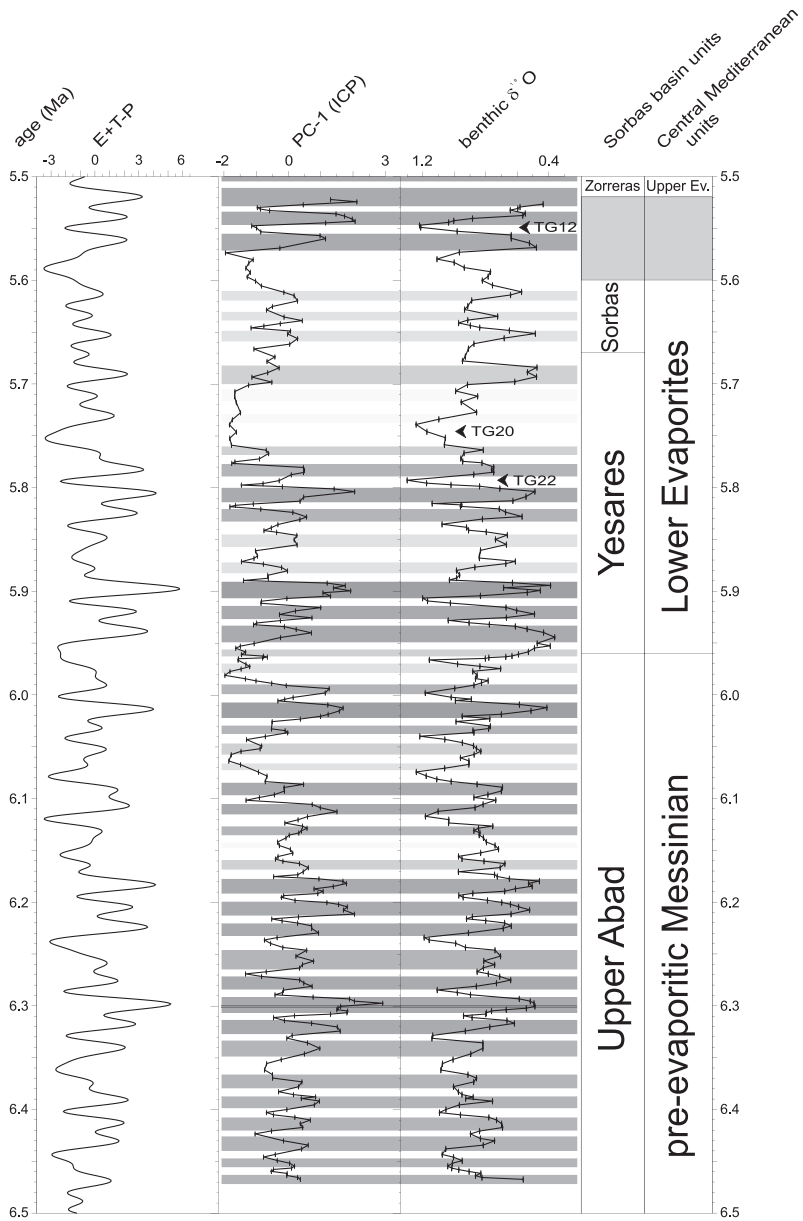


Figure 5.3 Comparison of the PC-1 (ICP) and benthic $\delta^{18}\text{O}$ records of the Ain el Beida section with the combined ETP (eccentricity, obliquity, negative precession) curve of La2004_(1,1) [Laskar et al., 2004]. Peak glacial stages TG22, TG20 and TG12 are indicated.

necessary to obtain a reproducible counting for each slide. The abundance in number of specimens is expressed relative to unit area of the slide (specimens per mm²). This methodology has the advantage to express the absolute abundance of species and to take rare species into account; some rare species have a more significant ecological signal than more abundant species.

Based on designation of temperature-sensitive (see Appendix 1) species, a Sea Surface Temperature (SST) record is calculated as the ratio of warm water indicators versus the sum of warm and cool water indicators. From the beginning it was evident that many different species had to be counted with high accuracy to obtain a SST curve that reveals small temperature variations. Of a total of 209 recorded taxa, 87 were quantitatively counted to determine their dependence on lithology, i.e. whether they are associated with the reddish layers (and thus with summer insolation maxima) or the beige layers (and hence insolation minima). Only species that are well observable in phase contrast and not too common were counted. Overall, none of the species counted represent more than 14% of the total nannofossil assemblage used to calculate the SST values. Using this procedure, it is avoided that the ecological signal depends on or is diluted by the abundance of one or two species only.

Counting of planktonic foraminifera was performed on the species level, whereby at least 200 individuals were picked from each sample and mounted on Chapman slides. In this study we focused on the abundance variations in the *Globigerinoides* group, sinistrally-coiled *Neogloboquadrina* (*N. sin*) and *Globorotalia margaritae* (*G. margaritae primitiva* and *G. margaritae margaritae*). The habitat characteristics of these species are listed in Appendix 2. In addition, Principal Component Analysis (PCA, SPSS software) was performed on the total assemblage of planktonic foraminifera. This analysis yielded two significant principal components, the first of which revealed primarily a major long-term trend and will not be discussed here. Only the second component, PC-2 (Plankton), will be discussed, because it shows both a strong precession and obliquity-related cyclicity. Finally, we will use the foraminiferal flux record (number of foraminifera per gram sediment) as a measure for dilution by terrigenous material.

5.3.4 Chemical parameters

Stable isotope measurements were performed on the calcitic tests of the planktonic foraminiferal species *Globigerinoides obliquus* and the benthic foraminiferal species *Planulina ariminensis* and are reported as per mil (‰) relative to the PeeDee belemnite (PDB) standard. For each sample, about 10-15 specimens of *P. ariminensis* were picked as well as about 30-40 specimens of *G. obliquus*. In order to remove any organic remains, each sample was roasted for 30 minutes at 470°C under vacuum. The samples were analyzed using an ISOCARB, which is directly coupled to the mass spectrometer and has the capacity to measure 44 samples, of which 1 international (IAEA-CO-1) and 9 in-house (NAXOS) standards, during a run. Each sample reacted with 103% phosphoric acid (H₃PO₄) for 6 to 7 minutes at 90°C. The analytical precision and accuracy were determined by replicate analyses of samples and by the comparison with the IAEA-CO-1. The relative standard deviations, analytical precision and accuracy were better than 0.1‰.

For geochemical analyses, the samples were dried in a furnace, after which they were crushed, powdered and homogenized in an agate mortar. Approximately 125 mg of each sample was dissolved in 2.5 ml HF (40%) and 2.5 ml of a two-acid mixture of HNO₃ (16.25%) and HClO₄ (45.5%) and heated at 90°C in closed teflon bombs for a minimum of 8 hours. The solutions were subsequently evaporated (in open bombs) at a temperature of 160°C, after which 25 ml HNO₃ (4.5%) was added to each residue. The resulting solutions were analyzed using a Perkin Elmer Optima 3000 ICP-OES apparatus for the elements Al, Ba, Ca, Co, Cr, Cu, Fe, K, Li, Mg, Mn,

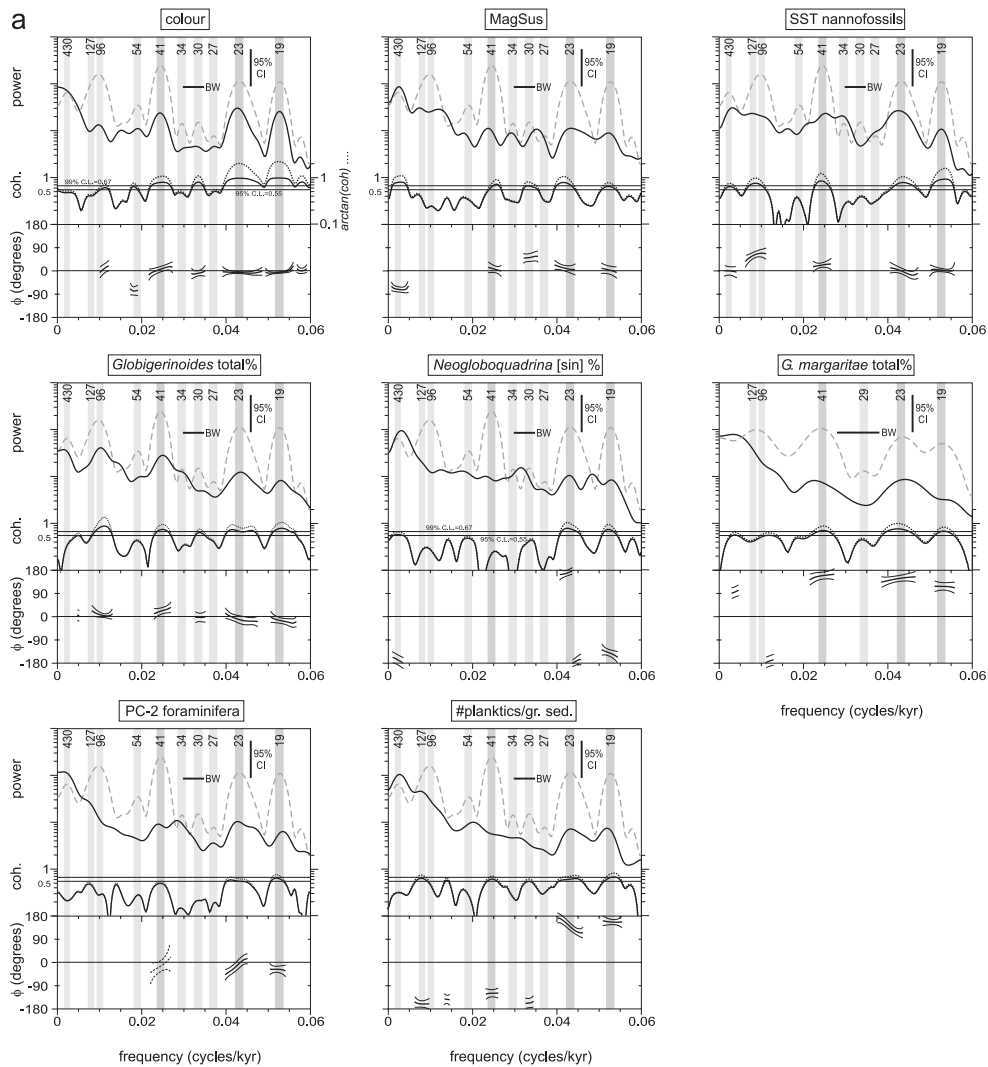
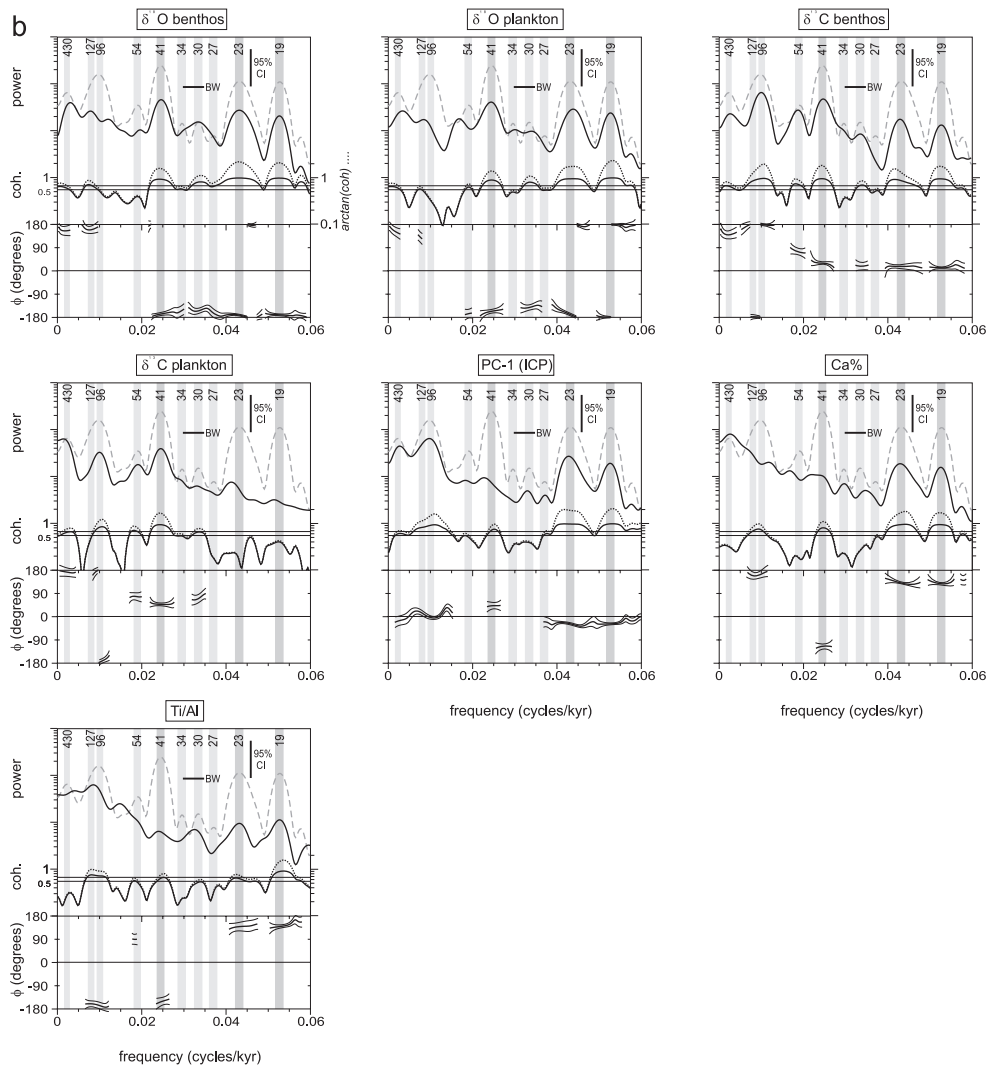


Figure 5.4 Cross-spectral results for studied physical and biological (a) and geochemical (b) (next page) proxies of the AEB section. Each proxy was subjected to cross-spectral analysis against ETP based on solution La2004_(1,1). Each panel shows the normalized variance density spectrum (top), coherency (middle) spectrum and the phase of the time series with respect to ETP (bottom). Dashed line in upper part of each panel represents the ETP spectrum. Bandwidth (BW, horizontal bar) is 0.0053 for the total record and 0.0097 and 0.0105 for the pre-MSC and MSC parts of the record, respectively. The 95% confidence interval (CI) is marked by the vertical bar. The 99% and 95% confidence levels (0.67 and 0.55, respectively) of non-zero coherency are marked by the two horizontal lines in the coherency spectrum. The uncertainty in the phase is indicated by upper and lower phase limits. Phase is only shown for coherences above 95% significance level.



Na, Ni, P, S, Sc, Sr, Ti, V, Y and Zn. The relative error in duplicate measurements of international standards was lower than 3% for all elements.

The total assemblage of elements that were measured using ICP-OES was subjected to a standardized Principal Component Analysis (PCA, SPSS software) to simplify the data matrix by combining samples similar in element composition into a small number of independent variables/components.

5.4 Age model and time series analysis

An accurate and high-resolution astronomical age model was recently developed for the AEB section [Krijgsman et al., 2004] of which details can be found in **Chapter 2**. Here we will present

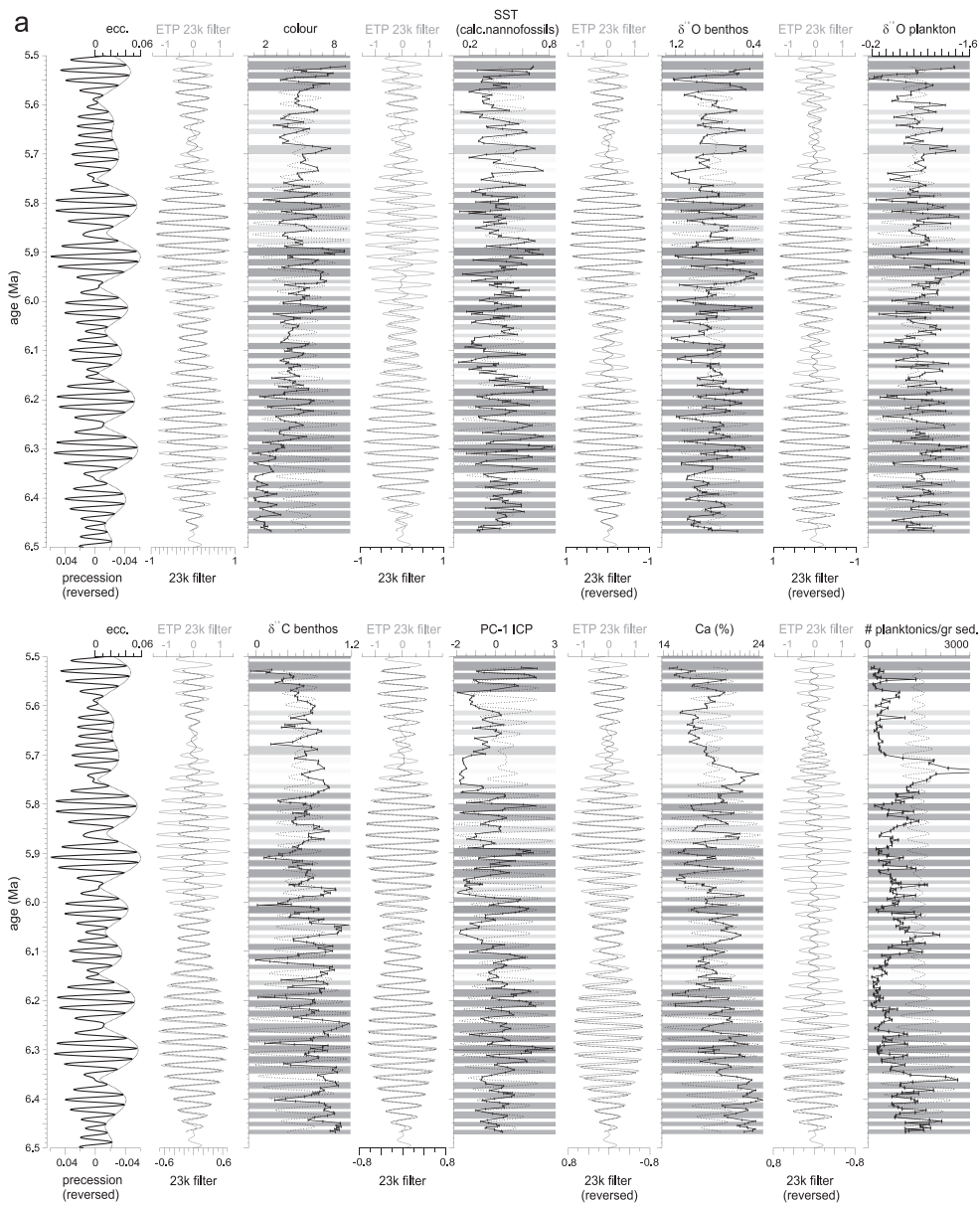
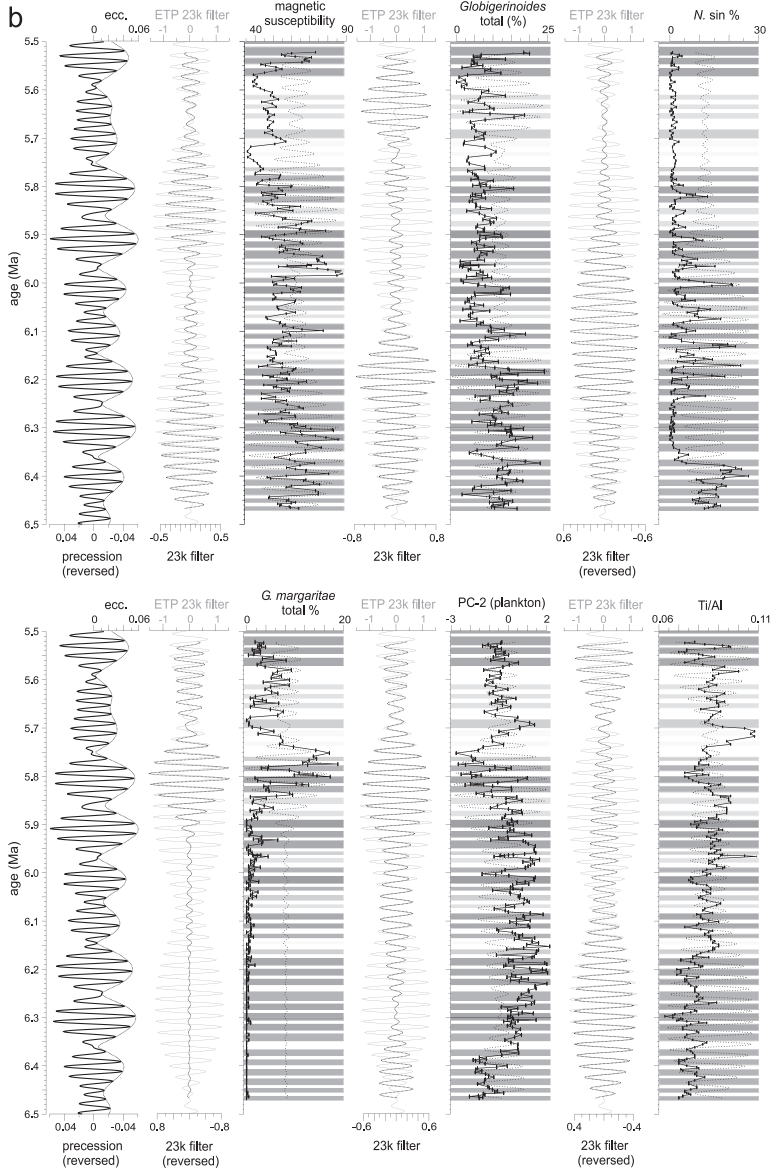


Figure 5.5 (a) and (b) (next page) Comparison of 23-kyr filtered components in the studied proxies and the 23-kyr filtered ETP component (reflecting 23 kyr precession). The 23-kyr components were extracted using a Gaussian band-pass filter with central frequencies of 0.0425-0.044 cycles/kyr and a bandwidth of 0.007-0.012 cycles/kyr. The filtered components are shown as dotted overlays on the original data (black) and extracted ETP component (gray).



a brief summary. First-order age control is based on the position of three magnetic reversal boundaries (top C3An.2n, bottom and top C3An.1n) and a single bioevent [PF-4 of Sierro et al., 1993]. In Chapter 2, the colour cycles have been tuned to the 65°N summer insolation curve of the La93_(1,1) astronomical solution [Laskar et al., 1993] [see also Krijgsman et al., 2004]. Here we will make use of the latest astronomical solution La2004_(1,1) [Laskar et al., 2004] resulting in only slightly different (~1 kyr) ages for the control points. The midpoints of the reddish and beige layers were used as calibration points, whereby reddish layers are correlated to insolation maxima and beige layers to insolation minima. The thickest and most pronounced reddish layers have been

Table 5.1 Cross-spectral results in terms of coherency and phase between orbital components in individual proxy records and the respective orbital component in the ETP record for solution La2004_(1,1). Results are shown for the 100, 41, 23 and 19 kyr components, and for the entire record as well as for the pre-MSC and MSC time slices. Coherency (k) is considered significant when exceeding a 95% confidence level (0.55). Phase (ϕ) is given in degrees

period (kyr)	proxy	k	ϕ (°)	low.	up.	limit \pm	ϕ (kyr)	limit \pm
maximum eccentricity (~100 kyr)								
Total record								
88	colour	0,61	13	-5	31	18	3,2	4,3
99	MS	0,25	46	-9	101	55	12,7	15,3
118	SST (nanno)	0,75	64	52	76	12	20,9	3,9
90	Globig'des%	0,88	4	-3	12	7	1,1	1,8
111	N.sin%	0,30	68	23	112	44	20,8	13,6
135	PC-2 plankton	0,52	-91	-114	-69	22	-34,2	8,3
126	#planktics/gr sed	0,74	-162	-174	-149	12	6,4	4,4
134	$\delta^{18}\text{O}$ benthos	0,70	-22	145	172	14	-8,1	5,1
135	$\delta^{18}\text{O}$ plankton	0,57	-47	114	153	20	-17,5	7,4
94	$\delta^{13}\text{C}$ benthos	0,96	178	174	182	4	-0,5	1,0
94	$\delta^{13}\text{C}$ plankton	0,84	-172	-181	-163	9	2,1	2,3
92	PC-1	0,92	-5	-11	1	6	-1,3	1,5
108	Ca	0,75	161	149	173	12	-5,7	3,5
126	Ti/Al	0,77	-160	-172	-149	11	6,9	4,0
during MSC								
100	colour	0,55	-30	-51	-10	21	-8,4	5,7
95	MS	0,38	61	28	94	33	16,1	8,7
100	SST (nanno)	0,60	47	29	65	18	13,0	5,0
112	Globig'des%	0,62	33	16	51	17	10,4	5,3
*	N.sin%	*	*	*	*	*	*	*
112	G.margaritae%	0,46	165	138	191	27	-4,7	8,2
111	PC-2 plankton	0,42	-67	-97	-38	29	-20,7	9,1
106	#planktics/gr sed	0,59	-140	-158	-121	19	11,8	5,4
125	$\delta^{18}\text{O}$ benthos	0,59	-46	115	152	19	-16,1	6,5
136	$\delta^{18}\text{O}$ plankton	0,63	-57	106	140	17	-21,5	6,3
104	$\delta^{13}\text{C}$ benthos	0,91	177	171	183	6	-0,9	1,8
90	$\delta^{13}\text{C}$ plankton	0,69	175	161	189	14	-1,2	3,6
100	PC-1	0,89	9	2	16	7	2,5	1,9
106	Ca	0,63	178	162	195	17	-0,6	4,9
112	Ti/Al	0,65	-145	-161	-129	16	10,8	4,9
before MSC								
85	colour	0,38	-8	-41	26	34	-1,8	8,0
93	MS	0,38	-42	-76	-9	34	-10,9	8,7
121	SST (nanno)	0,70	70	57	84	14	23,6	4,6
90	Globig'des%	0,83	7	-2	16	9	1,8	2,3
103	N.sin%	0,29	73	27	119	46	20,8	13,1
103	PC-2 plankton	0,65	-165	-181	-149	16	-47,3	4,6
90	#planktics/gr sed	0,70	159	145	173	14	-5,2	3,4
103	$\delta^{18}\text{O}$ benthos	0,72	14	-179	-153	13	4,1	3,7
103	$\delta^{18}\text{O}$ plankton	0,11	177	-183	177	180	50,9	51,7
89	$\delta^{13}\text{C}$ benthos	0,94	-3	172	182	5	-0,8	1,3
94	$\delta^{13}\text{C}$ plankton	0,71	-174	-188	-161	14	1,5	3,5
85	PC-1	0,87	-4	-11	4	8	-0,9	1,8
98	Ca	0,65	143	127	159	16	-10,1	4,3
89	Ti/Al	0,88	-179	-186	-171	7	0,4	1,8

(°) and kyr and accompanied by a lower (low.) and upper (up.) confidence limit. A positive phase denotes a lag, a negative phase a lead with respect to the orbital forcing parameter. For the phase of both $\delta^{18}\text{O}$ records, 180° was added to change $\delta^{18}\text{O}$ in $-\delta^{18}\text{O}$ consistent with the phase relation for $-\delta^{18}\text{O}$ with maximum ETP forcing.

period (kyr)	proxy	k	\emptyset (°)	low.	up.	limit \pm	\emptyset (kyr)	limit \pm
maximum obliquity (41 kyr)								
Total record								
40,1	colour	0,79	10	-1	20	10	1,1	1,2
39,3	MS	0,73	5	-8	18	13	0,6	1,4
41,4	SST (nanno)	0,85	23	14	31	9	2,6	1,0
40,1	Globig'des%	0,74	24	12	36	12	2,7	1,4
39,7	N.sin%	0,25	-173	-227	-118	55	0,8	6,1
41,0	PC-2 plankton	0,54	-15	-36	7	21	-1,7	2,4
40,5	#planktics/gr sed	0,70	-120	-134	-106	14	6,8	1,6
41,3	$\delta^{18}\text{O}$ benthos	0,92	12	-174	-163	6	1,3	0,7
41,0	$\delta^{18}\text{O}$ plankton	0,88	23	-165	-150	7	2,6	0,8
41,3	$\delta^{13}\text{C}$ benthos	0,95	30	26	35	4	3,5	0,5
41,0	$\delta^{13}\text{C}$ plankton	0,93	47	42	53	5	5,4	0,6
39,7	PC-1	0,74	42	30	54	12	4,6	1,4
40,5	Ca	0,80	-115	-125	-105	10	7,3	1,1
39,7	Ti/Al	0,70	-150	-164	-136	14	3,3	1,5
during MSC								
39,6	colour	0,85	-8	-16	1	8	-0,8	0,9
41,3	MS	0,25	73	19	127	54	8,3	6,2
42,2	SST (nanno)	0,61	34	16	52	18	4,0	2,1
43,2	Globig'des%	0,71	11	-2	25	14	1,4	1,6
*	N.sin%	*	*	*	*	*	*	*
40,4	G.margaritae%	0,71	160	146	173	14	-2,3	1,5
42,2	PC-2 plankton	0,81	-7	-17	3	10	-0,9	1,2
40,4	#planktics/gr sed	0,42	-180	-210	-150	30	0,0	3,4
40,9	$\delta^{18}\text{O}$ benthos	0,79	3	-187	-166	11	0,4	1,2
43,2	$\delta^{18}\text{O}$ plankton	0,69	14	-180	-151	14	1,7	1,7
40,9	$\delta^{13}\text{C}$ benthos	0,83	29	20	38	9	3,3	1,0
41,1	$\delta^{13}\text{C}$ plankton	0,78	58	47	68	11	6,6	1,2
38,8	PC-1	0,66	12	-4	27	16	1,2	1,7
38,0	Ca	0,51	-111	-134	-88	23	7,3	2,5
41,3	Ti/Al	0,63	164	147	181	17	-1,9	1,9
before MSC								
41,8	colour	0,80	40	30	50	10	4,6	1,2
38,7	MS	0,88	0	-7	7	7	0,0	0,8
40,2	SST (nanno)	0,78	14	3	25	11	1,6	1,2
38,3	Globig'des%	0,62	34	17	51	17	3,6	1,8
41,1	N.sin%	0,22	167	102	231	65	19,0	7,4
40,6	PC-2 plankton	0,20	-18	-87	51	69	-2,0	7,8
40,6	#planktics/gr sed	0,72	-106	-119	-93	13	8,3	1,5
40,6	$\delta^{18}\text{O}$ benthos	0,92	21	-165	-154	6	2,3	0,6
39,8	$\delta^{18}\text{O}$ plankton	0,90	26	-161	-148	7	2,8	0,7
41,8	$\delta^{13}\text{C}$ benthos	0,91	31	25	37	6	3,6	0,7
38,9	$\delta^{13}\text{C}$ plankton	0,87	44	36	51	8	4,7	0,8
41,0	PC-1	0,47	68	42	93	26	7,7	2,9
41,8	Ca	0,71	-120	-133	-106	14	7,0	1,6
41,0	Ti/Al	0,74	-115	-127	-102	12	7,5	1,4

Table 5.1 continued

period (kyr)	proxy	k	Ø (°)	low.	up.	limit ±	Ø (kyr)	limit ±
minimum precession (23 kyr)			Total record					
23,3	colour	0,97	-6	-10	-2	4	-0,4	0,2
24,2	MS	0,79	12	2	23	10	0,8	0,7
23,0	SST (nanno)	0,78	-2	-13	9	11	-0,1	0,7
24,2	Globig'des%	0,74	-1	-13	12	12	-0,1	0,8
23,6	N.sin%	0,78	170	159	181	11	-0,7	0,7
24,3	PC-2 plankton	0,67	-32	-47	-17	15	-2,1	1,0
22,6	#planktics/gr sed	0,73	124	111	136	13	-3,5	0,8
23,2	δ ¹⁸ O benthos	0,98	9	-174	-168	3	0,6	0,2
22,7	δ ¹⁸ O plankton	0,94	4	-180	-171	5	0,3	0,3
24,1	δ ¹³ C benthos	0,92	17	11	23	6	1,1	0,4
23,1	δ ¹³ C plankton	0,15	75	-31	181	106	4,8	6,8
24,0	PC-1	0,96	-23	-27	-19	4	-1,5	0,2
22,6	Ca	0,95	129	124	133	5	-3,2	0,3
23,6	Ti/Al	0,65	138	122	154	16	-2,8	1,0
during MSC								
22,6	colour	0,95	-11	-16	-7	5	-0,7	0,3
22,1	MS	0,78	8	-3	19	11	0,5	0,7
22,1	SST (nanno)	0,75	-56	-68	-44	12	-3,4	0,7
22,9	Globig'des%	0,37	-9	-43	26	34	-0,6	2,2
*	N.sin%	*	*	*	*	*	*	*
23,8	G.margaritae%	0,76	147	136	158	11	-2,2	0,8
24,0	PC-2 plankton	0,88	-13	-20	-6	7	-0,9	0,5
22,9	#planktics/gr sed	0,32	172	131	214	42	-0,5	2,7
23,2	δ ¹⁸ O benthos	0,94	4	-181	-171	5	0,3	0,3
22,4	δ ¹⁸ O plankton	0,86	5	-183	-167	8	0,3	0,5
22,1	δ ¹³ C benthos	0,76	14	2	25	12	0,8	0,7
23,0	δ ¹³ C plankton	0,25	37	-18	91	55	2,3	3,5
23,2	PC-1	0,90	-27	-34	-20	7	-1,7	0,4
22,4	Ca	0,88	145	138	153	7	-2,1	0,5
25,0	Ti/Al	0,58	96	77	115	19	-5,8	1,3
before MSC								
23,0	colour	0,94	0	-5	5	5	0,0	0,3
23,6	MS	0,77	-35	-46	-24	11	-2,3	0,7
23,3	SST (nanno)	0,93	17	12	23	5	1,1	0,3
23,3	Globig'des%	0,91	-6	-12	0	6	-0,4	0,4
23,2	N.sin%	0,76	176	165	188	12	-0,2	0,7
24,9	PC-2 plankton	0,26	-31	-82	21	51	-2,1	3,6
23,3	#planktics/gr sed	0,86	131	122	139	8	-3,2	0,5
22,7	δ ¹⁸ O benthos	0,91	10	-176	-164	6	0,6	0,4
23,5	δ ¹⁸ O plankton	0,90	13	-174	-161	7	0,8	0,4
23,8	δ ¹³ C benthos	0,96	24	20	28	4	1,6	0,3
20,8	δ ¹³ C plankton	0,47	18	-8	44	26	1,0	1,5
22,8	PC-1	0,96	-29	-33	-25	4	-1,8	0,2
23,0	Ca	0,95	120	116	125	5	-3,8	0,3
23,0	Ti/Al	0,84	161	152	169	9	-1,2	0,6

period (kyr)	proxy	k	Ø (°)	low.	up.	limit ±	Ø (kyr)	limit ±
minimum precession (19 kyr)			Total record					
19,0	colour	0,98	-6	-9	-3	3	-0,3	0,2
19,1	MS	0,66	4	-12	19	16	0,2	0,8
18,7	SST (nanno)	0,92	2	-4	8	6	0,1	0,3
18,8	Globig'des%	0,79	-16	-27	-5	11	-0,8	0,6
18,9	N.sin%	0,78	-139	-150	-129	11	2,1	0,6
19,2	PC-2 plankton	0,76	-26	-37	-14	12	-1,4	0,6
18,7	#planktics/gr sed	0,81	156	146	166	10	-1,2	0,5
19,0	δ ¹⁸ O benthos	0,97	9	-174	-167	3	0,5	0,2
18,8	δ ¹⁸ O plankton	0,98	0	177	182	3	0,0	0,1
19,1	δ ¹³ C benthos	0,94	12	7	16	5	0,6	0,3
19,0	δ ¹³ C plankton	0,40	-38	-70	-7	31	-2,0	1,7
18,8	PC-1	0,97	-27	-31	-24	4	-1,4	0,2
19,1	Ca	0,94	130	125	135	5	-2,7	0,3
18,7	Ti/Al	0,92	141	135	146	6	-2,0	0,3
during MSC								
19,0	colour	0,95	-1	-6	4	5	-0,1	0,2
18,8	MS	0,63	-4	-21	13	17	-0,2	0,9
18,4	SST (nanno)	0,78	-14	-25	-3	11	-0,7	0,6
18,8	Globig'des%	0,76	-30	-41	-18	12	-1,5	0,6
*	N.sin%	*	*	*	*	*	*	*
18,8	G.margaritae%	0,69	118	103	132	14	-3,3	0,8
18,8	PC-2 plankton	0,73	-24	-36	-11	13	-1,2	0,7
19,0	#planktics/gr sed	0,66	-165	-181	-150	16	0,8	0,8
18,8	δ ¹⁸ O benthos	0,89	6	-181	-167	7	0,3	0,4
18,8	δ ¹⁸ O plankton	0,96	-4	172	180	4	-0,2	0,2
18,8	δ ¹³ C benthos	0,80	20	10	30	10	1,0	0,5
18,9	δ ¹³ C plankton	0,14	-51	-159	57	108	-2,7	5,7
18,3	PC-1	0,89	-18	-25	-11	7	-0,9	0,4
19,0	Ca	0,87	155	147	162	8	-1,3	0,4
18,4	Ti/Al	0,76	132	120	143	12	-2,5	0,6
before MSC								
19,0	colour	0,94	-11	-16	-6	5	-0,6	0,2
18,3	MS	0,72	-43	-56	-30	13	-2,2	0,7
18,8	SST (nanno)	0,94	8	3	13	5	0,4	0,3
19,0	Globig'des%	0,66	-4	-19	12	15	-0,2	0,8
18,9	N.sin%	0,78	-139	-150	-129	11	2,1	0,6
19,9	PC-2 plankton	0,51	-22	-45	1	23	-1,2	1,3
18,3	#planktics/gr sed	0,84	138	129	147	9	-2,1	0,4
18,8	δ ¹⁸ O benthos	0,96	12	-172	-164	4	0,6	0,2
18,5	δ ¹⁸ O plankton	0,95	3	-182	-173	5	0,2	0,2
18,6	δ ¹³ C benthos	0,94	9	4	14	5	0,5	0,3
19,1	δ ¹³ C plankton	0,24	-24	-82	35	58	-1,3	3,1
19,3	PC-1	0,98	-32	-35	-29	3	-1,7	0,2
18,8	Ca	0,94	118	113	123	5	-3,2	0,3
18,6	Ti/Al	0,92	147	141	153	6	-1,7	0,3

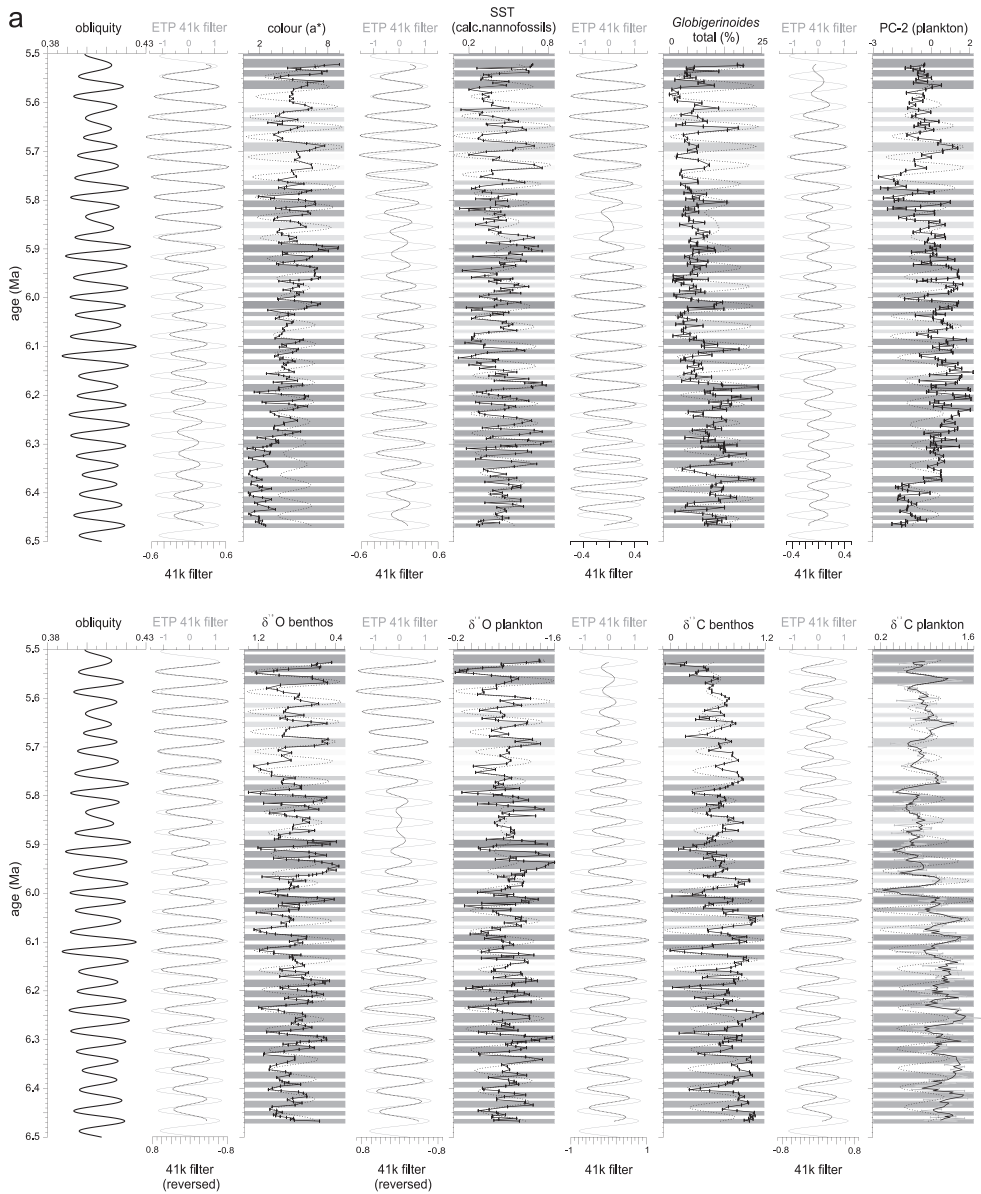
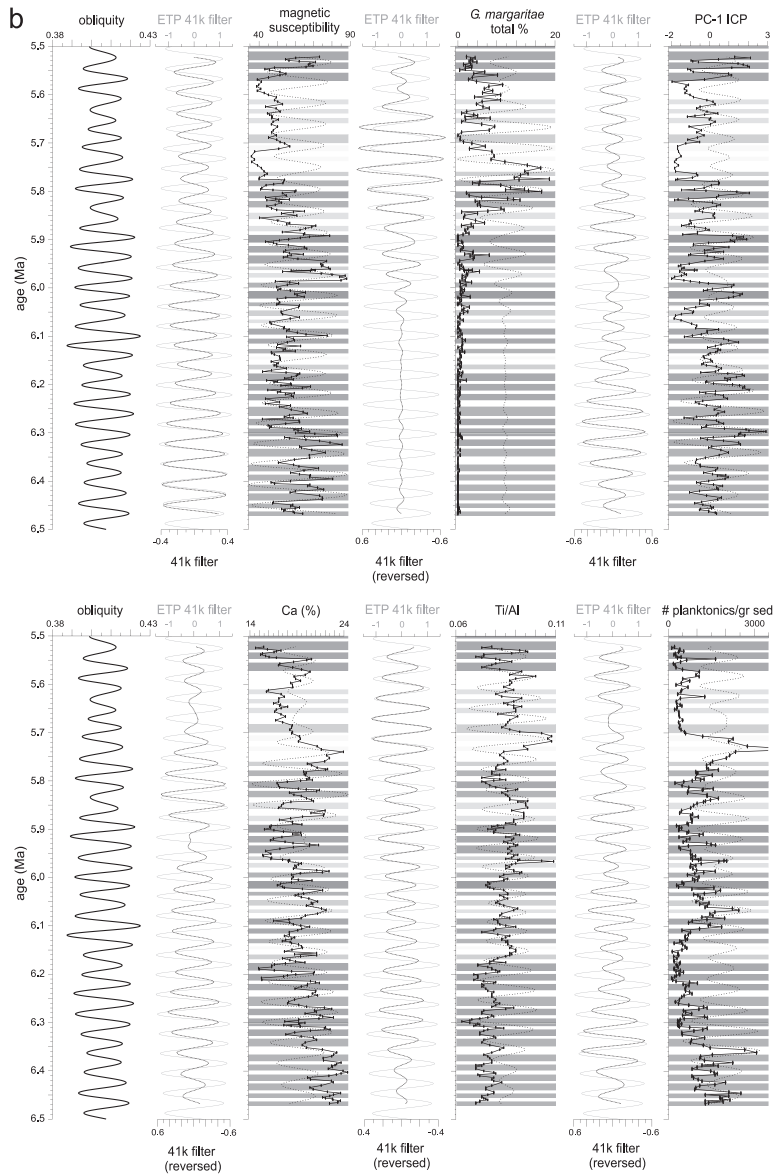


Figure 5.6 (a) and (b) (next page) Comparison of 41-kyr filtered components in the studied proxies and the 41-kyr filtered ETP component (reflecting 41 kyr obliquity). The 41-kyr components were extracted using a Gaussian band-pass filter with central frequencies of 0.0235-0.025 cycles/kyr and a bandwidth of 0.005-0.012 cycles/kyr. The filtered components are shown as dotted overlays on the original data (black) and extracted ETP component (gray).



linked unambiguously to the most extreme summer insolation maxima (precession minima) at times of maximum eccentricity, when precession amplitudes are at maximum [Krijgsman et al, 2004]. The AEB section covers a time span of nearly one million years, ranging in age from 6.47 to 5.52 Ma.

The age model was employed to convert proxy records from the depth domain into the time domain, whereby the age of each sample was obtained by linear interpolation between the age-depth control points. Subsequently, the Analyseries software package [Paillard et al, 1996] was used to apply (cross-) spectral analysis in order to determine statistically significant frequency dependent variability in the proxy time series and to link these variations to the Earth's orbital

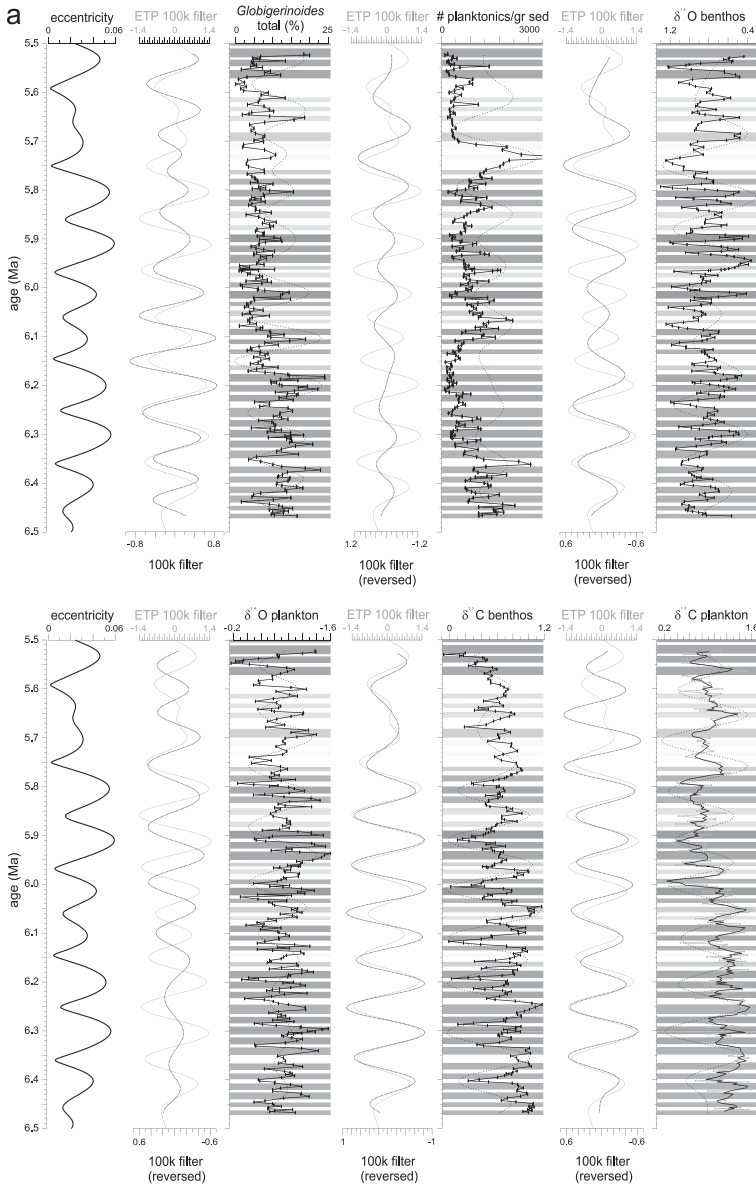
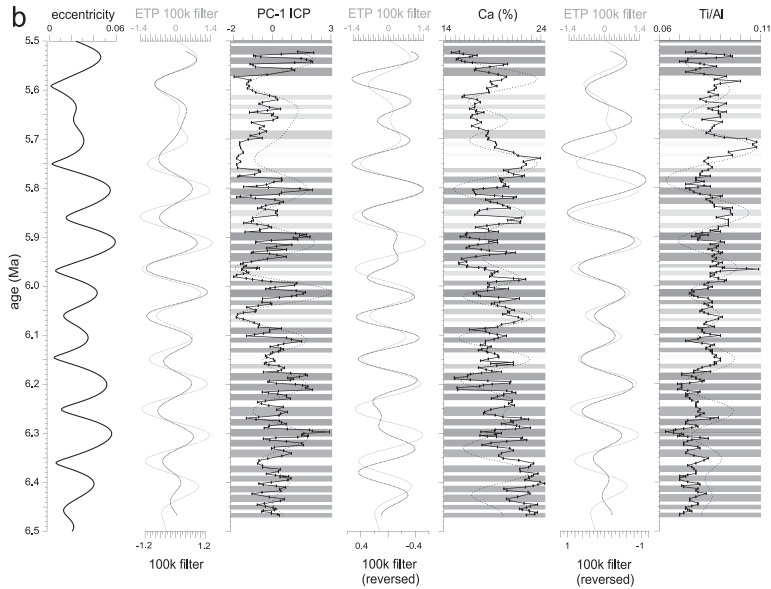


Figure 5.7 (a) and (b) Comparison of ~100-kyr filtered components in the studied proxies and the ~100-kyr filtered ETP component (reflecting short eccentricity). The ~100-kyr components were extracted using a Gaussian band-pass filter with central frequencies of 0.0085-0.011 cycles/kyr and a bandwidth of 0.005-0.009 cycles/kyr. The filtered components are shown as dotted overlays on the original data (black) and extracted ETP component (gray).



cycles in terms of coherency and phase. For this purpose, each proxy time series was first linearly detrended, after which the Blackman-Tukey spectral method was applied using a Bartlett window. Cross-spectral analysis was performed against the ETP record (Fig. 5.3), a combination of normalized Eccentricity, Tilt (obliquity) and Precession multiplied by -1 [Imbrie et al., 1984], because most proxy records exhibit significant variance in all orbital frequency bands. Coherency (k) is a measure of the linear correlation between two time series over a given frequency band when the phase difference is set to zero, and is considered statistically significant when k exceeds a 95% confidence level ($k \geq 0.55$). Phase (ϕ) estimates over a specific frequency band indicate the temporal (lead/lag) relationships between the two time series. Finally, band-pass filtering was applied to extract important frequency components from the proxy time series. By plotting these filters as overlays on the time series, the coherency and phase relationships between the time series and the orbital parameter in question are visualized. Note that we will not discuss the ~ 19 -kyr filtered component because it shows large similarities with the ~ 23 -kyr component.

5.5 Results

5.5.1 Colour reflectance

Sediment colour varies predominantly with lithology, whereby a^* (red-green) values are overall higher in the reddish layers than in the beige layers (Fig. 5.2). Highest amplitude variations occur in the clusters of prominent reddish layers that correspond to long- and short-term eccentricity maxima. The exception to this is the lowermost interval (0-10 m; 6.47-6.3 Ma) where overall low values are recorded. Most spectral power occurs in the precession band (23/19 kyr) with additional variance in the obliquity band (41 kyr) (Fig. 5.4a).

The 23-kyr colour cycle is strongly coherent and in-phase with the 23-kyr precession cycle in ETP, whereby both cycles show an identical amplitude pattern and a near zero phase relationship

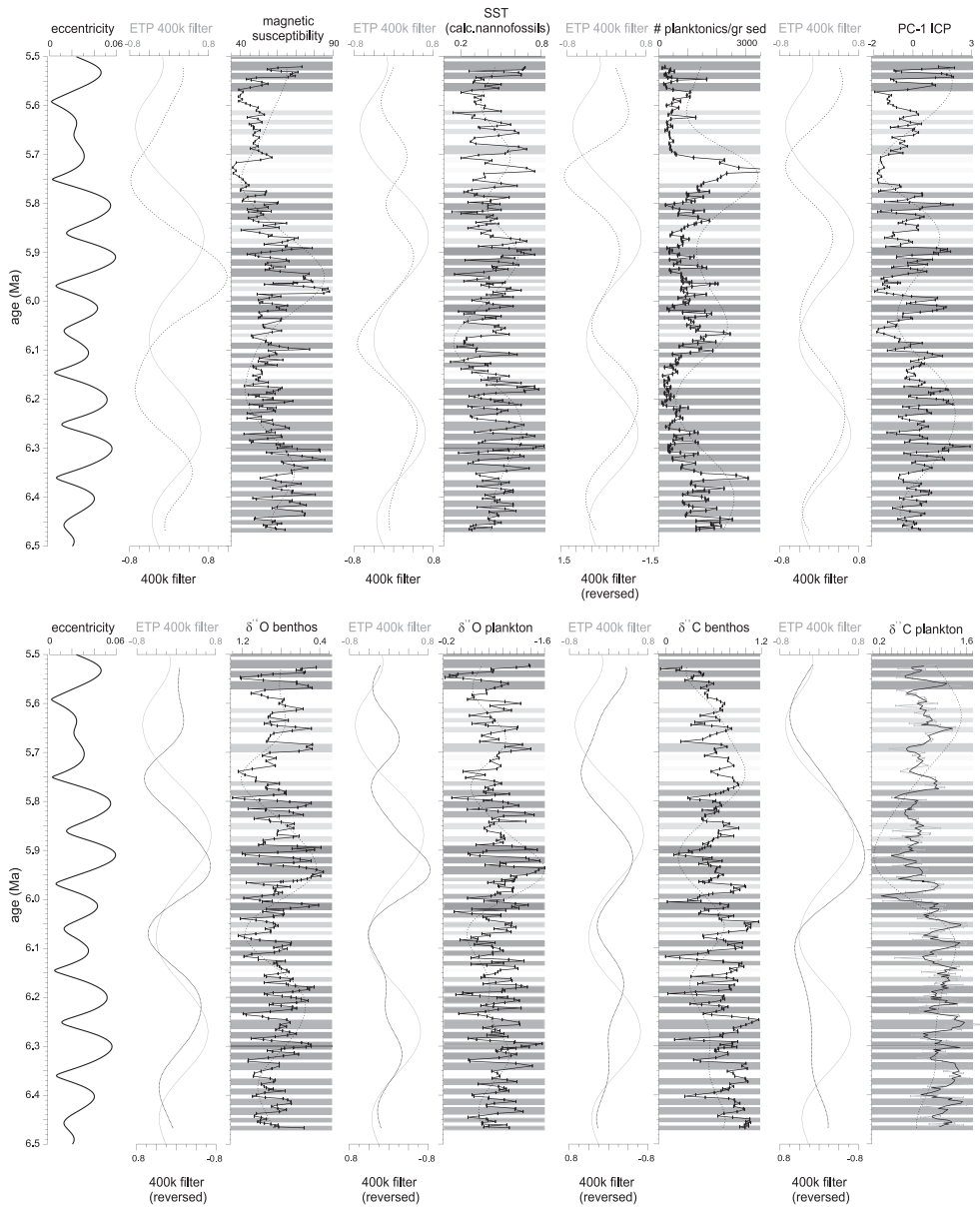


Figure 5.8 Comparison of ~ 400 -kyr filtered components in the studied proxies and the ~ 400 -kyr filtered ETP component (reflecting long eccentricity). The ~ 400 -kyr components were extracted using a Gaussian band-pass filter with central frequencies of 0.0025-0.00325 cycles/kyr (planktonic $\delta^{18}\text{O}$) and a bandwidth of 0.005-0.0065 cycles/kyr. The filtered components are shown as dotted overlays on the original data (black) and extracted ETP component (gray).

for the entire record (Figs. 5.4a, 5.5a and 5.9; Tab. 5.1). Colour maxima correspond to Northern Hemisphere insolation maxima (i.e. ETP maxima and precession minima). The 23-kyr colour cycle reaches highest amplitudes in the large-scale clusters of prominent reddish layers related to 400-kyr eccentricity maxima (Fig. 5.5a).

The 41-kyr colour cycle is strongly coherent and in-phase with the 41-kyr ETP cycle (Figs. 5.4a, 5.6a and 5.9; Tab. 5.1), indicating that colour maxima also correspond with (high-latitude) summer insolation maxima in the obliquity frequency band. The 41-kyr colour cycle is high in amplitude and in-phase with 41-kyr ETP between 5.95 and 5.55 Ma. Prior to 6.0 Ma, 41-kyr colour variations are less distinct and of a low amplitude (Fig. 5.6a).

A significant short (~100-kyr) eccentricity related spectral peak is lacking in the colour reflectance record (Fig. 5.4a). Nevertheless, the filtered ~100-kyr component (not shown) seems in-phase with the 100-kyr ETP cycle between ~6.15 and 5.7 Ma with colour maxima during eccentricity maxima (Fig. 5.9).

5.5.2 Magnetic Susceptibility

Magnetic susceptibility (MS) generally shows higher values in the reddish layers and lower values in the beige layers (Fig. 5.2). This relation is most clear in the lower and uppermost parts of the record, where high-amplitude variations occur during the short eccentricity maxima. The remainder of the record reveals MS maxima irregularly occurring in beige layers next to the maxima in the reddish layers. During eccentricity minima when distinct reddish layers are absent, MS values are low. The exceptions to this are the extreme MS maxima at ~5.98 Ma and ~5.96 Ma. Spectral analysis revealed coherent power in the precession, obliquity and long (~400 kyr) eccentricity frequency bands (Fig. 5.4a).

The highest coherence is found for the 23-kyr component, which appeared in-phase with precession (Figs. 5.4a, 5.5b and 5.9; Tab. 5.1), indicating that MS maxima correspond to insolation maxima (ETP maxima and precession minima). The pattern of the 23-kyr MS cycle is similar to that of the 23-kyr colour cycle, but of lower amplitude. The largest precession-related variability in MS occurs from 6.45 to 6.18 Ma and 5.95 to 5.77 Ma (Fig. 5.5b). Between 6.45 and 6.3 Ma (i.e., pre-MSC), the 23-kyr MS component slightly leads ETP (Fig. 5.9; Tab. 5.1), because MS maxima occur in the bottom part of the reddish layers. During the MSC, the 23-kyr MS component slightly lags ETP (Fig. 5.9; Tab. 5.1), because MS maxima mostly occur in the upper part of the reddish layers.

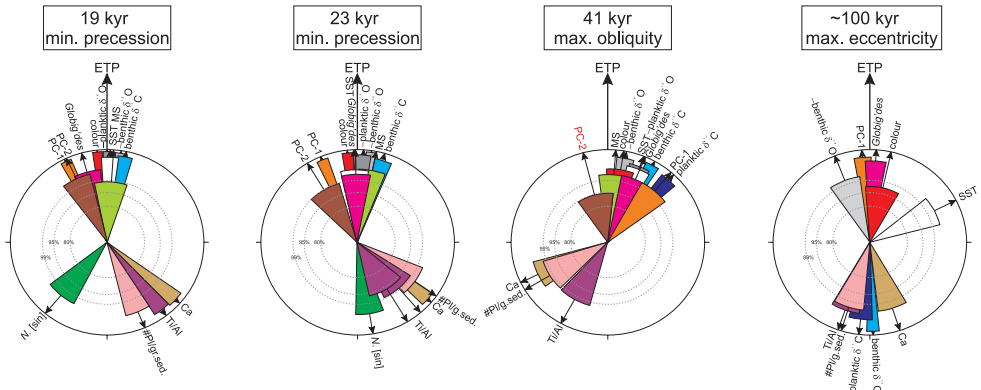
The 41-kyr MS cycle is coherent and in-phase with 41-kyr ETP for the pre-MSC interval (Figs. 5.4a, 5.6b and 5.9; Tab. 5.1) with MS maxima corresponding to summer insolation maxima (ETP and obliquity maxima). The filter amplitudes are generally low, however, except for the lowermost interval. After 6.0 Ma the phase with respect to obliquity is not constant (Fig. 5.6b). This results in a very low coherency with obliquity during the MSC (Tab. 5.1).

The influence of the short eccentricity cycle is not directly apparent in the MS spectrum (Fig. 5.4a). In particular, the ~100-kyr filtered component (not shown) seems to be biased by the two strong MS maxima that occur during the ~100-kyr eccentricity minimum at ~5.97 Ma. The ~400-kyr MS cycle is coherent (at the 99% level) with long eccentricity, though with a lead of ~73° (~70 kyr) (Figs. 5.4a and 5.8; Tab. 5.1).

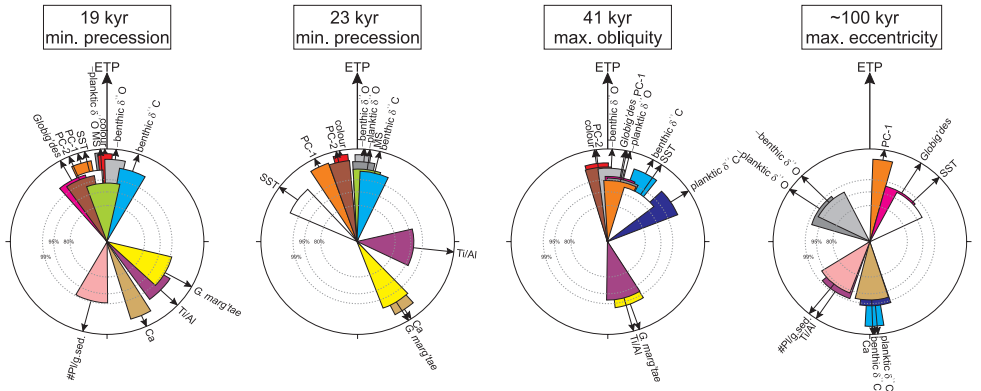
5.5.3 Nannofossils-based Sea Surface Temperature record

The nannofossils-based Sea Surface Temperature (SST) record reveals high-amplitude lithology-bound fluctuations with SST maxima in the reddish layers (Fig. 5.2). Highest SSTs are reached

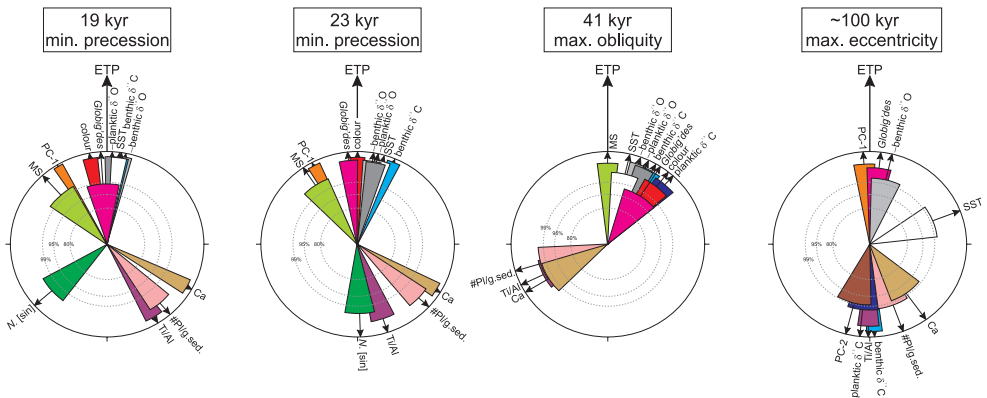
Total record



during MSC



before MSC



within the distinct reddish layers at 10, 19 and 43 m (i.e., 6.3, 6.2 and 5.9 Ma, respectively). The SST spectrum reveals strongest power in the precession band with additional power in the main obliquity and eccentricity bands (Fig. 5.4a).

The 23-kyr SST component is strongly coherent and in-phase with precession (Figs. 5.4a, 5.5a and 5.9; Tab. 5.1), implying that SST maxima correspond to insolation maxima (ETP maxima and

← **Figure 5.9** Phase wheels for all proxy records with respect to maximum ETP (i.e. maximum eccentricity, maximum obliquity and minimum precession) for solution La2004_(1,1). Upper part shows results for the total record, while the middle and lower part show the outcome for the MSC and pre-MSC time slices. For the phase of planktonic and benthic $\delta^{18}\text{O}$, 180° was added to change $\delta^{18}\text{O}$ in $-\delta^{18}\text{O}$ consistent with the phase relation for $-\delta^{18}\text{O}$ with maximum ETP forcing. Phases plotted clockwise with respect to maximum ETP forcing denote a lag while counterclockwise they denote a lead to maximum ETP. Radius of sectors displays coherency with ETP. Width of sectors indicates upper and lower phase limits. Dotted circles indicate the 80% (inner circle), 95% and 99% (outer circle) coherency levels. Only proxies having a coherency higher than 95% ($k \geq 0.55$) with the respective orbital parameter have been plotted. All numerical coherency and phase values are presented in Table 5.1.

precession minima). Between 6.4 and 6.18 Ma, when precession amplitudes are strongly enhanced due to a ~ 400 -kyr eccentricity maximum, the highest amplitudes in the 23-kyr filter and the best fit with the 23-kyr precession component are observed (Fig. 5.5a). In addition, the pre-MSC interval reveals a very high coherency between the 23- and 19-kyr SST components and their inferred precession cycles with a near-zero phase. The coherence is clearly lower in the MSC interval (Fig. 5.9; Tab. 5.1).

The 41-kyr SST component is coherent and in-phase with obliquity (Figs. 5.4a, 5.6a and 5.9; Tab. 1) with SST maxima corresponding to summer insolation maxima (ETP and obliquity maxima). The filtered 41-kyr component is higher in amplitude between 6.35 and 6.0 Ma, but in particular between ~ 5.8 and ~ 5.5 Ma during the MSC (Fig. 5.6a). In this interval, SST lags obliquity by roughly 4 kyr, but with a considerably lower coherence ($< 95\%$) (Figs. 5.4a and 5.9; Tab. 1).

The ~ 100 -kyr SST component (not shown) reveals a more or less constant lag of ~ 25 kyr relative to 100-kyr ETP between 6.35 and 5.85 Ma (Tab. 1). This lag is explained by the observation that highest SSTs occur in the top part of small clusters of prominent reddish layers related to short eccentricity maxima. Especially, an almost anti-phase relationship between the 100-kyr SST and ETP is found between 6.1 and 6.0 Ma.

The ~ 400 -kyr SST component is coherent at the 95% level and in-phase with the long eccentricity cycle (Figs. 5.4a and 5.8). Around 5.7 Ma the ~ 400 -kyr SST cycle becomes distorted because the filter starts to pick up the high SST values linked to the obliquity-related cyclicity.

5.5.4 *Globigerinoides* group

The *Globigerinoides* group abundance record (Fig. 5.2) shows strongest fluctuations and reaches highest values between 0 and 19 m (6.47–6.18 Ma). The record varies with lithology and maximum *Globigerinoides* percentages occur in the reddish layers. Lower-frequency variations between *Globigerinoides* maxima with a spacing of about two colour cycles or small-scale clusters are also apparent. The power spectrum reveals significant peaks at all orbital frequencies (Fig. 5.4a).

The 23-kyr *Globigerinoides* component is coherent and in-phase with 23-kyr precession (Figs. 5.4a, 5.5b and 5.9; Tab. 1) with *Globigerinoides* maxima corresponding to Northern Hemisphere summer insolation maxima (ETP maxima and precession minima). The filtered precession related signal reaches highest amplitudes between 6.4 and 6.15 Ma and between 5.7 and 5.6 Ma. The interval of the MSC reveals, however, an overall very low coherency between the 23-kyr *Globigerinoides* and ETP cycles (Tab. 5.1).

The 41-kyr *Globigerinoides* component is strongly coherent and in-phase with obliquity (Figs. 5.4a, 5.6a and 5.9; Tab. 5.1), whereby *Globigerinoides* maxima correspond to summer insolation maxima (ETP and obliquity maxima). Highest amplitudes are observed between 6.2 and 5.95 Ma

and between 5.75 and 5.52 Ma. High amplitude variations are also found in the oldest part of the record, but with a significant lag. This is most likely an artificial 41-kyr cycle, because the filter picks up every second peak of the 23-kyr signal (Fig. 5.6a).

The ~100-kyr *Globigerinoides* component is strongly coherent and in-phase with the short eccentricity cycle (Figs. 5.4a, 5.7a and 5.9; Tab. 5.1) with *Globigerinoides* maxima corresponding to ETP maxima. A less good fit between the band-pass filter and the ~100-kyr ETP cycle is observed between 5.95 and 5.65 Ma because of relatively low-amplitude variations (Fig. 5.7a).

5.5.5 Sinistrally-coiled *Neogloboquadrina*

The distribution of sinistrally-coiled *Neogloboquadrina* (*N. sin.*) shows high abundances (10–30%) in the oldest part of the record up to ~4 m (~6.38 Ma, Fig. 5.2); i.e., the level of the main sinistral to dextral coiling shift termed event PF-4 [Sierro et al., 1993; see also Krijgsman et al., 2004]. Following this shift, *N. sin.* reveals low abundances interrupted by excursions of up to 25% between 13 and 48 m (~6.25 and 5.8 Ma). Except for the strong peak in cycle 17 and two other peaks in cycles 21 and 31, these excursions occur in beige layers and are thus related to precession maxima. The spectrum shows overall low variance but with highly significant power in the precession band; an additional strong peak is observed around 400 kyr in the long-term eccentricity band (Fig. 5.4a).

The 23-kyr component of *N. sin.* is coherent and in anti-phase with precession (Figs. 5.4a, 5.5b and 5.9; Tab. 5.1); *N. sin.* maxima thus correspond to Northern Hemisphere summer insolation minima (ETP minima and precession maxima). Highest amplitudes in the 23-kyr filter and a good fit with precession are observed in the interval between 6.25 and 5.9 Ma. Remarkable are the high peak occurrences within the 400-kyr eccentricity minimum at 6.05 Ma.

The ~400-kyr *N. sin.* component is coherent at the 95% level and in anti-phase with 400-kyr ETP (Fig. 5.4a), which implies that ~400-kyr *N. sin.* maxima are in-phase with 400-kyr eccentricity (ETP) minima. However, the ~400-kyr filter (not shown) displays a rather ‘loose’ character due to the one-sided response pattern of *N. sin.*

5.5.6 *Globorotalia margaritae*

The *Globorotalia margaritae* record (Fig. 5.2) reveals very low numbers and almost no variations below ~40 m (i.e., prior to 6.0 Ma). However, percentages up to 20% are recorded in the interval between 47 and 55 m (5.8 and 5.75 Ma) accompanied by high-amplitude variations. Low-amplitude variations of 0–10% are recorded between 57 and 68 m (5.7 and 5.55 Ma). Peaks in *G. margaritae* are almost exclusively restricted to the beige layers and, hence, are linked to precession maxima. We limited the (cross-) spectral procedure to the youngest (MSC) part of the record because of the very low variations prior to 6.0 Ma. The spectrum reveals that power is concentrated in the precession and obliquity bands (Fig. 5.4a).

The 23-kyr component of *G. margaritae* is coherent and in anti-phase with precession (Figs. 5.4a, 5.5b and 5.9; Tab. 5.1), implying that maxima in *G. margaritae* correspond to Northern Hemisphere summer insolation minima (ETP minima and precession maxima). High amplitudes in the filtered 23-kyr component are observed in the interval between 5.9 and 5.7 Ma (Fig. 5.5b).

The 41-kyr component of *G. margaritae* is coherent and in anti-phase with obliquity (Figs. 5.4a, 5.6b and 5.9; Tab. 5.1). Maxima in *G. margaritae* thus correspond to summer insolation minima (ETP and obliquity minima). High filter amplitudes occur around 5.7 Ma, but the fit with the data is only moderate (Fig. 5.6b).

5.5.7 PC-2 (Plankton)

The second principal component, PC-2 (Plankton) of the planktonic foraminiferal assemblage revealed positive loadings for species that are mostly associated with the reddish layers (i.e. *Globigerinoides*, the *Globigerinoides obliquus* group, *Globorotalia scitula*, and dextrally-coiled neogloboquadrinids (*N. sin*)) and negative loadings for species that are related to the beige layers (i.e. sinistrally-coiled neogloboquadrinids (*N. sin.*), *Globorotalia margaritae* s.l. and *Globorotalia miotumida*) (Tab. 2, see Appendix 2). As such, PC-2 (Plankton) seems to discriminate between associations of generally warm-water species mostly recorded in the reddish layers and a group of overall cold-water species related to the beige layers. The major part of the PC-2 (Plankton) record shows maxima in the reddish layers (Fig. 5.2), but below 13 m (i.e., before 6.25 Ma) these maxima are mostly restricted to the beige layers. The record starts with overall low values up to 4 m (6.38 Ma), when a sudden increase takes place related to the major sinistral-dextral coiling shift in *Neogloboquadrina* [PF-4 event of Sierro et al., 1993]. Between 21 and 55 m (6.15 and 5.75 Ma), a high-amplitude interval is observed that is marked by gradually declining values and a strong lithology-related cyclicity. In addition, a period that consists of about two colour cycles is observed. Between 54 and 57 m (5.75 and 5.7 Ma) a strong increase in PC-2 (Plankton) parallels – and probably is due to – the strong decline in total *G. margaritae* (Fig. 5.2), after which PC-2 (Plankton) remains relatively constant until the top of the record. Spectral power is mainly concentrated in the precession band with some variance in the obliquity band (Fig. 5.4a).

The 23-kyr PC-2 (Plankton) component is coherent at the 95% level and in-phase with precession (Figs. 5.4a, 5.5b and 5.9; Tab. 5.1); PC-2 (Plankton) maxima thus correspond to Northern Hemisphere summer insolation maxima (ETP maxima and precession minima). However, an opposite phase relationship is observed before 6.25 Ma, when PC-2 (Plankton) maxima are recorded in the beige layers. Note that this is related to the negative weight of *N. sin* on PC-2 (Plankton). Coherency between the 23-kyr PC-2 (Plankton) and ETP components prior to 6.0 Ma is therefore low (Tab. 5.1). The highest filter amplitudes occur between 5.95 and 5.75 Ma, when an overall decline in PC-2 (Plankton) takes place (Fig. 5.5b).

The 41-kyr PC-2 (Plankton) component shows increased amplitudes and a perfect in-phase relation with obliquity between 6.15 and 5.95 Ma and in particular between 5.85 and 5.65 Ma, although in the latter interval increased amplitudes are partly due to the strong increase in PC-2 (Plankton) between 5.75 and 5.7 Ma (Fig. 5.6a). PC-2 (Plankton) maxima thus generally correspond to insolation maxima (ETP and obliquity maxima). Despite the presence of a clear 41-kyr signal, coherency with 41-kyr ETP is not significant at the 95% level (Figs. 5.4a and 5.9; Tab. 5.1). This is most likely due to the inverse relation with lithology before 6.2 Ma, because when this interval is left out during the cross-spectral procedure, coherency with obliquity is strong.

The 100-kyr PC-2 (Plankton) component (not shown) is coherent at the 95% level and in anti-phase with the short eccentricity cycle only before the MSC, from 6.5 to 6.0 Ma. In this interval, PC-2 (Plankton) maxima correspond to eccentricity minima (Fig. 5.9; Tab. 5.1).

5.5.8 Planktonic foraminiferal flux

The record of the number of planktonic foraminifera per gram sediment varies mainly with lithology, including overall low numbers in the reddish and higher numbers in the beige layers (Fig. 5.2). Very low numbers of planktonic foraminifera are recorded in the thicker, more prominent reddish layers and are, hence, connected to strong precession minima at times of eccentricity maxima. In addition, very low numbers are observed in the more vague reddish layers and beige layers of cycles 38-41 (57-65 m, 5.71-5.6 Ma) in the upper part of the record. A pronounced

peak of very high numbers of planktonic foraminifera is recorded in the upper part of the beige layer of cycle 35 at 55 m (~5.73 Ma) concomitant with a period of very low sedimentation rates (see Fig. 3.2 in **Chapter 3**). Additional strong peaks occur in beige layers that are connected to eccentricity minima and, thus, minimum precession amplitudes (except for the interval between 57–65 m) when sedimentation rates are generally low [see also Van der Laan et al., 2005]. The power spectrum reveals peaks in the precession band and an additional peak in the long (400-kyr) eccentricity band (Fig. 5.4a). Although no clear peaks are observed in the obliquity and short eccentricity bands, coherency with ETP in these bands is higher than 95% (Tab. 5.1).

The 23-kyr component of the planktonic foraminiferal flux is coherent and in anti-phase with precession (Figs. 5.4a, 5.5a and 5.9; Tab. 5.1), implying that maximum numbers of planktonic foraminifera correspond to Northern Hemisphere summer insolation minima (ETP minima and precession maxima). Amplitudes of the filtered 23-kyr component are relatively low, presumably due to the trends and sudden spikes in the record, but higher amplitudes are observed in the oldest part of the record, though accompanied by a small lead (Fig. 5.5a); coherency is considerably lower during the MSC.

The 41-kyr component is coherent and in anti-phase with obliquity, implying that maxima in the planktonic foraminiferal flux correspond to summer insolation minima (ETP and obliquity minima) (Figs. 5.4a, 5.6b and 5.9; Tab. 5.1). However, the fit between the 41-kyr filter and the actual record is rather poor as the filter picks up mostly the ‘double’ peaks in the precession-related signal. The youngest part (5.8–5.5 Ma) of the record shows a poorly developed 41-kyr signal due to the pronounced peak in the flux at ~5.73 Ma and the overall low numbers of foraminifera thereafter (Fig. 5.6b).

The 100-kyr component is coherent at the 95% level and appears in anti-phase with the short eccentricity cycle; maximum values in the flux thus correspond to eccentricity minima (Figs. 5.4a, 5.7a and 5.9; Tab. 5.1). Also the ~400-kyr component appears in anti-phase with the long-term eccentricity cycle (Fig. 5.8), although with very low coherence (Fig. 5.4a).

5.5.9 Oxygen isotopes ($\delta^{18}\text{O}$)

The benthic and planktonic $\delta^{18}\text{O}$ records of AEB have been described in **Chapter 3**. The benthic record has been correlated to benthic $\delta^{18}\text{O}$ records from the open ocean and to the nearby Salé record and fits well into a standard oxygen isotope stratigraphy and astronomically tuned chronology that reflect dominantly obliquity-driven glacial cycles of the latest Miocene [Van der Laan et al., 2005]. The benthic and planktonic $\delta^{18}\text{O}$ records are moderately highly covariant (correlation coefficient = 0.56) and show high-frequency changes with maximum amplitudes of 0.9‰ and 1.3‰, respectively (Fig. 5.2). Changes related to lithology are manifest by shifts to light values in the reddish layers and to heavy values in the beige layers. The most depleted $\delta^{18}\text{O}$ values occur in the clusters of more pronounced and thicker reddish layers linked to eccentricity maxima, yet the precession and eccentricity related variations do not dominate the $\delta^{18}\text{O}$ signal. Instead, both $\delta^{18}\text{O}$ spectra show the strongest peak in the obliquity frequency band (Fig. 5.4b).

The 23-kyr $\delta^{18}\text{O}$ cycles are highly coherent and essentially 180° out-of-phase with the precession cycle (Figs. 5.4b, 5.5a and 5.9; Tab. 5.1), indicating that $\delta^{18}\text{O}$ maxima correlate with Northern Hemisphere summer insolation minima (ETP minima and precession maxima). The filtered 23-kyr $\delta^{18}\text{O}$ components show a very similar pattern as the 23-kyr ETP cycle, with strongly enhanced amplitudes at times of 400-kyr eccentricity maxima (Fig. 5.5a).

The 41-kyr benthic and planktonic $\delta^{18}\text{O}$ cycles show a very strong coherency and anti-phase relationship with the 41-kyr ETP cycle (Figs. 5.4b, 5.6a and 5.9; Tab. 5.1). Maximum values

in $\delta^{18}\text{O}$ thus correspond to summer insolation minima (ETP and obliquity minima). High amplitudes in the 41-kyr filtered components of both $\delta^{18}\text{O}$ records show a good fit with the obliquity cycle throughout the section, except in the interval between 5.97 and 5.8 Ma (Fig. 5.6a).

The ~100-kyr $\delta^{18}\text{O}$ components are coherent and in anti-phase with ETP (Figs. 5.4b, 5.7a and 5.9; Tab. 5.1). The 100-kyr $\delta^{18}\text{O}$ minima are generally found in clusters of distinct reddish layers associated with the short eccentricity maxima. However, it seems that the dominant obliquity (and precession) related $\delta^{18}\text{O}$ variations distort the position of the filtered ~100-kyr $\delta^{18}\text{O}$ component relative to 100-kyr ETP, in particular in the interval between ~6.2 and 5.8 Ma. The 400-kyr $\delta^{18}\text{O}$ components are coherent and in anti-phase with the long eccentricity cycle (Figs. 5.4b and 5.8). $\delta^{18}\text{O}$ maxima thus correspond to 400-kyr ETP (eccentricity) minima.

5.5.10 Carbon isotopes ($\delta^{13}\text{C}$)

The benthic and planktonic $\delta^{13}\text{C}$ records are shown in Figure 5.2. Maximum amplitude is ~1.8‰ for planktonic $\delta^{13}\text{C}$ versus ~1.2‰ for benthic $\delta^{13}\text{C}$. Both records reveal a long-term decrease in $\delta^{13}\text{C}$. The planktonic $\delta^{13}\text{C}$ record shows a highly fluctuating, erratic pattern. After running a 3-point moving average, the planktonic $\delta^{13}\text{C}$ record reveals a high covariance with the benthic record (correlation coefficient = 0.61). A short (~20 kyr) but prominent negative excursion of ~1.0‰ at 31-32 m (~6.0 Ma) is a striking feature in the planktonic $\delta^{13}\text{C}$ record, while absent in the benthic record. This excursion is accompanied by a shift in mean values from ~1.3‰ to ~0.7‰. A close link between lithology and planktonic $\delta^{13}\text{C}$ is not directly observed, although $\delta^{13}\text{C}$ minima occur mainly in the small-scale clusters of distinct reddish layers. Variations in planktonic $\delta^{13}\text{C}$ with a spacing of about two colour cycles are also observed.

The benthic $\delta^{13}\text{C}$ record reveals a strong relation with lithology with distinct minima in the beige layers corresponding to precession maxima, especially in the lower part of the record before 5.95 Ma. In addition, $\delta^{13}\text{C}$ minima are observed with a spacing of about two colour cycles, pointing to the additional influence of obliquity. Finally, the benthic $\delta^{13}\text{C}$ record reveals overall shifts to lighter values in clusters of distinct reddish layers which correspond to eccentricity maxima. These ~100-kyr $\delta^{13}\text{C}$ minima are characterized by depletions of about 0.4 to 0.7‰. Both $\delta^{13}\text{C}$ spectra are dominated by peaks at 41 kyr (obliquity) and ~100 kyr (short eccentricity) (Fig. 5.4b). Additional precession variance is found in benthic, but not in planktonic $\delta^{13}\text{C}$, which is in line with the lithology-bound character of benthic $\delta^{13}\text{C}$ as opposed to planktonic $\delta^{13}\text{C}$.

The 23-kyr benthic $\delta^{13}\text{C}$ cycle is essentially in-phase and strongly coherent with 23-kyr ETP (Figs. 5.4b, 5.5a and 5.9; Tab. 5.1), whereby $\delta^{13}\text{C}$ maxima correspond to Northern Hemisphere summer insolation maxima (ETP maxima and precession minima). The filtered 23-kyr benthic $\delta^{13}\text{C}$ component shows highest amplitudes and a good fit with precession between 6.45 and 6.1 Ma when the 400-kyr eccentricity cycle reached maximum values.

The 41-kyr benthic and planktonic $\delta^{13}\text{C}$ cycles are in-phase and coherent with obliquity, with $\delta^{13}\text{C}$ maxima corresponding to summer insolation maxima (ETP and obliquity maxima). Nevertheless, small time lags relative to obliquity are observed (Figs. 5.4b, 5.6a and 5.9; Tab. 5.1). In the middle part of the record (between ~6.2 and 5.9 Ma), the 41-kyr $\delta^{13}\text{C}$ components reveal the highest amplitudes and best fit with 41-kyr ETP, though with a small lag of 3 to 6 kyr (Fig. 5.6a).

The ~100-kyr benthic and planktonic $\delta^{13}\text{C}$ cycles are strongly coherent and in anti-phase with short eccentricity, indicating that $\delta^{13}\text{C}$ maxima correspond to eccentricity minima (Figs. 5.4b, 5.7a and 5.9; Tab. 5.1). The 400-kyr $\delta^{13}\text{C}$ components are coherent and in anti-phase with the long eccentricity cycle (Figs. 5.4b and 5.8). $\delta^{13}\text{C}$ maxima thus correspond to 400-kyr ETP (eccentricity) minima.

Table 5.2 Loadings on the axis of the second principal component (PC-2 (Plankton)) of planktonic foraminifera after Principal Component Analysis. Species that have abundances lower than 3% in any of the studied samples have been left out.

Loadings of 34 species	PC-2
<i>Globigerinoides obliquus</i> group	0,58
<i>Globigerinoides</i> total	0,53
<i>Globorotalia scitula</i> dextral	0,52
<i>N.</i> 4-chambered dextral	0,49
<i>Globorotalia scitula</i> total	0,47
<i>N.</i> dextral total	0,29
<i>N. acostaensis</i> dextral	0,28
<i>Globoquadrina altispira</i>	0,24
<i>Globigerinita glutinata</i>	0,23
<i>Hastigerina siphonifera</i>	0,23
<i>Globigerina falconesis/bulloides</i>	0,23
<i>Globigerina falconensis</i>	0,21
<i>Globigerinoides bollii</i>	0,14
<i>Globigerina apertura</i>	0,10
<i>Globigerinoides trilobus</i>	0,09
<i>Globigerinoides sacculifer</i>	0,08
<i>Globigerina obesa</i>	0,04
<i>Globigerina bulloides</i>	0,03
<i>Orbulina</i> group	0,03
<i>Globigerina cf. obliquus</i>	0,00
<i>Globigerina decoraperta</i>	-0,10
<i>N. spp.</i> dextral	-0,13
<i>N.</i> total	-0,18
<i>Globigerina juanai</i>	-0,22
<i>Turborotalita quinqueloba</i>	-0,22
<i>Globigerina nepenthes</i>	-0,22
<i>Globorotalia margaritae margaritae</i>	-0,26
<i>Globorotalia miotumida</i> total	-0,29
<i>Globorotalia miotumida</i> sinistral	-0,29
<i>Globorotalia margaritae primitiva</i>	-0,30
<i>N.</i> 4-chambered sinistral	-0,41
<i>N. spp.</i> sinistral	-0,43
<i>N. acostaensis</i> sinistral	-0,58
<i>N.</i> sinistral total	-0,61

5.5.11 PC-1 (ICP)

Principal Component Analysis (PCA) yielded two statistically significant components of which the first Principal Component (PC-1) describes 55% of the total variance in the data set. The interpretation of PC-1 (ICP) is based on the loadings of the elements on this first principal component. Very high positive loadings are observed for the elements K, Al, Ni, Ti, Li, V and Fe (in decreasing order) and strongly negative loadings for Ca and P (Tab. 5.3). All elements that contribute positively to PC-1 (ICP) are main components of aluminosilicate minerals and often show a high covariance in fine-grained sediments. Variations in their concentrations thus reflect the relative contribution of terrigenous clastics versus carbonate and may be used as a

Table 5.3 Loadings on the axis of the first principal component (PC-1 (ICP)) of the elements that were subjected to Principal Component Analysis.

element	PC-1 (ICP)		
	total record	pre MSC	MSC
K	0,97	0,97	0,96
Al	0,96	0,97	0,96
Ni	0,94	0,94	0,94
Ti	0,94	0,94	0,95
Li	0,92	0,96	0,91
V	0,90	0,90	0,93
Fe	0,90	0,91	0,93
P	-0,56	-0,63	-0,49
Ca	-0,41	-0,39	-0,60

proxy for the input of fine-grained clastic material. PC-1 (ICP co-varies predominantly with lithology (Fig. 5.2). High PC-1 (ICP) values are found in the reddish layers and low values in the beige layers, with maximum values within the most pronounced reddish layers related to short eccentricity maxima. As expected, the PC-1 (ICP) spectrum reveals strong peaks in the precession and short-term eccentricity bands, with only minor obliquity variance (Fig. 5.4b). Evidently, PC-1 (ICP) shows a remarkable peak-to-peak correlation with ETP with the exception of the interval between 5.75 and 5.65 Ma where precession amplitudes are reduced due to a ~400-kyr eccentricity minimum (Fig. 5.3).

The 23-kyr component of PC-1 (ICP) is strongly coherent and in-phase with precession; thus with 23-kyr filtered maxima values corresponding to Northern Hemisphere summer insolation maxima (ETP maxima and precession minima). The 23-kyr filter reaches highest amplitudes and shows a very good fit with the 23-kyr ETP cycle at times of 400-kyr eccentricity maxima (Figs. 5.4b, 5.5a and 5.9; Tab. 5.1).

Despite the minor variance in the obliquity band (Fig. 5.4b), the 41-kyr component of PC-1 (ICP) is coherent with obliquity at the 95% confidence level and in-phase with obliquity (Fig. 5.9; Tab. 5.1). Nevertheless, the band-pass filter shows relatively low amplitudes and an inconsistent phase relation with obliquity (Fig. 5.6b).

The ~100-kyr component of PC-1 (ICP) shows a very good correlation with the short eccentricity cycle with similar amplitude modulations and a near-zero phase difference (Figs. 5.4b and 5.7b; Tab. 5.1); maximum PC-1 (ICP) values thus correspond to eccentricity maxima (ETP maxima, Fig. 5.9). The same holds for the ~400-kyr PC-1 (ICP) component (Fig. 5.8).

5.5.12 Calcium (%)

The Ca (%) record shows a clear relation with lithology with high-frequency changes superimposed on longer-term variations. Maximum values are generally recorded in the beige layers and minimum values in the reddish layers (Fig. 5.2b). Comparison with the PC-1 (ICP) record after removing the linear trend in both records reveals a strong inverse correlation (correlation coefficient = -0.637). This is not surprising when we keep in mind that an increased input of terrigenous clastics will cause a reduction in carbonate production.

Highest amplitude variations and lowest values are found in the clusters of prominent reddish layers that correspond to ~100-kyr eccentricity maxima. Highest Ca values (~25%) are recorded

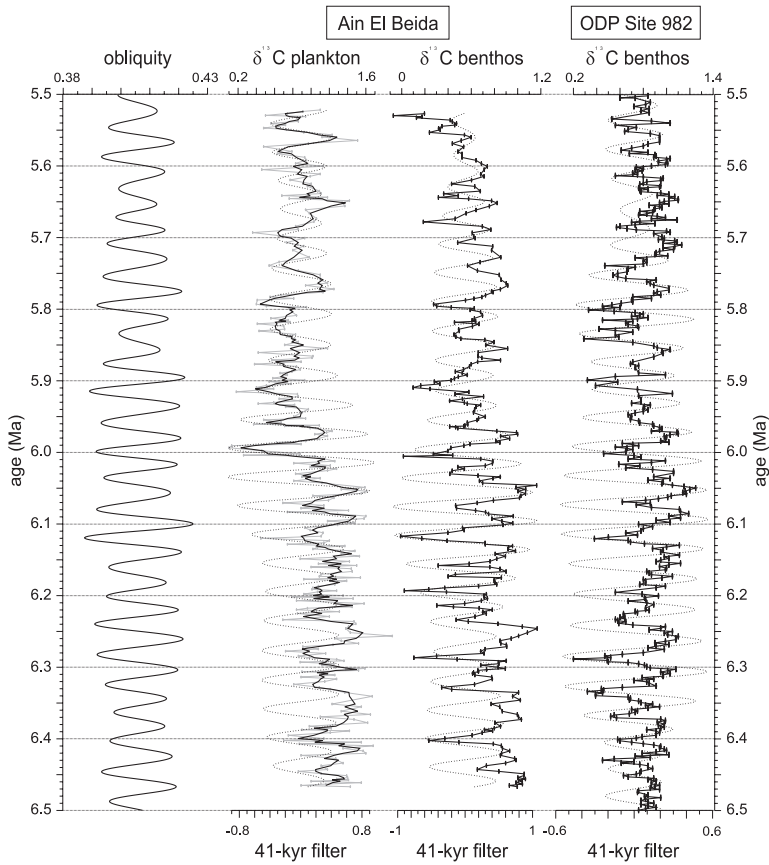


Figure 5.10 Comparison between the 41-kyr components (dotted overlays) in the $\delta^{13}\text{C}$ records of AEB and the benthic $\delta^{13}\text{C}$ record of Site 982 [Hodell et al, 2001, modified after Van der Laan et al., 2005], and obliquity of solution La2004_(1,1). The 41-kyr component of the Site 982 benthic $\delta^{13}\text{C}$ record was extracted using a Gaussian band-pass filter with a central frequency of 0.0245 cycles/kyr and a bandwidth of 0.009 cycles/kyr.

at ~6.4 Ma and mark the onset of a declining trend to ~6.1 Ma. Another strong maximum at 5.75 Ma is coincident with a ~100-kyr eccentricity minimum and is followed by an interval with extremely low amplitude variations that corresponds to the 400-kyr eccentricity minimum around 5.6 Ma. The Ca (%) spectrum reveals precession related peaks but most variance is concentrated in the long-term eccentricity band with minor power in the obliquity and short eccentricity bands (Fig. 5.4b).

The 23-kyr component in the Ca (%) record is strongly coherent and in anti-phase with precession; i.e., Ca maxima occur during Northern Hemisphere summer insolation minima (ETP minima and precession maxima). The 23-kyr Ca (%) component shows on average a small lead with respect to precession (Figs. 5.4b, 5.5a and 5.9; Tab. 5.1). This is especially apparent in the lower part of the record. As was observed for the 23-kyr PC-1 (ICP) component, highest amplitudes and the best fit with precession coincides with the 400-kyr eccentricity maxima (Fig. 5.5a).

The Ca (%) spectrum displays minor variance in the main obliquity band, but shows nevertheless a high coherency with obliquity (Fig. 5.4b; Tab. 5.1). The 41-kyr filtered Ca (%) component reveals maximum values during obliquity minima (Figs. 5.6b and 5.9), but as for PC-1 (ICP), the amplitudes are low and the phase is inconsistent with respect to obliquity. This can partly be explained by ‘doubling’ of the 23-kyr Ca (%) cycle in large parts of the record.

The ~100-kyr Ca signal is strongly coherent and in anti-phase with ~100-kyr ETP; Ca maxima thus correspond to eccentricity (ETP) minima (Figs. 5.4b, 5.7b and 5.9; Tab. 5.1). Small differences between the 100-kyr filtered Ca (%) record and short eccentricity occur in the oldest part of the record, where Ca (%) values are relatively high, and around 5.96 Ma, where a strong Ca (%) minimum induces a ‘shoulder’ in the extracted ~100-kyr Ca component (Fig. 5.7b). Despite strong variance in the long eccentricity band, the ~400-kyr Ca component (not shown) displays a low coherency with long eccentricity probably due to the long-term trend and the strong Ca minima during short eccentricity maxima that bias the ~400-kyr filter.

5.5.13 Titanium/Aluminum ratio

Apart from PC-1 (ICP), assumed to mainly represent the fine-grained non-carbonate component in the sediment, we focused on Ti/Al, because this elemental ratio is often considered indicative of the relative contribution of coarser grainsizes to the terrigenous fraction in marine sediments [e.g., Shimmield, 1992; Schenau et al., 1999; Lourens et al., 2001]. Ti/Al varies between 0.06 and 0.11 and reveals a distinct relation with lithology with maximum values in the beige and minimum values in the reddish layers (Fig. 5.2). Ti/Al shows overall shifts to lower values in the clusters of reddish layers that correspond to eccentricity maxima. Ti/Al reaches extremely high values of about 0.11 during the eccentricity minimum at 5.97 and 5.71 Ma. It further shows a long-term trend towards increasing values. The spectrum reveals main power in the short-term eccentricity and precession bands, with minor power in the obliquity band (Fig. 5.4b).

The 23-kyr component in Ti/Al is coherent at the 95% level and in anti-phase with precession (Figs. 5.4b, 5.5b and 5.9; Tab. 5.1), implying that Ti/Al maxima correspond to Northern Hemisphere summer insolation minima (ETP minima and precession maxima). Highest amplitudes in the filtered record and best fit with precession are observed in the oldest part of the record (Fig. 5.5b).

A clearly obliquity related cyclicity is not apparent in the Ti/Al record, despite its relatively high coherency with obliquity (Tab. 5.1). Maxima in the 41-kyr filtered Ti/Al component correspond to summer insolation minima (ETP and obliquity minima, Figs. 5.6b and 5.9). The two extreme Ti/Al maxima at 5.97 and 5.71 Ma are picked up by the 41-kyr filter, but the fit between the 41-kyr Ti/Al and ETP signals is moderate and amplitudes are overall low.

The ~100-kyr Ti/Al component is highly coherent and in anti-phase with short eccentricity (Figs. 5.4b and 5.9; Tab. 5.1), although an almost in-phase relationship is observed between 5.8 and 5.65 Ma, because of the strong increase in Ti/Al between 5.75 and 5.71 Ma (Fig. 5.7b).

5.6 Discussion

5.6.1 Precession-forced variations

The colour cycles that are readily observed at Ain el Beida are dominantly precession controlled. In addition, the influence of eccentricity is reflected in the cycle patterns with thicker and more prominent reddish layers deposited at times of maximum eccentricity and, hence, maximum

precession amplitudes. The reddish layers themselves were initially linked to precession minima [Krijgsman et al., 2004] based on the correspondence with climate proxy signals observed in Mediterranean sapropels ($\delta^{18}\text{O}$ minima and *Globigerinoides* maxima) for which the phase relation with precession is known [Hilgen, 1991b; Lourens et al., 1992, 2001]. This initial assumption was consistent with intricate details of cycle patterns in the Oued Akrech section. It is however important to realize that our age model, which is based on correlating midpoints of reddish and beige layers to summer insolation maxima and minima, respectively, locks the phase relation between the astronomical forcing and our key proxy indicators. The tuning thus automatically constrains the (general) direction of the response in other climate proxies. Most proxies show a strong precession signal with maxima in colour, *Globigerinoides*, PC-2 (Plankton), SST, benthic $\delta^{13}\text{C}$, PC-1 (ICP) and minima in $\delta^{18}\text{O}$, planktonic flux, Ca, and Ti/Al in the reddish layers; these signals are thus linked to precession minima and Northern Hemisphere summer insolation maxima (Fig. 5.9). In addition, prominent peaks in sinistrally-coiled *Neogloboquadrina* and *Globorotalia margaritae* are reached in some of the beige layers and are thus linked to precession maxima and summer insolation minima. Most proxies show an instantaneous or almost instantaneous response to precessional insolation forcing with a very short lag (< 3 kyr), although PC-1 (ICP) and PC-2 (Plankton) maxima, and planktonic flux, Ca (%) and Ti/Al minima lead maxima in insolation by roughly 1 to 3 kyr (Fig. 5.9 and Tab. 5.1).

5.6.1.1 Mediterranean sapropels and regional climate change

The planktonic $\delta^{18}\text{O}$ signal in the reddish layers is similar to that observed in Mediterranean sapropels, although the amplitude of $\sim 1\text{‰}$ is considerably smaller than generally found in the Mediterranean where shifts of up to 5‰ in planktonic $\delta^{18}\text{O}$ are recorded during the late Neogene [e.g., Lourens et al., 2004]. The very large amplitudes of the planktonic $\delta^{18}\text{O}$ signal during sapropels are generally attributed to a reduced excess evaporation (e.g., increased river runoff) in the eastern Mediterranean [Thunell and Williams, 1989; Rohling, 1994, 1999]. Combined high-resolution data sets on sea-surface temperatures (SST) (estimated from U_{37}^k indices) and planktonic $\delta^{18}\text{O}$ across late Pleistocene sapropel intervals show that $\delta^{18}\text{O}$ decreased (between 1 and 4.6‰) and SST increased (between 0.7 and 6.7°C) [Emeis et al., 2003]. From these results it was estimated that maximal seawater $\delta^{18}\text{O}$ depletion (between 0.5 and 3.0‰) of eastern Mediterranean surface waters is most pronounced at sapropel bases, in agreement with an initial sudden input of monsoon-derived freshwater. In all but one case the eastern Mediterranean sapropel-bound depletions exceeded those found in a western Mediterranean core. Most sapropels coincide with warming trends of SST.

The precession related planktonic $\delta^{18}\text{O}$ signal at AEB can similarly be interpreted to reflect the effect of surface water warming and/or enhanced fluvial runoff but the amplifying effect of the Mediterranean [see e.g., Kouwenhoven et al., 1999] is absent. Remarkably enough, benthic $\delta^{18}\text{O}$ reveals a very similar pattern of precession-related variations although amplitudes are less by about 0.5‰ . This similarity suggests that benthic and planktonic foraminiferal assemblages somehow share the same water mass characteristics and that part of the larger amplitude surface water signal is transferred to deeper waters. This might not be impossible in view of the relatively shallow depth of deposition of AEB between approximately 500 and 1000 m [Benson and Rakic-El Bied, 1996; T. Kouwenhoven and D. van Hinsbergen, pers. comm., 2004]. In particular, the strong peaks of sinistrally-coiled neogloboquadrinids in several of the beige layers suggest intensified upwelling of cold and nutrient-rich deep waters to the surface [e.g., Ufkes et al., 2000 and references therein] during precession maxima, whereas *Globigerinoides* spp., the calcareous nannofossils-based SST

and PC-2 (Plankton) records clearly indicate that maximum surface water temperature conditions were reached during precession minima (i.e., reddish layers).

Detailed correlations between the benthic $\delta^{18}\text{O}$ record of AEB and those of more open ocean sites showed that the precession-induced $\delta^{18}\text{O}$ variability is a common constituent of global climates during the Messinian [Van der Laan et al., 2005]. At present it not understood whether this precession-related signal mirrors ice volume or deep-sea temperature variations. If ice volume, one may expect that $\delta^{18}\text{O}$ would lag precession by several kyrs. This lag is not evident, however, from the results of cross-spectral analysis, which show an in-phase relation with precession, suggesting that temperature may have been most important.

The minimum Ti/Al values in the reddish layers of AEB have also been found in Mediterranean sapropels, although often with a larger amplitude [e.g., Wehausen and Brumsack, 2000; Lourens et al., 2001]. Ti/Al variations in sapropel-bearing successions are interpreted to reflect variations in the relative contribution of eolian versus riverine sources. According to this scenario, Ti/Al minima in sapropels indicate enhanced fluvial input during the humid phase of the precession-related climate cycle, whereas the Ti/Al maxima point to more arid conditions and enhanced eolian input [Shimmield, 1992; Schenau et al., 1999; Lourens et al., 2001]. Accordingly, the Ti/Al record of AEB indicates that the reddish layers correspond to more humid climate conditions. The enhanced fluvial input during deposition of the reddish layers would also explain the increase in PC-1 (ICP) and the decrease in Ca-content, as well as the strong reduction in the number of foraminifera per gram dry weight, and the increase in sedimentation rates (see also **Chapter 3**) [Van der Laan et al., 2005]. Hence, we consider that the carbonate signal of AEB mainly reflects dilution by fine-grained terrigenous clastics of a fluvial origin, as maxima in Ti/Al are synchronous with maxima in Ca and the planktonic flux record, suggesting that an eolian component plays a minor role in the total dilution signal. Enhanced carbonate productivity in the beige layers as suggested by the peak occurrences of sinistrally-coiled neogloboquadrinids, keeled globorotaliids (*G. margaritae*) and negative excursions in benthic $\delta^{13}\text{C}$ may have played a role, although we consider it of secondary importance.

Summarizing, key proxy indicators $\delta^{18}\text{O}$, *Globigerinoides* and Ti/Al reveal similar signals in the reddish layers of AEB and Mediterranean sapropels. The same phasing of the planktonic flux, Ca (%) and Ti/Al records and the inverse correlation between Ca (%) and the PC-1 (ICP) record suggest that the marine calcium carbonate (CaCO_3) record is not diluted by terrigenous wind-blown material but by terrigenous material transported by rivers. Thus, the similarity in proxy signals suggests that very similar climate conditions existed during deposition of reddish layers and sapropels. The question arises whether the same or different dominantly precession-controlled climate forcing mechanisms were operating in the (circum-) Mediterranean region and Northwest Morocco.

5.6.1.2 African monsoon or Atlantic climate system?

The assumed increase in humidity during deposition of the reddish layers at Ain el Beida can be attributed to two different climate systems: the African monsoon and the Atlantic climate system. The (eastern) Mediterranean sapropels have been linked to strongly enhanced outflow of the river Nile during strong precession minima [Rossignol-Strick, 1983, 1985] when the African monsoon was intensified and the Intertropical Convergence Zone (ITCZ) positioned further north [e.g., Prell and Kutzbach, 1987]. However, rather than the monsoonal system, humid climate conditions during deposition of the reddish layers can also be related to enhanced activity of Atlantic westerly depressions during winter that bring rain to Northwest Morocco today [Griffiths, 1972; Knippertz

et al., 2003]. Satellite images of Morocco show clear examples of runoff by river transport linked to Atlantic depressions during winter or early spring (<http://visibleearth.nasa.gov/>).

Kuhlmann et al. [2004] recently focused on separating the influence of the monsoon and Atlantic climate systems during the Holocene pluvial phase and placed the transition zone of the two systems between 27 and 30°N based on differences in the signature of terrigenous input in cores off Northwest Africa located at 31°N and 27°N. Holz et al. [2004], comparing dust fallout and seabed samples collected along the Moroccan-Mauretanian coast, found evidence of fluvially discharged mud (with mean grainsizes between 3-5 μ) next to fine eolian dust being deposited in the northern part of the study area (around 30-33°N) while further to the south (between 17-28°N) the overprint of coarse eolian dust may hint at the moisturing effect of the North Atlantic climate system. In addition, the northwesternmost part of Africa and especially Morocco has been shown to respond differently to insolation forcing than the more equatorial regions [e.g., Ruddiman et al., 1989; Paeth and Friederichs, 2004], with rainfall mostly in boreal winter and affected by atmospheric processes (such as the North Atlantic Oscillation, NAO) in the extratropics [Cullen and deMenocal, 2000; Knippertz et al., 2003].

The similarity in the proxy signals between the reddish layers and Mediterranean sapropels thus satisfactorily explains the AEB colour cycles in terms of a direct response of regional climate to low latitude precession dominated insolation forcing. The inferred local increase in precipitation may come from the African monsoon or the Atlantic system. It seems difficult, however, to attribute increased rainfall during reddish layer deposition directly to intensified monsoonal circulation in view of the northward location of AEB (34°N); this position may have prevented the African monsoon from directly affecting the region, probably also during the Messinian [Tuenter, pers. comm. 2005]. Such a scenario is consistent with early Pliocene well log records from the Gulf of Cadiz, which reveal increased fluvial input during precession minima [Sierro et al., 2000]. Moreover, the carbonate dilution cycles of Plio-Pleistocene age that were recovered by deep-sea drilling off-shore Northwest Africa at ~20°N reveal an opposite phase relation with precession, indicating that in contrast to our AEB results the terrigenous input is here of eolian origin [e.g., Tiedemann et al., 1994]. Other studies performed in the equatorial Atlantic off Africa also show maximum wind strength and eolian input during precession maxima on the basis of pollen records [e.g., Hooghiemstra et al., 1989] and enhanced Al contributions [Matthewson et al., 1995], the latter being used as a proxy for wind strength. These eolian dust records from lower latitudes are generally linked to the Saharan Air Layer (SAL) associated with the African Easterly Jet (AEJ). Thus, these carbonate dilution cycles seem to exclude a direct monsoonal explanation for the carbonate (colour) cycles of AEB, because they show the strongest terrigenous input – of eolian origin – at times of precession maxima while the drilling sites are located further south than AEB and should thus contain a stronger monsoonal signal, unless they are outside the area of river influence.

5.6.1.3 Fluvial or eolian origin of the terrigenous material?

Apart from Mediterranean sapropels and contrary to the open marine carbonate cycles situated further south, the AEB colour cycles also share many similarities with carbonate cycles in cores spanning the last 225-250 kyr that were recovered Northeast of the Canary Islands off Morocco between 30 and 32°N [Moreno et al., 2001; Bozzano et al., 2002]. Carbonate minima in these sediments show a similar in-phase relation with precession minima, leading the precession signal in planktonic $\delta^{18}\text{O}$ with ~4 kyr, and have similarly been interpreted as dilution cycles. However, the carbonate dilution at these sites is attributed to an eolian rather than a fluvial component,

because the site locations are about 200 km off the Moroccan margin in the pathway of present-day dust plumes originating in the Sahara. The enhanced eolian input has been related to increased storminess and atmospheric turbulence at tropical latitudes at times of precession minima which in turn would have triggered the generation, uptake and transport of dust from North African source areas [Moreno et al., 2001; Bozzano et al., 2002]. The eolian interpretation is based on the fact that 23-kyr maxima in Fe/Al and Al and minima in Ca are in anti-phase with each another (and in-phase with precession minima), where Al is a proxy for the amount of fine grained terrigenous clastics and Fe (or Fe/Al) for the eolian component [Bozzano et al., 2002]. This eolian dust influx at somewhat higher latitudes might not be linked to the SAL but is related to the low-level north-eastern trade winds [e.g., Stuut et al., 2005], while sirocco winds may play an additional role (see also <http://visibleearth.nasa.gov/>).

One would thus expect to find a similar relation of the late Pleistocene carbonate cycles with precession as observed for the AEB colour cycles, namely that prominent carbonate minima and Al maxima coincide with high amplitude precession minima at times of eccentricity maxima. The two strongest Ca(CO₃) minima and Fe/Al and Al maxima occur, however, at times of minimum precession amplitude and eccentricity minima during full glacial stages MIS 4 and 6 [Moreno et al., 2001; Bozzano et al., 2002], suggesting an overprint by the ~100 kyr glacial cycle. One possible explanation might be that these two distinct CaCO₃ minima represent dissolution events [see Bozzano et al., 2002]. In case they are indeed caused by dilution, it is plausible that the terrigenous clastics are of eolian rather than of fluvial origin in view of the more arid climate conditions in Northwest Africa during glacial periods. Accordingly, the same (eolian) mechanism might also be true both for precession-induced carbonate cycles that occur during late Pleistocene interglacial periods (i.e., at times of maximum eccentricity) and the AEB colour (carbonate) cycles.

The interpretation of an eolian origin for minima in carbonate content recorded during precession minima by Moreno et al. [2001] and Bozzano et al. [2002] is consistent with pollen records from Northwest Morocco and the northern borderlands of the Mediterranean, indicating more arid climate conditions during the early Holocene [Cheddadi et al., 1998; COHMAP, 1988]. Most studies show, however, that the early Holocene is a period of humid climate conditions in northern Africa, the so-called African Humid or Pluvial Period, linked to a strengthening of the African monsoon in response of the last Northern Hemisphere summer insolation maximum (i.e., precession minimum) at 10.5 ka [e.g., Gasse and Van Campo, 1994; deMenocal et al., 2000 and references therein]. In line with this evidence, long pollen records from marine piston cores suggest a southward expansion of Mediterranean vegetation to the expense of the Sahelian type during precession minima [e.g., Hooghiemstra, 1987]. Unfortunately, pollen are extremely rare in sediments from AEB and, hence, do not provide a conclusive answer to whether climate became more humid or arid during deposition of the reddish layers. Additional studies of the terrigenous fraction, including clay mineral analysis and chemical characterization and electron microscopic examination of the different grain-size components may therefore be required to solve this enigma.

5.6.2 Eccentricity-related variations

Apart from precession, eccentricity related peaks show up in most spectra of the physical, chemical and biological records. The expression of eccentricity is particularly evident in PC-1 (ICP), Ca (%), *Globigerinoides* and colour, and less obvious in MS, SST and the stable isotope records, except the benthic $\delta^{13}\text{C}$, which reveals a very strong 100-kyr signal. Evidently, the studied set of proxies are all strongly related to lithology and, hence, to the colour cycles which reveal the expression of the 100-kyr and 400-kyr eccentricity as small- and large-scale clusters of more prominent reddish

layers, respectively. The presence of ~100-kyr and ~400-kyr spectral peaks does not reflect the direct climate response to eccentricity itself (even though eccentricity is the only cycle that affects the total insolation annually received by the Earth), but most likely the non-linear response to the climatic precession cycle, which is modulated by eccentricity. This non-linearity is evident from the fact that the magnitude of the shifts in these proxies follow the amplitude changes in precession in one direction only, namely that of precession minima. Shifts in the opposite direction almost never cross a baseline. This is particularly the case for the Ti/Al record, which, in spite of a trend to higher values through time, shows shifts to lower values in the reddish layers only and relatively constant values of about 0.085–0.095 in the beige layers. Such a ‘clipped response’ is well known from Pleistocene proxy records that reflect the intensity of the African monsoon in North Africa [e.g., Ruddiman, 2001]. From this it seems reasonable to expect that the monsoonal system plays a major role in the formation of the colour cycles at AEB in view of the clipped response in some proxy records. It is anticipated, however, that such a clipped response does not exclusively apply for the African monsoon, but could also count for the Atlantic system.

The above scenario of a non-linear climate response to low-latitude insolation forcing might also explain the very strong 100-kyr signal in benthic $\delta^{13}\text{C}$, since there is no direct evidence for 100-kyr fluctuations in Antarctic ice volume during the late Miocene. Below we will show that the benthic $\delta^{13}\text{C}$ record of AEB shows a striking similarity with benthic $\delta^{13}\text{C}$ records from the open ocean, suggesting that we are dealing with a global phenomenon. Bickert et al. [2004], in a study of ODP Site 999 in the Caribbean, put forward that the 100-kyr cycles in benthic $\delta^{13}\text{C}$ they observe are the result of global changes in the $\delta^{13}\text{C}$ of the dissolved inorganic carbon linked to variations in terrigenous input to the oceans. In particular, they found that the strong 100-kyr cyclicity in the benthic $\delta^{13}\text{C}$ record of ODP Site 999 correlates inversely with the MS record of ODP Site 926 from Ceara Rise. They explained the strong 100-kyr cycle in the terrigenous input (MS) by a nonlinear response of precession to eccentricity, which drives variations in the intensity of trade winds and the precipitation and weathering intensity over the South American continent [e.g., Harris and Mix, 1999]. In accord, the strong 100-kyr cycle in benthic $\delta^{13}\text{C}$ of AEB coincides with eccentricity maxima, and with maxima in the 100-kyr component of the terrigenous influx, i.e. PC-1 (ICP) (Fig. 5.9), suggesting that low-latitude precession-related climate (i.e., arid versus humid) cycles are controlling the short eccentricity related variations in deep-sea $\delta^{13}\text{C}$.

5.6.3 Obliquity-paced climate cycles

5.6.3.1 Indirect response through glacial-interglacial cycles

The benthic and planktonic $\delta^{18}\text{O}$ records of Ain el Beida (see also **Chapter 3**) have recently been published and fit perfectly into a standard oxygen isotope stratigraphy and astronomically tuned chronology for the latest Miocene [Van der Laan et al., 2005]. The dominance of the obliquity-related signal in both $\delta^{18}\text{O}$ records confirms that obliquity-driven glacial cycles exerted an overriding control on benthic oxygen isotope records of that time [Hodell et al., 1994, 2001; Shackleton et al., 1995b; Vidal et al., 2002, among others]. An important obliquity component is also present in the $\delta^{13}\text{C}$ records of AEB (with shifts of 0.2 to 0.5‰), which is almost inversely related to the benthic $\delta^{18}\text{O}$ record. The 41-kyr maxima (minima) in benthic $\delta^{13}\text{C}$ lag minima (maxima) in benthic $\delta^{18}\text{O}$ by ~2 kyr (Fig. 5.9; Tab. 5.1) and we therefore attribute these shifts to glacial-interglacial bound variations in the storage of carbon between reservoirs as found for the Plio-Pleistocene glacial cycles [Shackleton, 1977].

To support our interpretation of a prime glacial-interglacial control on the observed obliquity-related $^{13}\text{C}/^{12}\text{C}$ shifts, we compared the $\delta^{13}\text{C}$ records of AEB with the benthic $\delta^{13}\text{C}$ record of ODP Site 982 in the North Atlantic [Hodell et al., 2001] for which an improved chronology was established [Van der Laan et al., 2005]. The benthic $\delta^{13}\text{C}$ records reveal a near peak-to-peak correlation, with similar (obliquity-related) shifts and an interval between 5.8 and 5.5 Ma when both obliquity and precession amplitudes were reduced (Fig. 5.10). Results of band-pass filtering and cross-spectral analysis reveal a nearly in-phase relationship between 41-kyr $\delta^{13}\text{C}$ maxima, $\delta^{18}\text{O}$ minima, and maximum obliquity for both AEB and ODP Site 982. Moreover, variations in the amplitude of the filtered components are the same for all three records and can be linked to similar variations in obliquity amplitude (Fig. 5.10). Therefore, the similarities between the $\delta^{13}\text{C}$ records from AEB and Site 982 are most likely due to obliquity-driven glacial-interglacial bound variations in $\delta^{13}\text{C}$ despite their different latitudinal positions and oceanographic settings.

A first possible explanation for glacial-controlled changes in $\delta^{13}\text{C}$ is that isotopically light terrestrial carbon is stored in the deep ocean during glacial periods as found for the Pleistocene [e.g., Shackleton and Pisias, 1985; Oppo et al., 1995]. An alternative explanation for lowered $\delta^{13}\text{C}$ during glacials is an increase in ocean alkalinity because the $^{13}\text{C}/^{12}\text{C}$ ratios of the calcite shells of foraminifera decrease with increasing seawater CO_3^{2-} [Spero et al., 1997]. But this mechanism is less likely in view of the location of AEB north of the reach of Antarctic Intermediate Waters, which may transmit water enriched in CO_3^{2-} to low latitudes during glacial times.

Pleistocene data show that shifts in benthic $^{13}\text{C}/^{12}\text{C}$ ratios associated with glacial-interglacial variability on obliquity timescales are in the order of 0.35–0.4‰ [see Ruddiman, 2001, pp. 244], which is in the same order of magnitude in AEB. Because the planktonic and benthic $\delta^{13}\text{C}$ records revealed a strong covariance with obliquity-related shifts of about the same magnitude, it is likely that planktonic $\delta^{13}\text{C}$ experienced these glacial-interglacial bound $\delta^{13}\text{C}$ variations as well. The reason why 41-kyr planktonic $\delta^{13}\text{C}$ minima show a small time lag relative to 41-kyr benthic $\delta^{13}\text{C}$ minima is less clear (Figs. 5.9 and 5.10). Possibly there is an additional factor influencing the obliquity-related signal in planktonic $\delta^{13}\text{C}$ that is unrelated to glacial-interglacial carbon storage, e.g., $\delta^{13}\text{C}$ changes due to CO_2 exchanges between surface waters and the atmosphere and/or the deep ocean. Note that the planktonic $\delta^{13}\text{C}$ record was smoothed with a 3 point moving average (see results).

Changes in $\delta^{13}\text{C}$ due to variations in the formation in North Atlantic Deep Water (NADW) may also have played a role. A reduction in NADW formation during glacial times may lead to a decrease in $\delta^{13}\text{C}$ in the study area because NADW is relatively enriched in $\delta^{13}\text{C}$. The reduction of a southward moving NADW would have been accompanied by an increased northward influence of $\delta^{13}\text{C}$ -depleted Southern Ocean Water (SOW), consisting of Antarctic Bottom Water (AABW) and recirculated Pacific Deep Water [e.g., Raymo et al., 1989]. However, AEB is not directly located within the transport path of NADW and its paleodepth of 500–1000 m seems too shallow to pick up the deep water signal.

Obliquity-related variations are not only present in $\delta^{18}\text{O}$ and $\delta^{13}\text{C}$ but also in SST, colour, PC-2 (Plankton) and *Globigerinoides* records of AEB. The 41-kyr cycles in *Globigerinoides* and PC-2 (Plankton) are dominantly present but the 41-kyr SST and colour cycles are less obvious due to the strong precession influence. The obliquity-controlled variations in these proxies are well defined at times of the 400-kyr eccentricity minima around 5.6 and 6.1 Ma, whereby 41-kyr maxima in SST, PC-2 (Plankton), colour and *Globigerinoides* are strongly coherent and in-phase with 41-kyr $\delta^{18}\text{O}$ minima, and, thus, with obliquity and insolation minima. This suggests that

obliquity-controlled glacial cycles influenced local SSTs and associated nutrient levels especially at times of 400-kyr eccentricity minima when precession amplitude is strongly reduced.

The influence of glacial cycles on regional African climates during the late Pliocene and Pleistocene has been addressed by many authors [e.g., Sarnthein et al., 1982; Pokras and Mix, 1985; deMenocal et al., 1993; Ruddiman et al., 1989] and extensively modeled [e.g., Manabe and Broccoli, 1985; Kutzbach and Guetter, 1986; Broccoli and Manabe, 1987]. From these studies it appeared that the glacial-interglacial influence on African climate proceeds via heating and cooling of North Atlantic surface waters, thereby influencing the northeasterly low-level trade winds as well as the moisture transport over Northwest Africa. Accordingly, the 41-kyr components in SST and PC-2 (Plankton) most likely reflect the direct thermal response to ice sheet and sea ice extension and retreat in the North Atlantic. In addition, SSTs could have also been lowered during glacial periods through an intensified atmospheric circulation, resulting in stronger Northeast trade winds along Northwest Africa [Sarnthein et al., 1982; Hooghiemstra et al., 1987; McIntyre et al., 1989; deMenocal and Rind, 1993; Bertrand et al., 1996; Martinez et al., 1999]. This intensification would have increased upwelling of deep and thus colder waters, which provide the surface waters with nutrients causing higher productivity conditions. The shifts to light values in benthic $\delta^{13}\text{C}$ and the increase in the difference between planktonic and benthic $\delta^{13}\text{C}$ are consistent with a glacially enhanced productivity scenario, although the changes in $\Delta\delta^{13}\text{C}$ are largely dictated by benthic $\delta^{13}\text{C}$ and not by the planktonic $\delta^{13}\text{C}$ record. It should be taken into account however that the planktonic $\delta^{13}\text{C}$ record is derived from *Globigerinoides obliquus*, which is not an upwelling related species and thus may bias the planktonic $\delta^{13}\text{C}$ record to the more oligotrophic season of the year. Sinistrally-coiled neogloboquadrinids do not show a strong obliquity signal in their spectrum (Fig. 5.4a) to confirm a glacial-controlled productivity scenario.

A direct effect of obliquity-paced glacial cyclicity on regional climate may also explain the obliquity component in colour, which like SST and PC-2 (Plankton) is most prominent during the 400-kyr eccentricity minimum between ~5.75-5.6 Ma (Fig. 5.6a) that coincides with some strong glacial stages as observed in both $\delta^{18}\text{O}$ records (e.g., TG20 at 5.75 Ma) [Van der Laan et al., 2005]. In this interval, maximum values in the filtered 41-kyr components of colour, *Globigerinoides* spp., benthic $\delta^{13}\text{C}$, SST and PC-2 (Plankton), and minimum values in the 41-kyr components of both $\delta^{18}\text{O}$ records, *G. margaritae* and Ti/Al coincide with obliquity maxima. The Ca (%) and PC-1 (ICP) records do not reflect a clear obliquity signal in this interval, suggesting that the obliquity-related variations in colour do not reflect purely changes in terrigenous input as inferred for the precession-bound variations. Probably, they reflect changes in the terrigenous composition. This would imply that the most distinct red-coloured layers (i.e., highest a^* values) occur during interglacial periods, when the dust flux input (i.e., low Ti/Al values) is at a minimum due to the overall more humid climate conditions. It can be argued that these wetter climate conditions during interglacial periods resulted from more active Atlantic depressions, when surface waters were warmer and air temperatures higher; as a consequence the air could contain more moisture. During glacial periods, arid climate conditions prevailed, leading to maximum dust flux (i.e. maximum Ti/Al values) and hence will have suppressed the formation of a precession-related reddish layer (i.e., low a^* values). This interpretation is in line with an eolian origin for the 41-kyr paced dilution cycles of the Pliocene and Pleistocene when atmospheric circulation is enhanced at times of minimum obliquity and glacial stages [Sarnthein et al., 1982; McIntyre et al., 1989; Tiedemann et al., 1989; Balsam et al., 1995].

5.6.3.2 Direct response to astronomical forcing and the African monsoon

Although an obliquity-induced glacial-interglacial effect on regional climate may explain the obliquity-controlled variations in SST, PC-2 (Plankton), *Globigerinoides* spp. and colour variations, here we will discuss the possibility of a more direct coupling between obliquity forcing and regional climate changes. Today, the climate in Northwest Africa is similar to that experienced by the Mediterranean with warm and dry summers and cool and wet winters, although the amount of precipitation is relatively low. Summer conditions are largely determined by the strength of the Azores High, while winter conditions are controlled by the Atlantic system with precipitation being related to cyclonic activity of the Westerlies and positively correlated with the NAO (North Atlantic Oscillation) [e.g., Moulin et al., 1997; Knippertz et al., 2003].

Intermediate complexity climate modeling experiments, including present-day boundary conditions, have shown that maximum obliquity configurations caused increased precipitation conditions in the region, especially during autumn [Tuenter, 2004], although it should be mentioned that precipitation is difficult to model with these type of models for mid-latitudes. This simulation, however, is consistent with the wetter climate conditions during obliquity maxima found at AEB, and with the interpretation of obliquity controlled variations in sonic logs from drill-sites in the Gulf of Cadiz [Sierra et al., 2000]. In addition, obliquity controlled variations are further known from Middle-Upper Miocene cyclic lacustrine to distal alluvial fan-floodplain successions in Spain [Abdul Aziz et al., 2003]. At that time obliquity controlled glacial cyclicity was either lacking or not distinctly present, suggesting that the 41-kyr dry-wet climate alternations in Northwest Africa and Spain are the result of a direct response to the obliquity forcing.

The 41-kyr signal in the above proxies may alternatively be related to variations in the strength of the African monsoon, which was recently shown to contain an obliquity signal, mainly related to summer heating of the Eurasian continent during obliquity maxima [Tuenter et al., 2003]. However, as already mentioned, the major obstacle hereby is the question whether the monsoon, which mainly influences the moisture budget at tropical latitudes, could have directly affected the region of NW Morocco around 35°N where AEB is located.

An intriguing aspect is that similar obliquity related variations are found in the sapropel patterns of the Mediterranean [Lourens et al., 1996]. These patterns, reflecting precession-obliquity interference, are clearly related to obliquity induced changes in regional climate because they are consistently found throughout the last 14 myr also at times that obliquity-paced glacial periods were absent. It is important to note that similar correlative precession-obliquity interference patterns are also clearly present in the colour cycles of the Oued Akrech section located in Northwest Morocco, which is slightly older than AEB and was used to define the Tortonian-Messinian boundary [Hilgen et al., 2000].

In essence, the main goal would be to discriminate between 41-kyr components in SST, PC-2 (Plankton), *Globigerinoides* spp. and colour cycles that reflect a direct ice driven response to glacial-interglacial cycles and those that are linked to a direct obliquity forcing of regional climate. Our cross-spectral results of the various proxy records, however, did not reflect a clear “early” and a “late” response group [see Imbrie et al., 1992].

5.6.4 Trends and events

Apart from cyclic variability, long-term trends and short-term events can also be recognized in the proxy records of AEB. Next to trends related to the expression of the long-period (400-kyr) eccentricity cycle (Fig. 5.8), several proxies, such as colour, Ca (%), Ti/Al and other element/Al ratios [E. van der Laan, unpublished data], show an overall long-term trend. This trend in

elemental ratios may reflect the ongoing aridification of regional climate in the course of the late Messinian or an overall increase in grain size caused by shallowing of the site of deposition [see Warny et al., 2003].

The colour record shows much reduced values in the lowermost part of the section, but this interval corresponds to the very fresh basal part which did not show signs of weathering (the lowermost 5 m were actually dug with the help of an excavator). The following paragraphs deal with two events that are particularly evident and occur at the onset of the Messinian Salinity Crisis around 6 Ma and during the interval from 5.8 to 5.73 Ma.

5.6.4.1 The ~6 Ma event

One of the most conspicuous aberrations in the proxy records of AEB is the marked ~1.0‰ negative excursion in planktonic $\delta^{13}\text{C}$ that occurs between 6.01 and 5.99 Ma and that is associated with glacial stage TG34 (Fig. 5.10). This event has an amplitude that is as strong as the well-known 'late Miocene carbon shift' across the Tortonian/Messinian boundary [e.g., Hodell et al., 2001]. This glacial-bound excursion does not show an exceptional signature in the benthic $\delta^{13}\text{C}$ records of AEB and ODP Site 982 in the North Atlantic, suggesting that the planktonic $\delta^{13}\text{C}$ signal is strongly amplified by changes in the surface water characteristics of the water mass residing in the area of Northwest Morocco. Because AEB was located in the opening of the Rifian Corridor, within the pathway of outflowing Mediterranean waters (here denoted as Mediterranean Outflow Water, MOW), the $\delta^{13}\text{C}$ of this MOW is likely to have affected $\delta^{13}\text{C}$ values at AEB. The modern MOW, leaving the Mediterranean through the Strait of Gibraltar at a depth of about 800 m, has been reported as a water mass with heavy $\delta^{13}\text{C}$ values of about 1.3‰ [Duplessy, 1972; Zahn et al., 1987]. This value approximately equals the mean $\delta^{13}\text{C}$ value observed at AEB prior to the marked excursion at ~6.0 Ma, just before the initiation of the Messinian Salinity Crisis dated at 5.96 Ma [Krijgsman et al., 1999a]. Krijgsman et al. [1999a] report the final closure of the eastern end of the Rifian Corridor around ~6.0 Ma. Assuming that this had a pronounced effect on the outflow of MOW, a sudden decrease in this outflow would have resulted in a strong decrease in $\delta^{13}\text{C}$ values at AEB. Because the strong shift is only observed in planktonic $\delta^{13}\text{C}$, conditions in the corridor may have been restricted to such an extent that Mediterranean waters flowed out at relatively shallow depths by that time. The strong covariance between the planktonic and benthic $\delta^{13}\text{C}$ records and the small $\Delta\delta^{13}\text{C}$ values after 6.0 Ma suggests that both $\delta^{13}\text{C}$ records display a roughly similar isotopic composition that might be related to ongoing restriction in the Rifian Corridor.

Just after the strong planktonic $\delta^{13}\text{C}$ shift, several other proxy records show marked excursions in the interval between 5.99 and 5.95 Ma that corresponds to a 100-kyr eccentricity minimum characterized by more vague reddish layers due to low precession amplitudes. At the same time obliquity reaches a maximum at 5.98 Ma. MS shows strong peaks at 5.99 and 5.96 Ma and Ti/Al peaks at 5.97 Ma, falling exactly in between the MS maxima. The Ti/Al peak (almost) exactly coincides with the marked peak in sedimentation rate [Van der Laan et al., 2005], and with a prominent low in gamma ray attenuation (GRA) values at 5.96 Ma reflected in Site 982 [Hodell et al., 2001, modified after Van der Laan et al., 2005]. This peak in sedimentation rate, that coincides with the base of the lower evaporite unite in the Mediterranean [Krijgsman et al., 1999a; Sierro et al., 2001], is truly remarkable, because it falls within a 400-kyr eccentricity minimum when normally reduced sedimentation rates are reached [Van der Laan et al., 2005].

5.6.4.2 The 5.8 to 5.73 Ma event

Between 5.8 and 5.73 Ma, *G. margaritae* shows peak abundances up to 20% in the beige layers. These peaks coincide exactly with peak glacial stages TG22 at 5.79 Ma and TG20 at 5.75 Ma as observed in the benthic and planktonic $\delta^{18}\text{O}$ records from AEB that can be correlated with records from the open ocean [Van der Laan et al., 2005]. This suggests a close link between peak glacial periods and high *G. margaritae* abundances. The first *G. margaritae* peak coincides with a strong precession maximum associated with a 100-kyr maximum in eccentricity around 5.8 Ma and in addition coincides with an obliquity minimum. The second peak interval is rather broad and shows increased numbers between 5.78 and 5.74 Ma, just after the maximum in eccentricity. This interval can be divided in two parts: the first part shows a narrow peak in the beige layer of cycle 34 that coincides with a strong precession maximum and is almost coincident with an obliquity maximum; the second part falls together with a minimum in obliquity at 5.75 Ma corresponding to peak glacial stage TG20. It thus appears that peaks in *G. margaritae* are not only connected to obliquity minima but also to precession maxima; the same relation can also be found in the beige layers of cycles 31 and 32 that correspond to precession maxima at 5.84 and 5.82 Ma, respectively. During peak glacial times connected to minima in obliquity, the enhanced atmospheric circulation over Northwest Africa could have promoted vertical mixing, thereby creating favourable conditions for *G. margaritae* in analogy to the peak occurrences of *Globorotalia truncatulinoides* found in late Pleistocene sediments of the Arabian Sea [Reichart et al., 1998].

The period from 5.8 to 5.73 Ma also stands out, as a striking increase to very high values is observed in Ti/Al (and other element/Al ratios, unpublished data) and in the number of planktonic foraminifera per gram dry sediment. The strong increase in Ti/Al (in particular after 5.75 Ma) could be explained by more arid conditions in Northwest Africa and an enhanced atmospheric circulation during peak glacial stage TG22 at 5.79 Ma but in particular during and after stage TG20 at 5.75 Ma. However, the concomitant strong increase in the planktonic flux record suggests that, if more arid conditions prevailed, either the eolian component in the terrigenous material did not play a significant role in the dilution of the stratigraphic succession at AEB (as inferred for the precession-related variations), or that a more or less sudden input of Ti-rich material occurred due to a glacio-eustatic lowering of the base level of erosion. Minimum sedimentation rates, however, suggests that e.g. winnowing could have played a role here, implying that we are dealing with a local event. This is confirmed by the absence of reduced sedimentation rates in the same interval in the nearby Salé core.

5.7 Conclusions

The studied interval between 6.5 and 5.5 Ma of the Ain el Beida section clearly shows the imprint of all orbital parameters. The precession related signal is prominent in the lithological colour cycles and most of the studied proxies suggesting that during precession minima, warmer and more humid climate conditions prevailed in Northwest Africa, as indicated by maxima in e.g. SST, the fine-grained terrigenous component (PC-1 (ICP)) and benthic $\delta^{13}\text{C}$, and minima in $\delta^{18}\text{O}$, the dilution signal (planktonic flux and Ca) and Ti/Al. During precession maxima, more arid conditions prevailed. We attribute the more humid conditions during deposition of the reddish layers to the enhanced precipitation derived from the Atlantic system rather than from the African monsoon.

Obliquity-controlled glacial-interglacial cycles dominate the planktonic and benthic $\delta^{18}\text{O}$ records of AEB, and to a lesser degree SST and humidity (i.e. Ti/Al) variations in Northwest Africa. We attribute the observed warmer and wetter climates during interglacial periods to more active Atlantic depressions, associated with a direct thermal response to the waning ice sheets. Similar to the Pliocene and Pleistocene, the obliquity controlled variations in $\delta^{13}\text{C}$ are inversely related to those in $\delta^{18}\text{O}$, with more depleted values during glacial stages, including a small time lag (~ 2 kyr). The stable carbon isotope records of AEB show a striking resemblance to ODP Sites 982 and 926, suggesting large-scale glacial-bound changes in the deep-sea carbon reservoir.

Next to the orbital related variations, there is a clear imprint of the Messinian Salinity Crisis at AEB. The planktonic $\delta^{13}\text{C}$ record shows a marked negative excursion of $\sim 1.0\%$ at 6.0 Ma that is ascribed to a final step in the closure of the Rifian Corridor which caused a decrease in the outflow of Mediterranean waters enriched in $\delta^{13}\text{C}$. The excursion is followed by a prominent peak in Ti/Al at ~ 5.97 Ma that could as well be related to tectonic closure.

Acknowledgements

Geert Ittmann and Gerrit van 't Veld are thanked for washing samples for foraminiferal analyses. Arnold van Dijk performed the stable isotope analyses. Helen de Waard took care of the ICP-OES measurements. Henry Hooghiemstra from the Institute for Biodiversity and Ecosystem Dynamics of the University of Amsterdam is thanked for fruitful discussions on the climate in northwest Africa. This research was financially supported by the Netherlands Organization for Scientific Research NWO (PIONEER grant to F.J. Hilgen and E. van der Laan).

Astronomical tuning as the basis for high resolution chronostratigraphy: The intricate history of the Messinian Salinity Crisis

with F. Hilgen¹, K. Kuiper^{2,3}, W. Krijgsman² and E. Snel¹

¹ *Dept. of Earth Sciences, Faculty of Geosciences, Utrecht University, Budapestlaan 4, 3584 CD Utrecht, The Netherlands*

² *Paleomagnetic Laboratory Fort Hoofddijk, Faculty of Geosciences, Utrecht University, Budapestlaan 17, 3584 CD Utrecht, The Netherlands*

³ *Isotope Geochemistry, Faculty of Earth and Life Sciences, Free University, De Boelelaan 1085, 1081 HV Amsterdam, The Netherlands*

This chapter has been published in *Stratigraphy* as: Hilgen, F.J., K. Kuiper, W. Krijgsman, E. Snel, and E. van der Laan, 2007. Astronomical tuning as the basis for high resolution chronostratigraphy: the intricate history of the Messinian Salinity Crisis, *Stratigraphy*, 4, 231-238.

Abstract

The Messinian Salinity Crisis (MSC) in the Mediterranean resulted from a complex interplay between tectonic gateway closure and climate evolution. The climate factor, in turn, can be separated into two components, one associated with dominantly precession controlled regional climate change and the other with dominantly obliquity related glacial cyclicality. The influence of these climate changes occurred superimposed on the long(er)-term tectonic trend. Discrimination into the various forcing factors only recently came within reach due to the development of an integrated high-resolution stratigraphy and astronomically tuned age models, both for the Messinian (pre-) evaporate successions in the Mediterranean and for benthic oxygen isotope records from the open ocean.

The application of these time scales in combination with a high-resolution integrated stratigraphic approach showed that 1) the onset of the MSC proper at 5.96 Ma is not related to glacio-eustatic sealevel lowering but can best be attributed to the influence of the 400-kyr eccentricity cycle on regional climate superimposed on a tectonic trend, 2) the main desiccation phase between the Lower and Upper Evaporites coincides with the twin peak glacials TG12-14 suggesting a glacio-eustatic control, 3) the beginning of the Upper Evaporites and Lago Mare phase coincides with the onset of the major deglaciation following peak glacial TG 12, indicating that glacio-eustatic sealevel rise played a role, 4) the Pliocene flooding of the Mediterranean is not related to a glacio-eustatic sealevel rise, and 5) the evaporite cycles are controlled by precession induced regional climate changes

rather than by obliquity forced glacio-eustatic sealevel change. Our astronomical age model for the Mediterranean Messinian is consistent with $^{40}\text{Ar}/^{39}\text{Ar}$ ages of ash layers intercalated in Messinian successions in the Mediterranean. However the intercalibration between astronomical and $^{40}\text{Ar}/^{39}\text{Ar}$ dating has to be taken into account for a direct comparison of these ages.

6.1 Introduction

The Messinian Salinity Crisis is recognized as one of the key events in Earth history attracting a great deal of scientific interest and fuelling imagination with huge waterfalls during the basal Pliocene reflooding of the Mediterranean following desiccation [Hsü et al., 1973]. During the crisis vast amounts of evaporites were deposited when the Mediterranean became progressively isolated from the world oceans (Fig. 6.1); these evaporites are locally sandwiched in between deep marine sediments of Tortonian and Zanclean (Pliocene) age. Scientific debate focused on whether the isolation of the Mediterranean was caused by a (dominant) tectonic or glacio-eustatic control [e.g., Ryan et al., 1973; Kastens, 1992]. Following the glacial scenario, basin isolation resulted from Antarctic ice growth rather than from tectonic closure of the gateways connecting the Mediterranean with the adjacent Atlantic Ocean. However, also the opposite causal relationship has been suggested with ice growth triggered by a reduction in ocean seawater salinity resulting from salt extraction [Ryan et al., 1973].

It became increasingly clear that only a high-resolution age model based on astronomical tuning would provide the necessary means to unravel the intricate and fascinating history of the Messinian Salinity Crisis and, in particular, to discriminate between the role of tectonics and climate. However the Messinian was not incorporated in the astronomical time scale initially developed for the Mediterranean late Neogene because the characteristic diatomaceous and evaporitic sediments of the Messinian were considered less suitable for establishing a reliable magnetostratigraphy and astronomical tuning. Only after most of the Tortonian had been tuned, attention focused again on the Messinian. The first preliminary attempts were based on simple cycle counts in the successive lithostratigraphic units of the Mediterranean Messinian [Hilgen et al., 1995; Vai, 1997]. The tuning of the complete pre-evaporite Messinian resulted in an age of 7.25 Ma for the base of the Messinian and of 5.96 Ma for the onset of the evaporite formation and, hence, the salinity crisis proper [Hilgen and Krijgsman, 1999; Krijgsman et al., 1999a]; these ages are now generally accepted. More problematical, however, proved the tuning of the evaporites themselves, even though these evaporites are arranged in a cyclic fashion as well. This tuning, which is based on cycle counts rather than on cycle patterns, hinted at the presence of a hiatus of ~90 kyr in marginal basins between the Lower and Upper Evaporites, covering an interval when sealevel was significantly lowered in the Mediterranean [Krijgsman et al., 1999a; 2001].

In this paper we will briefly review the progress made in dating the classical Messinian, present the current state of the astronomical tuning, compare it in detail with oxygen isotope records from the open ocean and discuss the implications.

6.2 Definition of the Messinian

The Messinian Stage, named after the town of Messina on Sicily in Italy, was introduced by Mayer-Eymar in 1867 and more precisely defined in 1868 to fill up the gap between the Tortonian

and the now obsolete Astian (sensu lato, equivalent to the present Lower and Middle Pliocene stages of the Zanclean and Piacenzian). Mayer-Eymar [1868] explicitly stated that the middle Messinian is represented by gypsum and associated limestones throughout the Apennines. In the lower Messinian, he included “gelbliche bis schwärzliche Schiefertone” which represent the equivalent of the Tripoli diatomite Formation of Sicily. The upper Messinian contains continental deposits, which indicate a regressive phase prior to the (basal) Pliocene transgression. More recently, Selli [1960] defined the Messinian as the “*intervallo di tempo compreso fra il Tortoniano (strati di Tortona) e il Pliocene (strati di Tabiano), caratterizzato in tutto il Mediterraneo da una crisi di salinità e in Italia essenzialmente da un ambiente iperalino e da sedimenti evaporitici*”.

Selli [1960] argued that the Tortonian/Messinian (T/M) boundary should be placed 25 meter below the local base of the Tripoli diatomite formation in the neostatotype section of the Messinian at Pasquasia–Capodarso on central Sicily, at the level that coincides with the first marked environmental change indicated by dystrophic faunal elements, which he interpreted as the actual beginning of the Messinian salinity crisis. This paleo–environmental criterion made it difficult to export the boundary to the extra-Mediterranean realm lacking the clear expression of the salinity crisis itself. However calcareous plankton biostratigraphy was successfully employed for correlating this level with the adjacent Atlantic [d’Onofrio et al., 1975] and the First Occurrence of *Globorotalia conomiozea* became the new guiding criterion for recognizing the boundary [Colalongo et al., 1979]. The Messinian GSSP or base of the Messinian is now formally defined at the base of the reddish layer of colour cycle no. 15 in the Oued Akrech section located in the Bou Regreg area on the Atlantic side of Morocco [Hilgen et al., 2000]. This level closely coincides with the first common occurrence of the *Globorotalia miotomida* group [Sierro et al., 1993; *G. conomiozea*

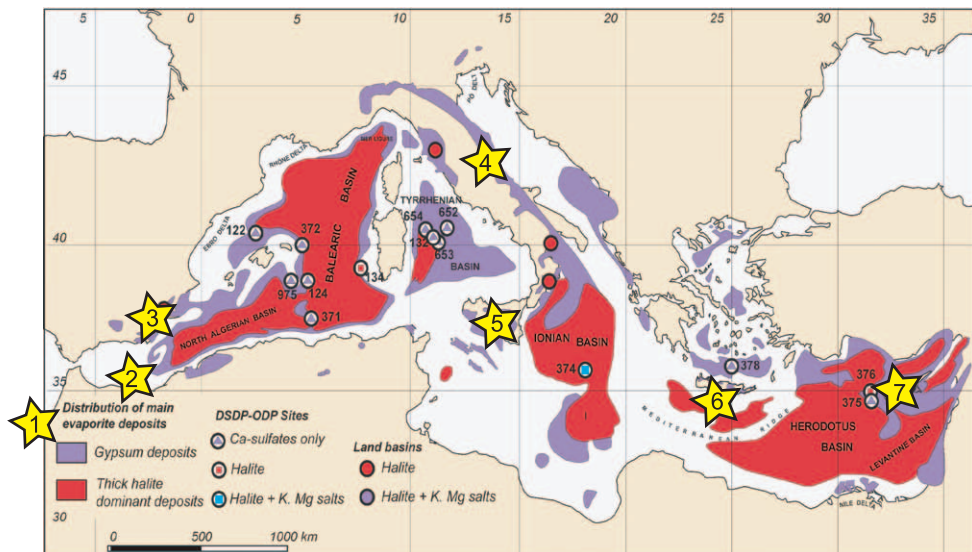


Figure 6.1 Map showing key locations used to construct the astrochronological framework for the Messinian: 1) Bou Regreg; 2) Melilla; 3) Sorbas/Nijar; 4) Northern Apennines; 5) Sicily; 6) Crete/Gavdos; 7) Cyprus. It also shows the distribution and extent of the Messinian evaporites in the Mediterranean with location of the DSDP-ODP sites that recovered evaporitic deposits [modified after Rouchy and Caruso, 2006].

group of Hilgen et al., 1995], falls within the interval of reversed polarity that corresponds to Chron C3Br.1r, and has an astronomical age of 7.25 Ma [Hilgen et al., 2000].

The Messinian-Zanclean (Miocene-Pliocene) boundary also underwent drastic changes in definition in addition to changes in its chronostratigraphic position [e.g., Van Couvering et al., 2000]. Cita [1975], following the discovery of the Pliocene flooding event in deep-sea cores of the successful DSDP Leg 13 in the Mediterranean proposed to define the Miocene-Pliocene boundary at the base of the deep marine Trubi marls in the Zanclean neostatotype section [Cita and Gartner, 1973] at Capo Rossello on southern Sicily. Despite several opposing views, the proposal to keep the Miocene-Pliocene boundary coincident with the base of the Trubi marls and Zanclean Stage, as defined in the Mediterranean at Eraclea Minoa (25 km NW of Capo Rossello), received overwhelming support and was formally accepted [Van Couvering et al., 2000].

6.3 An astrochronology for the Messinian in the Mediterranean Basin

The classic Messinian sequence in the Mediterranean as described from Sicily [Decima and Wezel, 1971] starts with cyclic alternations of open marine marls and sapropels, passes via diatomites into the Lower Evaporites (LE; gypsum, evaporitic limestone and halite), and ends, above an erosional surface and sometimes angular unconformity, with the Upper Evaporites (UE; gypsum, marls) and fresh to brackish water deposits of Lago Mare facies. Here we define the MSC as the interval of evaporite deposition and Lago Mare sedimentation in the Mediterranean starting at 5.96 Ma and ending with the Pliocene reflooding at 5.33 Ma.

6.3.1 Messinian pre-evaporite sequences

Continuous pre-evaporite sequences from all over the Mediterranean were subjected to integrated high-resolution stratigraphic studies in order to construct a cyclostratigraphic framework and develop an astronomical age model that would allow accurate dating of the onset of the MSC. Cyclostratigraphic correlations between the Mediterranean sections are rather straightforward and were confirmed by high-resolution planktonic foraminiferal biostratigraphy. Astronomical tuning of Messinian pre-evaporite cycles to successive insolation peaks generally shows a good to excellent fit between the characteristic sedimentary cycle patterns and the astronomical target curve, including precession/obliquity interference patterns in insolation [Hilgen and Krijgsman, 1999; Sierro et al., 2001; see also Fig. 6.2]. Alternating thick/thin beds correlate in a consistent way with high/low amplitude variations in insolation, proving that no sedimentary cycles are missing and that alternative correlations can be excluded. Additional paleoclimatic studies confirmed that the sedimentary cycles of the Messinian pre-evaporites reflect – precession induced – changes in (circum) Mediterranean climate [Nijenhuis et al., 1996; Sierro et al., 1999].

6.3.2 The “Lower Evaporite” units

The resultant astrochronology shows that the transition to the evaporites occurs at exactly the same sedimentary cycle in sections located in the Western, Central and Eastern Mediterranean [Hilgen and Krijgsman, 1999; Krijgsman et al., 1999a, 2002]. It proves that the MSC is a synchronous event over the entire Mediterranean, the onset of which is dated astronomically at 5.96 ± 0.02 Ma. The pre-evaporitic marl-sapropel cycles are replaced by gypsum-marl cycles of the Lower Evaporites, indicating that the evaporite cycles are related to precession controlled oscillations in (circum) Mediterranean climate as well. As a consequence, gypsum beds correspond to precession

maxima (insolation minima) and relatively dry climate [Krijgsman et al., 2001]. The total amount of cycles in the Lower and Upper Evaporites also excludes an obliquity control; hence, glacio-eustatic sealevel changes are not responsible for the evaporite cycles [Krijgsman et al., 1999a].

The total number of evaporite (gypsum) cycles in the Lower Evaporites of Spain (17 cycles) and Italy (16 cycles) is in good agreement and implies a total duration of approximately 350-370 kyr for the LE [Vai and Ricci Lucchi, 1976; Krijgsman et al., 2001] (Fig. 6.2). Deposition of the LE is thus independent of the paleogeographic and geodynamic setting of the individual basins. Moreover, these evaporites are marine requiring a continuously marine environment, thereby excluding a relative sea level fall that exceeds the paleodepth of the marginal basins (i.e. < 200 m). This scenario favours a deep water model instead of a shallow water (repetitive process of desiccating and reflooding) model for the deep (> 1000 m) Mediterranean basins.

It should be noted here that all the information on the Lower Evaporite units comes from basins indicating a marginal setting during the Messinian. Researchers have traditionally assigned the “N” reflectors (below the salt) as the deep basin equivalents of the marginal Lower Evaporites, but there is thus far no direct evidence of repetitive gypsum/marl cycles in the very deep basins [Roveri and Manzi, 2006; Ryan, 2007].

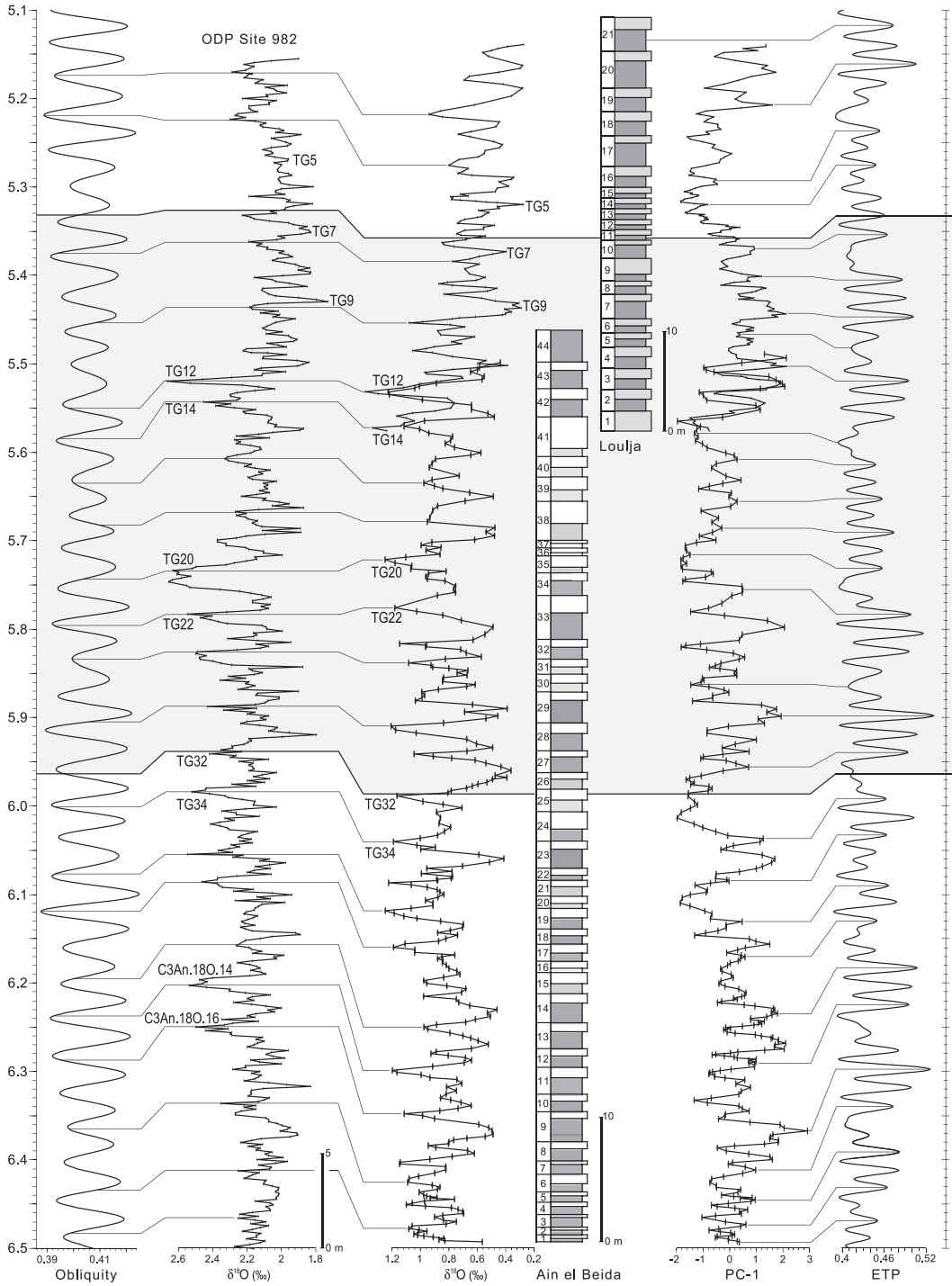
6.3.3 The “Upper Evaporite” units

Complete isolation and possible desiccation were only established after deposition of the Lower Evaporites, when the Mediterranean water level dropped more than 1000 meters as evidenced by incised canyons of the Rhone, Ebro, Po and Nile rivers in the Mediterranean margins [e.g., Clauzon, 1973; see also Ryan, 2007 and references therein]. Deposition of the Upper Evaporite unit, overlying erosional surfaces, took place in an essentially non-marine, deep Mediterranean basin forming a large Lago Mare [e.g., Ruggieri and Sprovieri, 1976]. The UE and lateral equivalents of the Mediterranean uppermost Messinian also display a marked cyclicity, comprising in general seven to eight sedimentary cycles in the Upper Evaporites of Sicily [Decima and Wezel, 1971], the so-called post-evaporitic deposits of Northern Italy [Vai, 1997] and the Zorreras/Feos units of southeast Spain [Fortuin and Krijgsman, 2003]. The total number of sedimentary cycles is in good agreement with the total number of precession peaks (Fig. 6.2), whereas there is clearly not time enough for an obliquity control, thus excluding glacio-eustasy. As the average periodicity for precession in Neogene times is 21.7 kyr, the Upper Evaporite units were deposited in approximately 175 kyr.

Unfortunately, the tuning of the UE is not fully certain because it is based on counting and tuning the number of supposedly precession related UE cycles from the Miocene-Pliocene boundary downward which itself is well tuned. Only the UE at Eraclea Minoa reveal a pattern that can be recognized in the astronomical target curve (Fig. 6.2). Tentatively calibrating the post-evaporite cycles to the insolation curve leaves only a small “Messinian gap” (between 5.59 and 5.50 Ma) during which the desiccation of the Mediterranean, deposition of halite, and the accompanying isostatic rebound processes (tectonic tilting and erosion) must have occurred.

Recent studies in northern Italy indicate that the Colombacci Formation with its characteristic limestone beds that were initially listed as being the full equivalent of the Upper Evaporites, covers a significantly reduced time span. It is now suggested that it corresponds to the younger part of the Upper Evaporites only [Roveri and Manzi, 2006]. The older part of the UE is contained in part by the underlying *Formazione di Tetto*. This unit has been deposited in a deep basin equivalent of the marginal rimmed basins in which the LE were deposited. The older part of the *Formazione di Tetto* consists of reworked evaporites and supposedly covers the so-called Messinian gap (see

extra-Mediterranean - Atlantic



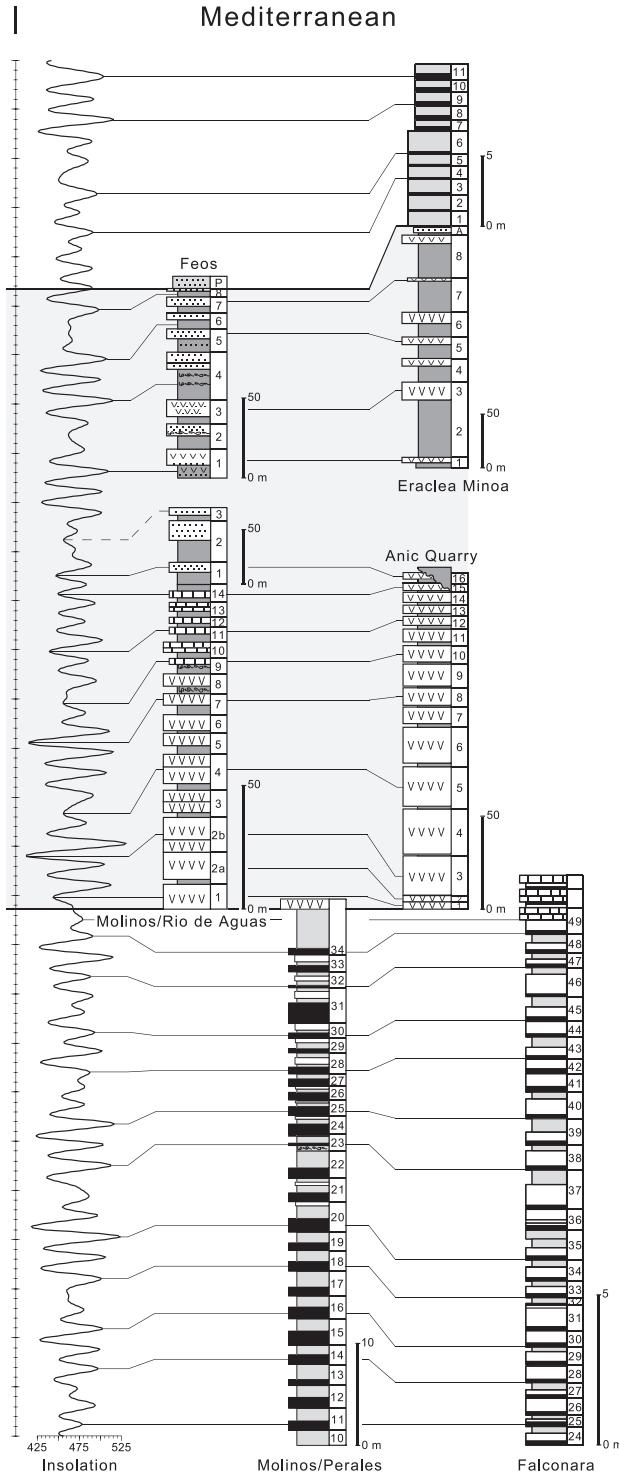


Figure 6.2 Astronomical tuning of Messinian key sections located in the Mediterranean or in the adjacent Atlantic [after Lourens et al., 1996; Fortuin and Krijgsman, 2003; Hilgen and Krijgsman, 1999; Sierro et al., 2001; Krijgsman et al., 2001; Van der Laan et al., 2005, 2006; Hodell et al., 2001] (see Fig. 6.1 for locations). Also shown is the astrochronology of benthic oxygen isotope and geochemical records of Ain el Beida, Loulja and ODP site 982. The first Principal Component of the geochemical element data (ICP) of Ain el Beida and Loulja shows a striking similarity with the precession dominated colour cycles used for the tuning, while the oxygen isotope records are dominated by obliquity. Marked glacial and interglacial stages have been indicated in the isotope records. Shading marks the interval of the Messinian Salinity Crisis.

above) inferred from marginal basins, suggesting that the deep basins in Northern Italy did not experience any desiccation event [Roveri and Manzi, 2006].

6.4 Correlation to the benthic $\delta^{18}\text{O}$ record from the open ocean

Benthic oxygen isotope records are instrumental to test the glacio-eustatic hypothesis for the MSC by unraveling potential linkages between ice volume and evaporite deposition. Clearly these isotope records had to come from outside the Mediterranean, the Messinian in the Mediterranean itself being totally unsuitable for constructing such a record due to aberrant environmental conditions and the (partial) absence of (benthic) foraminiferal faunas. The first high-resolution isotope record covering the interval of the evaporitic Messinian was published by Keigwin [1987] from single hole DSDP Site 522 in the North Atlantic. The Lower and Upper Evaporites were correlated to two successive glacial episodes around 5.2 and 4.8 Ma. Other detailed but better dated isotope records followed and were used to decipher the succession of glacials in the latest Miocene [Hodell et al., 1994, 2001; Shackleton et al., 1995b; Shackleton and Hall, 1997; Vidal et al., 2002; Van der Laan et al., 2005]. A nomenclature for late Miocene isotope stages was introduced by Shackleton et al. [1995b] who numbered distinctly positive isotope peaks from young to old and assigned them to specific magnetic chrons. This numbering scheme was extended by Hodell et al. [1994]. The initial tuning of the isotope records has been modified to some extent over the last years and the tuning seems now well established [Van der Laan et al., 2005, 2006; Fig. 6.2]. Although it is difficult to separate the bottom water temperature from the ice volume signal in benthic $\delta^{18}\text{O}$, amplitudes for glacio-eustatic sealevel lowerings associated with late Messinian glacials have been estimated in the order of ~50 m for peak glacials [Kastens, 1992; Shackleton et al., 1995b]. Note that such amplitudes in the glacial-interglacial signal are comparable with those reached during the late Pliocene and early Pleistocene.

6.4.1 No glacio-eustatic control for the onset of the MSC

Although it was initially tempting to link the onset of evaporite formation to peak glacial stages TG20 and 22 as suggested by Hodell et al. [1994], improved age control showed that this is not the case [Hodell et al., 2001] (Fig. 6.2). In fact the onset of the MSC evaporites at 5.96 Ma coincides with the glacio-eustatic sealevel rise following glacial stage TG32 and can best be explained by the influence of the 400-kyr eccentricity cycle on regional climate and, hence, Mediterranean water budget, which occurs superimposed on the ongoing trend in tectonic isolation of the basin [Krijgsman et al., 1999a].

The oxygen isotope records in particular portrayed a late Messinian glacial interval ranging from ~6.3 to 5.5 Ma marked by heavier values and high-frequency fluctuations, the latter reflecting dominantly obliquity controlled glacial cycles. This interval is particularly evident at ODP Site 982 but is somewhat less obviously expressed in other sites as well. This glacial series contains two prominent peak glacials TG20 and 22 in the lower reversed Gilbert Chron, with astronomical ages of 5.75 and 5.79 Ma (Fig. 6.2); these glacials correspond to the *Globorotalia margaritae* acme in the Bou Regreg area [Benson and Rakic-el Bied, 1996; Krijgsman et al., 2004]. The whole glacial interval ends with two other conspicuous obliquity controlled glacials, TG12 and 14 (with astronomical ages of 5.548 and 5.582 Ma), followed by a marked stepwise deglaciation from TG12 to TG 9 (5.445 Ma) recognized in all oceanic basins [e.g., Shackleton and Hall, 1997; Vidal et al., 2002] (Fig. 6.2). This deglaciation is associated with a distinct glacio-eustatic sealevel rise and is

marked by invasions of the warm water planktonic foraminiferal species *Globorotalia menardii* and *Neogloboquadrina dutertrei* in the Bou Regreg area on the Atlantic side of Morocco that denote this key event in Miocene paleoceanographic history [Van der Laan et al., 2006].

6.4.2 A glacio-eustatic cause for the Mediterranean desiccation phase

The much improved age control suggest that the base of the Upper Evaporites is intimately linked to the beginning of the major stepwise deglaciation between TG12 and TG9 from 5.55 to 5.45 Ma, or more correctly with the first step of the deglaciation between 5.55 and 5.52 Ma [Van der Laan et al., 2006]. This leaves the option that the hiatus, or so-called Messinian gap, between the LE and UE observed in marginal basins corresponds to the last two peak glacials TG12-14 of the Messinian glacial interval. The reason why glacio-eustatic sealevel lowering associated with twinned glacials TG14-12 rather than the more prominent peak glacials TG22-20 resulted in the final desiccation of the Mediterranean is explained by the additional influence of the ongoing trend in the tectonically controlled isolation of the basin. This scenario suggests a strong link between Messinian glacial history and associated glacio-eustatic sealevel change, and the final desiccation/drawdown of the Mediterranean and the subsequent refill at the base of the Upper Evaporites and Lago Mare. If this correlation holds, it may explain why (marginally) marine influences are reported from the Upper Evaporites/Lago Mare [Carnevale et al., 2006] although indications exist that the dominant environmental conditions were not fully marine but dominantly hyposaline. In this way it may even be argued that the “Pliocene” flooding already started at the base of the UE.

6.4.3 End of the MSC: Pliocene flooding of the Mediterranean

The Messinian glacial history and final phases of the MSC made it tempting to link the Pliocene reflooding of the Mediterranean to a significant sea-level rise resulting from deglaciation. Hodell et al. [1994] incorrectly linked the main flooding event to the TG12-9 transition through linear extrapolation of the sedimentation rate in the Salé drill hole. However, improved time constraints revealed that the M/P boundary was significantly younger. Suc et al. [1997] therefore attributed the Pliocene flooding to the abrupt deglaciation associated with TG5 which occurs in the M/P boundary interval and is particularly evident in the record from ODP site 846 [Shackleton et al., 1995b]. Close inspection of the benthic isotope record of the Loulja section (Bou Regreg area) tuned to precession revealed that the M/P boundary (as currently formally defined in the Mediterranean) does not coincide with any major deglaciation [Van der Laan et al., 2006] (Fig. 6.2). This outcome renders credibility to alternative scenarios such as the headward erosion of fluvial incisions in the Gibraltar area [Blanc, 2002; Loget et al., 2005].

6.5 Independent confirmation: $^{40}\text{Ar}/^{39}\text{Ar}$ dating

Independent confirmation of our astronomical age model for the Messinian and the MSC in particular comes from $^{40}\text{Ar}/^{39}\text{Ar}$ dating of ash layers intercalated in tuned cyclic (pre-) evaporite successions or their (carbonate) equivalents in marginal settings. Absolute age uncertainties must be taken into account when $^{40}\text{Ar}/^{39}\text{Ar}$ and astronomical ages are compared. For $^{40}\text{Ar}/^{39}\text{Ar}$ ages the absolute uncertainty is in excess of 2.5% due to uncertainties in the decay constants and ages of the primary dating standards; this full error is in sharp contrast with the generally published much smaller analytical errors. However, intercalibration with the astronomical dating method reduces the absolute uncertainties in $^{40}\text{Ar}/^{39}\text{Ar}$ dating [Kuiper et al., 2004] and has the advantage that a

direct comparison can be made between both dating methods for samples/sections other than the ones used for the intercalibration.

Kuiper et al. [2004] obtained single crystal and multiple fusion $^{40}\text{Ar}/^{39}\text{Ar}$ sanidine ages from ash layers in astronomically tuned sections of the pre-evaporite Messinian. The resultant $^{40}\text{Ar}/^{39}\text{Ar}$ ages are in good agreement with previously published $^{40}\text{Ar}/^{39}\text{Ar}$ ages of the same ash layers but proved to be systematically younger than the astronomical ages by $\sim 0.7\text{--}0.8\%$ if the widely used age of 28.02 ± 0.28 Ma for the Fish Canyon (Tuff) sanidine dating standard [FCs, Renne et al., 1998] was used to calculate the $^{40}\text{Ar}/^{39}\text{Ar}$ ages of the ash layers. Importantly, the systematic bias does not result from errors in the tuning but from uncertainties in the $^{40}\text{Ar}/^{39}\text{Ar}$ dating method mentioned above. Assuming that the astronomical ages are reliable, an intercalibrated astronomical age of 28.20 ± 0.01 Ma could be derived for the FCs standard [Kuiper et al., 2008]. This intercalibration is critical if one aims to directly compare astronomical and $^{40}\text{Ar}/^{39}\text{Ar}$ ages.

More or less synchronously with the development of an astronomical time scale for the Messinian, the first reliable $^{40}\text{Ar}/^{39}\text{Ar}$ biotite ages for the Tortonian/Messinian (T/M) boundary interval were published from northern Italy. The boundary was first dated at 7.23 Ma [Vai et al., 1993] and later bracketed between 7.08 and 7.16 Ma [Laurenzi et al., 1997], both studies using an age of 27.55 Ma for the FCT-3 biotite dating standard. These T/M boundary ages would increase by ~ 170 kyr if recalculated against the astronomically calibrated age of 28.20 Ma for the FCs (or even >200 kyr when the intercalibration between FC sanidine and biotite is also taken into account) [Dazé et al., 2003]. The recalculated ages of Laurenzi et al. [1997] are very close to the astronomical tuned age of 7.25 Ma for the T/M boundary [Hilgen et al., 2000] despite the fact that biotite is considered less suitable for $^{40}\text{Ar}/^{39}\text{Ar}$ than sanidine and no single crystal dates were obtained.

Some of the ash layers from the basinal succession in the Melilla Basin used for the intercalibration of astronomical and $^{40}\text{Ar}/^{39}\text{Ar}$ time have also been dated in nearby exposed shallow marine successions from the basin margin [Roger et al., 2000; Münch et al., 2006]; these ages are consistent with the results from the basinal succession [Kuiper, 2003; Kuiper et al., 2008]. However also some younger ash layers from the Terminal Carbonate Complex (TCC) in the Melilla Basin have been dated; this TCC is considered to be the lateral equivalent of the Lower Evaporites. The – recalculated – ages of these ash layers are consistent with the astronomical age model of Krijgsman et al. [2001], but incompatible with the age model of Riding et al. [1998]. The latter age model starts from a major erosional unconformity that marks a significant hiatus spanning hundreds of thousands of years between the Abad pre-evaporite marls and the Yesares gypsum in the Sorbas and Nijar basins in SE Spain.

Finally, Odin et al. [1997] obtained a $^{40}\text{Ar}/^{39}\text{Ar}$ plateau age of 5.51 ± 0.04 Ma and a total gas age of 5.50 ± 0.04 Ma for biotites from an ash layer intercalated in the Formazione di Tetto directly above the erosional unconformity that developed on top of the LE in northern Italy. The biotite HD-B1 with a K/Ar age of 24.21 Ma was used as monitor dating standard. Intercalibration studies for HD-B1 and FCs have not been published and recalibration to an astronomically calibrated standard is therefore difficult.

Summarizing our astronomical age model for the Mediterranean Messinian is consistent with and thus confirmed by $^{40}\text{Ar}/^{39}\text{Ar}$ ages that are presently available.

Bibliography

- Abdul Aziz, H., W. Krijgsman, F.J. Hilgen, D.S. Wilson, and J.P. Calvo, 2003. An astronomical polarity time scale for the late middle Miocene based on cyclic continental sequences, *Journal of Geophysical Research*, 108 (B3), 2159. doi:10.10129/2002JB001818
- Aguirre, J., and I.M. Sánchez-Almazo, 2004. The Messinian post-evaporitic deposits of the Gafares area (Almería-Níjar basin, SE Spain). A new view of the “Lago-Mare” facies, *Sedimentary Geology*, 168, 71–95. doi:10.1016/j.sedgeo.2004.03.004
- Backman, J., and I. Raffi, 1997. Calibration of Miocene nannofossil events to orbitally tuned cyclostratigraphies from Ceara Rise, *Proceedings of the Ocean Drilling Program, Scientific Results*, 154, 83–99. doi:10.2973/odp.proc.sr.154.101.1997
- Balsam, W.L., B.L. Otto-Bliesner, and B.C. Deaton, 1995. Modern and last glacial maximum eolian sedimentation patterns in the Atlantic Ocean interpreted from sediment iron oxide content, *Paleoceanography*, 10 (3), 493–507.
- Benson, R.H., K. Rakic-El Bied, and G. Bonaduce, 1991. An important current reversal (influx) in the Rifian corridor (Morocco) at the Tortonian-Messinian boundary: the end of Tethys Ocean, *Paleoceanography*, 6 (1), 165–192. doi:10.1029/90PA00756
- Benson, R.H., L.-A.C. Hayek, D.A. Hodell, and K. Rakic-El Bied, 1995. Extending the climatic precession curve back into the late Miocene by signature template comparison, *Paleoceanography*, 10 (1), 5–20. doi:10.1029/94PA02539
- Benson, R.H., and K. Rakic-El Bied, 1996. The Bou Regreg section, Morocco: Proposed Global Boundary Stratotype Section and Point of the Pliocene, *Notes et Mémoires du Service Géologique du Maroc*, 383, 51–150.
- Berger, A., and M.F. Loutre, 1991. Insolation values for the climate of the last 10 million years, *Quaternary Science Reviews*, 10, 297–317.
- Bertrand, P., G.B. Shimmield, P. Martinez, F.E. Grousset, F. Jorissen, M. Paterne, C. Pujol, I. Bouloubassi, P. Buat-Menard, J.-P. Peyrouquet, L. Beaufort, M.-A. Sicre, E. Lallier-Verges, J.M. Foster, and Y. Ternois, 1996. The glacial ocean productivity hypothesis: the importance of regional temporal and spatial studies, *Marine Geology*, 130, 1–9.
- Bickert, T., G.H. Haug, and R. Tiedemann, 2004. Late Neogene benthic stable isotope record of Ocean Drilling Program Site 999: Implications for Caribbean paleoceanography, organic carbon burial, and the Messinian Salinity Crisis, *Paleoceanography*, 19. doi:10.1029/2002PA000799.
- Bijma, J., W.W. Faber Jr., C. Hemleben, 1990. Temperature and salinity limits for growth and survival of some planktic foraminifera in laboratory cultures, *Journal of Foraminiferal Research*, 20, 95–116.
- Blanc, P.L., 2002. The opening of the Plio-Quaternary Gibraltar Strait: assessing the size of a cataclysm, *Geodinamica Acta*, 15, 303–317.
- Bloemendal, J., and P. B. deMenocal, 1989. Evidence for a change in the periodicity of tropical climate cycles at 2.4 Myr from whole-core magnetic susceptibility measurements, *Nature*, 342, 897–899.

- Bossio, A., K. Rakic-El Bied, L. Gianelli, R. Mazzei, A. Russo, and G. Salvatorini, 1976.** Correlation de quelques sections stratigraphiques du bassin Mediterranean sur la base des Foraminifères planktoniques, *Atti Soc. Tosc. Sci. Natl. Mem., Ser. A*, 83, 121-137.
- Bozzano, G., H. Kuhlmann, and B. Alonso, 2002.** Storminess control over African dust input to the Moroccan Atlantic margin (NW Africa) at the time of maxima boreal summer insolation: a record of the last 220 kyr, *Palaeogeography, Palaeoclimatology, Palaeoecology*, 183, 155-168.
- Bradley, W.H., 1938.** Mediterranean sediments and Pleistocene sea-levels, *Science*, 88, 376-379.
- Bramlette, M.N., and F.R. Sullivan, 1961.** Coccolithophoreids and related nannoplankton of the early Tertiary in California, *Micropaleontology*, 7 (2), 129-188.
- Broccoli, A.J., and S. Manabe, 1987.** The influence of continental ice, atmospheric CO₂, and land albedo on the climate of the last glacial maximum, *Climate Dynamics*, 1, 87-99.
- Bukry, D., 1973.** Low-latitude coccolith biostratigraphic zonation, *Initial Reports of the Deep Sea Drilling Project*, 15, 685-703.
- Cande, S.C., and D.V. Kent, 1992.** A new geomagnetic polarity time scale for the Late Cretaceous and Cenozoic, *Journal of Geophysical Research*, 97, 13917-13951.
- Cande, S.C., and D.V. Kent, 1995.** Revised calibration of the Geomagnetic Polarity Time Scale for the Late Cretaceous and Cenozoic, *Journal of Geophysical Research*, 100, 6093-6095.
- Carnevale, G., W. Landini, and G. Sarti, 2006.** Mare versus Lago-mare: marine fishes and the Mediterranean environment at the end of the Messinian Salinity crisis, *Journal of the Geological Society*, 163, 75-80.
- Castradori, D., 1998.** Calcareous nannofossils in the basal Zanclean of the Eastern Mediterranean Sea: remarks on paleoceanography and sapropel formation, *Proceedings of the Ocean Drilling Program, Scientific Results*, 160, 113-124. doi:10.2973/odp.proc.sr.160.005.1998.
- Cheddadi, R., H.F. Lamb, J. Guiot, and S. van der Kaars, 1998.** Holocene climatic change in Morocco: a quantitative reconstruction from pollen data, *Climate Dynamics*, 14, 883-890.
- Chen, J., J.W. Farrell, D.W. Murray, and W.L. Prell, 1995.** Timescale and paleoceanographic implications of a 3.6 m.y. oxygen isotope record from the northeast Indian Ocean (Ocean Drilling Program site 758), *Paleoceanography*, 10, 21-47.
- Cita, M.B., 1975.** The Miocene-Pliocene boundary: history and definition, In: Saito, T. and Burckle, L.D. (Eds.), *Late Neogene Epoch Boundaries*, Micropaleontology Press, Special Publication, 1, 1-30.
- Cita, M.B., and S. Gartner, 1973.** Studi sul Pliocene e sugli strati del passaggio dal Miocene al Pliocene, IV. The stratotype Zanclean. Foraminiferal and nannofossil biostratigraphy, *Rivista italiana di Paleontologia et Stratigrafia*, 79, 503-558.
- Cita, M.B., and W.B.F. Ryan, 1978.** The Bou Regreg section of the Atlantic coast of Morocco. Evidence, timing and significance of a late Miocene regressive phase, *Rivista Italiana Paleontologia*, 84, 1051-1082.
- Clauzon, G., 1973.** The eustatic hypothesis and the pre-Pliocene cutting of the Rhône Valley, In: Ryan, W.B.F. and Hsü, K.J. (Eds.), *Initial Reports of the Deep Sea Drilling Project*, 13, Washington, D.C., U.S. Government Printing office, 1251-1256.
- Clauzon, G., J.-P. Suc, F. Gautier, A. Berger, and M.F. Loutre, 1996.** Alternate interpretation of the Messinian salinity crisis: Controversy resolved? *Geology*, 24, 363-366.
- Clemens, S.C., D.W. Murray, and W.L. Prell, 1996.** Nonstationary phase of the Plio-Pleistocene Asian monsoon, *Science*, 274, 943-948.
- COHMAP Members (Anderson, P.M., et al.), 1988.** Climatic changes of the last 18,000 years: observations and model simulations, *Science*, 24, 1043-1052.

- Colalongo, M.L., A. Di Grande, S. D'Onofrio, L. Gianelli, S. Iaccarino, R. Mazzei, M.F. Poppi Brigatti, M. Romeo, A. Rossi, and G. Salvatorini, 1979.** A proposal for the Tortonian/Messinian boundary, *Annales géologiques des Pays Helléniques*, Tome hors série, 1, 285-294.
- Cullen, H.M., and P.B. deMenocal, 2000.** North Atlantic influence on Tigris-Euphrates streamflow, *International Journal of Climatology*, 20, 853-863.
- Dazé, A., J.K.W. Lee, and M. Villeneuve, 2003.** An intercalibration study of the Fish Canyon sanidine and biotite $^{40}\text{Ar}/^{39}\text{Ar}$ standards and some comments on the age of the Fish Canyon Tuff, *Chemical Geology*, 199, 111-127.
- Decima, A., and F.C. Wezel, 1971.** Osservazioni sulle evaporiti Messiniane della Sicilia centro-meridionale, *Rivista Mineraria Siciliana*, 22 (130-132), 172-187.
- deKaenel, E., and G. Villa, 1996.** Oligocene – Miocene calcareous nannofossil biostratigraphy and paleoecology from the Iberia abyssal plain, *Proceedings of the Ocean Drilling Program, Scientific Results*, 149, 79-145.
- deMenocal, P.B., 1995.** Plio-Pleistocene African Climate, *Science*, 270, 53-59.
- deMenocal, P.B., W. F. Ruddiman, and E. M. Pokras, 1993.** Influences of high- and low-latitude processes on African climate: Pleistocene eolian records from equatorial Atlantic Ocean Drilling Program Site 663, *Paleoceanography*, 8 (2), 209-242.
- deMenocal, P.B., and D. Rind, 1993.** Sensitivity of Asian and African climate to variations in seasonal insolation, glacial ice cover, sea-surface temperature, and Asian orography, *Journal of Geophysical Research*, 98, 7265-7287.
- deMenocal, P.B., J. Ortiz, T. Guilderson, J. Adkins, M. Sarnthein, L. Baker, and M. Yarusinsky, 2000.** Abrupt onset and termination of the African Humid Period: rapid climate responses to gradual insolation forcing, *Quaternary Science Reviews*, 19, 347-361.
- Deuser, W.G., E.H. Ross, and L.S. Waterman, 1976.** Glacial and Pluvial Periods: Their Relationship Revealed by Pleistocene Sediments of the Red Sea and Gulf of Aden, *Science*, 191, 1168-1170.
- Di Stefano, E., R. Sprovieri, and S. Scarantino, 1996.** Chronology of biostratigraphic events at the base of the Pliocene, *Palaeopelagos*, 6, 401-414.
- D'Onofrio, S., L. Giannelli, S. Iaccarino, E. Morlotti, M. Romeo, G. Salvatorini, M. Sampo, and R. Sprovieri, 1975.** Planktonic foraminifera of the Upper Miocene from some Italian sections and the problem of the lower boundary of the Messinian, *Bollettino della Società Paleontologica Italiana*, 14, 177-196.
- Driever, B.W.M., 1988.** Calcareous nannofossil biostratigraphy and paleoenvironmental interpretation of the Mediterranean Pliocene, *Utrecht Micropaleontological Bulletins*, 36, pp. 1-248.
- Duplessy, J.C., 1972.** La géochimie des isotopes stables du carbone dans la mer, Thesis, Note CEA-N-1565, Centre d'Etudes Nucleaires de Saclay, France, pp. 40-50.
- Emeis, K.-C., H. Schulz, U. Struck, M. Rossignol-Strick, H. Erlenkeuser, M. W. Howell, D. Kroon, A. Mackensen, S. Ishizuka, T. Oba, T. Sakamoto, and I. Koizumi, 2003.** Eastern Mediterranean surface water temperatures and $\delta^{18}\text{O}$ composition during deposition of sapropels in the late Quaternary, *Paleoceanography*, 18 (1), PA1005. doi:10.1029/2000PA000617.
- Feinberg, H., and H.G. Lorenz, 1970.** Nouvelles données stratigraphiques sur le Miocene supérieur et le Pliocene du Maroc Nord Occidental, *Notes et Mémoires du Service géologique, Maroc*, 30, 21-26.

- Flecker, R., S. de Villiers, and R.M. Ellam, 2002. Modelling the effect of evaporation on the salinity – $^{87}\text{Sr}/^{86}\text{Sr}$ relationship in modern and ancient marginal-marine systems: the Mediterranean Messinian Salinity Crisis, *Earth and Planetary Science Letters*, 203, 221–233. doi:10.1016/S0012-821X(02)00848-8
- Fortuin, A.R., and W. Krijgsman, 2003. The Messinian of the Nijar Basin (SE Spain): sedimentation, depositional environments and paleogeographic evolution, *Sedimentary Geology*, 160, 213–242. doi:10.1016/S0037-0738(02)00377-9
- Foucault A., and F. Mélières, 2000. Palaeoclimatic cyclicity in central Mediterranean Pliocene sediments: the mineralogical signal, *Palaeogeography, Palaeoclimatology, Palaeoecology*, 158 (3), 311–323.
- Gartner, S., 1992. Miocene nannofossil chronology in the North Atlantic, DSDP Site 608, *Marine Micropaleontology*, 18, 307–313.
- Gasse, F., and E. van Campo, 1994. Abrupt post-glacial climate events in West Asia and North Africa monsoon domains, *Earth and Planetary Science Letters*, 126, 435–456.
- Griffiths, J.F., 1972. The Mediterranean Zone, In: Landsberg, H.E. (Ed.), World survey of climatology, 10: Climates of Africa, chapter 2, Amsterdam London New York, Elsevier, 37–74.
- Herbert, T.D., 1994. Reading orbital cycles distorted by sedimentation: models and examples, In: Orbital forcing and cyclic sequences (Spec. Publ. Int. Ass. Sediment.), 19, 483–507.
- Hilgen, F.J., 1991a. Astronomical calibration of Gauss to Matuyama sapropels in the Mediterranean and implication for the Geomagnetic Polarity Time Scale, *Earth and Planetary Science Letters*, 104, 226–244.
- Hilgen, F.J., 1991b. Extension of the astronomically calibrated (polarity) timescale to the Miocene/Pliocene boundary, *Earth and Planetary Science Letters*, 107, 349–368.
- Hilgen, F.J., and C.G. Langereis, 1993. A critical evaluation of the Miocene/Pliocene boundary as defined in the Mediterranean, *Earth and Planetary Science Letters*, 118, 167–179. doi:10.1016/0012-821X(93)90166-7.
- Hilgen, F.J., L.J. Lourens, A. Berger, and M.F. Loutre, 1993. Evaluation of the astronomically calibrated time scale for the late Pliocene and earliest Pleistocene, *Paleoceanography*, 8, 549–565.
- Hilgen, F.J., W. Krijgsman, C.G. Langereis, L.J. Lourens, A. Santarelli, and W.J. Zachariasse, 1995. Extending the astronomical (polarity) timescale into the Miocene, *Earth and Planetary Science Letters*, 136, 495–510.
- Hilgen, F.J., and W. Krijgsman, 1999. Cyclostratigraphy and astrochronology of the Tripoli diatomite formation (pre-evaporite Messinian, Sicily, Italy), *Terra Nova*, 11, 16–22.
- Hilgen, F.J., L. Bissoli, S. Iaccarino, W. Krijgsman, R. Meijer, A. Negri, and G. Villa, 2000. Integrated stratigraphy and astrochronology of the Messinian GSSP at Oued Akrech (Atlantic Morocco), *Earth and Planetary Science Letters*, 182, 237–251. doi:10.1016/0012-821X(91)90082-S
- Hilgen, F.J., K. Kuiper, W. Krijgsman, E. Snel, and E. van der Laan, 2007. Astronomical tuning as the basis for high resolution chronostratigraphy: the intricate history of the Messinian Salinity Crisis, *Stratigraphy*, 4, 231–238.
- Hodell, D.A., and J.P. Kennett, 1986. Late Miocene-early Pliocene stratigraphy and paleoceanography of the South Atlantic and southwest Pacific Oceans: A synthesis, *Paleoceanography*, 1, 285–311.

- Hodell, D.A., R.H. Benson, J.P. Kennett, and K. Rakic-El Bied, 1989. Stable isotope stratigraphy of latest Miocene sequences in northwest Morocco: The Bou Regreg section, *Paleoceanography*, 4, 467-482. doi:10.1029/89PA00550.
- Hodell, D.A., R.H. Benson, D.V. Kent, A. Boersma, and K. Rakic-El Bied, 1994. Magnetostratigraphic, biostratigraphic, and stable isotope stratigraphy of an Upper Miocene drill core from the Salé Briqueterie (northwestern Morocco): A high-resolution chronology for the Messinian stage, *Paleoceanography*, 9 (6), 835-855. doi:10.1029/94PA01838
- Hodell, D.A., J.H. Curtis, F.J. Sierro, and M.E. Raymo, 2001. Correlation of late Miocene to early Pliocene sequences between the Mediterranean and North Atlantic, *Paleoceanography*, 16, 164-178. doi:10.1029/1999PA000487
- Holz, C., J.-B. Stuut, and R. Henrich, 2004. Terrigenous sedimentation processes along the continental margin off NW Africa: implications from grain-size analysis of seabed sediments, *Sedimentology*, 51, 1145-1154.
- Hooghiemstra, H., 1989. Variations of the NW African trade wind regime during the last 140,000 years: changes in pollen flux evidenced by marine sediment records, In: Leinen, M., and Sarnthein, M. (Eds.), *Paleoclimatology and Paleometeorology: Modern and Past Patterns of Global Atmospheric Transport*, NATO ASI Series, Kluwer, Dordrecht, 733-770.
- Hooghiemstra, H., A. Bechler, and H.J. Beug, 1987. Isopollen maps for 18,000 years B.P. of the Atlantic offshore Northwest Africa: Evidence for paleowind circulation, *Paleoceanography*, 2, 561-582.
- Hrouda, F., 1994. A technique for the measurement of thermal changes of magnetic susceptibility of weakly magnetic rocks by the CS-2 apparatus and KLY-2 Kappabridge. *Geophysical Journal International*, 118 (3), 604-612.
- Hsü, K.J., W.B.F. Ryan, and M.B. Cita, 1973. Late Miocene desiccation of the Mediterranean, *Nature*, 242, 240-244.
- Iaccarino, S.M., and A. Bossio, 1999. Paleoenvironment of uppermost Messinian sequences in the Western Mediterranean (Sites 974, 975, and 978), *Proceedings of the Ocean Drilling Program, Scientific Results*, 161, 529-541. doi:10.2973/odp.proc.sr.161.246.1999
- Iaccarino, S.M., D. Castradori, M.B. Cita, E. Di Stefano, S. Gaboardi, J.A. McKenzie, S. Spezzaferri, and R. Sprovieri, 1999. The Miocene-Pliocene boundary and the significance of the earliest Pliocene flooding in the Mediterranean, *Memorie della Societa Geologica Italiana*, 54, 109-131.
- Imbrie, J., J.D. Hays, D.G. Martinson, A. McIntyre, A.C. Mix, J.J. Morley, N.G. Pisias, W.L. Prell, and N.J. Shackleton, 1984. The orbital theory of Pleistocene climate: Support from a revised chronology of the marine $\delta^{18}\text{O}$ record, In: Berger, A., Imbrie, J., Hays, J.D., Kukla, G., Saltzman, B. (Eds.), *Milankovitch and Climate*, NATO ASI Series 126, D. Reidel, Norwell, Mass., 269-305.
- Imbrie, J., E.A. Boyle, S.C. Clemens, A. Duffy, W.R. Howard, G. Kukla, J. Kutzbach, D.G. Martinson, A. McIntyre, A.C. Mix, B. Molino, J.J. Morley, L.C. Peterson, N.G. Pisias, W.L. Prell, M.E. Raymo, N.J. Shackleton, and J.R. Toggweiler, 1992. On the structure and origin of major glaciation cycles: 1. Linear responses to Milankovitch forcing, *Paleoceanography*, 7, 701-738.
- Kastens, K.A., 1992. Did glacio-eustatic sea level drop trigger the Messinian salinity crisis? New evidence from Ocean Drilling Program site 654 in the Tyrrhenian Sea, *Paleoceanography*, 7, 333-356.

- Keigwin, L.D., 1987. Toward a high-resolution chronology for latest Miocene paleoceanographic events, *Paleoceanography*, 2, 639-660.
- Knappertsbusch, M., 2000. Morphologic evolution of the coccolithophorid *Calcidiscus leptoporus* from the early Miocene to Recent, *Journal of Paleontology*, 74, 712-730.
- Knippertz, P., M. Christoph, and P. Speth, 2003. Long-term precipitation variability in Morocco and the link to the large-scale circulation in recent and future climates, *Meteorology and Atmospheric Physics*, 83, 67-88.
- Kouwenhoven, T.J., M.-S. Seidenkrantz, and G.J. van der Zwaan, 1999. Deep-water changes: the near-synchronous disappearance of a group of benthic foraminifera from the Late Miocene Mediterranean, *Palaeogeography, Palaeoclimatology, Palaeoecology*, 152 (3), 259-281.
- Krijgsman, W., F.J. Hilgen, I. Raffi, F.J. Sierro and D.S. Wilson, 1999a. Chronology, causes and progression of the Messinian salinity crisis, *Nature*, 400, 652-655.
- Krijgsman, W., C.G. Langereis, W.J. Zachariasse, M. Boccaletti, G. Moratti, R. Gelati, S. Iaccarino, G. Papani, and G. Villa, 1999b. Late Neogene evolution of the Taza-Guercif basin (Rifian Corridor, Morocco) and implications for the Messinian salinity crisis, *Marine Geology*, 153, 147-160.
- Krijgsman, W., A.R. Fortuin, F.J. Hilgen, and F.J. Sierro, 2001. Astrochronology for the Messinian Sorbas Basin (SE Spain) and orbital (precessional) forcing for evaporite cyclicity. *Sedimentary Geology*, 140, 43-60. doi:10.1016/S0037-0738(00)00171-8
- Krijgsman, W., M.M. Blanc-Valleron, R. Flecker, F.J. Hilgen, T.J. Kouwenhoven, D. Merle, F. Orszag-Sperber, and J.-M. Rouchy, 2002. The onset of the Messinian salinity crisis in the Eastern Mediterranean (Pissouri Basin, Cyprus), *Earth and Planetary Science Letters*, 194, 299-310.
- Krijgsman, W., and L. Tauxe, 2004. Shallow bias in Mediterranean paleomagnetic directions caused by inclination error, *Earth and Planetary Science Letters*, 222, 685-695.
- Krijgsman, W., S. Gaboardi, F.J. Hilgen, S. Iaccarino, E. de Kaenel, and E. van der Laan, 2004. Revised astrochronology for the Ain el Beida section (Atlantic Morocco): No glacio-eustatic control for the onset of the Messinian Salinity Crisis, *Stratigraphy*, 1 (1), 87-101.
- Kuhlmann, H., H. Meggers, T. Freudenthal, and G. Wefer, 2004. The transition of the monsoonal and the N Atlantic climate system off NW Africa during the Holocene, *Geophysical Research Letters*, 31. doi:10.1029/2004GL021267.
- Kuiper, K.F., 2003. Direct intercalibration of radio-isotopic and astronomical time in the Mediterranean Neogene. PhD-Thesis, Utrecht University, *Geologica Ultraiectina*, 235, 224 p.
- Kuiper, K.F., F.J. Hilgen, J. Steenbrink, and J.R. Wijbrans, 2004. $^{40}\text{Ar}/^{39}\text{Ar}$ ages of tephras intercalated in astronomically tuned Neogene sedimentary sequences in the eastern Mediterranean, *Earth and Planetary Science Letters*, 222, 583-597.
- Kuiper, K.F., A. Deino, F.J. Hilgen, W. Krijgsman, P.R. Renne, and J.R. Wijbrans, 2008. Synchronizing rock clocks of Earth history, *Science*, 320, 500-504.
- Kullenberg, B., 1952. On the salinity of the water contained in marine sediments. *Goteborgs Kungl. Vetenskaps Vitterhets-Samhäl. Handlingar*, 6B, 3-37.
- Kutzbach, J.E., 1981. Monsoon climate of the early Holocene: climate experiment with the Earth's orbital parameters for 9000 years ago. *Science*, 214, 59-61.
- Kutzbach, J.E., and P.J. Guetter, 1986. The influence of changing orbital parameters and surface boundary conditions on climate simulations for the past 18,000 year, *Journal of Atmospheric Science*, 43, 1726-1759.

- Laskar, J., F. Joutel, and F. Boudin, 1993. Orbital, precessional, and insolation quantities for the Earth from -20 Myr to +10 Myr, *Astronomy and Astrophysics*, 270, 522-533.
- Laskar, J., P. Robutel, F. Joutel, M. Gastineau, A.C.M. Correia, and B. Levrard, 2004. A long-term numerical solution for the insolation quantities of the Earth, *Astronomy and Astrophysics*, 428 (1), 261-285. doi: 10.1051/0004-6361:20041335
- Laurenzi, M.A., F. Tateo, I.M. Villa, and G.B. Vai, 1997. New radiometric datings bracketing the Tortonian/Messinian boundary in the Romagna potential stratotype sections (northern Apennines, Italy), In: Montanari, A., Odin, G.S. and Coccioni, R. (Eds.), Miocene stratigraphy: An integrated approach, *Developments in Palaeontology and Stratigraphy*, 15, 493-530.
- Londeix, L., 2004. Synthetic Messinian dinoflagellate cyst record from Sicily. 4th International Congress Environment and Identity in the Mediterranean: the Messinian Salinity Crisis revisited, Università di Corsica Pasquale Paoli, Corte, France, Abstracts, 57.
- Lourens, L.J., F.J. Hilgen, L. Gudjonsson, and W.J. Zachariasse, 1992. Late Pliocene to early Pleistocene astronomically forced sea surface productivity and temperature variations in the Mediterranean, *Marine Micropaleontology*, 19, 49-78.
- Lourens, L.J., A. Antonarakou, F.J. Hilgen, A.A.M. van Hoof, C. Vergnaud-Grazzini, and W.J. Zachariasse, 1996. Evaluation of the Plio-Pleistocene astronomical timescale, *Paleoceanography*, 11, 391-413.
- Lourens, L.J., R. Wehausen, and H.-J. Brumsack, 2001. Geological constraints on tidal dissipation and dynamical ellipticity of the Earth over the past three million years, *Nature*, 409, 1029-1033.
- Lourens, L.J., F.J. Hilgen, J. Laskar, N.J. Shackleton, and D.S. Wilson, 2004. The Neogene Period, In: Gradstein, F.M., Ogg, J.G., and Smith, A.G. (Eds.), *A Geologic Timescale 2004*, Cambridge University Press, Cambridge, pp. 409-440.
- Loget, N., J. van den Driessche, and P. Davy, 2005. How did the Messinian Salinity Crisis end? *Terra Nova*, 17, 414-419.
- Manzi, V., Lugli, S., Roveri, M. and B.C. Schreiber, 2009. A new facies model for the Upper Gypsum of Sicily (Italy): chronological and palaeoenvironmental constraints for the Messinian salinity crisis in the Mediterranean, *Sedimentology*, 56, 1937-1960.
- Manabe, S., and A.J. Broccoli, 1985. The influence of continental ice sheets on the climate of an ice age, *Journal of Geophysical Research*, 90, 2167-2190.
- Martinez, P., P. Bertrand, G.B. Shimmield, K. Cochrane, F. Jorissen, J.M. Foster, and M. Dignan, 1999. Upwelling intensity and ocean productivity changes off Cape Blanc (Northwest Africa) during the last 70.000 years: geochemical and micropalaeontological evidence, *Marine Geology*, 158, 57-74.
- Martini, E., 1971. Standard Tertiary and Quaternary calcareous nannoplankton zonation. *Proceedings II Planktonic Conference, Roma 1970*, 2, 739-785.
- Matthewson, A.P., G.B. Shimmield, D. Kroon, and A.E. Fallick, 1995. A 300-kyr high-resolution aridity record of the North African continent, *Paleoceanography*, 10 (3), 677-692.
- Mayer-Eymar, K., 1867. *Catalogue systématique et descriptif des fossiles des terrains tertiaires qui se trouvent du Musée fédéral de Zürich*, Zürich.
- Mayer-Eymar, K., 1868. *Tableau synchronistique des terrains tertiaires supérieurs*, IV ed., Zürich.
- Mazzei, R., I. Raffi, D. Rio, N. Hamilton, and M.B. Cita, 1979. Calibration of late Neogene calcareous plankton datum planes with the paleomagnetic record of Site 397 and correlation

- with Moroccan and Mediterranean sections. *Initial Reports of the Deep Sea Drilling Program*, 47, 375-389.
- McFadden, P.L.**, and M.W. McElhinny, **1988**. The combined analysis of remagnetization circles and direct observations in paleomagnetism, *Earth and Planetary Science Letters*, 87, 161-172. doi:10.1016/0012-821X(88)90072-6
- McIntyre, A.**, W.F. Ruddiman, K. Karlin, and A.C. Mix, **1989**. Surface water response of the equatorial Atlantic Ocean to orbital forcing, *Paleoceanography*, 4, 19-55.
- McKenzie, J.A.**, S. Spezzaferri, and A. Isern, **1999**. The Miocene/Pliocene boundary in the Mediterranean and Bahamas: implications for a global flooding event in the earliest Pliocene, *Memorie della Società Geologica Italiana*, 54, 93-108.
- Meijer, P.Th.** and E. Tuenter, **2007**. The effect of precession-induced changes in the Mediterranean freshwater budget on circulation at shallow and intermediate depth. *Journal of Marine Systems*, 68, 349-365.
- Millies-Lacroix, A.**, **1974**. Carte géotechnique de la région de Rabat. Editions du Service Géologique du Maroc, Notes et Mémoires, 238.
- Moreno, A.**, J. Targarona, J. Henderiks, M. Canals, T. Freudenthal, and H. Meggers, **2001**. Orbital forcing of dust supply to the North Canary Basin over the last 250 kyr, *Quaternary Science Reviews*, 20, 1327-1339.
- Moulin, C.**, C. Lambert, F. Dulac, and U. Dayan, **1997**. Control of atmospheric export of dust from North Africa by the North Atlantic oscillation, *Nature*, 387, 691-694.
- Müller, C.**, **1990**. Nannoplankton biostratigraphy and paleoenvironmental interpretations from the Tyrrhenian Sea, ODP Leg 107 (western Mediterranean), *Proceedings of the Ocean Drilling Program, Scientific Results*, 107, 495-511. doi:10.2973/odp.proc.sr.107.146.1990
- Münch, P.H.**, J.J. Cornee, F. Feraud, J.-P. Saint Martin, M. Ferrandini, F. Garcia, F. Conesa, S. Roger, and M. Moullade, **2006**. Precise $^{40}\text{Ar}/^{39}\text{Ar}$ dating of volcanic tuffs within the upper Messinian sequences in the Melilla carbonate complex (NE Morocco): implications for the Messinian Salinity Crisis. *International Journal of Earth Sciences (Geologische Rundschau)*, 95, 491-503. doi:10.1007/s00531-005-0038-6.
- Nijenhuis, I.A.**, S.J. Schenau, C.H. van der Weijden, F.J. Hilgen, L.J. Lourens, and W.J. Zachariasse, **1996**. On the origin of upper Miocene sapropelites: A case study from the Faneromeni section, Crete (Greece), *Paleoceanography*, 11, 633-645.
- Odin, G.S.**, G.B. Vai, M. Cosca, F. Tateo, and J.C. Hunziker, **1997**. Integrated stratigraphy of the Maccarone section, In: Montanari, A., Odin, G.S. and Coccioni, R. (Eds.), Miocene stratigraphy: An integrated approach. *Developments in Palaeontology and Stratigraphy*, 15, 531-545.
- Ogniben, L.**, **1957**. Petrografia della Serie Solfifera Siciliana e considerazioni geologiche relative, *Memorie Descrittive della Carta Geologica d'Italia*, 33, 275 pp.
- Okada, H.**, and D. Bukry, **1980**. Supplementary modification and introduction of code numbers to the low-latitude coccolith biostratigraphic zonation (Bukry, 1973; 1975), *Marine Micropaleontology*, 5, 321-325.
- Oppo, D.W.**, M.E. Raymo, G.P. Lohmann, A.C. Mix, J.D. Wright, and W.L. Prell, **1995**. A $\delta^{13}\text{C}$ record of Upper North Atlantic Deep Water during the past 2.6 Million years, *Paleoceanography*, 10 (3), 373-394.
- Paeth, H.**, and P. Friederichs, **2004**. Seasonality and time scales in the relationship between global SST and African rainfall, *Climate Dynamics*, 23, 815-837.

- Paillard, D., L. Labeyrie, and P. Yiou, 1996.** Macintosh program performs time-series analysis, *Eos Transactions American Geophysical Union*, 77, 379.
- Peck, D.M., T.M. Missimer, D.H. Slater, S.W. Wise Jr., and T.H. O'Donnell, 1979.** Late Miocene glacial-eustatic lowering of sea level: Evidence from the Tamiami Formation of south Florida, *Geology*, 7 (6), 285-288.
- Petit-Maire, N., and Z. Guo, 1997.** Holocene precipitation over the present-day Sahara desert: Implications for the future, *Episodes*, 20, 232-234.
- Pokras, E.M., and A.C. Mix, 1985.** Eolian evidence for spatial variability of late Quaternary climates in tropical Africa, *Quaternary Research*, 24, 137-149.
- Prell, W.L., and J.E. Kutzbach, 1987.** Monsoon variability over the past 150,000 years, *Journal of Geophysical Research*, 92, 8411-8425.
- Raffi, I., and J.-A. Flores, 1995.** Pleistocene through Miocene calcareous nannofossils from eastern Equatorial Pacific Ocean (Leg 138), *Proceedings of the Ocean Drilling Program, Scientific Results*, 138, 233-286.
- Raffi, I., J. Backman, and D. Rio, 1998.** Evolutionary trends of tropical calcareous nannofossils in the late Neogene, *Marine Micropaleontology*, 35, 17-41. doi:10.1016/S0377-8398(98)00014-0
- Raffi, I., C. Mozzato, E. Fornaciari, F.J. Hilgen, and D. Rio, 2003.** Late Miocene calcareous nannofossil biostratigraphy and astrobiochronology for the Mediterranean region, *Micropaleontology*, 49, 1-26.
- Raymo, M.E., W.F. Ruddiman, J. Backman, B.M. Clement, and D.G. Martinson, 1989.** Late Pliocene variation in northern hemisphere ice sheets and North Atlantic deep water circulation, *Paleoceanography*, 4, 413-446. doi:10.1029/PA004i004p00413
- Reichart, G.J., L.J. Lourens, and W.J. Zachariasse, 1998.** Temporal variability in the northern Arabian Sea Oxygen Minimum Zone (OMZ) during the last 225,000 years, *Paleoceanography*, 13 (6), 607-621.
- Renne, P.R., C.C. Swisher, A.L. Deino, D.B. Karner, T.L. Owens, and D.J. De Paolo, 1998.** Intercalibration of standards, absolute ages and uncertainties in $^{40}\text{Ar}/^{39}\text{Ar}$ dating, *Chemical Geology*, 145, 117-152.
- Riding, R., J.C. Braga, J.M. Martin, and I.M. Sanchez-Almazo, 1998.** Mediterranean Messinian Salinity Crisis: constraints from a coeval marginal basin, Sorbas, southeastern Spain, *Marine Geology*, 146, 1-20.
- Rio, D., E. Fornaciari, and I. Raffi, 1990.** Late Oligocene through Early Pleistocene calcareous nannofossils from Western Equatorial Indian Ocean (Leg 115), In: Duncan, R.A., Backman, J., and Peterson, L.C. (Eds.), *Proceedings of the Ocean Drilling Program, Scientific Results*, 115, 175-235.
- Rio, D., J.E.T. Channell, R. Bertoldi, M.S. Poli, P.P. Vergerio, I. Raffi, R. Sprovieri, and R.C. Thunell, 1997.** Pliocene sapropels in the northern Adriatic area: chronology and paleoenvironmental significance, *Palaeogeography, Palaeoclimatology, Palaeoecology*, 135, 1-25. doi:10.1016/S0031-0182(97)00027-8.
- Roger, S., P. Münch, J.J. Cornée, J.-P. Saint Martin, G. Féraud, S. Pestrea, G. Conesa, and A. Ben Moussa, 2000.** $^{40}\text{Ar}/^{39}\text{Ar}$ dating of the pre-evaporitic Messinian marine sequences of the Melilla basin (Morocco): A proposal for some bio-sedimentary events as isochrons around the Alboran sea, *Earth and Planetary Science Letters*, 179, 101-113.
- Rohling, E. J., 1994.** Review and new aspects concerning the formation of Mediterranean sapropels, *Marine Geology*, 122, 1-28.

- Rohling, E.J., 1999. Environmental controls on salinity and $\delta^{18}\text{O}$ in the Mediterranean, *Paleoceanography*, 14, 706-715.
- Rohling, E.J. and F.J. Hilgen, 1991. The eastern Mediterranean climate at times of sapropel formation, *Geologie & Mijnbouw*, 70, 253-264.
- Rosell, L., F. Orti, A. Kasprzyk, E. Playa, and T.M. Peryt, 1998. Strontium geochemistry of Miocene primary gypsum; Messinian of southeastern Spain and Sicily and Badenian of Poland, *Journal of Sedimentary Research*, Section A: Sedimentary Petrology and Processes, 68 (1), 63-79.
- Rossignol-Strick, M., 1983. African monsoons, an immediate climate response to orbital forcing, *Nature*, 304, 46-49.
- Rossignol-Strick, M., 1985. Mediterranean quaternary sapropels, an immediate response of the African Monsoon to variation of insolation, *Palaeogeography, Palaeoclimatology, Palaeoecology*, 49, 237-263.
- Rossignol-Strick, M., 1987. Rainy periods and bottom water stagnation initiating brine accumulation and metal concentrations: 1. The Late Quaternary, *Paleoceanography*, 2, 333-360.
- Rouchy, J.M., F. Orszag-Sperber, M.M. Blanc-Valleron, C. Pierre, M. Rivière, N. Combourieu-Nebout, and I. Panayides, 2001. Paleoenvironmental changes at the Messinian-Pliocene boundary in the eastern Mediterranean (southern Cyprus basins): significance of the Messinian Lago-Mare, *Sedimentary Geology*, 145, 93-117. doi:10.1016/S0037-0738(01)00126-9
- Rouchy, J.M., and A. Caruso, 2006. The Messinian salinity crisis in the Mediterranean basin: A reassessment of the data and an integrated scenario, *Sedimentary Geology*, 188, 35-67.
- Roveri, M. and V. Manzi, 2006. The Messinian salinity crisis: looking for a new paradigm? *Palaeogeography, Palaeoclimatology, Palaeoecology*, 238, 386-398.
- Ruddiman, W.F., 2001. *Earth's Climate: Past and Future*. W.H. Freeman and Company, New York, U.S.A., 465 p.
- Ruddiman, W.F., M.E. Raymo, and A. McIntyre, A., 1986. Matuyama 41,000-year cycles: North Atlantic Ocean and northern hemisphere ice sheets, *Earth and Planetary Science Letters*, 80, 117-129. doi:10.1016/0012-821X(86)90024-5
- Ruddiman, W.F., M. Sarnthein, J. Backman, J.G. Baldauf, W. Curry, L.M. Dupont, T. Janecek, E.M. Pokras, M.E. Raymo, B. Stabell, R. Stein, and R. Tiedemann, 1989. Late Miocene to Pleistocene evolution of climate in Africa and the low-latitude Atlantic: overview of Leg 108 results, *Proceedings of the Ocean Drilling Program, Scientific Results*, 108, 463-484.
- Ruggieri, G., 1967. The Miocene and later evolution of the Mediterranean Sea, In: Adams, C.G., and Ager, D.V. (Eds.), *Aspects of Tethyan biogeography*, London, Systematic Studies Association, Publ. 7, 283-290.
- Ruggieri, G., and R. Sprovieri, 1976. Messinian salinity crisis and its paleogeographical implications, *Palaeogeography, Palaeoclimatology, Palaeoecology*, 20, 13-21.
- Ryan, W.B.F., K.J. Hsü, et al., 1973. *Initial reports of the Deep Sea Drilling Project*, 13, US Government Printing Office, Washington, DC, 1447 pp.
- Ryan, W.B.F., 2007. Decoding the Mediterranean Salinity Crisis, In: Cita, M.B., and Bernoulli, J.M.D. (Eds.), *Major Discoveries in Sedimentary Geology in the Mediterranean Realm from a Historical Perspective to New Developments*. Special Publication International Association of Sedimentologists.
- Sarnthein, M., J. Thiede, U. Pflaumann, H. Erlenkeuser, D. Fütterer, B. Koopmann, H. Lange, and E. Seibold, 1982. Atmospheric and oceanic circulation patterns off northwest Africa

- during the past 25 million years, In: Von Rad, U., Sarnthein, M., and Seibold, E. (Eds.), *Geology of the Northwest African Continental Margin*, Springer-Verlag, New York, 584-604.
- Schenau, S.J., A. Antonarakou, F.J. Hilgen, L.J. Lourens, I.A. Nijenhuis, C.H. van der Weijden, and W.J. Zachariasse, 1999. Organic-rich layers in the Metochia section (Gavdos, Greece): evidence for a single mechanism for sapropel formation during the past 10 My, *Marine Geology*, 153, 117-135.
- Schreiber, B.C., 1997. Messinian and younger deposition in the southern Caltanissetta Basin: Stop 5, Eraclea Minoa, In: Grasso, M., and Lentini, F. (Eds.), *Neogene basins of the Mediterranean region: controls and correlation in space and time. Excursion guidebook of the Interim Colloquium R.C.M.N.S.*, 4-9 November 1997. Università di Catania, Istituto di Geologia e Geofisica, Catania, Italy, pp. 50-55.
- Selli, R., 1960. Il Messiniano Mayer-Eymar 1867. Proposta di un neostatotipo, *Giornale di Geologia*, 28, 1-34.
- Shackleton, N.J., 1977. Carbon-13 in Uvigerina: tropical rainforest history and the equatorial Pacific carbonate dissolution cycles, In: Andersen, N.R., and Malahoff, A. (Eds.), *The Fate Of Fossil Fuel CO₂ in the Oceans*, Plenum, New York, 401-427.
- Shackleton, N.J., and N.G. Pisias, 1985. Atmospheric carbon dioxide, orbital forcing, and climate, In: Sundquist, E.T., and Broecker, W.S. (Eds.), *The Carbon Cycle and Atmospheric CO₂: Natural Variations Archean to Present*, *AGU Monograph*, 32, 303-317.
- Shackleton, N.J., S. Crowhurst, T. Hagelberg, N.G. Pisias, and D.A. Schneider, 1995a. A new late Neogene timescale: Application to leg 138 sites, *Proceedings of the Ocean Drilling Program, Scientific Results*, 138, 73-101.
- Shackleton, N.J., M.A. Hall, and D. Pate, 1995b. Pliocene stable isotope stratigraphy of site 846, *Proceedings of the Ocean Drilling Program, Scientific Results*, 138, 337-353.
- Shackleton, N.J., and S. Crowhurst, 1997. Sediment fluxes based on an orbitally tuned time scale 5 Ma to 14 Ma, site 926, *Proceedings of the Ocean Drilling Program, Scientific Results*, 154, 69-82.
- Shackleton, N.J., and M.A. Hall, 1997. The late Miocene stable isotope record, site 926, *Proceedings of the Ocean Drilling Program, Scientific Results*, 154, 367-373.
- Shackleton, N.J., H. Pälike, and M.F. Loutre, 1999. Improved astronomically tuned timescales for the late Neogene, *Journal of Conference Abstracts (EUG)*, 4 (1), 235.
- Shimmield, G.B., 1992. Can sediment geochemistry record changes in coastal upwelling palaeoproductivity? Evidence from northwest Africa and the Arabian Sea, *Geological Society, London, Special Publications*, 64, 29-46.
- Sierro, F.J., J.A. Flores, J. Civis, J.A. González Delgado, and G. Francés, 1993. Late Miocene globorotaliid event-stratigraphy and biogeography in the NE Atlantic and Mediterranean, *Marine Micropaleontology*, 21, 143-168.
- Sierro, F.J., J.A. Flores, I. Zamarreño, A. Vázquez, R. Utrilla, G. Francés, F.J. Hilgen, and W. Krijgsman, 1999. Messinian pre-evaporite sapropels and precession-induced oscillations in western Mediterranean climate, *Marine Geology*, 153, 137-146.
- Sierro, F.J., S. Ledesma, J.A. Flores, S. Torrescusa, and W. Martinez del Olmo, 2000. Sonic and gamma-ray astrochronology: cycle to cycle calibration of Atlantic climatic records to Mediterranean sapropels and astronomical oscillations, *Geology*, 28 (8), 695-698.
- Sierro, F.J., F.J. Hilgen, W. Krijgsman, and J.A. Flores, 2001. The Abad composite (SE Spain): A Messinian reference section for the Mediterranean and the APTS, *Palaeogeography, Palaeoclimatology, Palaeoecology*, 168, 141-169.

- Spero, H.J., J. Bijma, D.W. Lea, and B.E. Bemis, 1997. Effect of seawater carbonate concentration on foraminiferal carbon and oxygen isotopes, *Nature*, 390, 497-500.
- Spezzaferri, S., M.B. Cita, and J.A. McKenzie, 1998. The Miocene/Pliocene boundary in the Eastern Mediterranean: results from Sites 967 and 969, *Proceedings of the Ocean Drilling Program, Scientific Results*, 160, 9-28. doi:10.2973/odp.proc.sr.160.026.1998
- Sprovieri, R., E. Di Stefano, A. Caruso, and S. Bonomo, 1996. High resolution stratigraphy in the Messinian Tripoli Formation in Sicily, *Paleopelagos*, 6, 415-435.
- Steenbrink, J., N. van Vugt, F.J. Hilgen, J.R. Wijbrans, and J.E. Meulenkamp, 1999. Sedimentary cycles and volcanic ash beds in the lower Pliocene lacustrine succession of Ptolemais (NW Greece): Discrepancy between $^{40}\text{Ar}/^{39}\text{Ar}$ and astronomical ages, *Palaeogeography, Palaeoclimatology, Palaeoecology*, 152, 283-303.
- Suc, J.P., G. Clauzon, and F. Gautier, 1997. The Miocene/Pliocene boundary: Present and future, In: Montanari, A., Odin, G.S. and Coccioni, R. (Eds.), *Miocene Stratigraphy: An Integrated Approach. Developments in Palaeontology and Stratigraphy*, 15, Elsevier, Amsterdam, pp. 149-154. doi:10.1016/S0920-5446(06)80014-2
- Taberner, C., J.M. Rouchy, J.J. Pueyo, and M. Thirlwall, 2004. Origin of solutes and evaporite deposition at the end of the Messinian Salinity Crisis. The onset of "Lago Mare" sedimentation. 4th International Congress Environment and Identity in the Mediterranean: the Messinian Salinity Crisis revisited, Università di Corsica Pasquale Paoli, Corte, France, Abstracts, 83.
- Takayama, T., 1993. Notes on Neogene calcareous nannofossil biostratigraphy of the Ontong Java Plateau and size variations of Reticulofenestra coccoliths, *Proceedings of the Ocean Drilling Program, Scientific Results*, 130, 179-229.
- Tauxe, L., and D.V. Kent, 2004. A new statistical model for the geomagnetic field and the detection of shallow bias in paleomagnetic inclinations: was the ancient magnetic field dipolar? In: Channell, J.E.T., Kent, D.V., Lowrie, W., and Meert, J. (Eds.), *Timescales of the Internal Geomagnetic Field, AGU Monograph, American Geophysical Union*, Washington DC.
- Thunell, R.C., D.F. Williams, and J.P. Kennett, 1977. Late Quaternary paleoclimatology, stratigraphy and sapropel history in eastern Mediterranean deep-sea sediments, *Marine Micropaleontology*, 2, 371-388.
- Tiedemann, R., M. Sarnthein, and R. Stein, 1989. Climatic changes in the western Sahara: Aeolo-marine sediment record of the last 8 million years, *Proceedings of the Ocean Drilling Program, Scientific Results*, 108, 241-278.
- Tiedemann, R., M. Sarnthein, and N.J. Shackleton, 1994. Astronomic timescale for the Pliocene Atlantic $\delta^{18}\text{O}$ and dust flux records of Ocean Drilling Program site 659, *Paleoceanography*, 9 (4), 619-638. doi:10.1029/94PA00208
- Tuenter, E., 2004. Modeling orbital induced variations in circum-Mediterranean climate. PhD-thesis, 152 p.
- Tuenter, E., S.L. Weber, F.J. Hilgen, and L.J. Lourens, 2003. The response of the African summer monsoon to remote and local forcing due to precession and obliquity, *Global and Planetary Change*, 36, 219-235.
- Ufkes, E., J.H.F. Jansen, and R.R. Schneider, 2000. Anomalous occurrences of Neogloboquadrina pachyderma (left) in a 420-ky upwelling record from Walvis Ridge (SE Atlantic), *Marine Micropaleontology*, 23-42.
- Vai, G.B., 1997. Cyclostratigraphic estimate of the Messinian Stage duration, In: Montanari, A., Odin, G.S. and Coccioni, R. (Eds.), *Miocene Stratigraphy: An Integrated Approach*.

- Developments in Palaeontology and Stratigraphy, 15, Elsevier, Amsterdam, pp. 463-476.
doi:10.1016/S0920-5446(06)80035-X
- Vai, G.B., and F. Ricci Lucchi, 1976. The Vena del Gesso in northern Apennines: growth and mechanical breakdown of gypsified algal crusts, *Memorie della Società Geologica Italiana*, 16, 217-249.
- Vai, G.B., I.M. Villa, and M.L. Colalongo, 1993. First direct radiometric dating of the Tortonian/Messinian boundary, *Les Comptes rendus de l'Académie des sciences, Paris*, 316, 1407-1414.
- Van Couvering, J.A., D. Castradori, M.B. Cita, F.J. Hilgen, and D. Rio, 2000. The base of the Zanclean Stage and of the Pliocene Series, *Episodes*, 23 (3), 179-187.
- Van der Laan, E., S. Gaboardi, F.J. Hilgen, and L.J. Lourens, 2005. Regional climate and glacial control on high-resolution oxygen isotope records from Ain el Beida (latest Miocene, northwest Morocco): A cyclostratigraphic analysis in the depth and time domain, *Paleoceanography*, 20, PA1001, doi:10.1029/2003PA000995.
- Van der Laan, E., E. Snel, E. de Kaenel, F.J. Hilgen, and W. Krijgsman, 2006. No major deglaciation across the Miocene-Pliocene boundary: Integrated stratigraphy and astronomical tuning of the Loulja sections (Bou Regreg area, NW Morocco), *Paleoceanography*, 21, PA3011, doi:10.1029/2005PA001193.
- Van Hinsbergen, D.J.J., T.J. Kouwenhoven, and G.B. van der Zwaan, 2005. Paleobathymetry in the backstripping procedure: distinguishing between tectonic and climatic effects on depth estimates, *Palaeogeography, Palaeoclimatology, Palaeoecology*, 221 (3-4), 245-265. doi:10.1016/j.palaeo.2005.02.013
- Van Os, B.J.H., L.J. Lourens, F.J. Hilgen, G.J. De Lange, and L. Beaufort, 1994. The formation of Pliocene sapropels and carbonate cycles in the Mediterranean: Diagenesis, dilution, and productivity, *Paleoceanography*, 9, 601-617.
- Van Vugt, N., J. Steenbrink, C.G. Langereis, F.J. Hilgen, and J.E. Meulenkamp, 1998. Magnetostratigraphy-based astronomical tuning of the early Pliocene lacustrine sediments of Ptolemais (NW Greece) and bed-to-bed correlation to the marine record, *Earth and Planetary Science Letters*, 164, 535-551.
- Vidal, L., T. Bickert, G. Wefer, and U. Röhl, 2002. Late Miocene stable isotope stratigraphy of SE Atlantic ODP Site 1085: Relation to Messinian events, *Marine Geology*, 180 (1-4), 71-85. doi:10.1016/S0025-3227(01)00206-7
- Von Dobeneck, T., and F. Schmieder, 1999. Using rock magnetic proxy records for orbital tuning and extended time series analyses into the super- and sub-Milankovitch bands, In: Fischer, G., and Wefer, G. (Eds.), *Use of Proxies in Paleoclimatology: Examples from the South Atlantic*, Springer-Verlag Berlin Heidelberg, 601-633.
- Warny, S.A., P.J. Bart, and J.-P. Suc, 2003. Timing and progression of climatic, tectonic and glacioeustatic influences on the Messinian Salinity Crisis, *Palaeogeography, Palaeoclimatology, Palaeoecology*, 202, 59-66.
- Weedon, G.P., 1989. The detection and illustration of regular sedimentary cycles using Walsh power spectra and filtering, with examples from the Lias of Switzerland, *Journal of the Geological Society*, 146, 133-144. doi:10.1144/gsjgs.146.1.0133
- Wehausen, R., and H.J. Brumsack, 2000. Chemical cycles in Pliocene sapropel-bearing and sapropel-barren eastern Mediterranean sediments, *Palaeogeography, Palaeoclimatology, Palaeoecology*, 158, 325-352.

- Weijermars, R., 1988. Neogene tectonics in the western Mediterranean may have caused the Messinian salinity crisis and an associated glacial event, *Tectonophysics*, 148, 211-219.
- Wernli, R., 1977. Les foraminifères planktoniques de la limite mio-pliocène dans les environs de Rabat (Maroc), *Eclogae Geologicae Helvetiae*, 70, 143-191.
- Young, J.R., 1990. Size variation of Neogene Reticulofenestra coccoliths from Indian Ocean DSDP cores, *Journal of Micropalaeontology*, 9, 71-86.
- Zahn, R., M. Sarnthein, and H. Erlenkeuser, 1987. Benthic isotope evidence for changes of the Mediterranean outflow during the late Quaternary, *Paleoceanography*, 2, 543-559.
- Zijderveld, J.D.A., 1967. A.c. demagnetization of rocks: analysis of results, In: Collinson, D.W., Creer, K.M., and Runcorn, S.K. (Eds.), *Methods in palaeomagnetism*, Elsevier, Amsterdam, pp. 254-286.

Appendix 1

Habitat characteristics of calcareous nannofossils

1) *Cryptococcolithus mediaperforatus* (< 5 mm) (cold/13.81%) and 2) *Cryptococcolithus mediaperforatus* (>5 mm) (warm/12.89%)

Larger forms (>5 mm) of *C. mediaperforatus* have higher frequency in reddish layers (warm intervals) (7.30%) than in beige layers (cold intervals) (5.59%) but mean values are very similar (0.90 versus 0.87 specimens per mm²). At the opposite, smaller forms (<5 mm) of *C. mediaperforatus* have different mean values (0.99 versus 1.11 specimens per mm²). These results imply that temperature is controlling size variation and distribution of *C. mediaperforatus*. No obvious examples of water temperature effects on coccolithophore sizes are reported in literature, but species with delicate structures and open central area preferred warmer water (Young 1990, 1994). *C. mediaperforatus* is a placolith with an open central area covered by a very delicate net and consequently larger specimens with larger net are more frequent in warmer water. Indexes of reliability for both forms are low (t-values of 0.84 for forms smaller than 5 mm and of 0.25 for forms larger than 5 mm). *C. mediaperforatus* belongs to the Type I nannofossil assemblage.

3) Holococcolith group warm (warm, 12.89%)

This group includes 4 extant holococcolith species: *Syracolithus confusus* (= *Helicosphaera carteri* holococcolith), *Syracolithus schilleri* (= *Calcidiscus* holococcolith), *Syracolithus ponticuliferus* (*Helicosphaera* holococcolith) and *Calyptrolithina multipora* (*Coronosphaera* holococcolith). Detailed taxonomic descriptions and of the combinations between holococcolith-heterococcolith are well documented in the extant coccolithophore guide of Young et al. (2003). Some of the holococcoliths (warm and cold groups) have never been reported from Miocene sediments, even if the heterococcolith forms have been widely observed. The presence of extant coccoliths in Miocene sediments provides some very useful information on the environmental preferences of the SST nannofossil species. In general, high diversities and highest relative frequencies of Holococcoliths indicate oligotrophic conditions (Kleijne, 1991). The most frequently species in the AEB sediments are *S. schilleri* (8.89% or 0.69 specimen per mm²) and *S. ponticuliferus* (3.19% or 0.41 specimen per mm²), which are holococcolith types equivalent to respectively *Calcidiscus* and *Helicosphaera* species.

The holococcolith group warm is mostly recorded in warm intervals (7.54% with an average mean of 1.01 specimen per mm²) versus in cold intervals (5.31% and 0.89 specimen per mm²). The index of reliability with warm intervals is low (t-value of 1.19) for the group. Individually, *S. ponticuliferus* has a high index of reliability of 2.19. This species is almost absent from the lower part of the AEB section. The holococcolith group warm belongs to the Type II nannofossil assemblage.

4) *Calcidiscus macintyreii* (>11mm) (cold/7.94%)

This large morphotype of *Calcidiscus leptoporus*, which are typical of mid-latitude North Atlantic nannofossil assemblage, have been studied in detail by Knappertsbush et al. (1997). They observed

low correlation coefficients between coccolith size and temperature and suggested that other factors such as strength of surface water currents and upwelling currents may have influenced the distribution of large form of *Calcidiscus*. The extant species *C. leptoporus* is characteristic of the upper photic zone (0 to 80 m). *C. macintyreii* has a very high index of reliability with cold interval (t-value of 3.01). *C. macintyreii* is a typical species of assemblage Type II and is absent in the lower part of the AEB section where surface water was still influenced by Mediterranean current. It reoccurs in sample AEB 59 at 6.202 Ma.

5) *Oolithotus fragilis* (cold/6.47%)

Species of the *Oolithotus* genus are other placoliths counted to calculate the SST curve (with genera *Cryptococcolithus* and *Calcidiscus*). This extant species is predominantly recorded in lower photic zone nannofossil assemblages (depth between 120 and 220 m) (Okada and McIntyre, 1977) and in upwelling areas (Kleijne, 1993). In the AEB section, *O. fragilis* is mostly recorded in cold intervals (average mean of 0.54 specimen per mm²) versus in warm intervals (0.43). According to Okada and Matsuoka (1996), increasing abundances of lower photic taxa during glacial periods indicate weakened monsoon system. *O. fragilis* has a high index of reliability with cold interval (t-value of 2.21) and belongs to the Type II nannofossil assemblage.

6) *Discoaster quinqueramus* group (warm/6.22%)

This group includes five-rayed discoasters of the *D. quinqueramus* lineage: *D. quinqueramus*, *D. quinqueramus* var. A, *D. quintatus*, and *D. berggrenii*. This group of discoasters is very sensitive to ecological changes. Its low and sporadic occurrence in the upper part of the AEB section, a period of high diversity in this group, reflects extreme negative environmental conditions. Discoaster abundance decreases with increasing latitude or with decreasing water temperature. They are usually considered as warm water taxa indicators. Based on the study of Chepstow-Lusty (1996), discoaster abundance decreases with increasing upwelling conditions due to increased productivity pressure. But if the upwelling site is located in warm waters, discoaster abundances are increasing.

The *D. quinqueramus* group is predominant in warm intervals (4.90%) with a mean abundance value of 0.97 specimens per mm² versus an abundance of 1.32% in cold intervals with a mean abundance of 0.6 specimens per mm². As for most of the other discoaster groups, the index of reliability (t-value of 1.23) with warm intervals is low indicating that other factors than temperature variations as upwelling conditions are controlling the *D. quinqueramus* group abundance fluctuations. At the opposite of the other discoaster groups, the *D. quinqueramus* group is indicative of Type II assemblage.

7) *Hayella challengerii* (cold/6.07%)

H. challengerii was described for medium-sized tubular placolith (holotype 7.2 mm). In this study, only forms that are 7 mm or more were counted. *H. challengerii* is predominant in cold intervals with an abundance of 3.39 % (mean abundance: 0.59 specimens per mm²) versus 2.69% in warm intervals (mean abundance: 0.43). The reliability index with cold intervals is very high (t-value of 2.84). This species belongs to the Type II nannofossil assemblage, which is characteristic of upwelling conditions

8) *Amaurolithus delicatus* group (cold/5.76%)

This group includes 3 ceratolithids of the *Amaurolithus primus* lineage: *A. primus*, *A. delicatus*, and *A. ninae*. This *Amaurolithus delicatus* group has a higher abundance in cold intervals (3.26%)

with a mean abundance of 0.54 specimen per mm² versus 2.50% in cold intervals and a mean abundance of 0.36 specimen per mm². The *Amaurolithus delicatus* group presents the highest reliability index with cold intervals (t-value of 3.55) and belongs to the Type I assemblage. The extant species *Ceratolithus cristatus*, which is the equivalent holococcolith stage of *N. coccolithomorpha* (see discussion below on *N. coccolithomorpha*), is reported from eastern North Atlantic and Mediterranean Sea *Emiliana huxleyi* assemblages (Kleijne, 1993). These assemblages occur in relatively colder waters and its frequencies decrease with increasing temperature. The *Amaurolithus delicatus* group has a consistent occurrence throughout the AEB section, but with several abundance peaks in the lower part of the AEB section (maximum abundance in sample AEB 291 at 6.453 Ma).

9) *Discoaster brouweri* group (warm/5.11%)

This group includes two six-rayed discoasters: *Discoaster brouweri brouweri* and *Discoaster brouweri streptus*. The *D. brouweri* group has a higher abundance in warm intervals (3.21%) with a mean abundance of 0.6 specimen per mm² versus 1.90% in cold intervals and a mean abundance of 0.49 specimen per mm². *D. brouweri* is considered as a warm taxa indicator but its abundance decreases with increasing upwelling conditions (Chepstow-Lusty et al., 1992). In this regard, the distribution of the *D. brouweri* group in the AEB section is very significant of the paleoecological changes. *D. brouweri* has a consistent occurrence in the lower part of the AEB section with some high abundance peak zones indicating strong influences of warm Mediterranean current (AEB 290 to 3). From sample AEB 189 (5.959 Ma) up to sample AEB 263 (5.534 Ma), *D. brouweri* group has very low and sporadic occurrences characteristic of upwelling conditions. Increasing abundances are observed at the top of the AEB section indicating warmer surface water conditions with a peak zone in the top three samples (AEB 267 to 269). The *D. brouweri* group belongs to the Type I nannofossil assemblage.

10) *Calciosolenia brasiliensis* (cold/4.91%)

C. brasiliensis{=*Scapholithus fossilis* (Deflandre, 1954)} has a persistent occurrence in the AEB section. This extant species is predominant in warm intervals with a mean abundance value of 0.45 specimens per mm² (versus 0.36 in cold intervals) and has a relatively good reliability index (t-value of 1.70) with warm intervals. *C. brasiliensis* occurs more frequently in colder waters and in upwelling areas. In subtropical waters, *C. brasiliensis* is characterizing the middle photic zone (80 to 120 m) coccolithophorid assemblage (Jordan and Winter, 2000). *C. brasiliensis* is included in the Type II nannofossil assemblage.

11) *Scyphosphaera* group warm (warm, 4.28%) and 13) *Scyphosphaera* group cold (cold, 1.71%)

Many species of the genus *Scyphosphaera* were observed in the late Miocene of the Ain El Beida section. This genus is highly polymorphic and the Messinian also corresponds to the peak of number of *Scyphosphaera* species living in the oceans. A total of 41 scyphosphaerid species were observed.

Based on statistical analysis, 9 morphogroups are identified (Table 2), which are grouped into 3 major groups: *Scyphosphaera* group cold, group warm, and group eurythermal,

Species in each morphogroup are grouped according to the shape of the margin and to their lithological affinities for warm or cold periods. Morphogroups are named according to the most common species in each group.

Temperature is controlling the distribution of *Scyphosphaera* species: 22% preferred cold water, 37% of the species preferred warm water, and 41% don't have any special affinities (Table 3). These later species are likely to be eurythermal species. At the opposite, abundances and diversities are very similar between both cold and warm periods and therefore not controlled by temperature variations. The average total abundance per sample is of 0.75 specimens per mm² (0.76 in cold and 0.75 in warm intervals). Average diversity per sample among cold periods is of 2.6 species and of 2.5 species during warm periods. These unexpected results indicate that the total abundance of the *Scyphosphaera* genus has no temperature affinity during the late Messinian age in mid-latitude North Atlantic, but that speciation (shape, size and basal plate variations) within the genus is controlled by temperature fluctuations. Indexes of reliability are relatively high with respectively t-values of 2.24 and 2.80. The *Scyphosphaera* group warm belongs to the Type II nannofossil assemblage whereas the *Scyphosphaera* group cold to the Type I.

12) *Pontosphaera messinae* (cold/3.05%)

Several species of *Pontosphaera* have been differentiated and counted separately. *P. japonica* (1.65 % of the total assemblage counted), *P. messinae* (2.42 %) and *P. scutellum* (0.1%) didn't show any strong temperature affinities. These three extant species are differentiated according to the number and position of the central plate perforations. *P. japonica* has numerous perforations covering entirely the central plate, *P. messinae* has small perforations restricted to the center of the central area and *P. scutellum* has almost no perforation. Based on the mean abundance values, *P. japonica* is more related to warm intervals, *P. messinae* to cold intervals and *P. scutellum* has precisely the same distribution between the different intervals. Indexes of reliability (t-values) are very low for these three species. As for *C. mediaperforatus*, higher number of perforations indicates warmer surface water temperature. Only *P. messinae* was used to calculate the SST values. *P. messinae* belongs to the Type II nannofossil assemblage.

14) *Discoaster variabilis* (3, 5) group (cold/2.11%)

As for many other discoasters, *D. variabilis* shows considerable variations in the number of rays and inter-ray angles. Takayama (1969) produces some perfect drawings of many of these morphologic variants. The typical 6-rayed specimens are the most frequent. In this *D. variabilis* group, only specimens with 3 and 5-rayed were counted: *D. variabilis* (3 ray), *D. variabilis* (5 ray), and *D. variabilis* (5 ray asymmetric). Because discoasters became extinct at the end of the Pliocene, very little is known about the arrangement of discoasters in the organism responsible for their production. Most of the time, discoasters are found isolated in the sediments, but some very rare stacking up of 3 specimens have been observed (2 six-rayed specimens with one 5-rayed specimen in the middle). It is not understood yet if the occurrence of 5-rayed (and other numbers of rays) discoasters is due to ecological changes or if they are part of the discoaster cellular structure. Takayama (1969) pointed that 3 to 5-rayed discoasters changed their frequency through time.

D. variabilis (3,5) group has a higher mean abundance in cold intervals (0.26 specimen per mm²) versus 0.21 in warm intervals and a relatively low index of reliability with cold intervals (t-value of 1.57). As for the other discoaster groups, this low t-value indicates that environmental changes other than temperature variations, are responsible for the *D. variabilis* (3,5) group abundance fluctuations. *D. variabilis* (3,5) group belongs to the Type I nannofossil assemblage characteristic of the lower AEB section.

15) Holococcolith group cold (cold, 1.71%)

This group includes 2 extant holococcolith species: *Syracolithus dalmaticus* (?= *Helicosphaera walichii* holococcolith) and *Crystallolithus rigidus* (= *Calcidiscus leptoporus* ssp. *leptoporus* holococcolith). The holococcolith group cold has a higher mean abundance in cold intervals (0.30 specimen per mm²) versus in warm intervals (0.28). The index of reliability with cold intervals is very low (t-value of 0.28) indicating that this group is not controlled by temperature variations but by variations in nutrient levels. Holococcoliths are characterized oligotrophic environment. The holococcolith group cold belongs to the Type I nannofossil assemblage

16) *Pontosphaera nitea* (warm/1.19%)

P. nitea is another extant species and two varieties have been differentiated in this study according to the width of the rim: *P. nitea* with thick rim (*P. nitea* s.s.) and *P. nitea* with thin rim (*P. nitea* thin). Because of the development of the rim and on high birefringence patterns, *P. nitea* is regarded as muroliths of a lopadolith (schyphosphaerid) coccospheres. *P. nitea* has a relatively good index of reliability with warm intervals (t-value of 1.64) and higher abundance in warm intervals (0.74%) versus in cold intervals (0.45%). *P. nitea* belongs to the Type II nannofossil assemblage as the other pontosphaerid *P. messinae*. No ecological preferences are available from modern oceans, pontosphaerids being most of the time not differentiated. In the Atlantic subtropical zone, they represent a very low percentage of the coccolith assemblage, but pontosphaerids could be very abundant in some western mediterranean sapropel layers or in epicontinental areas.

17) *Discoaster neorectus* (cold/0.65%)

D. neorectus is a thick and large form of *D. brouweri* (³20 mm) with straight, non bent rays. Its extinction is recorded in sample AEB 128 at 5.940 Ma (Krijgsman et al., 2004). *D. neorectus* has a higher mean abundance in cold intervals (0.17 specimen per mm²) versus in warm intervals (0.13) and a high index of reliability with cold intervals (t-value of 2.06). *D. neorectus* belongs to the Type I nannofossil assemblage as the *D. brouweri* group.

Most discoasters favored warm water but large forms or forms with thick rays are indicative of cold water masses. As explained by Young (1994), coccoliths tend to be more heavily calcified in cold water due to changes of water density and viscosity.

18) *Discoaster quadramus* group (cold/0.57%)

This group includes 2 forms of 4-rayed *Discoaster pentaradiatus*: *D. quadramus* with rays at 90° and *D. quadramus* with inter-ray angles of 60° and 120°. *D. quadramus* group is mostly recorded in cold intervals (0.35 %) versus in warm intervals (0.22%) but the index of reliability is low (t-value of 1.20). This is probably due to the fact that *D. quadramus* (120°) has the same mean abundance (0.12 specimen per mm²) in both type of intervals. The 3-rayed *D. pentaradiatus* has not been included in the SST values. This form has the same mean abundance (0.14 specimen per mm²) in both type of intervals and consequently a very low t-value of 0.13 which is interpreted as indicative of eurothermal species. *D. pentaradiatus*, the 5-rayed variant, is the most abundant (up to 25 specimen per mm²) in both warm and cold intervals. The high abundance of the 5-rayed *D. pentaradiatus* make it unreliable to use in the SST formula. Precise countings of abundant species are most of the time very inaccurate and will have strongly decrease the ecological signals of rare to common species. The *D. quadramus* group belongs to the Type I nannofossil assemblage.

19) *Anacanthoica salomonica* (warm/0.44%)

Two forms with different basal plates and distal spines were differentiated and grouped in *A. salomonica*. Based on their birefringence pattern, this species is probably an holococcolith and need to be transferred in a new genus (Varol, pers. comm.). This rhabdolite type species has a higher abundance in warm intervals (0.35%) versus in cold intervals (0.09%). *A. salomonica* has a high index of reliability with warm intervals (t-value of 2.03) and belongs to the Type II nannofossil assemblage. Most of the extant rhabdosphaerid species are warm waters species of the upper photic zones, but some are on the other hand characteristic of the lower photic zones (below 120m) and can survive in cold water.

20) *Lithostromation perdurum* (warm/0.39%)

L. perdurum is a relatively large nannofossil typical of hemipelagic sediment and confined to epicontinental areas. *L. perdurum* is considered as warm taxa based on its index of reliability with warm interval (t-value of 2.02) and on its higher abundance in warm interval (0.24%) versus in cold interval (0.15%). *L. perdurum* belongs to the Type I nannofossil assemblage.

21) *Oolithotus antillarum* (warm/0.37%)

This second extant species of the genus *Oolithotus* was separated from *O. fragilis*. Okada and McIntyre (1977) found that this species is predominant in middle photic zones. In upwelling area, *O. antillarum* and, to a lesser degree, *O. fragilis* increase in frequency in surface water (Kleijne, 1993). In the AEB section, *O. antillarum* is mostly recorded in the warm intervals (0.21 %) versus in the cold intervals (0.16%). *O. antillarum* and *O. fragilis* are both characteristic of the Type II nannofossil assemblage and may be used as indicator of increasing upwelling currents.

22) *Amaurolithus amplificus* (warm/0.30%)

A. amplificus has been separated from the other *Amaurolithus* species grouping based on its reliability index (t-value of 1.90) and on its higher abundance (0.17%) in warm intervals. But all amauroliths are included in Type I assemblage. *A. amplificus* shows significant morphological differences with other *Amaurolithus* and has been placed in the genus *Nicklithus* by Raffi et al. (1998). The extinction of the very robust and large species *A. amplificus* occurs in sample AEB 183 (at 5.973 Ma) at the transition between dominance of Type I assemblage to Type II. Because the extinction of *A. amplificus* is considered to be an almost synchronous worldwide event, the ecological changes at the origin of its extinction are certainly controlled by important climatic variations and not by local variations in surface water currents. This interval also corresponds to the onset of the Messinian salinity crisis (see below the principal component analysis chapter).

23) *Tintinnabuliformis* group (warm/0.23%)

This group includes 2 species of *Tintinnabuliformis*: *T. unicorn* and *T. unicorn* var. A, a form missing the proximally extending horn. These forms have a bell-shaped and a distal opening as in scyphosphaerid but with very different structures. Species of *Tintinnabuliformis* are more frequent in warm intervals (0.15%) than in cold intervals (0.08%) and their distribution is similar to the *Scyphosphaera* warm grouping. The index of reliability with warm intervals is low (t-value of 1.23). Both groups belong to the Type II nannofossil assemblage.

24) *Neosphaera coccolithomorpha* (cold/0.19%)

Only type of *N. coccolithomorpha* with large shield and large central opening were observed (8 mm across, opening 0.34x total diameter). According to Young et al. (2003), the extant *Neosphaera* species represent the heterococcolith stage of the *Ceratolithus* genus. The first occurrence of *N. coccolithomorpha* is recorded in the AEB section in sample AEB 88 (at 6.127 Ma) suggesting that *Amaurolithus* species are equivalent to holococcolith stage in other taxa. The first *Ceratolithus* species only occurs in the early Pliocene. *N. coccolithomorpha* is slightly more abundant in cold interval (average mean of 0.13 specimen per mm²) versus in warm interval (0.11) but the reliability index is very low (t-value of 0.9). At the opposite, species of the *Amaurolithus delicatus* group has a very high index of reliability (t-value of 3.55) with cold intervals. *A. amplificus* has a t-value of 1.90 with warm intervals. The principal component analysis indicates that *N. coccolithomorpha* belongs to the Type II nannofossil assemblage and *Amaurolithus* species to Type I. According to Kleijne (1993), large type of *N. coccolithomorpha* are recorded in nannofossil assemblage of warm waters or in upwelling areas together with *O. fragilis*, *O. antillarum* and *Calciosolenia brasiliensis* (all of Type II nannofossil assemblage).

Appendix 2

Habitat characteristics of planktonic foraminifera

(partly adopted from and modified after Lourens, 1994 and references therein)

Globigerinoides obliquus is assumed to be the precursor of *Globigerinoides ruber*, and is assigned similar habitat characteristics. The latter lives in the low-fertility mixed layer of the tropical and subtropical regions (Bé and Hutson, 1977; Fairbanks et al., 1982; Thunell and Reynolds, 1984; Ravelo et al., 1990). This preference for oligotrophic conditions is assumed for the entire *Globigerinoides* group.

Globorotalia scitula is considered as a cool water indicator (Bé and Hutson, 1977; Hemleben et al., 1989) and has been reported widespread in the Mediterranean at glacial times (Jorissen et al., 1993). The dextrally coiled form is far more abundant in Ain el Beida than the sinistrally coiled form, generally showing maximum abundances in the reddish layers.

All living representatives of *Neogloboquadrina* belong to one biogeographic cline (Srinivisan and Kennett, 1976) and feed exclusively on phytoplankton (Hemleben et al., 1989). Phytoplankton in the tropical oceanic regions highly abundant in Deep Chlorophyll Maximum (DCM) layers and highest abundances of tropical neogloboquadrinids occur therefore in the DCM layer (Fairbanks et al., 1982; Ravelo et al., 1990). We assume here that the dextral and sinistral forms of *Neogloboquadrina* sp. had a similar feeding strategy in the late Miocene. The dextral form is by far the most abundant in the Ain el Beida section. Elevated percentages of sinistrally coiled morphotypes have been correlated to glacial isotope stages (Ruddiman et al., 1989), whereas dextrally coiled morphotypes show no such a relation. This suggests that the sinistral form is a cooler-water morphotype than the dextral form.

Sierro et al. (1993) reported the replacement of the *Globorotalia menardii* group II by the *Globorotalia miotumida* group (PF-Event 3) that has been related to a widespread southward migration of northern temperate faunas replacing the subtropical ones. The occurrence of *G. miotumida* at Ain el Beida is therefore associated with cooler waters.

Samenvatting in het Nederlands

(Summary in Dutch)

Het belangrijkste doel van dit proefschrift is om een beter inzicht te krijgen in de ontstaansgeschiedenis van de sedimentaire kleurencycli in het Bou Regreg gebied in noordwest Marokko. Van deze cycli van laat Miocene tot vroeg Pliocene ouderdom werd reeds gedacht dat ze gerelateerd waren aan precessie gestuurde variaties in klimaat op lage breedten; de cycli zijn mogelijk equivalenten van de welbekende, precessie gerelateerde, sapropelen (organisch rijke lagen) van Pliocene-Pleistocene ouderdom uit het Middellandse Zee gebied. De verwachting is dat er door de bestudering van deze laat Miocene open mariene 'parallel' secties aan de Atlantische kant van het Middellandse Zee gebied een beter inzicht wordt verkregen in de zogenaamde 'saliniteitscrisis' van het Messiniën. Deze periode tussen 5.96 en 5.33 miljoen jaar geleden in het laat Mioceen werd gekenmerkt door een sterk verslechterde mariene verbinding tussen de Middellandse Zee en de Atlantische Oceaan, leidend tot stagnatie van watermassa's in de Middellandse Zee en de afzetting van soms kilometers dikke zoutpakketten (zogenaamde evaporieten). De focus van deze studie ligt hierbij op het onderscheiden van twee mogelijke factoren die het begin en eind van de saliniteitscrisis hebben veroorzaakt, namelijk tektonische (plaat)bewegingen en globale en regionale klimaatsvariaties. Tevens ligt er een sterke nadruk op de faserelaties tussen individuele astronomische parameters (die de lange termijnveranderingen in het Aardse klimaat veroorzaken, zie Fig.) en de resulterende respons van specifieke klimaatsindicatoren (zogenaamde klimaats'proxies') verkregen uit de onderzochte afzettingen.

Om te beginnen wordt in **hoofdstuk 2** een geïntegreerd stratigrafisch en astronomisch gedateerd ouderdomsmodel van hoge resolutie (monsterdichtheid van ± 3000 jaar) gepresenteerd voor de Ain el Beida (AEB) sectie. Biostratigrafische en magnetostratigrafische gegevens zorgden voor een eerste ouderdomsindicatie en duiden meteen op de invloed van precessie in het ontstaan van de basale sedimentaire cycli (bestaande uit roodachtig en beige gekleurde lagen). Bovendien vertonen de 44 cycli van AEB een 1:5:20 verhouding, die gewoonlijk wordt aangetroffen in sedimentaire afzettingen die beïnvloed zijn door de astronomische parameters precessie en excentriciteit (zie Fig.). De kleurencycli zijn vervolgens astronomisch afgestemd op de berekende insolatiecurve (zonne-instralingscurve) voor 65° noorderbreedte van de astronomische oplossing La93_(1,1), de nieuwste en meest accurate astronomische oplossing die op dat moment voorhanden was. Deze afstemming resulteert in een laat Miocene ouderdom van de AEB sectie, nauwkeurig gedateerd tussen 6.47 en 5.52 miljoen jaar geleden.

Gedetailleerde analyses van stabiele zuurstofisotopen ($\delta^{18}\text{O}$) in planktonische foraminiferen (eencelligen) en tellingen van deze foraminiferen laten zien dat de roodachtige lagen in de cycli gekenmerkt worden door minima in $\delta^{18}\text{O}$ en maxima in *Globigerinoides* (een groep van planktonische foraminiferen die zijn gerelateerd aan voedselarm, relatief warmer water). Dit suggereert dat de roodachtige lagen equivalenten zijn van sapropelen in het Middellandse Zee gebied, waarin dezelfde kenmerken zijn aangetroffen. In de door ons nieuw opgezette astrochronologie van AEB konden we verschillende gebeurtenissen opnieuw dateren, waaronder enkele omkeringen van het Aardmagneetveld en enkele piek-glaciale perioden genaamd

TG22, TG20 en TG12 (gedateerd op respectievelijk 5.79, 5.75 en 5.55 miljoen jaar oud). De planktonische en benthische stabiele zuurstofisotopendata, waarin deze glaciële perioden duidelijk naar voren komen, laten cycli zien die gemiddeld 41 duizend jaar duren, wijzend op een forcering door obliquiteit (zie Fig.). De piek-glaciële perioden TG22 en TG22, die voorheen werden gekoppeld aan het begin van het ontstaan van de dikke zoutpakketten in het Middellandse Zee gebied (en dus aan de verslechterde verbinding met de Atlantische Oceaan), blijken ongeveer 200 duizend jaar jonger en dus niet de oorzaak te zijn van de saliniteitscrisis van het Messiniën. Daarnaast is er geen enkele indicatie dat het begin van de saliniteitscrisis (5.96 miljoen jaar geleden) samenhangt met een belangrijke zeespiegeldaling, omdat er geen significante piek in de benthische stabiele zuurstofisotopen curve te zien is die met deze daling zou moeten correleren.

In **hoofdstuk 3** gaan we uitgebreid in op de transformatie van de $\delta^{18}\text{O}$ gegevens van AEB vanuit het dieptebereik naar het tijdsbereik. De verhouding van pieken in de spectra van beide $\delta^{18}\text{O}$ gegevens bleek niet constant in het dieptebereik en het tijdsbereik. De oorzaak hiervan ligt in veranderingen in sedimentatiesnelheid die positief gecorreleerd zijn aan de amplitude van precessie alsmede aan een lange termijn trend in sedimentatiesnelheid. We gebruiken een simpel model om de veranderingen in positie van spectraalpieken te simuleren door de sedimentatiesnelheid niet-lineair te laten variëren als gevolg van de amplitude modulatie van precessie door excentriciteit. Cross-spectraal analyse laat zien dat het precessie gerelateerde $\delta^{18}\text{O}$ signaal in fase is met ETP (een berekende curve die Excentriciteit, Tilt (obliquiteit) en Precessie combineert). Deze 'in fase' relatie is gedeeltelijk een gevolg van de afstemmingsprocedure in Hoofdstuk 2. Het obliquiteit gerelateerde signaal in $\delta^{18}\text{O}$ laat een lichte vertraging van ongeveer 2 duizend jaar zien ten opzichte van obliquiteit, een vertraging die iets gereduceerd is ten tijde van de saliniteitscrisis. We schrijven deze vertraging toe aan de door obliquiteit geforceerde langzame opbouw van ijskappen, terwijl het precessie gerelateerde signaal hoofdzakelijk wordt toegeschreven aan regionale klimaatsveranderingen op een soortgelijke wijze als eerder is aangetoond voor de Mediterrane sapropelen van Plio-Pleistocene ouderdom. De $\delta^{18}\text{O}$ tijdseries van AEB passen uitstekend in een nieuw geconstrueerd globaal zuurstof isotopen raamwerk die de glaciële geschiedenis van het laat Messiniën laat zien.

Het bestudeerde interval van AEB eindigt rond 5.52 miljoen jaar geleden, net na piekglaciiaal TG12. De AEB sectie beslaat dus niet de periode ten tijde van het eindigen van de saliniteitscrisis gedateerd op 5.33 miljoen jaar geleden, de Mioceen-Pliocene grens. Het was dus noodzaak om het geïntegreerde (cyclo)stratigrafische raamwerk in het Bou Regreg gebied uit te breiden met een sectie die tenminste de Mioceen-Pliocene grens bevat. Dit werd gedaan door een nieuwe sectie, Loulja genaamd, niet ver van Ain el Beida, te onderzoeken. Deze sectie is ontsloten in twee groeves die beide al jonger werden verondersteld dan AEB. De geïntegreerde stratigrafie van de Loulja-A en -B secties is gepresenteerd in **hoofdstuk 4**. De oudere Loulja-A sectie laat een dominant door precessie gestuurde kleurencyliciteit zien gelijk aan dat van AEB. De astronomische afstemmingsprocedure naar precessie resulteert in een nauwkeurige datering van de Loulja secties tussen 5.59 en 5.12 miljoen jaar geleden. Ten tijde van het onderzoek aan de Loulja secties kwam een nieuwe astronomische oplossing tot onze beschikking, genaamd La04_(1,1), die slechts kleine verschillen liet zien in ouderdom van controlepunten ten opzichte van de oudere oplossing die gebruikt was in hoofdstuk 2. De datering van de Loulja secties hield in dat de Mioceen-Pliocene grens was bereikt en dat er een overlap van ongeveer 80 duizend jaar met de Ain el Beida sectie was gecreëerd. Net als voor AEB bleek het $\delta^{18}\text{O}$ signaal hoofdzakelijk door

obliquiteit geforceerd te zijn. Echter, de Mioceen-Pliocene grens in de Louja sectie valt samen met een lichte, precessie gerelateerde verschuiving naar lichtere $\delta^{18}\text{O}$ waarden. Deze verschuiving valt niet samen met de interglaciale periode TG5, zoals eerder verondersteld, maar met een 'extra' obliquiteit gerelateerde cyclus met een zwakke amplitude tussen interglacialen TG7 en TG5. We concluderen hieruit dat andere factoren dan (glacio-eustatische) zeespiegeldaling, bijvoorbeeld tektoniek, een kritische rol hebben gespeeld in het herstellen van 'normale' mariene condities in de Middellandse Zee. De opvallende 'stap'vormige deglaciatie die plaatsvindt tussen glaciaal TG12 en interglaciaal TG11 rond 5.54 miljoen jaar geleden, kan echter mogelijk worden gekoppeld aan het begin van de afzettingen van de zogenaamde 'Upper Evaporites' in het Middellandse Zee gebied. We suggereren dat de zeespiegelstijging die het gevolg is van deze deglaciatie wellicht ten dele verantwoordelijk is geweest voor een (tijdelijk) betere verbinding tussen de Atlantische Oceaan en de Middellandse Zee na de belangrijkste uitdrogingsfase.

Om de oorsprong van de kleurencycli en hun inhoud verder te onderzoeken, is een hoge resolutie multi-proxy studie uitgevoerd op de monsters van AEB. De resultaten hiervan zijn gepresenteerd in **hoofdstuk 5**. We koppelen de precessie gerelateerde variaties in de kleurencycli en in de chemische samenstelling van het sediment aan 'nat-droog' schommelingen in het klimaat van noordwest Afrika. Nattere omstandigheden worden hierbij gekoppeld aan precessie minima, terwijl drogere condities meer de overhand hebben tijdens precessie maxima. Dit scenario wordt toegeschreven aan het Atlantische klimaatstelsel en niet aan de Afrikaanse moesson, vanwege de noordelijke locatie van Ain el Beida in noordwest Afrika, dat waarschijnlijk buiten het bereik ligt van de invloed van de moesson.

Planktonische foraminiferen en kalkhoudende nannofossiel assemblages laten ook een belangrijke precessie component zien, die erop duiden dat de temperatuur van oppervlaktewater (SST, Sea Surface Temperature) toenam tijdens de nattere fase, terwijl produktiviteit lijkt toe te nemen tijdens de drogere fase. Zowel de korte- als de lange-termijn excentriciteitscycli (zie Fig.) zijn duidelijk te herkennen in veel van de bestudeerde klimaatsproxies. Dit is te verklaren door een niet-lineaire respons van het klimaat op de precessie forcering (excentriciteit moduleert de precessie amplitude). We stellen dat, over de hele linie, maxima in excentriciteit samenhangen met relatief nattere omstandigheden in noordwest Afrika, en vice versa. Naast de precessie gerelateerde variaties, domineren door obliquiteit geforceerde glaciale-interglaciale cycli de planktonische en benthische zuurstofisotopen van AEB (zoals al vermeld in hoofdstukken 2 en 3) en, in mindere mate, de variaties in SST en vochtigheid (Ti/Al, titaan:aluminium verhouding) in noordwest Afrika. We schrijven het warmere en nattere klimaat tijdens interglaciale periodes toe aan actievere Atlantische depressies geassocieerd aan een direct thermale reactie van tanende ijskappen. De hoofdzakelijk door obliquiteit geforceerde stabiele koolstofisotopen data ($\delta^{13}\text{C}$) van AEB zijn omgekeerd gerelateerd aan de $\delta^{18}\text{O}$ data, met lagere waarden tijdens glaciale perioden. Dit verband is bekend uit het Pliocene en Pleistoceen, en de gelijkensis met tussen de $\delta^{13}\text{C}$ data van AEB en die van de open oceaan kan wijzen op glaciale-interglaciale variaties op grote schaal in het koolstof reservoir van de diepzee. De planktonische $\delta^{13}\text{C}$ curve laat daarnaast een opvallende en relatief snelle verschuiving naar lagere waarden zien rond 6 miljoen jaar geleden, die we koppelen aan een laatste stap in het sluiten van de zeestraat die destijds door noord Marokko liep. Het sluiten van deze verbinding heeft waarschijnlijk gezorgd voor een sterke afname in uitstromend water uit de Middellandse Zee, dat verrijkt was in $\delta^{13}\text{C}$.

Tenslotte geven we in **hoofdstuk 6** een overzicht van het potentieel van astronomische afstemming om een chronostratigrafisch raamwerk te produceren, in dit geval toegepast op de saliniteitscrisis van de Middellandse Zee in het Messiniën. We stellen dat zowel het dicht drukken van zeestraten door tektonische plaatbewegingen als evolutie van het klimaat een rol hebben gespeeld in de evolutie van de saliniteitscrisis. De factor klimaat kan worden onderverdeeld in hoofdzakelijk door precessie geforceerde regionale klimaatveranderingen en in hoofdzakelijk door obliquiteit gestuurde glaciële cycli. De toepassing van een geïntegreerde hoge resolutie stratigrafie in combinatie met een astronomisch afgestemd ouderdomsmodel resulteert in een beter begrip van de verschillende stadia binnen de saliniteitscrisis in het Messiniën, en van de drijvende krachten die verantwoordelijk waren, of niet, voor haar stapvormige evolutie.

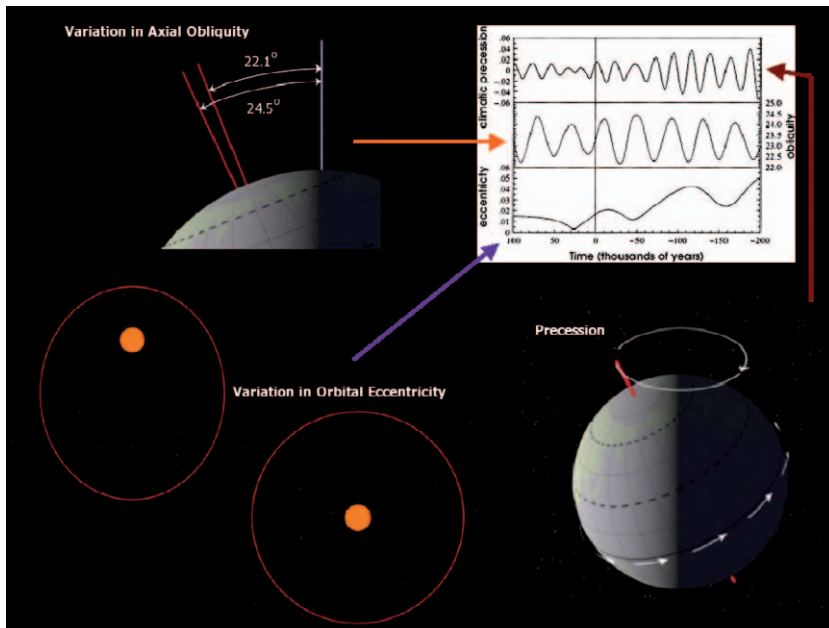


Figure taken from www.theresilientearth.com

Acknowledgements

Inevitably, with the finishing touch of a Ph.D thesis, the list of people I have to, and want to, thank comes in sight.

First of all, all of this would not have been possible without the help of my supervisor Frits Hilgen. He initiated the PIONEER project that I have very much enjoyed working for, he always had the time and patience to listen to me and watch over me (it was indeed necessary sometimes!). I really enjoyed the fieldworks at Monte dei Corvi and on the Tremiti Islands (I won't bring a young seagull with me next time), where I once again experienced Frits' unlimited enthusiasm and working spirit. We really should have some limoncello some time again, accompanied by real Italian pasta. Frits, dank je wel voor alles wat je me op het gebied van cyclostratigrafie hebt geleerd en de goede tijd!

Lucas Lourens, my 'second' supervisor, I thank for his help, efforts and comments on large parts of different manuscripts (every time Frits and I felt that large parts of text were in full shape, you came up with significant improvements), and for his joyful company and patience. Luc, as well as during my master thesis, I really enjoyed working with you, especially during the fieldworks in Sicily and Crotona. Bedankt!

I thank Johan Meulenkamp for being my initial promoter and for keeping a focused eye on the project. I hope you're having a good time now that we don't see you around anymore. Bert van der Zwaan I want to thank for taking Johan's place as my promoter and for continuity.

I am grateful to the insights and reviews of the members of the reading committee Elena Turco, David Hodell, Gert de Lange and Henk Brinkhuis.

My good colleague and 'partner in crime' Erik Snel I thank for his pleasant company, the endless discussions on cycle-counting during the fieldworks in Morocco, his patience (especially at the police station in Salé. I'll never make an effort to catch a young thief again – however maybe with a new pair of Adidas shoes!), and for his thorough thoughts and discussions on the Loulja paper. Erik, dank je wel!

My other fellow workers in the PIONEER group Frank Huiskamp, Julia Becker and Erik Tuentner I want to thank for the good times I had when we were roommates, for their company during fieldworks and for thorough discussions.

Thanks as well to my paranymphs Hemmo Abels and Wanda Link. Wanda, I've had a great time working with you, although, eventually, your grainsize data have not been included in this thesis (let's say there are always reasons for everything). We definitely should team up again on the grainsize topic. Thanks for your hard work, endless discussions and for your company during our

pleasant trip to Bremen. Hemmo, thanks for discussing almost anything on any topic, for your joyful company and all other times to come!

I very much enjoyed working and drinking coffee with my other colleagues from the Strat & Pal, Sedimentology, Pal & Pal and Geochemistry groups in Utrecht, some of you which helped me out often. I enjoyed your company, and although I might forget to mention some of you here, you're still in my head. Thank you Wout Krijgsman, Tanja Kouwenhoven, Sander Ernst, Ivo Duijnste, Sandra Langezaal, Hayfaa Abdul Aziz, Gert-Jan Reichart, Kees Hordijk, Elisa Guasti, Lennart de Nooijer, Jan van Dam, Douwe van Hinsbergen, Hans de Bruijn, Albert van der Meulen, Jan Willem Zachariasse, Wilma Wessels, Poppe de Boer, Cor Langereis, Tom van Hoof, Appy Sluijs, Henk Brinkhuis, Han Leereveld, Tim Lenssen, Klaudia Kuiper, Karoliina Koho, Martin Ziegler, Wolter Bosch, Lucy Stap and everybody else. For their strong support and help with the analyses of my samples I want to thank Arnold van Dijk, Geert Ittmann, Gerrit van 't Veld, Helen de Waard, Jan Drenth, Mark van Alphen, Tom van Hinte and Rinske Knoop. Special thanks to João Trabucho Alexandre for the work on my samples, we should definitely work things out in the near future!

People from abroad that have very much assisted me for which I am grateful: Eric deKaenel, Sandra Gaboardi, Silvia Iaccarino and Elena Turco. Katarzyna Bison and Helmut Willems are thanked for their pleasant company, their help with sample drilling and for extensive discussions during the field trip in Morocco. Nadia Barhoun is thanked for her help and hospitality in Morocco.

Filippo Biagianti, thanks for the good times in Utrecht and in Urbino and for being friends. We should definitely meet again soon!

Dank ook aan Margot Stoete, Ton Markus en Fred Trappenburg van Geomedia voor het realiseren van de layout van mijn proefschrift en voor hulp met het omzetten van mijn figuren (volgende keer geen Corel Draw, ok?).

Al mijn vrienden en bekenden (jullie weten wie jullie zijn) die mij in mijn 'proefschrift' periode hebben gesteund en opgevangen wil ik ook hartelijk bedanken.

Verder wil ik Erik de Bos bedanken voor zijn hulp met de omslag van mijn boekje en voor een goede vriendschap. Mijn ouders Roelf en Jannie hebben me altijd gesteund bij alles wat ik tot nu toe gedaan heb; jullie zijn zonder enige twijfel de fijnste ouders ter wereld. Mijn grootouders wil ik bedanken voor hun interesse in mijn onderzoek en de goede tijd die ik met hun heb gehad. Jammer dat we het op dit moment niet samen kunnen delen. Dank ook aan mijn broer Ronald en zijn vriendin Sumi voor vele goede tijden, en dat er nog maar vele mogen volgen. En, ten slotte, Krissie, bedankt voor je aanmoedigingen en liefde.

Curriculum Vitae

Erwin van der Laan was born on January 9, 1974, in the heart of Groningen. His teenage years he spent in the city of Hoogezand-Sappemeer, where at the age of 12 he decided to go to the Atheneum at the Aletta Jacobs Scholengemeenschap. After graduating here in 1992, he moved to the province of Utrecht where he started studying Geology at the University of Utrecht.

Under supervision of dr. Lucas Lourens, he performed his Master's research on the intriguing topic of the recognition of high-frequency astronomical variations (in the so-called sub-Milankovitch frequency band) in planktonic foraminiferal assemblages of the late Pliocene San Nicola section on Sicily in the Mediterranean. In 1999, he started working in the PIONEER project, initiated by dr. Frits Hilgen, on the impact of (sub-) Milankovitch variability on Neogene climate variability in the (circum-) Mediterranean. During his first period as a Ph.D, the promising results of his Master's research were further developed and incorporated in the Ph.D thesis of a colleague (Julia Becker) in the PIONEER group. He attended several fieldworks in Italy and northern Morocco, many under the inspired supervision of dr. Frits Hilgen, while developing his knowledge on cyclostratigraphy and sedimentary cyclicity in general. From the end of 2005 on, he started different jobs for various companies while working part-time on his Ph.D thesis.



Try to not control
 Try to not obey
 Try to not ignore
 Try to look
Try to understand
 Try to touch
those things in life
 of sheer beauty

